Analyzing subsidence in the Netherlands with attribute-enriched InSAR data

Marc F.D. Bruna

Technische Universiteit Delft

TU Delft Delft University of Technology

Challenge the future

[This page was intentionally left blank.]

Analyzing subsidence in the Netherlands with attribute-enriched InSAR data

by

Marc F.D. Bruna

in partial fulfillment of the requirements for the degree of

Master of Science
in Applied Earth Sciences

at the Delft University of Technology,
to be defended publicly on Wednesday March 11, 2020 at 2:00 PM.

Supervisor:	Prof. dr. ir. R. F. Hanssen,	TU Delft, Geoscience and Remote Sensing (CiTG)
Thesis committee:	Dr. ir. F. J. van Leijen,	TU Delft, Geoscience and Remote Sensing (CiTG)
	Prof. dr. ir. P. J. M. van Oosterom	TU Delft, GIS Technology (BK)

TU Delft Delft University of Technology

Preface

Almost a year of research has went by, and I am still learning so many new things in the field of radar remote sensing and surface deformation. It has changed my view on how to tackle problems and to see things from a different perspective. My fascination with the Earth as a system started at a young age. Therefore, I am thankful for the opportunities I have and my ability to work towards solving complex processes that can potentially benefit science, and the people that are affected by these processes.
In my bachelor program I have been given the tools and the necessary scientific knowledge to understand and discover the processes that shape the Earth as we know it, and the role of humans within this system. Since I am not only interested in the (deep) subsurface processes, my choice for the environmental engineering master program was based on incorporating the fields of remote sensing, hydrology and meteorology into my 'toolbox'. Since the topic of this research involves aspects of all these fields, while working towards a better environment, I am sure to have found my place in the fast-changing world of earth sciences and remote sensing.
This project would not have been possible without Ramon Hanssen, who I would like to thank for introducing me to the topic of radar interferometry and land deformation monitoring, and his excellent guidance and support throughout the entire project. I am also very thankful for the guidance and the constructive feedback of Freek van Leijen, who provided the necessary PSI datasets from SkyGeo. I would also like to thank Peter van Oosterom for sharing his expert knowledge on geographic information systems (GIS), which helped me in the implementation of the database management system used for the attribute-enrichment of the PSI points.
My gratitude goes out to my family and friends who were there through the whole process. I would like to thank my mother Huguette, my father Sierk and my sister Anne, who motivate me and make me strive for the best in everything I do. Finally, I am very grateful for the love and support from my girlfriend Daphne, who has somehow managed to bear with me throughout this endeavor.

Marc Bruna
Delft, March 2020

Abstract

Subsidence is affecting different parts of the Netherlands. The strongest subsidence is observed in the province of Groningen due to ongoing natural gas extraction. Subsidence is also observed at several locations in the province of South Holland, where the processes of peat oxidation, soil compaction and the withdrawal of groundwater are at the root of the problem. In South Limburg, the after-effects of coal mining are seen in the surface deformation, which is characterized by ground heave due to rising mine water, and the potential risks for sinkhole and local subsidence due to near-surface mining. Not only does subsidence cause damage to the natural and built environment, but it also increases the vulnerability towards flooding. Considering the rise in sea level, subsidence forms a pressing issue for low-lying countries, such as the Netherlands.

The combined efforts of interferometric synthetic-aperture radar (InSAR) data, global positioning system (GPS) points and gravity measurements have led to the recent Bodemdalingskaart 2018, which represents the nationwide subsidence in three statistically inferred products. These products are the the total surface deformation, the deformation caused by shallow subsurface processes, and the deformation caused by deep subsurface processes. This has triggered the discussion on how the deformation from 'shallow' and 'deep' processes can or should be better understood in a physical sense.

The aim of this research is to 'enrich' Sentinel-1 persistent scatterer interferometry (PSI) points with contextual information, i.e. 'attribute-enrichment', in order to better understand the origin of the observed deformation. Classifications from the Dutch 'basisregistraties' (base registries) are assigned to the PSI points, which are stored in a spatial database, using PostGIS as part of PostgreSQL. The classifications include information on the Dutch soil types and geomorphology, from the Bodemkaart and Geomorfologischekaart as part of Basisregistratie Ondergrond (BRO). The classifications from Bodemkaart are used in an analysis of nationwide extent, focused on the deformation behaviour of different soils and their groundwater levels. The nationwide average deformation of all track-results suggest subsiding trends of about -1.24 mm/yr for marine clay soils and -0.48 mm/yr for peat soils, whereas opposite trends of uplift are observed of, on average, +0.77 mm/yr for the river clay soils and +0.54 mm/yr for the sandy soils.

The soil and geomorphology datasets are also used in combination with the geographic classifications of the built environment from Basisregistratie Grootschalige Topografie (BGT) to study the distinction between deep and shallow-induced deformation in Groningen and South Holland. Here, the 2 $\times$2 km grid cell representation of deformation, applied in Bodemdalingskaart 2018 makes it possible to characterize areas with overall low PSI point density, e.g. the pastures in South Holland. In the localized deformation cases, the behaviour of classes from different attributes can be directly compared, e.g. road polygons intersecting with specific soil type polygons. For South Limburg, risk-assessment-based classifications by Heitfeld, Klunker, et al. 2016 are used to enrich the PSI points in the study the coal mining after-effects in the identified risk areas. The risk-deformation results suggest an overall slowing trend in the ground heave of the potential impact areas, which is in line with the overall decreasing rise in mine water identified in Heitfeld, Klunker, et al. 2016. The results from the case studies highlight the efficiency of attribute-enriched PSI datasets for the interpretation of deformation, based on both direct and indirect[1] physical classifications.

[1]For example, the classifications from potential risk zones are not directly based upon physical objects, but rather the assessment and the interpretation of physical processes that may potentially cause damage to the natural and built environment.

Contents

1

Introduction

The Earth's surface is part of a dynamic system, in which many physical processes alter its structure and properties. The results of these changes are observable in our everyday landscape. Where some physical processes, like the weather, are sensed over short periods of time, other processes are hardly noticeable from the human perspective. The latter is true for subsidence, which makes it an underrated problem. Subsidence, as part of land deformation in general, is a global phenomenon of which the causes and effects differ according to the environment it takes place in. With its history of land reclamation, and 26% of its land surface situated below mean sea level (MSL) (Schiermeier 2010), the Netherlands forms an interesting case as one of the many countries that faces the challenge of subsidence.

1.1. Subsidence in the Netherlands

Different surface deformation trends are observed in different parts of the Netherlands. The provinces of South Holland, Groningen, and Limburg present notable cases, frequently recurring in literature on the topic of subsidence in the Netherlands.

For centuries, coastal-deltaic subsidence and related relative sea-level rise have been observed and acknowledged in the Netherlands (Koster 2017; Blaupot Ten Cate 1910), adding to the country's vulnerability to flood events. As the coastal peatlands are drained for the creation of arable land, physical compaction and degradation by oxidation lead to subsidence and carbon dioxide (CO_2) emissions (Erkens, van der Meulen, and Middelkoop 2016).

In the northern part of the country, the Groningen gas field has shown considerable compaction and subsidence ever since its production started in the early 1960s (Thienen-Visser and Fokker 2017). The latest studies by the operator suggest that in 2080, the production induced subsidence at the center of the 'bowl' could be amount to anywhere between 50 and 70cm, and that seismic hazard in Groningen is largely attributed to tremors with magnitudes between 4.0 and 5.0 even at an annual probability of occurrence of less than 1% (de Waal, Muntendam-Bos, and Roest 2015).

Another display of ground movement in the Netherlands is observed in the South Limburg former coal mining areas. Extensive subsidence has occurred, exceeding 10m, as a result of longwall mining at depths of more than 800m (Bekendam and Pöttgens 1995). After abandonment of the last mines in the 1970s, the pumping of mine water ceased in 1994, leading to an ongoing rise in mine water. In turn this mine water rise causes ground heave and adversely affects the stability of roofs, pillars and shafts (Bekendam and Pöttgens 1995). Therefore, the risk for subsidence and the formation of sinkholes has increased in this area.

While subsidence-related damages for the Netherlands have occurred in the past, the future projections are not to be taken lightly. According to PBL (Planbureau voor de Leefomgeving), repairs and maintenance of infrastructure in urban areas due to structural damage from subsidence could sum up to €5.2 billion by the year 2050 (van den Born et al. 2016). In order for local water and environment authorities to intervene, the precise locations and rates of subsidence need to be known. To this end, the land deformation needs to be precisely monitored for extensive areas.

1.2. Monitoring Land Deformation

Land deformation monitoring has long been part of the geosciences and civil engineering. Spirit leveling used to be the conventional technique for measuring changes in elevation (USGS 2017). Developments in the field remote sensing imagery have facilitated the process of land deformation monitoring by providing high density measurements over large areas with mm-scale accuracy. InSAR (Interferometric Synthetic Aperture Radar), is known as the 'interferometric configuration' of the microwave imaging system Synthetic Aperture Radar (SAR), which allows for accurate measurements of the differential radiation travel path (Ferretti, Monti-Guarnieri, et al. 2007). The sensor of an Earth-orbiting satellite emits a radar signal, and subsequently the amplitude and phase of the backscattered signal are measured. When a second SAR measurment is performed of the same area at a later time, the deformation signal can be estimated, provided that the other phase contributers, e.g. the atmospheric delay, have already been removed. Thus, two SAR images are combined into a so-called 'interferogram', in which the interference of the two waves causes them to either reinforce or cancel one another (USGS 2016). Using interferometry, elevation can be derived for the creation of a digital elevation model (DEM). InSAR derived imagery can also be used for the optimal positioning of localized instrumentation, such as extensometers, leveling lines, and GPS networks (USGS 2017).

1.3. Shallow and Deep Subsidence

An important distinction is to be made between 'shallow' and 'deep' subsidence. As there is no fixed definition of these terms, in present literature these terms are used in different contexts. The distinction between shallow and deep subsidence has thus far been interpreted in different ways. One distinction found in the literature, i.e. Commissie Bodemdaling door aardgaswinning n.d. directly relates the labelling of 'shallow', 'deep' (and 'middle') to its causes, indicating the typical depths at which the causal processes take place. Another type of distinction between shallow and deep subsidence assigns them to the geological layers in which they are observed. A third and more recent distinction between the two is statistically based, as presented in (Bodemdalingskaart 2018). The three 'definitions' are introduced in the following subsections.

1.3.1. Causes & Depths

Following the terminology used in Commissie Bodemdaling door aardgaswinning n.d. 'shallow subsidence' is commonly referred to as the subsidence that takes place in the uppermost parts of the soil, typically at depths from 0 to 5m, resulting naturally from consolidation and settling. In the Netherlands, shallow subsidence is argued to be the result of the oxidation of organic material. The main anthropogenic cause identified for this oxidation process is the dewatering of rural peatland areas for agricultural usage.

The causes for deep subsidence take place at depths extending beyond 400m (Commissie Bodemdaling door aardgaswinning n.d.). Deep subsidence appears to be strongly tied to the extraction of hydrocarbons from the subsurface and to deep excavations for mining and/or construction purposes. Trends of deep subsidence are notably observed in the natural gas field of Groningen, and the salt mines in Groningen, Friesland and Overijssel. Natural causes for deep subsidence are attributed to tectonic activity and isostasy. Additionally, Commissie Bodemdaling door aardgaswinning n.d. uses the term 'middle-deep' subsidence to classify a third type of subsidence, typically at depths ranging from 20 to 400m. However, this categorization excludes any processes between 5m and 20m, which should also be considered. Anthropogenic causes for middle-deep subsidence would include the drainage of building excavations and the extraction of groundwater for consumption and industrial use, whereas the main natural cause of middle deep subsidence is identified as compaction (Commissie Bodemdaling door aardgaswinning n.d.).

1.3.2. Bodemdalingskaart Nederland

In the 'Actuele Bodemdalingskaart Nederland', or simply 'Bodemdalingskaart', presented in November 2018 by the NCG (Nederlands Centrum voor Geodesie en Geo-Informatica), the soil deformation measured between 2015 and 2018 is represented in the form of an interactive map (Bodemdalingskaart 2018). Measurements from three different observation techniques and data sets were used to this purpose, namely InSAR, GPS, and gravity measurements (TU Delft 2018). The distinction between shallow and deep subsidence has been implemented in the end product, where the user is given access to three

different map layers, showing deep, shallow or total subsidence, shown respectively in figures 1.1, 1.2, and 1.3.

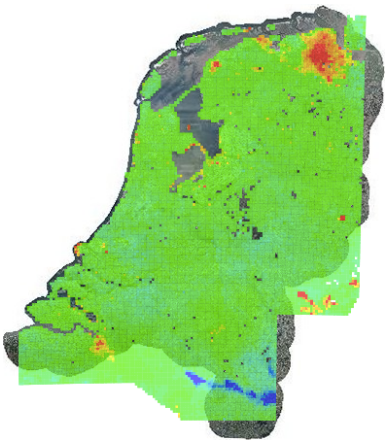

Figure 1.1: Subsidence (deep) (Bodemdalingskaart 2018)

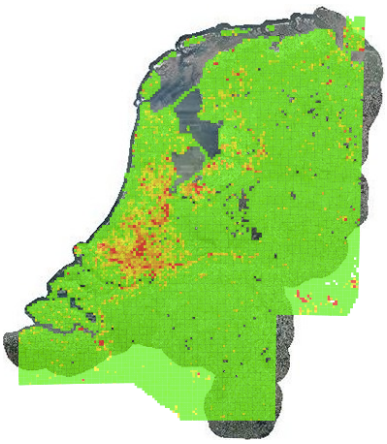

Figure 1.2: Subsidence (shallow) (Bodemdalingskaart 2018)

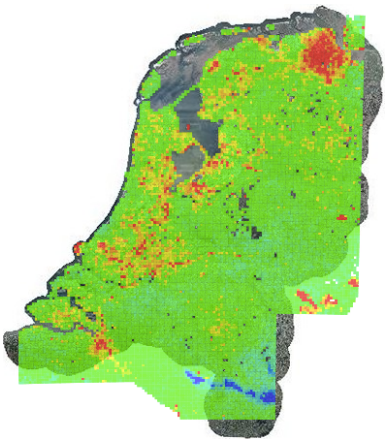

Figure 1.3: Subsidence (total) (Bodemdalingskaart 2018)

Each grid cell represents a 2 x 2 km area that can be selected in order to show a histogram of the distribution of the linear deformation (mm/yr) of all the data points it contains. Additionally, a time series is available for the selected grid point, showing the observed deformation with respect to the epoch in 2015, until the end of 2018[1]. Example outputs are shown in Figures 1.4 and 1.5 for a selected grid cell covering the northern part of De Lier in South Holland.

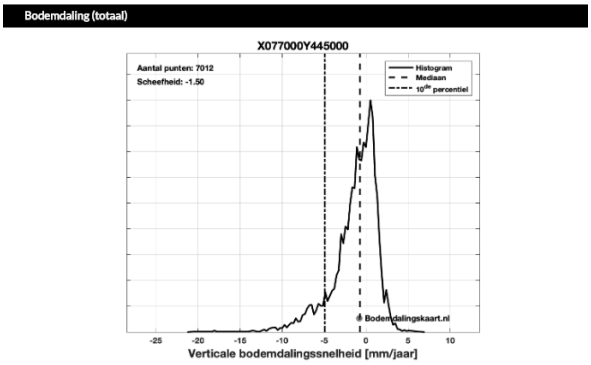

Figure 1.4: Histogram of subsidence in De Lier (total) (Bodemdalingskaart 2018)

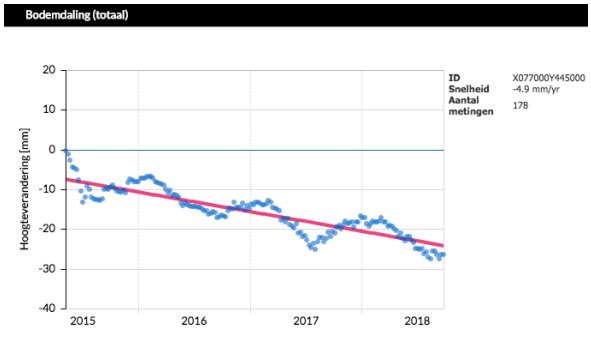

Figure 1.5: Time series of subsidence in De Lier (Bodemdalingskaart 2018)

As can be seen from the histogram, the distinction between the different types of subsidence is made based on statistical descriptors of the data points in the grid cell. Since most deformation data points are returned from stable objects, oftentimes coinciding with buildings and infrastructure that are founded on relatively deep subsurface layers and therefore provide coherent return signals, the median of the distribution is selected to represent deep subsidence. The value for total subsidence is selected as the 10th percentile of the distribution. This means that 10% of the measurement points are subsiding at a higher rate than the indicated value for total subsidence. Lastly, the shallow subsidence is set as the difference between the total and deep subsidence (Bodemdalingskaart 2018).

1.4. Research aim

This study focuses on the relationships between the InSAR deformation points and the environment that these characterise. A database approach is used to determine these relationships, by involving external classifications to enrich the InSAR observations. The possible links between the InSAR points and the

[1]This period holds for the latest update on November 18, 2018 and varies slightly per selected grid point.

physical characteristics of the natural and anthropogenic environments they represent can be used to explain the observed deformation trends themselves or their acquisition. Of particular interest for this study is the partitioning between deep and shallow subsidence, which has gained interest in recent years, ever since the causes and effects of deep vs. shallow subsidence have proven to differ substantially. In light thereof, the aim of this research is to better understand the distinction between shallow and deep processes that lead to surface deformation in the Netherlands, which leads to the main research question:

Can subsidence due to deep and shallow causes be differentiated using attribute-enriched PS-InSAR data?

To this end, the InSAR derived deformation is enriched with auxiliary datasets to characterize the deformation patterns observed in the Netherlands. A database approach is applied, which is meant to facilitate the discovery and characterisation of the InSAR observations. In order to answer the main research question, two sub-questions are presented, which serve as the main framework of this research;

1. What are the deformation trends observed in the Netherlands, and how do they relate to the country's soil distribution?
2. How does anthropogenic activity impact the deformation of the Dutch surface, and can these impacts be quantified?

The attribute-enrichment of the InSAR observations may bring new ideas or developments to the current version of the Bodemdalingskaart, which could be further explored and even applied. For example, the addition of a middle-deep subsidence map layer could be realized and implemented.
A series of additional questions is composed in order to clarify or expand on certain cases, ideas and topics throughout this study:

- Do the InSAR-estimated shallow deformation results accurately reflect the susceptibility of water-drained peatlands to (further) subsidence?
- Do the InSAR-estimated deep deformation results accurately reflect the natural gas -and salt extraction areas prone to (further) subsidence?
- If the aforementioned questioning cannot be not confirmed, which other physical -and/or environmental mechanisms are at hand in the subsiding areas?
- How do these (other) mechanisms appear in the InSAR product, and can the estimation thereof be further improved?
- Do the findings fit in the broader geological, geodetic, geographical, and hydrological context of the formation and evolution of the Netherlands?

1.5. Outline

With the current state of the research on subsidence and deformation monitoring, recent developments in this field have been discussed as these have pushed this topic forward. The outline of this study is as follows; First, a general theoretical background is given on surface deformation, including subsidence itself, and where it fits in the geological development of the Netherlands. Chapter 3 introduces the InSAR and PSI techniques, which make it possible to obtain large scale deformation data. In the next chapter, a database approach is presented and implemented in order to link the InSAR deformation data to their environment, which is characterized with the use of classifications or 'attributes'. Considering the two sub-questions, two approaches are applied in order to make the coupling that is set up in Chapter 4; The nationwide deformation analysis in Chapter 5 analyses the deformation trends of the main soil type groups observed in the Netherlands. Local analyses are presented in Chapter 6 in the form of case studies to focus on the deformation trends observed at three locations;

1. The uplift in former mining areas in South Limburg.
2. Shallow subsidence due to oxidizing peat lands in South Holland.
3. Deep subsidence attributed to natural gas extraction sites in Groningen.

In addition to the discussions provided on the various topics in their respective chapters, the concluding chapter aims to extract the most relevant findings.

2

Deformation Background

This chapter provides a theoretical background on the processes of subsidence and land deformation in general, and how these processes fit within the geological framework of the Netherlands, starting from the Carboniferous period (358.9 Ma ago) and extending to the more recent changes in the Dutch landscape, through changing land use as part of anthropogenic activity.

2.1. Subsidence

Subsidence is defined as 'the sudden sinking or gradual downward settling of the ground surface' (Neuendorf, Mehl Jr., and Jackson 2005), predominantly along the vertical axis. When using the term 'subsidence' to describe the gradual sinking of part of the Earth's surface, the associated velocities are typically expressed in units of mm/yr. Other cases involve subsidence as the near-instantaneous sinking of the surface, also known as sinkhole formation. Various causes have been identified for subsidence, often labeled as either 'anthropogenic' or 'natural' in type. For both types, the most commonly identified causes for subsidence are presented in the following sections.

Natural causes

Common natural processes that cause subsidence include plate tectonics, compression, compaction, consolidation and oxidation of organic material. These processes, unfolding at different spatial and temporal scales, involve different mechanisms in the process of subsidence. It is possible for different subsidence-inducing mechanisms to occur simultaneously and they can influence one another.

Plate Tectonics – Tectonic subsidence affects large areas through crustal plate movement and the accommodation of spaces created by faulting (Xie and Heller 2006). Extension, cooling and loading are the three mechanisms that are most common in tectonic environments where subsidence occurs (LSU Center for Geoinformatics n.d.);

- Extension – The Earth's crust stretches until faulting occurs, either by a system of normal faults, creating typical horst and graben structures, or by a system of listric faults, which means that the faults shallow with depth. Both faulting systems are depicted in Figures 2.1 and 2.2. As the region stretches, the thickness of the deformed crust decreases, which makes it prone to subsidence (Ceramicola et al. 2005).
- Cooling – As the lithosphere stretches and thins in rifting regions, a passive upwelling of the hot underlying asthenosphere occurs to replace the thinned mantle. During this process the asthenosphere cools and as a result of the associated densification of the mantle, subsidence is caused (McKenzie 1978).
- Loading – Through sedimentation from erosion or orogenic processes, load is applied to a low elevation accommodation space, causing subsidence in the same area (LSU Center for Geoinformatics n.d.).

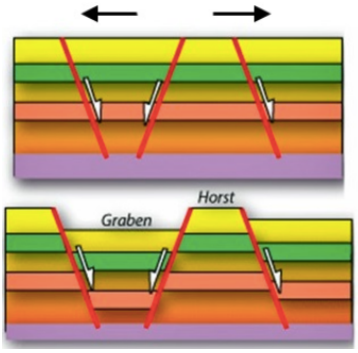

Figure 2.1: Horst-graben faulting system (Source: USYD 2003).

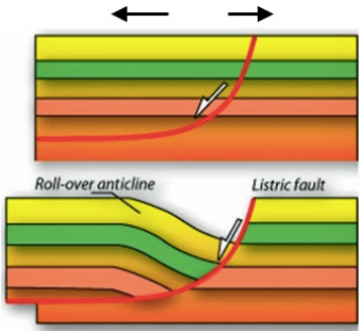

Figure 2.2: Listric faulting system (Source: USYD 2003).

Compression & Compaction– Even though the terms compression and compaction are often used interchangeably, they have different meanings. Compression is the change in in soil volume produced by the application of a static external load, whereas compaction is artificially produced by the momentary application of load, such as rolling, tamping or vibration (USDI 1974).

Consolidation – With consolidation, a volume change in saturated soils is caused by the expulsion of pore water and air from weight acting on it (UMass 2013).

Soil oxidation – The process by which organic carbon is converted to CO_2 and lost to the atmosphere is known as oxidation (Young 1980). As a biochemical process, oxidation is caused by microorganisms that utilize organic compounds as a source of energy and carbon (de Glopper and Ritzema 2006).

Anthropogenic causes

Subsidence can be the result of human activity. As briefly discussed in the first chapter, the extraction of subsurface resources, such as natural gas, coal, salt, and groundwater can lead to deep subsidence. Due to its localized nature, the rate, location and extent of mining-induced subsidence is relatively predictable. The extraction of hydrocarbons, such as oil and natural gas, leads to a reduction of formation fluid pressure and the subsequent compaction of reservoir rocks. Additionally, existing fractures are enhanced or new ones are created altogether (Gurevich and Chilingarian 1993). To a lesser amount, horizontal displacements may occur, as coupled stress-strain fields develop due to the withdrawal of fluids. However, this coupling is weak in most hydrogeological settings (Gambolati, Putti, and Teatini 1996). As an illustrative example of gas extraction driven subsidence, the primary and secondary ground motion mechanisms, are displayed in figure 2.3, based on TU Delft DeepNL n.d.

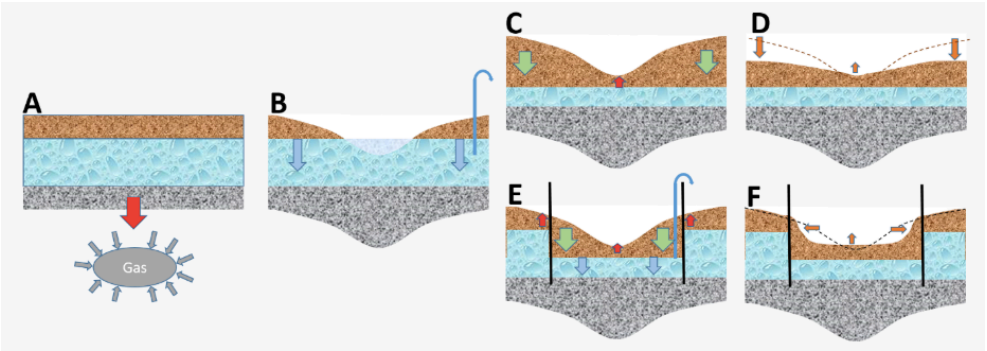

Figure 2.3: Primary and secondary ground motion steps, resulting from gas production on an area composed of organic soils (brown), and a groundwater table (blue). (A) Gas extraction acts as the main mechanism that causes subsidence. (B) The Water table rises to eventually form a lake. (C) Groundwater pumping yields compaction and oxidation (green arrows), and upward pressure yields uplift (red arrow). (D) The primary subsidence bowl widens and veers up in the center. In case of compartmentalization, (E) areas with an increased unsaturated or 'vadose' zone subside and vice versa. (F) Stronger spatial gradients deform the surface (Image and description source: TU Delft DeepNL n.d.).

Aside from the extraction of subsurface elements, the mere change in land use is enough to cause subsidence. Changes in land use can alter the hydrological system or increase the loading of the delta surface, resulting from increased agricultural production, population growth and urbanization (Minderhoud et al. 2018). This is especially true in developing countries, which show the highest rates of population growth and associated urbanization and land use. Amongst other countries with deltaic zones, the Netherlands shows similar developments in terms of its land use over a relatively limited space. Even though soil oxidation is listed under the natural causes of subsidence, the artificial lowering of the water table adds to this process.

2.2. Surface deformation in the Netherlands

To introduce the country's spatial and temporal deformation frame, the geological setting of the Netherlands is discussed according to the different sedimentary successions that have taken place. Concluding the timeline of sedimentary successions, the relatively recent developments in the country's surface deformation are discussed, regarding the influence of anthropogenic activity.

2.2.1. Sedimentary Successions

An overview is given of the sedimentary successions that have shaped the Netherlands. Following the geologic time scale (GTS), the geology of the Netherlands is characterized by the following geological era's; the Paleozoic Era (541 – 251.902 Ma ago), the Mesozoic Era (251.902 – 66 Ma ago), and the Cenozoic Era (66 Ma ago – present day), each discussed separately. Figure 2.4 serves as the geochronological reference for this geological overview.

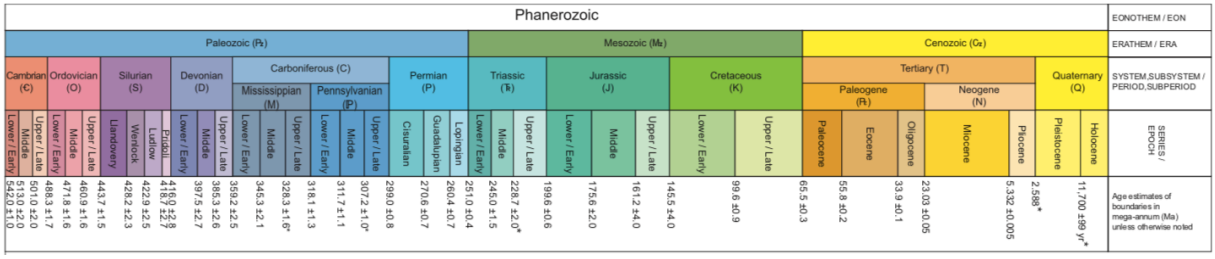

Figure 2.4: Geological timeline of the Phanerozoic Eon (Source: USGS 2010).

Paleozoic (541 – 251.902 Ma ago)

Paleozoic rocks occur only locally at or near the surface along the Netherlands' eastern and southern borders (Wong, Batjes, and Jager 2007). Outcrops from the Carboniferous period (358.9 – 298.9 Ma ago) are located in the Heimans Quarry in Limburg, near the village of Epen (Deltawerken 2004). Younger sediments from the Permian period (298.9 – 251.902 Ma ago) play an important role for the oil and gas reserves of the Netherlands. Parts of this layer, mainly eolian sandstones from the Rotliegend unit (lower Permian), act as a reservoir rocks for the Slochteren natural gas production fields in Groningen (Deltawerken 2004).

Mesozoic (251.902 – 66 Ma ago)

Depositions from the Triassic period (251.902 – 201.3 Ma ago) mark the start of the Mesozoic Era. These include sandstone, evaporite, chalk, dolomite, gypsum and shale, of which the latter has fully eroded (Deltawerken 2004). Subsequently the Jurassic period (201.3 – 145 Ma ago) is characterized by a 20 million year long sedimentation process, with the formation of petroleum-bearing rocks that make up the petroleum-rich soils in the North Sea (Deltawerken 2004).

During the Early Cretaceous, rifting tectonics of the Jurassic changed into regional subsidence. In addition, the rising sea level lead to sedimentation over platforms and highs, as it was previously restricted to basins (Wong, Batjes, and Jager 2007). Various Lower Cretaceous sandstones are excellent reservoirs, and may be oil or gas bearing (Wong, Batjes, and Jager 2007). For example, the Bentheim Sandstone of the Schoonebeek production field are underlain by the lacustrine Coevorden Formation, which acts as the source rock.

Cenozoic (66 – 0 Ma ago)

Mesozoic sediments were covered with younger sediments, among which clay layers from the Oligocene (33.9 – 23.03 Ma ago) that are mined in quarries for brick production (Deltawerken 2004). Miocene (23.03 – 5.333 Ma ago) quartz and brown coal were formed in the southeastern part of the Netherlands (Deltawerken 2004). The Rhine and the Meuse rivers, as we know them today, were formed during the Pliocene (5.333 – 2.58 Ma ago), transporting erosion material into the country (Wesselingh n.d.). During various ice ages, the advancing ice changed the rivers' courses (Deltawerken 2004).
Most of the recent Netherlands was formed during the Pleistocene (2.58 – 0.0117 Ma ago) and the current Holocene (11,7 – 0 ka ago). Depositions of the Early Pleistocene are mostly found in the northern parts of Brabant and Limburg where river terraces, i.e. 'Maasterrassen' can be observed in the landscape (Wesselingh n.d.). In the Middle Pleistocene, moraines, e.g. the Veluwe and Utrechtse Heuvelrug, were formed as the result of the maximum expansion of the Scandinavian glaciers reaching the Haarlem-Nijmegen line (Wesselingh n.d.). The subsequent Late Pleistocene was characterized by alternating transgressions and regressions, with layers of marine clay being deposited over peat layers (Deltawerken 2004).
At the end of Weichselien (116 – 11,7 ka), known as the last glacial, the average temperature rose, which lead to melting of the ice caps and subsequent sea level rise of about 120 m. The resulting transgression was accelerated by glacio-isostatic subsidence. This subsidence was the effect of the rising lithosphere in Scandinavia, moving back into place after the weight of its ice caps decreased because of melting. With the pivot point situated in Denmark, subsidence occurred for the Netherlands and Belgium (Wikipedia contributors 2018). Thus, approximately 7000 years ago, large parts of the western Netherlands were situated below sea level, where nowadays marine clay deposits are found (Wesselingh n.d.). The eastern land side of the Netherlands was characterized by river areas, and freshwater marshes alternated by natural levees. Moderate oak and linden forests developped on the more elevated sand soils (Wesselingh n.d.). In summary, Holocene deposits are divided into river deposits, such as clay, sand and gravel from the Formation of Echteld, peat from the Formation of Nieuwkoop, local aeolian sand deposits from the Boxtel Formation, and marine clay from the Westland Formation (Deltawerken 2004). At the end of the Neolithic (11 – 3 ka), the sea level reached it current position, as the coastline regressed back to the north and west. At that time, the landscape was changed through fluvial outwash and the formation of peat (Wesselingh n.d.). Also the influence of humans increased, as they rapidly started shaping the Dutch landscape to their needs.

2.2.2. Anthropogenic Activity

Since the emergence of the human race in the Quarternary, divided into the Pleistocene and the Holocene, humans have started shaping the environment. However, their influence remained relatively limited until around 5300 – 2000 BC (in the Neolithic), with the introduction of agriculture (Wesselingh n.d.). With the development of tools made from stone, and later from bronze and iron, advances were made in the processes of deforestation, agriculture and the construction of settlements.

Peat Cultivation & Dredging

In the late Middle Ages, around 1050 to 1500, the reclamation of peat marshlands started with the construction of dikes along rivers and the coastline, and the dewatering of peatlands through ditching (Wesselingh n.d.). In this period, the 'Grote Ontginning' (large extraction or reclamation) took place in the low plains of Holland and Utrecht. New technologies were developed to ease the process of dredging, such as the 'baggerbeugel' or 'dredging bracket' for so-called 'slagturven' (Wikipedia contributors 2018). Peat was also cultivated for domestic and crafting use as burning fuel instead of wood, which became more scarce as the population kept increasing (Wikipedia contributors 2018). Because of the widespread dredging activities, lakes and ponds emerged in the same areas, for example the Loosdrechtse plassen and the Vinkeveense plassen. Many of the moors were drained, and changed into the polders (Wikipedia contributors 2018).

Water Management & Flood Control

Resulting from the All Saints' Flood in 1170, and a series of storm surges in the 13th century causing erosion, former Lake Flevo was turned into a sea known as the Zuiderzee (Wikipedia contributors 2018). However, with the construction of the the 32.5 km long Afsluitdijk in 1932, this water body was again separated from the Wadden Sea in what is nowadays known as the IJsselmeer (Wikipedia contributors

2018). Improved flood protection works, known as the 'Delta Works', were rapidly conducted after the North Sea flood in 1953. These works involved the construction of dams, sluices, locks, dykes, levees and storm surge barriers to protect a large area around the Rhine-Meuse-Scheldt delta in the provinces of Zeeland and South Holland (Wikipedia contributors 2019c).

Resource Extraction

In relation to the observed total, shallow and deep causes for subsidence, and the country's sedimentary successions, the Netherlands is rich in natural resources. From the beginning of the 20th century to the midst of the 1970s, coal mines dominated the South Limburg area (TU Delft 2014). These coal layers date back to the Upper Carboniferous (Westphalien) age (313 – 304 Ma ago). Even though mining activities in the area can be traced back to the 12th century (Heitfeld, Klunker, et al. 2016), increased industrialisation and urbanisation in the 20th century sharply increased the demand for coal.
The same coal seams, mined in South Limburg, are present at larger depths between 3 and 4 km in the northern part of the Netherlands (TU Delft 2014). However, because of high temperatures and the lack of oxygen a this depth, the coal is degassed and the released CH_4 (methane) is trapped and conserved for million years in the porous sandstones of the Permian Rotliegend (TU Delft 2014). This is where the gas of the Slochteren field originates from. With its 900 km^2 area and total originally recoverable volume of 2700 billion m^3, the Groningen field is one of the largest natural gas fields in the world (NAM 2011). The Groningen gas was first discovered in 1959 by the Nederlandse Aardolie Maatschappij (NAM), and production started in the same year (NAM 2011). Currently, almost all of the Dutch houses are dependent on gas for central heating and hot water supply. In addition, gas is used as fuel on a large scale for the production of electricity.

2.2.3. Effects of Subsidence on Natural & Built Environment

As previously stated, the artificial lowering of the water table in the rural peatland areas, mainly used as permanent pasture. This dewatering process, with ditchwater levels up to 60 cm below surface (Recare-Hub 2018), comes at the cost of shallow subsidence. Periods of extensive drought add to the oxidation process in these areas, causing further subsidence. Due to subsidence in the inner dike areas of canals and other water bodies, elevation differences between the inner and outer dike areas are gradually increasing (Wikipedia contributors 2018), which increases the vulnerability of these areas to floods.
The remnants of the concessions of the Dutch State Mines (DSM), as well as state-owned mining areas, are still negatively affecting the natural and built environment of South Limburg. Abandoned shafts form risks of subsurface collapses and sinkhole formation, whereas ground heave is observed as a consequence of rising mine water (Heitfeld, Klunker, et al. 2016). The natural gas production activities in Groningen have shown to cause subsidence and tremors in the production fields and their surroundings, causing damages to houses and infrastructure. Additionally, due to increased water tables in the same areas, the construction of dikes, locks and pumping stations is hampered. After major dissatisfaction of the local residents and communities, the production of the Groningen-field has been lowered significantly and damage compensation measures have been implemented in recent years. In September of 2019, the Dutch government has stated that the gas extraction in Groningen will be terminated by 2022 (NOS 2019).

3

Radar Interferometry & The PS-InSAR Technique

The gathering of knowledge and data in the field of subsidence has benefited greatly from recent contributions in the field of remote sensing. With the emergence of radar interferometry, it is possible to obtain mm-scale measurements over extensive areas. Recent developments in the field of radar remote sensing are useful for a wide range of geophysical applications and the monitoring of natural hazards, slope stability, subsidence, and surface deformation in general. This chapter provides a theoretical overview on InSAR theory and the developments in radar interferometry, leading up to the PS-InSAR technique.

3.1. Radar

Radar, an acronym for 'RAdio Detection and Ranging', refers to a method, system, or technique, using beamed, reflected, and timed electromagnetic radiation to detect, locate, or track objects, to measure altitude and to acquire a terrain image (ESA 2014). The radar system uses a transmitter to produce electromagnetic signals, or pulses, which radiate at microwave to radio wave wavelengths into space by a transmitting antenna. The microwave and radio wave parts of the electromagnetic spectrum are presented in Figure 3.1.

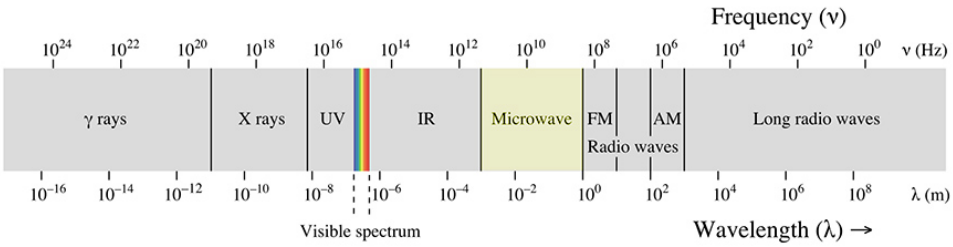

Figure 3.1: The electromagnetic spectrum is divided into different wave groups, of which the microwave domain is highlighted in yellow. The frequency ν-values are presented along with their respective wavelengths λ. (Source: HSU n.d.)

The reflected pulses are detected by a receiving antenna, which is oftentimes also the transmitting antenna. In this case we speak of a monostatic radar, whereas for a bistatic radar the transmitting and receiving antennas are physically separated (Skolnik 1962). The two-way travel time of the pulse is used to determine the range to the detected object and its backscatter intensity to infer physical quantities such as size or surface roughness (Hanssen 2001). Radio waves are only weakly absorbed by the medium through which they travel, enabling long range detection. Since atmospheric moisture is mostly transparent to radio waves as opposed to visible light, the observations are not hampered by unfavorable weather conditions and cloud cover. As an active remote sensing technique, the use of

radar for long range detection does not depend on natural illumination. Hence, radar systems operate both in daytime and at nighttime[1].

3.2. SAR

Synthetic Aperture Radar (SAR) is a coherent, mostly airbourne or spacebourne sidelooking radar system, which utilizes the flight path of the moving platform to simulate a large antenna or 'aperture' (Radartutorial n.d.). The imaging product either comes in the form of a two-dimensional image or that of a three-dimensional reconstruction of a target object (Kirscht and Rinke 1998). A typical SAR installation consists of a radar that is mounted on a moving platform, i.e. an aircraft or a satellite, with the antenna directed perpendicular with respect to its direction of movement (van der Horst 2017). A 'synthetic aperture' is produced by using the forward motion of the radar (ESA n.d.[b]). As the radar moves forward, it sequentially records the individual return pulses from a given scatterer. The combination of all the recorded signals is used to compute the synthetic aperture, which provides a much improved azimuth resolution (ESA n.d.[b]) of about three orders in magnitude (Hanssen 2001). A simplified representation of the geometry of a typical SAR system can be found in Figure 3.2.

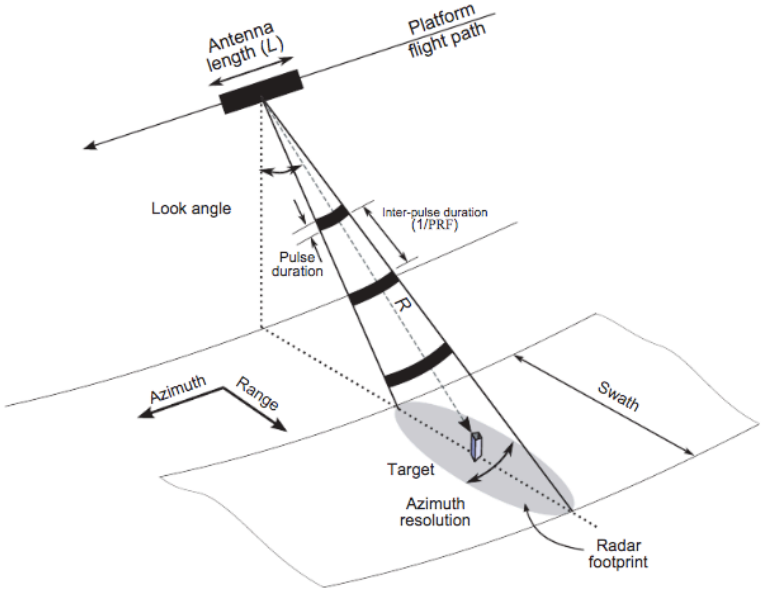

Figure 3.2: Radar imaging system geometry. As the satellite moves along the platform flight path, the antenna with length L is oriented 'sideways', perpendicular to its flight path at a certain look angle within the vertical plane. The swath plane, which is parallel to the flight path contains the radar footprint, shaded in the image. The distance from the antenna to the target is denoted by R, the slant range. Pulses of a certain duration are transmitted at a certain rate called the 'Pulse Repetition Frequency' (PRF) (Source: Bouaraba, Belhadj-Aissa, and Closson 2018).

3.2.1. Measurements: Amplitude & Phase

Two different quantities can be inferred from a typical SAR return signal, namely its amplitude and phase. As one type of the signal's retrievable information, the amplitude A is a measure for the strength of the reflection's intensity I, where $I = A^2$ (Simons and Rosen 2007).
The other useful quantity from the return signal is the phase. As the transmitted signal or 'chirp' is sinusoidal in nature, the delay τ is equivalent to a phase change ϕ between the transmitted and received signals. The phase change is proportional to the two-way travel distance $2R$ of the radiation, divided by the transmitted wavelength λ (Ferretti, Monti-Guarnieri, et al. 2007)

$$\phi = \frac{2\pi}{\lambda} 2R = \frac{4\pi}{\lambda} R. \tag{3.1}$$

[1]Radar imaging systems belong to the category of 'active' remote sensing techniques, as these systems emit their own radiation. Passive sensors, on the other hand, rely on naturally occurring energy, e.g. the sun illuminating the Earth.

The sinusoidal signal is illustrated in Figure 3.3.

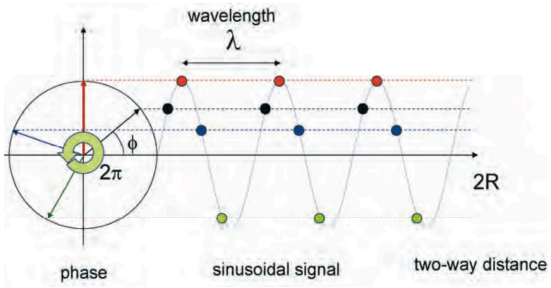

Figure 3.3: Sinusoidal signal $sin\phi$ with a 2π period. For a relative narrow-band SAR, the transmitted signal can be assimilated as first approximation to a pure sinusoid, with a linear dependence on the slant range coordinate R given by: $\phi = 2\pi R/\lambda$. Assuming a phase of the transmitted signal of zero, the received signal covers a distance of $2R$, showing a phase: $\phi = 4\pi R/\lambda$ (Source: Ferretti, Monti-Guarnieri, et al. 2007).

For radar images, each individual pixel contains radiometric information about the reflection it represents. Following Hanssen 2001 and van Leijen 2014, the total measurement for an individual pixel is denoted by the 'complex phasor' P, combining both the amplitude A and the fractional phase ψ of the received signal (Hanssen 2001; van Leijen 2014)

$$P = A\exp(i\psi). \tag{3.2}$$

With this complex notation of P, the real and imaginary parts, as part of a regular grid, are written as: $\mathrm{Re}(P) = A\cos(\psi)$ and $\mathrm{Im}(P) = A\sin(\psi)$ (van Leijen 2014). The relation between the real and imaginary parts and the amplitude A and range dependent phase ψ is (van Leijen 2014)

$$A = \sqrt{(\mathrm{Re}(P))^2 + (\mathrm{Im}(P))^2}, \tag{3.3}$$

$$\psi = \arctan\left(\frac{\mathrm{Im}(P)}{\mathrm{Re}(P)}\right). \tag{3.4}$$

3.3. InSAR

InSAR implements the interferometric combination of two SAR images, wich allows for accurate measurements of the radiation travel path through its coherence (Ferretti, Monti-Guarnieri, et al. 2007). With two or more SAR images, a map showing elevation or deformation can be estimated by using phase differences of the return waves (Hanssen 2001). At least one imaging parameter for the second SAR image should be different in order for it to provide additional information; i.e. flight path, acquisition time, or wavelength (Bamler and Hartl 1998). In terms of a difference in distance between two acquisition positions, this is referred to as the 'baseline'. Figure 3.4 shows a typical interferometry configuration, where the master and slave positions are shown with the baseline in between them.

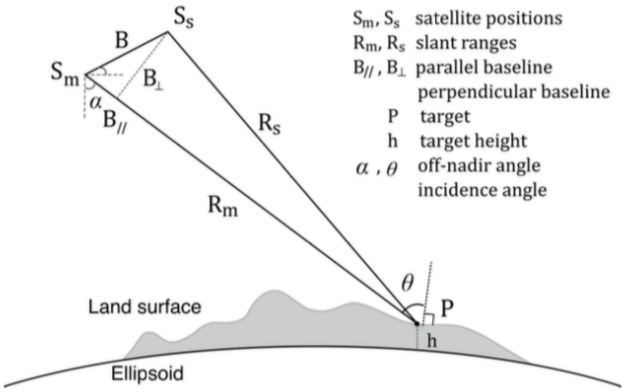

Figure 3.4: InSAR geometry configuration w.r.t. the land surface and the ellipsoid showing the master and slave positions, denoted with subscripts m and s respectively. The baseline B is shown with its alternative geometrical representations, i.e. parallel and perpendicular projections (Source: Xiong, Muller, and G. Li 2017).

The phase and amplitude information of the original SAR data is retained in the Single Look Complex (SLC), which is suitable for interferometric processing (NUS n.d.). In the following subsections, the SLC and interferometric phase are further discussed, along with the interferometric phase contributors; i.e. the flat Earth phase, the topographic phase, and the deformation phase. The latter is presented in greater detail, along with a three-dimensional decomposition of the deformation vector, which is particularly relevant for the scope of this study. In addition, a functional overview is provided on the typical InSAR processing steps involved in generating interferograms, and subsequently; elevation and deformation maps.

3.3.1. The SLC phase

As a typical level-1 product, intended for data users, SLC images are images in the slant range by azimuth imaging plane, within the image plane of the satellite acquisition (ESA n.d.[a]). Two SLC images, i.e. the master and the slave, are used to derive the interferometric phase. Level-1 SLC products consist of focused data with preserved phase information. To obtain these focused images, the orbit and altitude data from the satellite are used and provided in a zero-Doppler slant-range geometry (ESA n.d.[a]). Two SLC images serve as input for the generation of an interferogram (ESA 2007). For each individual pixel, the SLC phase is denoted by (van Leijen 2014)

$$\psi = -2\pi a + \psi_{\text{range}} + \psi_{\text{atmo}} + \psi_{\text{scat}} + \psi_{\text{noise}} \tag{3.5}$$

where a is the phase ambiguity, i.e. the number of full phase cycles, $[-\pi, +\pi]$, and the phase terms ψ relate (in order of appearance) to:

The range dependent phase – This term relates to the two-way geometric distance between the antenna and the scattering center[2](van Leijen 2014).

The atmospheric delay – Spatial heterogeneities in the atmospheric refractive index cause differences in the InSAR observations (Z. Li et al. 2019). Two terms in the atmospheric delay can be identified: the ionospheric and the tropospheric term[3]. In the ionosphere, the ultraviolet solar radiation ionizes the gas molecules present, as free electrons are released. As such, the electron density, or 'total electron content' (TEC), in the ionosphere varies with the diurnal cycle. Thus, the magnitude of the atmospheric delay is influenced by the state of the ionosphere as the signal passes through (Penn State College of Earth and Mineral Sciences 2018). Ionospheric effects usually affect the radar signal at large spatial scales, and have a limited effect on C and X-band interferograms (Z. Li et al. 2019). The tropospheric

[2]The virtual phasor location, resulting from coherent, i.e. 'similar', reflecting elements in the resolution plane (van Leijen 2014)

[3]The ionosphere extends between 75 and 1000km altitude. The troposphere extends between 0 and 16km in the tropics, and between 0 and 10km in the polar regions (McGraw-Hill 2014).

delay, or 'neutral' atmospheric delay, introduces errors in land surface motion estimates as it masks the various surface deformation mechanisms, e.g. tectonic activity, volcanic deformation, or glacier motions. On the other hand, the neutral delay can be useful in high-resolution mapping of non-differential atmospheric water vapor distributions (Z. Li et al. 2019).

The scattering phase – For 'point scatterers', i.e. a strongly reflecting object dominating the reflection, clutter originates from the object's surroundings. The case in which multiple smaller scattering objects together form the measurement, is referred to as 'distributed scattering' (van Leijen 2014).

The phase noise – Sources of signal 'decorrelation', relating to the phase standard deviation of the interferogram, include thermal and instrumental (i.e. processor) noise, differential and volumetric scattering, rotation of the satellite viewing geometry, and random motions over time (UNAVCO 2014).

Concluding, spatial and temporal decorrelation along with the atmospheric signal delay are the main error sources that limit the applicability of conventional InSAR techniques. Persistent Scatter Interferometry (PSI), as a time series approach to overcome these limitations based on the phase coherence of point scatterers (van Leijen 2014), is introduced and discussed further on in this chapter.

3.3.2. The interferometric phase

The interferometric phase is expressed according to its contributing terms as (van Leijen 2014; van der Horst 2017)

$$\phi^{ms} = \psi^{m} - \psi^{s}, \tag{3.6}$$

$$= -2\pi a + \phi_{\text{flat}} + \phi_{\text{topo}} + \phi_{\text{defo}} + \phi_{\text{atmo}} + \phi_{\text{scat}} + \phi_{\text{noise}} \tag{3.7}$$

where the interferometric phase ϕ^{ms} for a pixel is the difference between the master ψ^{m} and the slave ψ^{s} images. Most of the recurring subscripts represent similar contributions as their SLC counterparts in equation 3.5. The interferometric scattering phase ϕ_{scat} describes the difference in scattering characteristics between two separate acquisitions. Along with changes due to ϕ_{noise}, the combined effect results in signal 'decorrelation' (van Leijen 2014). The 'coherence' is a quantitative expression of the measure of decorrelation $\gamma \in [0, 1]$, and can be understood as the correspondence between two complex observations (van Leijen 2014). Amongst others, two main types of decorrelation are to be distinguished: geometric and temporal decorrelation. Geometric decorrelation results from non-overlapping spectral bands caused by a large baseline separation B in repeating orbits (van der Horst 2017; Hanssen 2001). Temporal decorrelation refers to changes in the surface's scattering characteristics over time for a resolution cell (van der Horst 2017; van Leijen 2014).
Several new differential phase terms: ϕ_{flat}, ϕ_{topo}, and ϕ_{defo} are introduced in equation 3.7, respectively denoting:

The Flat Earth phase – The phase contribution of the reference ellipsoid (included in Figure 3.4) is called the 'Flat Earth' phase, which represents the reference surface in the absence of topography.

The topography phase – The phase contribution of topography with respect to the reference ellipsoid is described by the topography phase term.

The deformation phase – Surface displacement is captured by the deformation phase term. As the deformation phase is of particular interest for this study, its contribution is discussed separately in the next subsection along with a vector decomposition of the deformation in a three dimensional space.

Alternatively, an additional term ϕ_{orb} could be added to equation 3.7, as errors are introduced in the orbiting parameters between the master and the slave acquisitions (van Leijen 2014). However, in this expression of the interferometric phase, the orbital error source is considered as part of the ϕ_{noise}-term.

3.3.3. Decomposition of the 3D deformation vector

Like the Flat Earth phase and the topography phase, the surface deformation phase can be inferred from changes in the signal travel path. As such, a differential phase term can be written for deformation (van Leijen 2014)

$$\phi_{\text{defo}} = \frac{-4\pi}{\lambda} D_{\text{LOS}} \tag{3.8}$$

where D_{LOS} is the measured deformation in the line of sight (LOS). The LOS deformation can be decomposed into both vertical and horizontal deformation components. This allows for a three dimensional vector representation of the deformation, denoted by three components: D_e, D_n, and D_u (or D_v), which represent the deformation along the East, North, and Upward direction respectively. As such, the LOS deformation measurement is a projection of the 3D deformation vector in the LOS direction (van Leijen 2014).

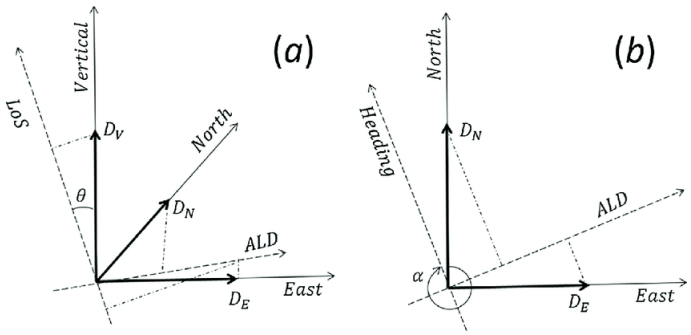

Figure 3.5: Decomposition of the LOS displacement into vertical and horizontal components.
(a) shows a front view of the 3D deformation decomposition with the vertical 'Up' component D_u, and the horizontal 'East' and 'West' components D_e and D_n, w.r.t. the azimuth look direction (ALD).
(b) shows a top view of the 3D deformation decomposition with the horizontal 'East' and 'West' components D_e and D_n, w.r.t. the azimuth look direction (ALD). (Source: Du et al. 2018)

The relation between the LOS deformation and its three-dimensional components for right and left-looking satellites in orbit with heading azimuth (α_h) can be written as (Hanssen 2001)

$$D_{\text{LOS,R}} = D_u \cos(\theta_{\text{inc}}) - D_{\text{ALD,R}} \sin(\theta_{\text{inc}}), \tag{3.9}$$

$$D_{\text{LOS,L}} = D_u \cos(\theta_{\text{inc}}) - D_{\text{ALD,L}} \sin(\theta_{\text{inc}}) \tag{3.10}$$

where θ_{inc} denotes the local incidence angle. The D_{ALD} -terms are the projections of the multiple horizontal components on the azimuth look direction (ALD). For a right-looking satellite, $(\alpha_h - 3\pi/2)$ corresponds with the angle to the ALD (van Leijen 2014)

$$\begin{aligned} D_{\text{ALD,R}} &= D_e \sin(\alpha_h - 3\pi/2) + D_n \cos(\alpha_h - 3\pi/2), && (3.11)\\ &= D_e \cos(\alpha_h) - D_n \sin(\alpha_h) && (3.12) \end{aligned}$$

whereas for a left-looking satellite, this angle becomes $(\alpha_h - \pi/2)$ (van Leijen 2014)

$$\begin{aligned} D_{\text{ALD,L}} &= D_e \sin(\alpha_h - \pi/2) + D_n \cos(\alpha_h - \pi/2), && (3.13)\\ &= -D_e \cos(\alpha_h) + D_n \sin(\alpha_h). && (3.14) \end{aligned}$$

From these equations, it follows that the difference between right and left-looking satellites merely involves a difference in sign for the horizontal terms[4]. The InSAR deformation observations are most sensitive to the vertical component of equations 3.9 and 3.10, considering near polar satellite orbits and the incidence angle of SAR satellites (20-30°) (Samieie-Esfahany et al. 2009).
As an example, following Samieie-Esfahany et al. 2009, the incidence angle is taken as $\theta_{\text{inc}} \approx 40°$, which is the average for all Sentinel-1 satellite tracks used in this study, and the heading as $\alpha_h \approx 200°$. For these parameters, a sensitivity decomposition of $D_{\text{LOS,R}}$ would result in $[0.77, 0.60, -0.22][D_u, D_e, D_n]^T$. Even

[4] As the configuration of right-looking satellites is most common, often a single D_{ALD} term is applied, e.g. in Samieie-Esfahany et al. 2009, thus encompassing the horizontal components of a right-looking satellite configuration.

though the sensitivity of LOS deformation towards the vertical component is largest, sensitivity towards the horizontal components, especially towards D_e, is also considerable. Thus the conversion of LOS deformation directly towards the vertical component, without considering the horizontal components, would result in an error ΔD_u in the vertical component[5] (Samieie-Esfahany et al. 2009)

$$\Delta D_u = \tan(\theta_{\text{inc}}) D_{\text{ALD}}. \tag{3.15}$$

It follows from equation 3.15 that, with $\theta_{\text{inc}} \approx 40°$, the maximum error amounts to $\tan(\theta_{\text{inc}})$, i.e. 84% of the horizontal component. This maximum error holds for scenarios in which the horizontal motion is parallel to the ALD. The minimum error of 0% applies for cases in which the horizontal component is perpendicular to the ALD, i.e. $D_{\text{ALD}} = 0$ (Samieie-Esfahany et al. 2009).

3.3.4. InSAR processing

This section provides a brief overview of the multiple processing steps involved in obtaining useful image products, i.e. interferograms and, subsequently, elevation and deformation maps from the initial satellite acquisitions. A typical InSAR processing flowchart is shown in Figure 3.6. Furthermore, descriptions of certain processing steps presented in this flowchart that need further explanation, are provided in the following items.

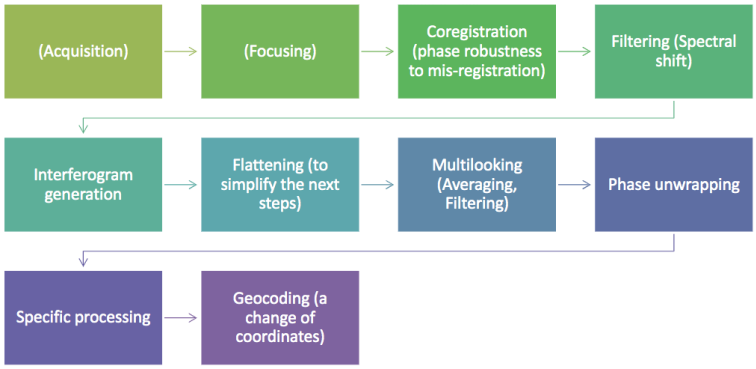

Figure 3.6: InSAR processing flowchart (Source: López Dekker et al. 2018a).

Co-registration

The co-registration step involves a procedure to determine the offset and differences in geometry, i.e. along the range and azimuth directional axes, between the two SLC's, i.e. the master and the slave images, obtained through the acquisition and focusing steps. Co-registration can either be done by a correlation algorithm based on the amplitude values per pixel, or by implementing a Digital Elevation Model (DEM) -based approach. In the latter approach, linear interpolation is used to obtain the offset value per individual pixel (van Leijen 2014). With the offset values, the slave image is re-sampled to the master image.

Filtering

Spectral filtering of the non-overlapping parts of the spectra of the master and the slave images reduces the level of noise in the interferogram. The filtering is applied separately in the azimuth and range direction (van Leijen 2014).

Interferogram generation

After the co-registration and spectral filtering steps, the interferogram is calculated by complex multiplication between the master m and the slave s image (van Leijen 2014):

$$P^{ms} = P^m P^{s*} = A^m A^s \exp(i(\psi^m - \psi^s)) \tag{3.16}$$

where $(.)^*$ denotes the complex conjugated term. From this equation, the expression for the interferometric phase follows, as seen in equation 3.7.

[5] Assuming a right-looking satellite configuration with notation $D_{\text{ALD}} = D_{\text{ALD,R}}$

Flattening

The 'flattening' of an interferogram involves the process of removing the phase component due to variation of the range distance across the image (Gamma Remote Sensing AG 2007), i.e. the term ϕ_{flat} in equation 3.7. As this leaves a 'flattened interferogram', the fringes no longer reflect the phase contributions of the reference ellipsoid, but only those of the remaining terms, i.e. topography, deformation, atmosphere, scattering differences, and noise.

Multilooking

'Multilooking', or simply 'averaging', is a filtering method to reduce the phase noise in SAR processing. Three different approaches for multi-look processing can be used, as presented and discussed in Huang and van Genderen 2014:

1. Several interferometric images are obtained from several multi-look processed image pairs. These images are then summed to obtain a final interferometric image.

2. An averaging operation is implemented in the single-look interferometric image to form the multilooked interferogram.

3. A weighted low-pass filter is implemented in the single-look interferometric image to form the multilooked interferogram.

Even though the second and third methods use a similar approach, the third method is most flexible and delivers the best interferometric results (Huang and van Genderen 2014).

Phase Unwrapping

As an interferogram is obtained, only information about the relative phase is known. The interferogram contains full color cycles $[-\pi, +\pi]$, which are referred to as 'fringes'. In other words, the interferometric phase is wrapped modulo 2π. Thus, besides real-valued parameters, the estimation problem also contains integer-valued parameters that occur in both the space (2D) and time domain (1D) (van Leijen 2014). These integer-valued parameters are refered to as the 'phase ambiguity'. As such, the amount of height change leading to a 2π change of the interferometric phase is called the 'height ambiguity'.
For further interpretation of these interferograms, the relative phase measures need to be translated to absolute phase information, from which topographic height and/or deformation values can be inferred. Therefore, an integer number of 2π must be added to recover the absolute difference in phase (Gamma Remote Sensing AG 2007). This translation process is known as 'phase unwrapping'. The spatial unwrapping process is based on the assumption of a smooth phase, meaning that neighbouring pixels have a phase difference $|\Delta\phi| < \pi$ (van der Horst 2017). However, phase jumps can occur that exceed the threshold of π rad, relating to decorrelation noise, undersampling (e.g. steep slopes), and discontinuities (e.g. faults, and glaciers) (Gamma Remote Sensing AG 2007).

Geocoding

Geocoding is the process of mapping the data from 'radar coordinates': (r, a, ϕ), to a map coordinate system, which can involve (López Dekker et al. 2018a):

- Earth-centered, earth-fixed (Cartesian) coordinates: (x, y, z),
- Geodetic coordinates: (ϕ, λ, h)[6],
- Local or geographic coordinates: $(^\circ E, ^\circ N, h)$.

For this study, the data is mapped in the Dutch 'Rijksdriehoek' (RD) reference system.

[6] In the context of geocoding ϕ, λ and h represent the latitude, longitude, and height coordinates, respectively.

3.4. PS-InSAR

As discussed in previous sections, conventional InSAR techniques have their limitations in regard to the atmospheric phase delay and spatial/temporal decorrelation. The technique 'persistent scatterer interferometry' (PSI) utilizes the time series of space borne radar acquisitions to select scattering objects that show relatively constant reflecting properties over time, and are therefore minimally affected by noise (Cuenca, van Leijen, and Hanssen 2010). A distinction is made between two extreme cases of reflection, namely point scattering and distributed scattering. For point scattering (PS), one strong reflecting stable object or 'point scatterer' dominates the radar measurement, whereas the surrounding only adds noise or 'clutter' (van Leijen 2014; van der Horst 2017). With distributed scattering (DS), the combination of multiple small scattering objects form the total measurement (van Leijen 2014; van der Horst 2017). This distinction is illustrated in Figure 3.7. Note that in both cases the scattering can be coherent or incoherent. The PSI technique uses isolated points with constant backscatter characteristics in time (van Leijen 2020), mainly relating to the term ϕ_{scat} in Equation 3.7. As such, the selection procedure is based on the coherence associated with the resolution cells. The following assumptions are made concerning the correlation characteristics of the different phase terms (van der Horst 2017; Hooper et al. 2012); deformation is temporally correlated, atmosphere is spatially correlated, and noise is uncorrelated both in space and time.

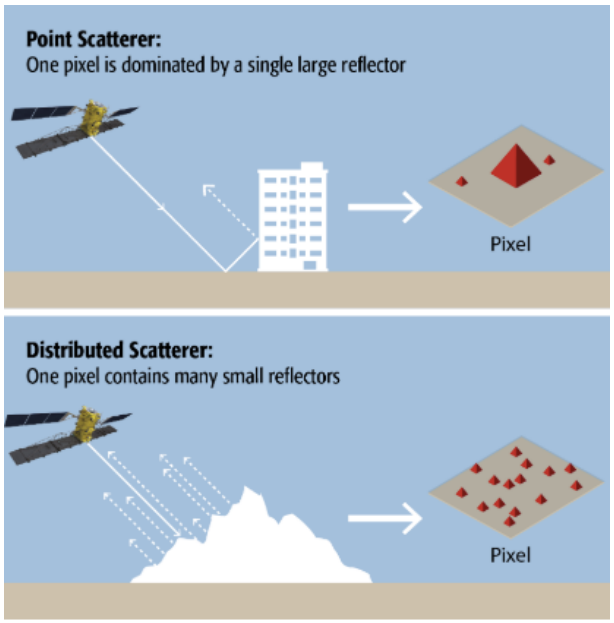

Figure 3.7: Concepts of point scattering and distributed scattering for an individual pixel (Source: Maxar Technologies n.d.).

The PSI algorithm involves a three step approach, which is presented first. Subsequently, the ambiguity function (AF), as one of three ambiguity resolution techniques, including integer least-squares (ILS) and integer bootstrapping (IB) (van Leijen 2014), is discussed as part of this study's prior processing steps.

3.4.1. PSI Algorithm

The PSI algorithm involves the following three-step approach on a radar interferometric stack (López Dekker et al. 2018b):

1) PS candidate selection – The best point scatterers in each grid cell are selected for analysis. For each pixel, the normalized amplitude (temporal) dispersion is expressed and computed as

$$D_a = \frac{\sigma_a}{m_a} \tag{3.17}$$

where σ_a is the standard deviation of the amplitude and m_a is the mean amplitude. A typical pixel selection threshold is applied: $D_a < 0.25$, which can vary according to the user's requirements. The

normalized amplitude temporal dispersion serves as a proxy for the persistance of the phase (van Leijen 2014). Since the detection of a PS depends on the consistency of the radar reflection over time and the smoothness of the deformation signal, PS are not detected at locations where the surface has changed significantly or the deformation is too strong or irregular (van Leijen 2020). On the other hand, objects and surfaces in the built environment, i.e. buildings or infrastructure, provide consistent reflection that result in PS detection. In case of distributed scatterers, the coherence is estimated and multilooked interferogram pixels are selected, again above a certain threshold. This preparation routine eases the correction process for the removal of atmospheric delay, and other noise contributors.

2) First-order network estimation – Based on the most coherent reflecting objects, a first-order network can be created to estimate displacement parameters and DEM error differences between neighbouring points, i.e. the nearest known point. This is done in order to reduce the atmospheric delay.

3) Second-order network integration – The parameters at the selected point locations are obtained through a least-squares (LS) integration w.r.t. to a reference point. Incorrect estimates and incoherent points are identified with the use of alternative hypothesis tests. As a result, the second-order network is more spatially dense than the first-order network, in which the deformation phase is separated from the atmospheric phase and noise terms. For example, Cuenca, van Leijen, and Hanssen 2010 obtain the following results through PSI[7]: 100 measurement points per km^2 in 'stable' urban areas with known position errors of 10m, and a high observation frequency of once a month or higher. From the second-order network it is possible to derive a full deformation velocity field.

3.4.2. Ambiguity Function

For the processing of the PSI datasets used in this project, a 'periodogram' approach was used. In signal processing in general, the periodogram provides an estimate of the spectral density of a signal, i.e. it can be regarded as the squared magnitude of the Fourier transform (FT) (McKilliam et al. 2010). For (PS-)InSAR processing, this approach is also known as the 'ambiguity function' technique (AF), of which the main purpose is to resolve the phase ambiguities through finding the parameters b that maximize the temporal coherence $|\gamma|$ (Ferretti, Prati, and Rocca 2000; van Leijen 2014)

$$\arg\max_b |\gamma| = \left|\frac{1}{S}\sum_{s=1}^{S} \exp(j(\vec{\phi}^{0s}_{\text{obs}} - \vec{\phi}^{0s}_{\text{model}}(b)))\right|, \tag{3.18}$$

$$= \left|\frac{1}{S}\sum_{s=1}^{S} \exp(j(\vec{e}^{0s}(b)))\right| \tag{3.19}$$

where S denotes the number of interferograms with respect to the same master image, $\vec{\phi}^{0s}_{\text{obs}}$ denotes the observed phase, and $\vec{\phi}^{0s}_{\text{model}}(b)$ denotes the modeled phase, based on the parameters b. The residual phase $\vec{e}^{0s}(b)$ is the difference between the observed and modeled phase terms (Ferretti, Prati, and Rocca 2000; van Leijen 2014).

[7] Cuenca, van Leijen, and Hanssen 2010 involves the application of PSI to estimate subsidence rates in the Dutch wetlands, i.e. in the 'Green Heart' of the Netherlands.

4

Data Management & Processing

As part of this study, a database approach is implemented in order to assign auxiliary information or 'attributes' to the PSI deformation data. The purpose of this approach is to analyze the deformation in its contextual environment, by studying and comparing the deformation observations of different classes and subsets. To this end, the distinction is made between the primary dataset, i.e. the PSI data, and the auxiliary datasets, which are selected to 'enrich' the PSI observations.
The first part of this chapter provides a theoretical understanding of the database approach. First, the concept of spatial data and the database management system (DBMS) are introduced. Subsequently, a discussion is provided on the required storage, operational steps involved in maintaining a DBMS, from which the user is able to efficiently retrieve information through so-called 'queries'.
The second part of this chapter presents the primary and secondary input datasets and their selection criteria for this particular study. Since the results of Chapters 5 and 6 require different inputs, they are summarized in a general overview at the start of Section 4.2. The final part of this chapter presents the overall implementation of the database approach in this study, leading up to the nationwide deformation analysis results in Chapter 5 and the three case study results in Chapter 6.

4.1. Database Approach

In order to bring together all sources of information, the main dataset, i.e. the InSAR data needs to be stored in the same environment as the auxiliary data, using a database approach. A database is a shared collection of logically related data, designed to meet the information needs of an organization (Connolly and Begg 2005). With a DBMS, the user is enabled to interact with a software system by defining, creating, maintaining, and controlling access to the database (Connolly and Begg 2005). To maintain the database, several operation steps are needed to facilitate the storage and exchange of information 'within', and 'outside' of the database. The goal of these operations, and the database approach in general, is to gain better insight in the processes that are described in the various datasets that are part of the database. In the following sections, the database approach is discussed in terms of the storage of information, the operational steps involved in e.g. inserting, selecting, updating, deleting and calling data, and the querying method.

4.1.1. Spatial Data

With the selection of auxiliary spatial datasets for this study, as discussed in Section 4.2., the main focus is centered around their applicability towards the enrichment of the primary dataset, containing the PSI measurements. Not coincidentally, the selected auxiliary datasets show similarities in terms of how they are collected, organized and structured. In most applications, spatial or geometric information is connected with non-spatial data, e.g. alphanumeric data (Güting 1994), such as labels, height information, notes, etc. This connection is reflected in the intricacies of the database systems that are able to store spatial data. The abstraction of spatial information is captured by so-called 'spatial data types' (SDTs) (Güting 1994) i.e. points, lines, and polygons or regions, as they are widely used in all sorts of GIS applications. Samet 1990 adds to the list of SDTs; rectangles, regions, surfaces, volumes, and even data of higher dimension, including time. PostGIS n.d.(b), which is the geographic information

system used in this study, supports the organization of spatial data types in a type hierarchy, in which each sub-type inherits the structure, i.e. attributes, and the behaviour, i.e. methods and functions, of its super-type. This hierarchy is illustrated in Figure 4.1 from PostGIS n.d.(b), showing the different geometry types and collections, bound to their spatial reference systems.

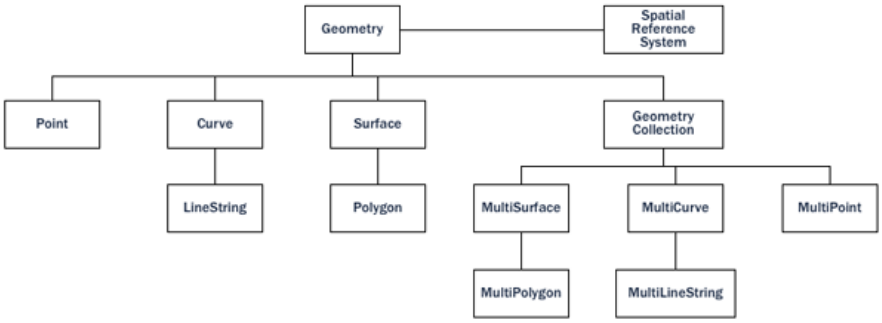

Figure 4.1: Geometry hierarchy, showing the connections between different spatial data types and the collections thereof, i.e. 'Multi' prefix, w.r.t. the spatial reference system (Source: PostGIS n.d.(b)).

The explicit storage of data is a common suggestion to parameterize the data, thus reducing spatial object to single points in a possibly higher dimensional space (Samet 1990). These points can easily be stored in the system as individual records with multiple attributes or fields attached to them. This method is well suited for the mere retrieval of data from the database, similar to the retrieval of non-spatial data (Samet 1990).
However, to account for spatial queries, such as proximity searches, the data is best stored implicitly. One approach to the representation of spatial data is to separate it from the non-spatial data while maintaining appropriate links between the two (Samet 1990; Aref and Samet 1991). This allows for spatial operations to be performed directly onto the spatial structures, and it adds flexibility to the choice for spatial storage structures, e.g. tree structures. Unlike conventional DBMS, spatial data poses different requirements on the sorting processes. As the storage of spatial data is tightly connected to the ability to perform spatial searches or queries, different DBMSs and their 'spatial indexing' methods are discussed in the following sections.

4.1.2. Storage

The database approach is implemented in order to facilitate the storage, administration, and exchange of spatial information. The main purpose of a database is to store information as an organized collection of data. The term 'organized' is used to highlight the intended or potential use of the information, as it should already be accounted for in the storage procedure. In regard to the necessity for organized storage, the concept of a 'relational' database management system (RDBMS) is introduced. From there, the section delves into spatial databases, and the steps involved in storing, organizing, and the overall managing of spatial data in 2D and 3D.

RDBMS

Since the 1980s, most DBMS operate based on the relational model of data, as proposed by Codd 1970. The software system that maintains a relational database is referred to as a RDBMS. In the relational model, the data is represented in sets of n-tuples, i.e. a sequence of n elements represented by positive integers, and grouped into relations, i.e. in which each individual element d_j is part of the data domain D. Attribute values are paired to a certain domain within the entire data domain. Structured Query Language (SQL)[1] follows the relational model, but applies more familiar terminology; rows represent the 'tuples' or 'records', columns represent the 'attribute' or 'field', the table represents the 'relation', and the 'view' represents the output, i.e. any set of tuples as a response of a query (Connolly and Begg 2005). These terms are illustrated in Figure 4.2, as they would be seen from the perspective of the database user. One of the most commonly used open-source object-RDBMS that implements SQL is PostgreSQL, also referred to as simply 'Postgres', developed by The PostgreSQL Global Development

[1]SQL is a programming language used to manage a RDBMS.

Group n.d. Postgres with its spatial extension PostGIS is the RDBMS used to construct and manage the spatial data gathered for this study, as presented in Section 4.2.

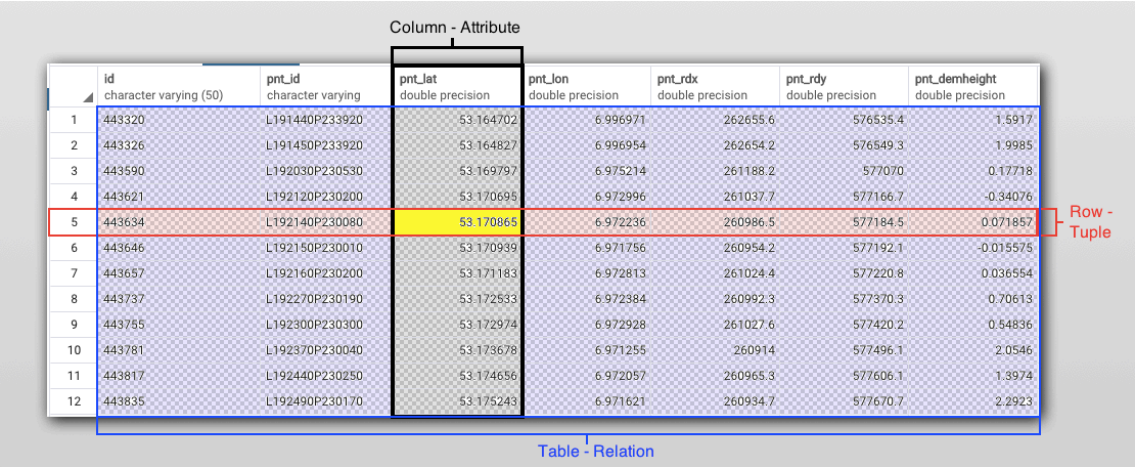

	id character varying (50)	pnt_id character varying	pnt_lat double precision	pnt_lon double precision	pnt_rdx double precision	pnt_rdy double precision	pnt_demheight double precision
1	443320	L191440P233920	53.164702	6.996971	262655.6	576535.4	1.5917
2	443326	L191450P233920	53.164827	6.996954	262654.2	576549.3	1.9985
3	443590	L192030P230530	53.169797	6.975214	261188.2	577070	0.17718
4	443621	L192120P230200	53.170695	6.972996	261037.7	577166.7	-0.34076
5	443634	L192140P230080	53.170865	6.972236	260986.5	577184.5	0.071857
6	443646	L192150P230010	53.170939	6.971756	260954.2	577192.1	-0.015575
7	443657	L192160P230200	53.171183	6.972813	261024.4	577220.8	0.036554
8	443737	L192270P230190	53.172533	6.972384	260992.3	577370.3	0.70613
9	443755	L192300P230300	53.172974	6.972928	261027.6	577420.2	0.54836
10	443781	L192370P230040	53.173678	6.971255	260914	577496.1	2.0546
11	443817	L192440P230250	53.174656	6.972057	260965.3	577606.1	1.3974
12	443835	L192490P230170	53.175243	6.971621	260934.7	577670.7	2.2923

Figure 4.2: Example of the relational model terms and their SQL meanings. The cell highlighted in yellow represents an example 'item' as part of its row, column and table. The table is taken as an example from the PostgreSQL database that was created for this study, viewed from the pgAdmin 4 graphical user interface (GUI). The contents of the table represent a selection of the first 12 PSI deformation points of a particular track, and the first 6 attributes (besides the default ID) that characterize them. Note that these have no further meaning in this context aside from their illustrative purpose.

Spatial Database

Based on Blasby 2001, the author defines spatial data as data that provides information either on the location or on the shape of a physical entity or object. Spatial objects are made up of either points, lines, regions, rectangles, surfaces, volumes, and even data of higher dimension, including time (Samet 1990), e.g. buildings, roads, lakes, parks, etc. The latter description implies the abstract and reductionist representation of these entities by a computer in terms of points, lines, and polygons[2] (Blasby 2001). With the definition of spatial data, a 'spatial database' is simply a database that stores information on spatial objects, and makes it possible to manipulate spatial objects like any first class database object by allowing for multiple functionalities, such as transactions, backups, integrity checks, multi-user support, security access and control, and locking Blasby 2001. The fundamental organization, indexing, functions and operations are handled by the database itself. Moreover, SQL expressions can be used to perform spatial operations, e.g. determining the area or length of objects, or applying intersections, unions, or making buffers (Blasby 2001).
Besides knowing the precise location of an object, the user of the database is also interested in understanding the relationships between the spatial objects. The relationships of interest would be the proximity or distance between the objects, their 'adjacency', i.e. if the objects touch one another, and their containment, i.e. if one object is inside the other or if they overlap (Blasby 2001). PostGIS, as a spatial extension of Postgres, has the ability to store data on spatial objects and allows the database user to establish complex relations.

Spatial Indexing

A spatial index is a data structure that is used to efficiently access a spatial object within the database (Zhang and Du 2017). Without spatial indexing, the search for a specific feature or object would result in a sequential scan of every record in the database (PostGIS n.d.[a]), resulting in a much longer processing time. During the search travel, a minimum bounding rectangle (MBR), also referred to as simply a 'bounding box', is used to approximate the sometimes complex geometry of objects. The MBR is a single rectangle that minimally encloses the geometry of the object in a 2D or even 3D plane, as represented in Figure 4.3 by Zhang and Du 2017. To test a relation, first the objects located outside of the bounding box are filtered out, and thus only the objects that overlap with the box are kept in the subset (Blasby 2001). Subsequently, the actual shape of the object in the subset of the first

[2] A 'polygon' is used as an umbrella term for multi-sided, multi-angled geometrical figures.

step is used to test the relation with the target object (Zhang and Du 2017). This is the key concept behind the so-called B-tree and R-tree structures. The Postgres RDBMS uses a Generalized Search Tree (GiST), which provides the indexing support for PostGIS. Different modules have been distributed by PostgreSQL, which have been developed with the use of GiST, e.g. R-tree and B-tree implementations. The different tree data structures, including the B-tree, R-tree, and the quadtree, are briefly discussed in the following subsection.

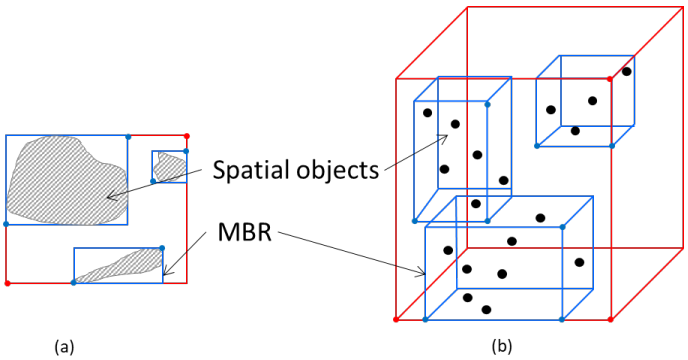

Figure 4.3: Minimal bounding rectangle (MBR) of an object in (a) a 2D plane and in (b) a 3D space (Source: Zhang and Du 2017).

Tree structures

For the indexing of any record R_j in a database, it is assigned a key value K_j. The goal of indexing structures is to keep the number of necessary key comparisons to a theoretical minimum (Knuth 2001). To this end, depending on the type of data that is stored in the database, various search methods have been devised. One of the search methods relies on the use of so-called tree structures. A 'tree' in terms of its computer science equivalent, is an abstract data type (ADT) that is widely used to store and access information in a hierarchical, i.e. 'parent-child', arrangement. A typical tree data structure comprises of nodes with a certain value attached to them, listing their subsequent 'child nodes' with respect to the order of succession. The links between the nodes are often referred to as 'arcs', 'edges' or 'paths'. The 'root' node, forming the starting point of the tree structure, has no parent (Allison 2019).

Binary tree – A binary search tree has at most two children per node, and is called 'self-balancing' when its 'height', i.e. the length of the longest path from the root to an external node, never differs by more than ± 1 from the height of the right subtree (Knuth 2001). This concept is illustrated in Figure 4.4. Thus for binary search, the method compares K to the middle key in the table, and determines which half of the table to search next. This process is repeated until the record is retrieved (Knuth 2001).

B-tree – The B-tree can be interpreted as a generalization of the binary tree in that a node can have more than two children (Comer 1979), and it is also self-balanced. The essential idea behind B-trees is their insertion algorithm, or 'split process' (Bayer 2008). Each node in a B-tree of order d contains a variable number of keys between d and $2d$, and between $d+1$ and $2d+1$ pointers to child nodes (Comer 1979), as illustrated in Figure 4.5. Being separate records of the index file, the separate nodes contain information on how many keys correctly reside in it (Comer 1979). B-trees allow for fast data retrieval, which is nearly independent of the size of the dataset, since the index grows only logarithmically with the size of the dataset (Bayer 2008). Thus, the height, i.e. the longest path in the B-tree, is $h = \log_d n$ (Comer 1979).

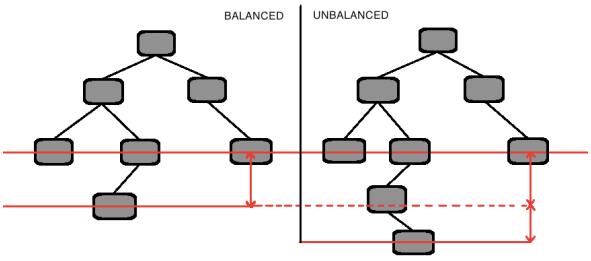

Figure 4.4: Balanced binary tree (level difference $\leqslant 1$) vs. unbalanced binary tree (level difference > 1) (Concept from: tutorialhorizon n.d.).

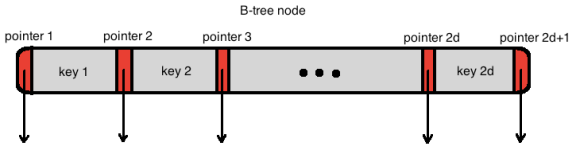

Figure 4.5: B-tree node with $2d$ nodes and $2d + 1$ pointers, where the integer d denotes the order of the B-tree (Concept from: Comer 1979).

R-tree – An R-tree is 'a height-balanced tree similar to a B-tree with index records in its leaf nodes containing pointers to data objects' (Guttman 1984), but designed specifically for the access of spatial objects. PostGIS features an implementation of the conventional R-tree approach. In the R-tree structure all geometries are generalized to their specific bounding boxes as an approximation, to which the overlapping objects are searched (Blasby 2001). Thus, effective spatial searches only require the visiting of a small number of nodes (Guttman 1984). The search is applied through guiding of the bounding rectangles or boxes that belong to a particular node of the tree. Following the MBR approach illustrated in Figure 4.3, the R-tree search procedure is illustrated in the following set of figures, showing the following example:
A search is performed in the 2D plane to retrieve the spatial object, represented by its tuple, by means of its bounding rectangles: R1, R3, and R8, shown in Figure 4.6. In turn, these relate to their respective nodes in the three-level tree structure, illustrated in Figure 4.7.

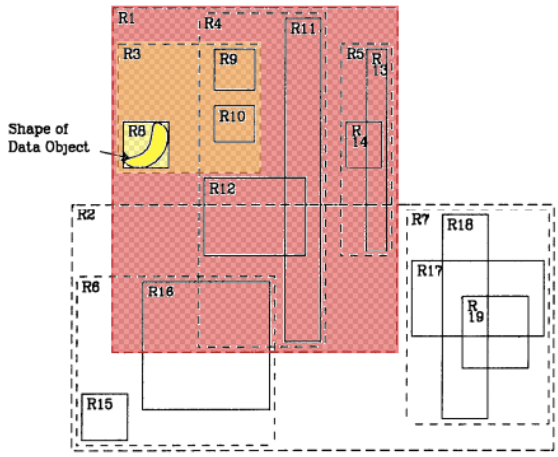

Figure 4.6: 2D spatial overview of an R-tree search for the spatial object (yellow) with the use of the highlighted bounding boxes according to nodes: R1, R3 and R8 (Adapted from Guttman 1984).

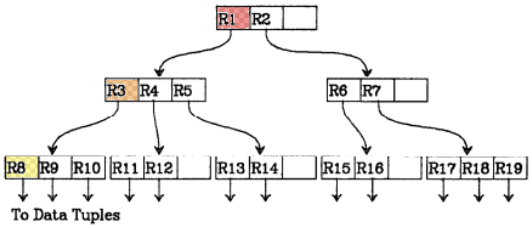

Figure 4.7: R-tree index structure with nodes R1, R3 and R8 highlighted, as they contain the spatial search object (Adapted from Guttman 1984).

R-trees are dynamic in the sense that the insertion and deletion of entries leads to heuristic reorganization of the index structure. If a new object is inserted, starting from the root, the tree is traversed through each level for the selection of a suitable leaf node. If the bounding rectangle of a certain node contains the object to be inserted, the associated subtree is searched. Otherwise, the optimal node for insertion is selected based on the minimal required enlargement of its bounding box. In case of multiple nodes meeting one of the previous criteria, the one with the smallest area is selected. If the leaf node is already full, it is split and, if necessary, the bounding rectangles of the node's ancestors is updated (SFU n.d.). The deletion of records from the R-tree may also require updates in the ancestors of the node involved. The effort to keep a balanced tree structure may require the deletion and reinsertion of entire subtrees to maintain the search efficiency.

Quadtree – Additionally, the quadtree structure is introduced as a tree structure variant. The quadtree utilizes an indexing structure of 4 children per node (Finkel and Bentley 1974). As such, a two-dimensional space is split into four rectangular quadrants in every iteration, or tree level. Conventional quatree cells are sensitive towards a certain capacity threshold. Thus, if a cell reaches full capacity, it is split into four children nodes, which is subsequently followed by the tree structure. The implementation of quadtree structures has increased in recent years, applied for example in the spatial representation or mapping of surface deformation.

4.1.3. Operations & Queries

With the spatial data stored according to a particular spatial index, it is common for various operations and queries to be performed onto them. In typical database systems, the focus with queries lies in the selection or retrieval of specific data from the dataset. For many applications, the 'create, read, update, delete' (CRUD) acronym is used to refer to the major functions that are implemented in RDBMSs (Martin 1983). In SQL, these functions translate to: 'insert, select, update, delete'.
For spatial databases however, SQL statements include a variety of spatial operations besides the retrieval of records from a system. Depending on the application, RDBMSs allow their users to perform various kinds of data analysis, spatial queries, evaluations, etc. For example, a proximity search is applied to retrieve all the database entries within a certain radius of a specific object or point.
Spatial operations or 'functions' are available for the user to analyze and manipulate geometric components, or to determine spatial relationships (PostGIS n.d.[b]). These are grouped according to the five categories presented in Table 4.1, based on PostGIS n.d.(b), and provided with some example functions. For brief descriptions of the example functions presented in Table 4.1, the reader is referred to Table A.1 in Appendix A. Note that these are only a few examples of the complete overview of PostGIS functions in PostGIS n.d.(c), selected to illustrate the five function groups.

Group	Subject	Example Functions
Conversion	geometries, external data formats.	ST_SetSRID, ST_Transform, ST_Geohash.
Management	information about spatial tables, administration.	AddGeometryColumn, DropGeometryColumn, Find_SRID, UpdateGeometrySRID.
Retrieval	geometry properties, geometry measurements.	GeometryType, ST_Boundary ST_Dimension, ST_Envelope.
Comparison	geometries – spatial relations	Bounding Box Operators, e.g. &&, @, ~=
Generation	new geometries from others	ST_Collect, ST_MakePoint, ST_MakeLine, ST_MakePolygon.

Table 4.1: The five spatial function groups, as defined in PostGIS n.d.(b), provided with example functions from the PostGIS functions catalog in PostGIS n.d.(c).

Another way of addressing 'spatial queries', as an umbrella term for spatial searches, operations, and functions, is by grouping them along the following three classes: thematic, geometric, and topological queries (GITTA 2016). These are all discussed in the following subsections.

Thematic queries

Thematic queries are used for the selection from the database of thematic information, i.e. without a spatial reference. As the thematic query relies on the analysis of attributes, GITTA 2016 identifies the following three search operators: relational operators, arithmetic operators, and logical operators. Relational operators test the relations between entries or groups of entries in the dataset, with the use of the following statements: $=, >, \geq, <, \leq, <>$ and additional SQL aggregate functions: Avg, Count, Min, Max, Sum, StDev, Var (GITTA 2016). Arithmetic operators are used for computations with number-attributes, including the following traditional operations: $+, -, *, /, \exp, \%$ (GITTA 2016). The logical operators, often used as program controls in SQL, are the following : All, And, Any, Between, Exists, In, Like, Not, Or, Some (W3Schools n.d.). With the use of brackets to manage the order of the previously seen expressions, the user is able to write 'nested queries', i.e. a query inside of another query.

Geometric queries

The geometry can be seen as a measurable attribute of an entity, or 'entry' as seen in a database environment. Here, the distinction between vectors and raster representations is of importance. For vector models the information is assigned to (x,y) points, and the other structures are derived from points, i.e. lines as a connection between points, and polygons as the area enclosed by connected lines forming a geometric shape. As such, the length of the connection line between points, the surface area, and the distance between objects are derived from coordinates assigned to the points (Bartelme 2000). Raster models make use of arrays or matrices, that store values in rows and columns. In the raster model representation; a point is the equivalent of a single cell within the array, a line is the product of cells connected at their edges or corners with just one or two neighbouring cells, and a polygon or 'area' is a group of neighbouring cells connected at the edges and corners (GITTA 2016).
Geometric measurement functions use both the vector and raster models, but with different methods and outcomes. In a vector model, the position of a point is returned by means of its map coordinates depending on the reference system configuration. Raster models use a block encoding, where the position of a point, i.e. a single cell is returned by means of its respective row and column. The distance between points in vector models is simply calculated as the Euclidean distance, corresponding to the shortest distance. In addition to the Euclidean distance, raster models compute the distance according to other methods, e.g. the Manhattan distance, as measured along axes at right angles (GITTA 2016), or by means of proximity search, i.e. nearest-neighbour search (NNS).
Another common geometric query is to compute the size of an object, referring either to the object's perimeter or area. For vector models, the perimeter is taken as the sum of the length of all the single line sections that form the polygon. The area is calculated as the sum of the areas of the simple shapes, i.e. triangles and rectangles, to which the object can be devised. In the raster model, the perimeter is taken as the number of cell edges that enclose the object multiplied by the cell resolution, and the area as the multiplication of the area of one cell with the total number of cells that make up the object (GITTA 2016).
Proximity analysis in the vector model is performed by creating a 'buffer' or spatial expansion around the object, e.g. point, line, or polygon. In the raster data model, the proximity is calculated for the entire grid. So-called 'distance zones' assign a distance value to each grid with respect to the source cell (GITTA 2016).

Topological queries

A GIS topology is a set of rules and behaviors that model how points, lines, and polygons share geometry, e.g. adjacent features will share a common edge (ESRI 2005). Topology is used to manage shared geometries between features, to define and enforce data integrity rules, to support topological queries, and to construct new features from unstructured geometry (ESRI 2005).
The 9-intersection scheme proposed by Egenhoffer 1993 is a well known classification for the topological configurations. It is supported by the main idea that each element in the topological relationship is composed of a 'boundary', an 'interior', and an 'exterior' also referred to as 'complement' (GITTA 2016). For an individual object, e.g. A, the topological relations are denoted as follows: the interior of a region $A(A^\circ)$, the boundary of a region $A(\partial A)$, and the exterior of a region $A(A^-)$ (Jena and Roehrig 2007). The topological relations between two objects A and B can be written as a set of 9 intersections $\cap$, represented in matrix notation as (Jena and Roehrig 2007; Egenhoffer 1993):

$$R(A,B) = \begin{bmatrix} A^\circ \cap B^\circ & A^\circ \cap \partial B & A^\circ \cap B^- \\ \partial A \cap B^\circ & \partial A \cap \partial B & \partial A \cap B^- \\ A^- \cap B^\circ & A^- \cap \partial B & A^- \cap B^- \end{bmatrix} \tag{4.1}$$

The different topological relations and their visual representations are summarized in Table 4.2. The table also includes the 9-intersection matrices for each topological relation, expressed in binary notation 0 and 1, respectively denoting 'empty' $\emptyset$ or 'non-empty' $\neg\emptyset$ intersections.

Topological Relation	9-Intersection Matrix	Illustration
Disjoint	$\begin{array}{c\|ccc} & B^\circ & \partial B & B^- \\ \hline A^\circ & 0 & 0 & 1 \\ \partial A & 0 & 0 & 1 \\ A^- & 1 & 1 & 1 \end{array}$	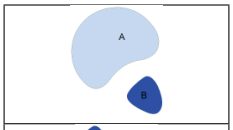
Meet	$\begin{array}{c\|ccc} & B^\circ & \partial B & B^- \\ \hline A^\circ & 0 & 0 & 1 \\ \partial A & 0 & 1 & 1 \\ A^- & 1 & 1 & 1 \end{array}$	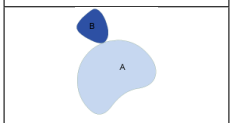
Equal	$\begin{array}{c\|ccc} & B^\circ & \partial B & B^- \\ \hline A^\circ & 1 & 0 & 0 \\ \partial A & 0 & 1 & 0 \\ A^- & 0 & 0 & 1 \end{array}$	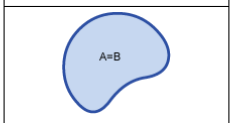
Inside	$\begin{array}{c\|ccc} & B^\circ & \partial B & B^- \\ \hline A^\circ & 1 & 0 & 0 \\ \partial A & 1 & 0 & 0 \\ A^- & 1 & 1 & 1 \end{array}$	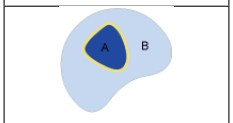
Contains	$\begin{array}{c\|ccc} & B^\circ & \partial B & B^- \\ \hline A^\circ & 1 & 1 & 1 \\ \partial A & 0 & 0 & 1 \\ A^- & 0 & 0 & 1 \end{array}$	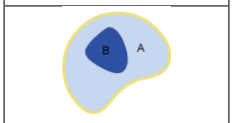
Covered by	$\begin{array}{c\|ccc} & B^\circ & \partial B & B^- \\ \hline A^\circ & 1 & 0 & 0 \\ \partial A & 1 & 1 & 0 \\ A^- & 1 & 1 & 1 \end{array}$	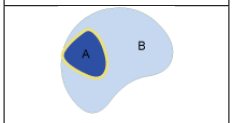
Covers	$\begin{array}{c\|ccc} & B^\circ & \partial B & B^- \\ \hline A^\circ & 1 & 1 & 1 \\ \partial A & 0 & 1 & 1 \\ A^- & 0 & 0 & 1 \end{array}$	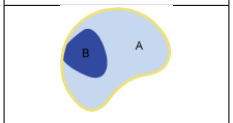
Overlap	$\begin{array}{c\|ccc} & B^\circ & \partial B & B^- \\ \hline A^\circ & 1 & 1 & 1 \\ \partial A & 1 & 1 & 1 \\ A^- & 1 & 1 & 1 \end{array}$	

Table 4.2: The topological relations between objects A and B, and their associated 9-intersection matrices. The list and matrix contents are based on and adapted from GITTA 2016; Jena and Roehrig 2007; Egenhoffer 1993. The illustrative figures of the topological relations originate from GITTA 2016.

Although most topological relations apply to polygons, there are also several cases to be discussed for the other two types of geometries, i.e. lines and points. As such, the topological relations between different geometries are presented in Table 4.3, except for those between a polygons and other polygons, as these are shown separately in Table 4.2. The topological relations between lines and points, in any combination, can also be expressed by the 9-intersection matrix.
Furthermore, it should be noted that two modifications are made with respect to the terminology used in GITTA 2016;

1. A line does not 'contain' a point, as no point is situated 'inside' a line. Nonetheless, a line can still meet with a point, show overlap with it, or the two can be disjoint.

2. If a point 'overlaps' with a line, the line continues onward beyond the intersection point, whereas it would stop in the case of the two 'meeting'.

The modified terminology for the point-line relations is reflected in Table 4.3.

Topological Relation	Point – Point	Point – Line	Point – Polygon	Line – Line	Line – Polygon
Disjoint					
Meet	-			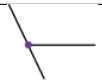	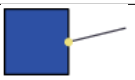
Equal		-	-		-
Inside	-	-		-	
Contains	-	-		-	
Covered by	-	-	-	-	
Covers	-	-	-	-	
Overlap	-		-		

Table 4.3: All combinations of the topological relations between points, lines, and polygons (except for the combination: polygon – polygon). The list of topological relations is based on and modified from GITTA 2016. The illustrative figures of the topological relations originate from GITTA 2016.

4.2. Input Datasets

This section presents a discussion on the various datasets gathered and used in this study. The datasets cover a mix of themes and classifications as these serve different purposes within the scope of this study on identifying, locating and quantifying potential causes for land subsidence and the potentially affected areas. Radar interferometry, as presented and discussed in chapter 3, serves as the main technique for estimating the level of surface deformation in a particular area. As such, the PSI dataset, presented along with multiple auxiliary datasets, serves as the starting point of the data management and processing steps applied in this chapter. The main idea is to enrich the primary PSI datasets with contextual information ranging from geological, hydrological and geographical attributes to street-level objects, i.e. buildings and infrastructure.

4.2.1. Primary Input – Sentinel-1 PSI Data

Higher-order PS densification datasets from Sentinel-1 (S1) serve as the primary input for this study. The acquisitions in these datasets have been conducted by the European Space Agency (ESA) as part of the Copernicus initiative. The Sentinel-1 mission comprises of a constellation of two C-band[3] SAR imaging satellites, providing continuous radar mapping of the Earth (ESA n.d.[c]). The information gathered in these datasets depends on the acquisition procedure, determined by the S1 operational mode, orbital parameters, coverage, and the PS-InSAR processing steps. These parameters are introduced in the following sections.

Operational Mode

The four Sentinel-1 standard operational modes are listed in Table 4.4. These modes are characterized by their swath widths, spatial resolutions, and their polarization settings. The latter specify the geometrical orientation of the oscillations of the EM wave, either horizontal (H) or vertical (V). Denoting the orientation setting for the transmission and the reception (respectively), the single polarization mode can be: HH or VV, and the dual polarization mode can be HH+HV or VV+HV (ESA n.d.[c]). Data

[3]C-band refers to the portion of the electromagnetic spectrum, where the frequency ranges from 4 to 8 GHz (Peebles 1998).

from the Interferometric Wide Swath Mode (IW) is the main mode over land, with its 250km swath provides coverage at medium spatial resolution of 5 x 20m.

S1 Acquisition Mode	Swath Width (km)	Spatial Resolution (m)	Polarization
Strip Map (SM)	80	5×5	Dual HH+HV, VV+VH, Single HH, VV
Interferometric Wide Swath (IW)	250	5×20	Dual HH+HV, VV+VH, Single HH, VV
Extra-Wide Swath (EW)	400	20×40	Dual HH+HV, VV+VH, Single HH, VV
Wave Mode	-	5×20	Single HH, VV

Table 4.4: Overview of the Sentinel-1 acquisition modes and their settings, including the swath width (km), spatial resolution (m×m) and the polarization, based on the Sentinel-1 user guide by ESA n.d.(c).

Orbital Parameters

The satellites have a sun synchronous, near-polar orbit with a 12-day repeat cycle at an altitude of 693 km, with a deviation of ±100 m (ESA n.d.[d]). This deviation is represented as an orbital Earth-fixed 'tube' with a 50 m radius, visualized in Figure 4.8. With both satellites in operation, the repeat cycle is 6 days (ESA n.d.[d]).

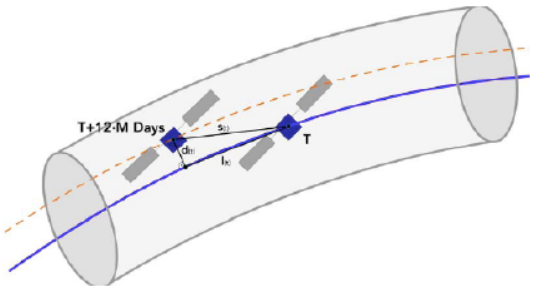

Figure 4.8: Sentinel-1 orbital Earth-fixed, 50 m radius tube with a 12-day repeat cycle (Source: ESA n.d.(d)).

PSI Datasets

The Sentinel-1 PSI datasets cover the Netherlands either through ascending or descending passes. The settings of a set of three ascending track acquisitions and three descending track acquisitions are summarized in Table 4.5. The amount of points differ per track, because of the differences in coverage between them. Some tracks cover only part of the Netherlands, whereas others (e.g. tracks 37 and 88) cover almost the entirety of the Netherlands, as seen in figure 4.9.

Track	Pass Direction	$\overline{\theta}_{\text{inc}}$	Resolution	No. points	No. acq.	Epoch	End Date
15	ascending	39.4°	24.2 ×6.1 m	2,111,508	166	2015-03-23	2019-01-01
88	ascending	39.4°	24.2 ×6.1 m	10,959,758	148	2015-07-26	2018-12-31
161	ascending	39.4°	24.2 ×6.1 m	9,257,353	141	2016-04-20	2018-12-30
37	descending	39.4°	24.2 ×6.1 m	11,930,586	146	2015-11-20	2018-12-28
110	descending	39.4°	24.2 ×6.1 m	6,199,539	165	2015-05-05	2018-12-27
139	descending	39.4°	24.2 ×6.1 m	3,419,673	156	2015-01-19	2018-12-29

Table 4.5: For each satellite track, denoted by the PS stack name, the following details and settings are provided: the pass direction: ascending or descending, the average incidence angle $\overline{\theta}_{\text{inc}}$ of 39.4° for all tracks, the resolution of 24.2 ×6.1 m for all tracks, the number of points, the number of acquisitions (in time), and the dates of the first (epoch) and last observation of the time series. For all the tracks, the direction of estimated deformation is in the line-of-sight (LOS).

The phase unwrapping procedure of the different sets of S1 acquisitions relies on the periodogram technique, as one of many processing steps involved in obtaining useful PSI deformation-specific results. For a more elaborate overview of the InSAR theory and the InSAR processing framework, the reader is referred to chapter 3 and in particular Section 3.4.2.

Spatial Coverage

The spatial extents of the PS input sets are visualized in Figure 4.9. Note that, depending on the path of the platforms and the differences in look-configurations, the coverage of the Netherlands can vastly differ between the different tracks. For example; ascending track 15 and descending track 139 only include information on the eastern part of the Netherlands, whereas ascending track 161 only provides images of the western part of the country. Nonetheless, most of these tracks are included in the nationwide analysis presented in chapter 5, with the exception of ascending track 161. This track is left out in the early stage of this study, as the scope was initially set to exclusively cover the province of Groningen. The inclusion of overlapping cover areas from the satellite tracks may be useful for validation and comparative purposes. Considering the observed differences between the ascending and descending tracks (as studied in Chapter 5, with additional results in Appendix B), these areas of overlap may prove to be especially insightful.

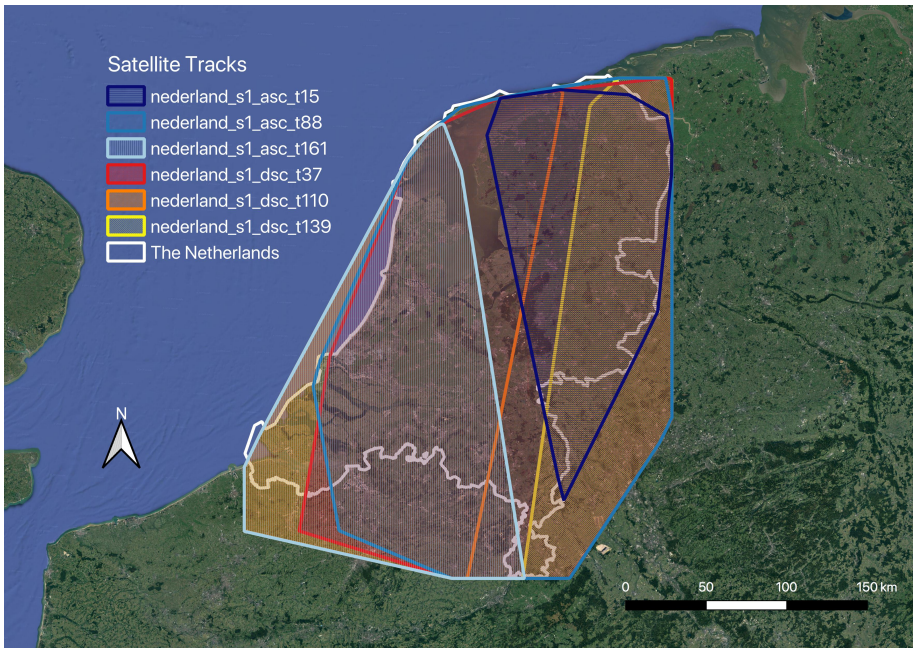

Figure 4.9: Spatial overview of the PSI dataset coverage of parts of the Netherlands, along the different satellite track covers: ascending tracks 15, 88 and 161, and descending tracks 37, 110 and 139. These representations are the convex hulls of the point sets, per individual track[4] (Data from SkyGeo). A Google Satellite map is featured in the background.

4.2.2. Secondary Input – Auxiliary Data

The auxiliary datasets are selected to enrich the 'base' PSI dataset with contextual information. For the Netherlands there are many different sources of auxiliary data available in the context of suface deformation and its causes and effects on the environment. Over the years, the Dutch government and associated institutions have provided multiple open source records and maps, featuring many of the country's geographic characteristics. Information about the local built environment, i.e. buildings, addresses, and the local infrastructure and water management per province are stored in various registries. Natural features, such as the different soil types, geomorphology, and hydrology are provided as well. To ease the process of managing a wide range of datasets, the various considerations regarding their selection are first clarified. Subsequently, the individual auxiliary datasets are presented and discussed according to their dimensional, topical or functional groups.

Additionally, in future studies on attribute-enrichment of PSI datasets, or any type of spatial data in general, the distinction can made between 'quasi-static' and dynamic data. The first shows relatively constant behaviour over time, whereas 'dynamic' data changes more frequently during the satellite lifetime, for example weather and soil moisture data. This distinction is further discussed in the recommendations part of this study, presented in Chapter 8.

Data selection

The selection of auxiliary datasets is based on the relation between the auxiliary dataset and the estimated surface deformation and/or the acquisition procedure of the InSAR data, the data type and storage capabilities, and the spatial and temporal dimensions of the information contained in the datasets. These considerations are discussed separately in the following items.

Relation to surface deformation or image acquisition – The auxiliary dataset is selected on the basis of the type of information that is in line with the scope of this research. This entails that the information is time and/or geographically bound to the area of interest, i.e. the Netherlands. The dataset relates to surface deformation as a direct or indirect cause or effect of it. If this not the case, the dataset should be linked to the image acquisition procedure of the PSI technique, directly or indirectly, or it should provide useful information about the natural or built environment affecting (or affected by) the observed phenomenon.

Data type & storage – The dataset should be available as machine-readable structured data. In other words, the information can be stored and queried upon in a table or matrix-like structure, consisting of rows and columns. The rows should represent the individual elements, provided of an identification (ID) key, and preferably stored in the correct reference system[5]. Columns represent unique attributes that illustrate the properties of the individual elements. In addition, the option to visualize the dataset in a mapping environment should be present. This again highlights the need for all dataset entries to be provided with geolocation features.

Space & Time dimensions – Since this study focuses on the deformation patterns of the Netherlands, the selection of auxiliary datasets is narrowed to the same spatial extent. The types of classifications relate to their spatial coverage. For example, soil type classifications or 'objects' from BRO and building objects from BGT, both presented in the following sections, can vastly differ in terms of the size of their representative polygons, i.e. km-to-m scales. Thus, the choice whether or not to include a particular dataset with objects of various sizes, in part, determines the level of detail of the analysis. This motivates the choice for the general two-part analysis of this study, focusing on the one hand on the widespread deformation patterns linked to soil type classifications of the entire country, i.e. the nationwide analysis in Chapter 5, and on the other hand focusing on individual case-settings with the inclusion of more auxiliary data sources (Chapter 6).
Since differences are present in the temporal dimensions between the different datasets, both primary (PSI) and auxiliary, a distinction between quasi-static and dynamic datasets may be considered with respect to the primary input dataset itself. As mentioned at the start of Section 4.2.2., this distinction is further elaborated on in the recommendations of this study. As the inclusion of dynamic auxiliary datasets implies a fundamentally different implementation of the database approach, the auxiliary datasets presented in the following sections may be assumed to be quasi-static with respect to the typical 7 to 10-year lifetime and the 6 day repeat cycle of the satellites, reflected in the temporal domains of the primary datasets, as seen in Table 4.5.

Overview

As discussed in the data selection procedure, the quasi-static datasets contain fairly time-invariant information, with respect to the primary PSI datasets. Table 4.6 presents an overview of the datasets used in this study, which are discussed separately in the following sections in terms of their contents, sources, dimensions, and applicability for the different parts of this study. These datasets involve the Dutch registry on geographic or 'topographic' information, known as Basisregistratie Grootschalige Topografie (BGT), and the Dutch registry on the subsurface, known as Basisregistratie Ondergrond (BRO), which includes the Dutch soil map 'Bodemkaart' and geomorphology map 'Geomorfologischekaart Nederland' (GKN).
Additionally, Appendix B is dedicated to the additional auxiliary datasets which are not directly implemented in this study, but the author deems relevant for the estimation of surface deformation and/or validation.

[5]For the Netherlands, the most commonly used reference system is the Rijksdriehoek (RD) system, which is coupled to the European Terrestrial Reference System 1989 (ETRS89).

Dataset	Organization	Contents	Layers	Record	Implementation
BGT	Kadaster	Topography	Vector	2014	ch6 (SH,G)
BRO	Ministerie BZK	Soil	Vector	2018	ch5 & ch6 (SH,G)[6]
Bodemkaart (BRO)	WUR	Soil type, groundwater	Vector	2017	ch5 & ch6 (SH,G)
GKN (BRO)	WUR	Geomorphology	Vector	2017	ch6 (SH,G)

Table 4.6: Overview of the auxiliary data sets implemented in this study for the nationwide analysis (Chapter 5) and/or the case study analyses (Chapter 6) of South Holland (SH) and Groningen (G). These are presented alongside their respective organizations, including descriptions of their contents, layer types (vector or raster), and the year of recording.

BGT

Basisregistratie Grootschalige Topographie (BGT) is a detailed large-scale geographical map of the Netherlands. It is designed to unambiguously register the locations of all physical objects, such as buildings, roads, water, railways, and agricultural areas (PDOK n.d.[b]). The BGT datasets are available as 20 cm -accurate maps, containing different topography object files. These are uniform in contents and quality for the entire country of the Netherlands (Ministerie van Infrastructuur en Milieu 2013). Figure 4.10 and Table 4.7 provide the main overview of the BGT physical objects and associated features.

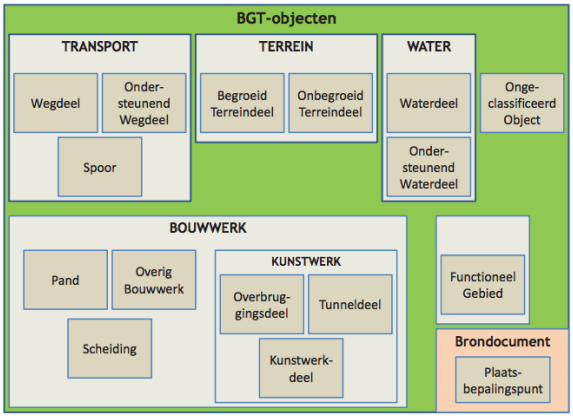

Figure 4.10: Overview of the different BGT physical objects in their respective feature classes. In some cases the physical objects remain unclassified, i.e. 'not part of the definition of NEN 3160 Gebouw' (Ministerie van Infrastructuur en Milieu 2013). Additionally the BGT contains 'Plaatsbepalingspunten' (PBPs), i.e. positioning points, with known coordinates. The PBPs are part of the limits of BGT objects (Source: Ministerie van Infrastructuur en Milieu 2013).

Feature Class	Object(s)
Transportation	Road section, Supporting road section, Railway.
Terrain	Vegetated terrain section, Non-vegetated terrain section.
Water	Water section, Supporting water section.
Construction	Building, Other construction, Division.
Structure	Bridging part, Tunnel part, Structure part.
Functional area	-
Unclassified object	-
Source document	Positioning point

Table 4.7: Listing of feature classes and physical objects present in the BGT dataset, based on the BGT catalogue by Ministerie van Infrastructuur en Milieu 2013.

The source holders of the information contained in the BGT datasets are identified as stakeholders in the deformation/subsidence discussion, i.e. the municipalities, provinces, water authorities, and the concerned ministries. The link between PSI deformation data and BGT features would help in managing the regional public space, housing and infrastructure. Other institutions concerned with managing the natural and built environment, civil and geo-engineering companies, non-governmental organizations, research institutions, and other stakeholders might benefit from the access to enriched deformation datasets as well.

BRO

Basisregistratie Ondergrond (BRO) is the Dutch registry that contains data on the shallow and deep subsurface. The goal of BRO is to provide uniform storage, management, and interchange of subsoil information (WUR n.d.). The BRO datasets contain a wide range of information, such as drill sample descriptions, groundwater monitoring well data, and geotechnical probes. Additionally, BRO contains various subsurface models, including a digital geological model (DGM), the GeoTOP model (GTM), and the REGIS II Hydrogeological model (HGM) (PDOK n.d.[c]).
As part of the BRO dataset in PDOK, two maps are of particular interest for this study, i.e. the 'Bodemkaart' and the 'Geomorfologische Kaart Nederland' (GKN), which are, respectively, the nation-

wide soil and geomorphology maps of the Netherlands. Both of these map records have been produced by Wageningen University & Research (WUR) at 1:50.000 scale. Bodemkaart and GKN contain spatially classified information in the form of vector features with various contextual attributes attached to them. For illustration purposes, the Bodemkaart and GKN are shown in Figures 4.11 and 4.12, as represented in PDOK n.d.(e).

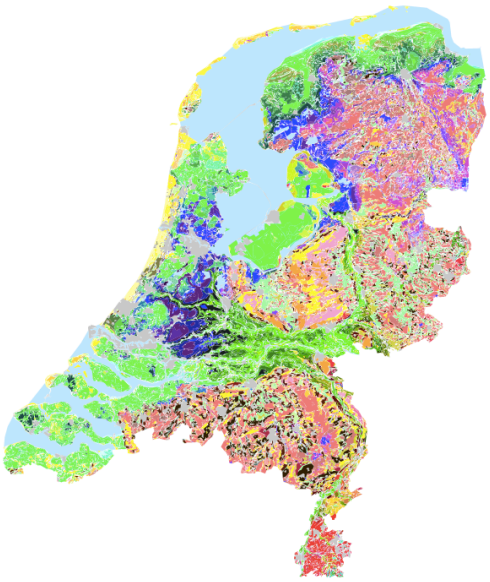

Figure 4.11: Bodemkaart of the Netherlands 1:50.000 (Source: PDOK n.d.(e))

Figure 4.12: Geomorfologische Kaart Nederland (GKN) 1:50.000 (Source: PDOK n.d.(e))

Figures 4.11 and 4.12 depict many objects, or in this case polygons, each represented in a different color according to their attributes. Note that the legend of these figures is not included, as their in-depth classifications and attributes are discussed separately in the following subsections.

Bodemkaart

For GIS applications, a 1:50.000 scale soil map or Bodemkaart of the Netherlands has been made available by WUR as part of BRO. Bodemkaart contains vector polygons of 19 main classes, further divided in more than 300 soil codes (WUR n.d.). It provides information on the Dutch shallow subsurface, assembled from 1.50 m deep drill samples. Additionally, groundwater table (GWT) information is include in Bodemkaart, divided in 11 different units. Table 4.8 provides an overview of the Bodemkaart attributes and their coded notations.

Attribute	Meaning	Type	Example 1	Example 2
gid	Object identification	N	19082	52612
Bodem_code	Soil code	AN	Hn23	Mn35A
Bodem_omschr	Soil description	A	Veldpodzolgronden; lemig fijn zand	Kalkrijke poldervaaggronden; lichte klei, profielverloop 5
GWT_code	GWT code	AN	VI	IV
GWT_omschr	GET description	AN	VI = H 40-80 L >120	IV = H >40 L 80-120
Voor	Topsoil	A	-	e
Letter	Subgroup	A	Hn	Mn
Cijfer	Texture	N	23	35
Kalk	Lime content	A	-	A
Achter	Underlying soil	A	-	-
Schop	Excavation code	A	F	-
Hel	Slope	A	-	-
Kleur_bod	Soil color	N	170	202
Kleur_gwt	GWT color	N	148	199

Table 4.8: Bodemkaart 1:50.000 attributes and their codes, provided with two example features. As specified by 'Type', the attribute codes either consist of letters, i.e. alpha (A), numbers, i.e. numeric (N), or a combination of both, i.e. alphanumeric (AN). This overview of the BRO bodemkaart attributes is based on de Vries, de Groot, et al. 2003.

As seen in Table 4.8, the main categorization of the dataset is based on the soil type. A complete list of the 19 main soil units is given in Table 4.9. The soils are further categorized into subgroups, according to the following characteristics (if applicable); peat type, nature and texture of the topsoil, profile, hydromorphology, and lime content (de Vries, de Groot, et al. 2003). These sub-categorizations are also included as their own soil map attributes. The 'Voor', 'Achter' and 'Cijfer' attributes in Table 4.8 provide additional information on the top and underlying soil layers with respect to the main soil layer, as well as the main soil texture. Since this study focuses primarily on the main soil types, described in 'Letter', the different 'Voor', 'Achter', and 'Cijfer' codes are excluded from the documentation. For a complete overview of all Bodemkaart attributes and their meanings, the reader is referred to de Vries, de Groot, et al. 2003. The 'Kalk' attribute indicates whether a given soil has a rich or poor lime content, respectively denoted with the letter 'A' or 'C'.

Soil Type (NL)	Soil Type (EN)	Code
Veengronden	Peat soils	V
Moerige gronden	Swampy soils	W
Podzolgronden	Podzolic soils	Y, H
Brikgronden	Argillic (B-horizon) soils	B
Dikke eerdgronden	Mollisol (Ap/Ah -horizon) soils	EZ, EL, EK
Kalkloze zandgronden	Non-calcareous sandy soils	Z...
Kalkhoudende zandgronden	Calcareous sandy soils	Z...A
Kalkhoudende bijzonder lutumarme gronden	Calcareous lutum-poor soils	S...A
Niet-gerijpte minerale gronden	Non-ripened mineral soils	MO-zeeklei, MO-rivierklei
Zeekleigronden	Marine clay soils	M
Rivierkleigronden	River clay soils	R
Oude rivierkleigronden	Old river clay soils	KR
Leemgronden	Loam soils	L
Mariene afzettingen ouder dan pleistoceen	Marine deposits older than Pleistocene	MA, MK, MZ
Fluviatiele afzettingen ouder dan pleistoceen	Fluvial deposits older than Pleistocene	FG, FK
Kalksteenverweringsgronden	Limestone weathering soils	KM, KK, KS
Ondiepe kleileemgronden	Shallow clay-loam soils	KX
Overige oude kleigronden	Remaining old clay soils	KT
Grindgronden	Gravel soils	G

Table 4.9: Overview of the 19 main soil classes (in Dutch) and their codes from the Alterra-report 811 in de Vries, de Groot, et al. 2003.

Of the 19 main soil units, a selection of overarching units are defined for the nationwide analysis performed in Chapter 5, namely: peat (P), sand (Z), marine clay (M), river clay (R), loam (L), and

gravel[7] (G). This selection is based on the 7 main soil classes identified in de Vries, de Groot, et al. 2003, with the exception of 'old clay soils', since their classifications most often occur in combination with river clay (R) and marine clay (M). The spatial distribution of this selection of 'main soil classes' for the nationwide analysis can be observed in Figure 4.13. As many of the PS-InSAR points coincide with buildings, which is also a class of its own in the Bodemkaart, it is included in the main selection of soil types for the nationwide analysis.

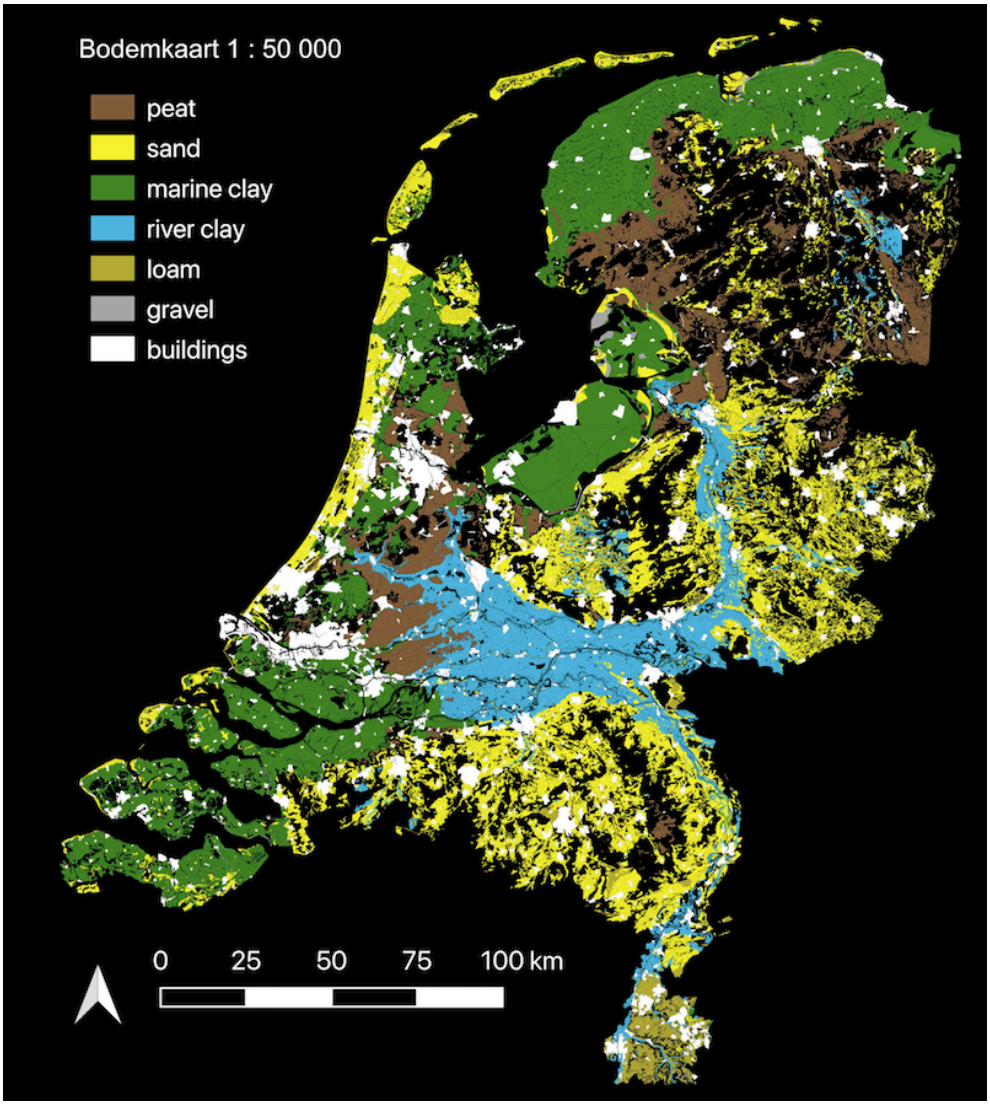

Figure 4.13: Map of the selection of the main Bodemkaart soil classes for the nationwide analysis: peat, sand, marine clay, river clay, loam, 'stone' (here denoted as 'gravel') and buildings. This selection is based on the main soil type classes from de Vries, de Groot, et al. 2003. Note: Even though the 'stone' class is not accurate in its representation of gravel, it still remains present in the remainder of this study. Thus, when present, the term 'gravel' as an overarching main soil type is denoted with quotation marks.

Aside from the soil type attributes, GWT information is available for the different soil map objects.

[7]The latter soil type, i.e. gravel, initially supposed to be denoted with the name 'stone' in the classification steps of chapter 5 is no longer accurate. Due to an erroneous code being assigned to represent this soil type, i.e. 'S' instead of 'G' for 'grind' or 'gravel', in the initial classification and querying procedures of this study, the name 'stone' no longer refers to gravel, but rather to 'Kalkhoudende bijzondere lutumarme gronden' and 'Kalkhoudende vlakvaaggronden'. These soil types are more specific in nature, and refer to calcareous lutum-poorsoils, composed of loamy and clayey -extremely fine sands. These soils types classified under the name 'stone', and the actual 'gravel' soils are present to a far lesser extent in the Netherlands than the other 'main soil types' used for the analysis, i.e. peat, sand, marine clay, river clay, and loam. Therefore, the so-called 'stone' samples remain in the nationwide analysis, as presented in chapter 5. In consideration of this, the 'stone' class term is from here on used with quotation marks.

Specifically, the 11 GWT attributes refer to the highest and lowest mean groundwater levels. Based on Dutch terminology, these are respectively referred to as 'gemiddeld hoogste grondwaterstand' (GHG) and 'gemiddeld laagste grondwaterstand' (GLG). An overview of the coded notations of the 11 different GWT codes with their meaning in terms of GHG and GLG, is provided in Table 4.10.

GWT Code	GHG (cm-mv)	GLG (cm-mv)
I	<40	<50
II	<40	50-80
IIb	25-40	50-80
III	<40	80-120
IV	>40	80-120
V	<40	>120
Vb	25-40	>120
VI	40-80	>120
VII	80-140	>120
VIII	>140	>160

Table 4.10: Groundwater table (GWT) codes and their corresponding mean highest and lowest groundwater levels (GHG and GLG respectively) expressed in cm with respect to ground level, i.e. 'maaiveld' (mv). The coded GWT notations were last updated and modified in 1988. These classifications are part of the soil map 1:50.000, found on PDOK n.d.(c). Earlier versions of the GWT classifications are documented in de Vries, de Groot, et al. 2003.

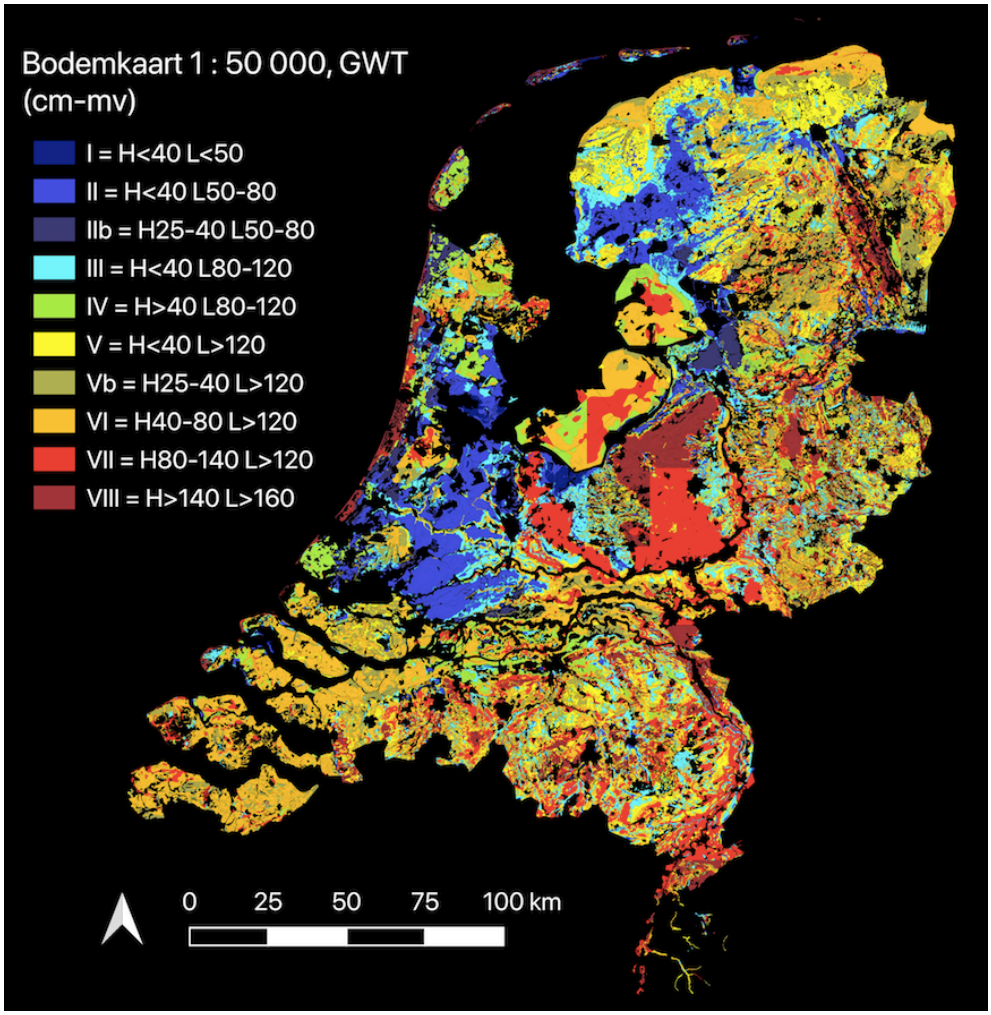

Figure 4.14: Map of the selection of the main Bodemkaart GWT classes: I, II, IIb, III, IV, V, Vb, VI, VII, VIII. These GWT classes are based on the GWT classes, referring to the mean highest and lowest water level, i.e. GHG and GLG, in cm-mv (cm w.r.t. ground level) from de Vries, de Groot, et al. 2003. Note: any remaining 'empty' areas have no GWT classification.

For the excavation and slope attributes, the coded notations are summarized in the two Tables 4.11 and 4.12. For Table 4.12, further elaboration is required on the codes 'F' and 'G', which would seem to have the same meaning; 'Excavated (1)' refers to 'terrains in which the soil profile is reworked into a heterogeneous mixture', whereas 'Excavated (2)' refers to 'soils that have been locally lowered through excavation, e.g. for the extraction of sand or clay' (Brouwer and van der Werff 2012).

Code	Slope (%)	Meaning
A	<2	Flat & Almost flat
B	2-5	Light slope
C	5-8	Medium slope
D	8-16	Strong slope
E	16-25	Quite steep
F	>25	Very steep

Table 4.11: The 'Hel' attribute codes, as single capital letters, and their meanings. These denote the slope (in %) of the uneven areas that some object are categorized under. This soil map classification is documented in de Vries, de Groot, et al. 2003.

Code	Excavation (NL)	Excavation (EN)
E	Geëgaliseerd	Flattened
F	Vergraven	Excavated (1)
G	Afgegraven	Excavated (2)
H	Opgehoogd	Heightened

Table 4.12: The 'Schop' attribute codes as single capital letters and their meanings. This soil map classification is documented in de Vries, de Groot, et al. 2003.

Even though the Bodemkaart is included in this study as a quasi-static dataset, there is a need for actualization as the soil information can be outdated. Through natural and anthropogenic induced changes in the environment, the distributions of different soil types and groundwater levels in the Netherlands are also prone to change. Around 1960, the former 'Stichting voor Bodemkartering' (Stiboka) started producing the Bodemkaart of the Netherlands at 1:50.000 scale. In 1995 the map was completed, as it covered the entirety of the Netherlands (Brouwer, de Vries, and D.J.J Walvoort 2018). Since 2010, updates are structurally performed on the Bodemkaart. The first update focused on the swampy soils and thin peat soils in the northern parts of the Netherlands (de Vries, Brus, et al. 2014). Between 2016 and 2017, the Bodemkaart was updated for the non-ripened clay areas in the provinces of Noord and Zuid-Holland (de Vries, D.J.J. Walvoort, and Brouwer 2017). Lastly in 2017, the thick peatlands in the Waterschap Drents Overijsselse Delta have been updated (de Vries, Brouwer, and D.J.J. Walvoort 2018).

GKN

Geomorfologische Kaart van Nederland (GKN) from WUR, presented as part of the BRO dataset in PDOK, is the countrywide digital geomorphology map of the Netherlands. Geomorphology is the science that studies the origin and development of landforms, such as hills, valleys, sand dunes and caves, and how those landforms combine to form landscapes (BSG n.d.). In other words, this branch of Earth sciences focuses on the characteristics of relief, elevation differences and slope angles, and on describing the nature and origin of these shapes (ten Cate and Maarleveld 1977). Like Bodemkaart, GKN is provided at 1:50.000 scale. Applications of GKN were developed in the late 1990s, including the assignment of geographical attributes, monitoring of changes in relief, detailed archeological mapping, spatial planning, and research and education oriented applications (Koomen and Maas 2004).
The different landforms, which make up the individual units on the map, are characterized by their own sets of attributes. The GKN classification is managed on three levels (WUR 2017). On the highest level, 11 landform groups are to be distinguished, based on their characteristics, e.g. terraces, valleys, and plains. Based on their genesis, the landforms are further categorized into subgroups, e.g. the plain group is divided into the subgroups: 'dekzandvlakten', plains of tidal deposits, and floodplains. The lowest classification level entails the landform units, in which the subgroups are further divided according to the landform relief, the presence of alternative geological deposits in the topsoil, and whether or not there is an active morphological process at hand (WUR 2017). The GKN classifications are summarized in Table 4.13 and illustrated with an example.

Class	Attribute	Type	Example
Group	Form group	A	R
Subgroup	Form group	A	R
	Genesis	N	2
	Subgroup no.	N	1
Unit	Relief	N	22
	Form group	A	R
	Genesis	N	2
	Subgroup no.	N	1
	Addition	A	dL
	Active process	A	()

Table 4.13: GKN object classifications from WUR 2017, with their corresponding attributes. The coded notation either consist of a letter, i.e. alpha (A), a numbers, i.e. numeric (N), or a combination of both, i.e. alphanumeric (AN). For illustration, an example object is provided, e.g. droogdal or 'dry valley' with a maximum height difference of 0.25 - 0.5 m (filled or covered with sand and/or sandy loess), with coded notation: 22R21dL, part of the subgroup R21 or 'dry valley', which is in turn part of group R or 'valley-shaped lows'.

In this study on land deformation, only the first level group attributes are taken into account, therefore their classifications are listed in Table 4.14. For a full listing of the possible GKN classification, including the subgroups, relief, and genesis attributes, the reader is referred to the GKN legend clarifications in WUR 2017. In addition, for each unit it is stated whether or not the geomorphological process is still active, i.e. 'D', or non-active, i.e. '()' (left open). In Figure 4.15, the landform groups are represented spatially for the entirety of the Netherlands, according to the classes listed in Table 4.14.

Code	Landform Group (NL)	Landform Group (EN)
A	Wanden	Walls
B	Geïsoleerde heuvels en heuvelruggen	Isolated hills and ridges
D	Plateaus	Plateaus
E	Terras-vormen	Terrace-forms
F	Plateau-achtige vormen	Plateau-like forms
G	Waaiervormige glooiingen	Fan-shaped slopes
H	Niet-waaiervormige glooiingen	Non-fan-shaped slopes
L	Heuvels en heuvelruggen met bijbehorende vlakten en laagten	Hills and ridges with associated plains and lows
M	Vlakten	Plains
N	Niet -dalvormige laagten	Non-valley-shaped lows
R	Dalvormige laagten	Valley-shaped lows

Table 4.14: Codes for the landform groups as the first level attributes of the GKN classification, from WUR 2017.

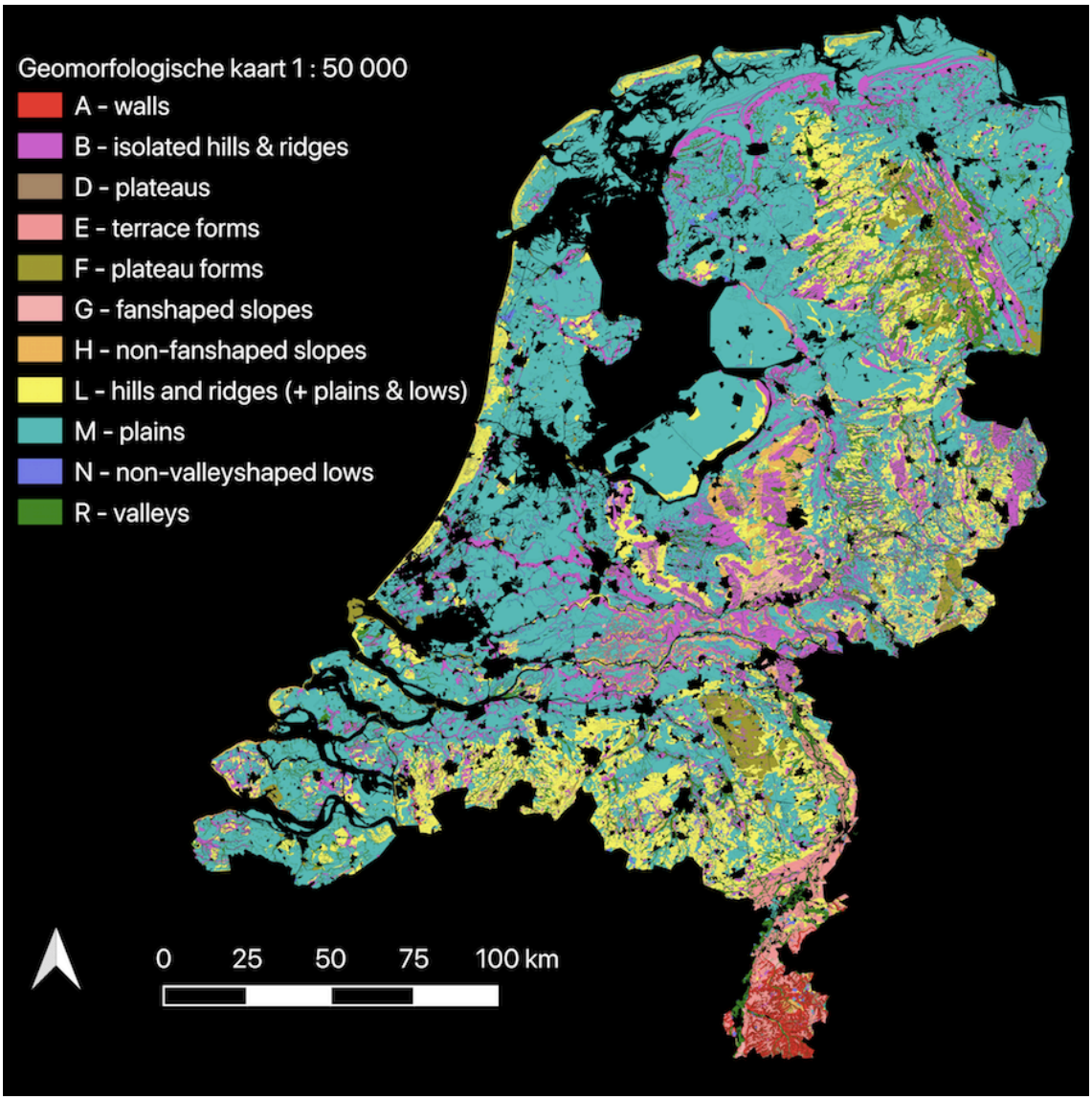

Figure 4.15: Landform group (level 1) classification of the Gemorfologische Kaart Nederland (GKN), based on the classifications presented in table 4.14 from WUR 2017. Note: any remaining 'empty' areas have no geomorphology classification, e.g. the city areas.

The addition of GKN classifications is useful for this study, as the processes that change the Dutch

landscape and that lead to differential height are well documented in a suitable format for GIS applications. Both natural and human-induced changes to the environment are accounted for in the GKN dataset. As for the Bodemkaart, the GKN is interpreted as a quasi-static dataset in the context of this study. The reason for this is that land surface changes are assumed to occur over relatively long periods of time with respect to the satellite observation lifetime. GKN has been subject to changes in its assembly and classification procedure. The first nationwide geomorphology overview map 1:50.000 was introduced in 1951, followed by a process of systematic mapping of the geomorphology of the Netherlands between 1966 and 1993. The addition of multiple map sheets altogether covered approximately two thirds of the Netherlands. Between 1998 and 2003 in a series of projects, a digital nationwide version of GKN was developed, leading to its first digital version in 2003 (Koomen and Maas 2004). This digital version is of main use to this study. As some of the GKN map sheets date back to the end of the 1960s, they need to be updated for changes due to construction, infrastructure, and developments in agricultural and natural areas (Koomen and Maas 2004).

4.3. Implementation – Operations & Queries

This section presents the general implementation of the database approach in this study, of which the results are presented in the later chapters. With the database approach discussed in the early parts of this chapter, a method is established to assign attributes to the points within the datasets, assorted according to their respective satellite tracks. From there, the main statistical relations and distributions are computed per attribute to better understand the rate of deformation these appear to show and their physical causes. With the input datasets presented for the nationwide analysis (Chapter 5), and the case study analyses (Chapter 6), the attribute-enrichment method is discussed in terms of the required storage, spatial operations, and the computational and visualization steps to obtain the results.

4.3.1. Method

Even though the InSAR technique provides useful and precise information on surface deformation, it does not explicitly tell the user from which object the signal returns. In terms of positioning and classification of the InSAR data, there are still improvements to be made. To obtain a nationwide view of the link between the different soil types, GWTs and the estimated deformation associated with these, a coupling is needed between the source observations and the contextual information.
The database approach forms the basis of the processes involved in selecting, sorting, and storing the data, as well as the possible operational steps that may be applied to the data. Based on this approach, the methodology for the various deformation analyses is divided in procedural steps. First, the spatial data selection is performed for the nationwide deformation analysis. Subsequently, the database is set up to store the various datasets. Furthermore, spatial joins are performed in order to spatially couple the base dataset with the auxiliary information. The necessary spatial queries are performed to load the enriched data selections into the computational environment, i.e. Matlab. Finally, the statistical analysis and visualization steps are performed in the computational environment.

4.3.2. Spatial datasets

A general overview of the auxiliary datasets is provided in table 4.6, which mainly consist of BGT and BRO (Bodemkaart and GKN) classifications. Since the selection of auxiliary data differs per analysis, i.e. the nationwide analysis in Chapter 5 and the three case studies in Chapter 6, a more in-depth overview is given in Table 4.15 of the PSI datasets and attributes are used in their respective analyses. Note that the selection of auxiliary data for the Limburg case study in Section 6.1 is not part of the Dutch basisregistratie (base registry) datasets, presented in Section 4.2. The South Limburg case is set around a risk analysis for sinkhole formation and differential ground movement, reported in Heitfeld, Klunker, et al. 2016. Thus, the associated attributes are introduced separately in the general introduction of the Limburg case in Section 6.1.

Analysis	Chapter	PSI Tracks	Auxiliary Dataset	Attribute/Object
Nationwide	5	15, 37, 88, 110, 139.	Bodemkaart	soil subgroup, GWT code.
South Limburg	6.1	37, 88.	Heitfeld, 2016	EK near surface mining (1 – 3), EK differential ground heave (1 – 3).
South Holland	6.2	37, 110.	BGT	road section, building, non-vegetated/vegetated terrain.
			Bodemkaart	soil code
			GKN	form subgroup code
Groningen	6.3	15, 37.	BGT	road section, building, non-vegetated/vegetated terrain.
			Bodemkaart	soil code
			GKN	form subgroup code

Table 4.15: Overview of the different analyses and their corresponding PSI tracks and auxiliary datasets, as part of the implementation of the database approach.

PSI data

The Sentinel-1 PSI datasets are used as the primary input dataset and stored in the PostgreSQL database. As seen in Figure 4.9, the different Sentinel-1 tracks together cover the entirety of the Netherlands, and are therefore sufficient in terms of their overall coverage for a nationwide study. As for the individual case studies, at least two PSI tracks are selected, as seen in Table 4.15, based on their coverage of their respective case studies.

As indicated in Table 4.16, the linear LOS velocity in mm/yr is one of the inherent attributes of the PSI datasets. This attribute is visualized for the different datasets, with the exception of track 161, listed in Table 4.5. The PSI data from track 161 is not part of the study, as the initial scope of the study was set on the observed deformation in Groningen. Similarly, track 110 was not initially part of the study. However, as the (spatial) scope of this study broadened, the observations from track 110 were later included [8]. For tracks 15, 88, 37, 110 and 139 the LOS linear deformation (mm/yr) is visualized in Figures 4.16 – 4.20.

Auxiliary datasets

From the auxiliary data inventory in Table 4.6, selections for PSI data-enrichment are made for each individual analysis, as reflected in Table 4.15. The Bodemkaart classifications, visualized in Figure 4.11, entail different levels of detail in their descriptions. For the nationwide analysis in Chapter 5 the focus is set on extracting the most relevant and indicative features of these datasets, i.e. the main overarching soil types and groundwater table (GWT) classes, as these are most suited to the nationwide extent of surface deformation. Therefore, it is more efficient for the interpretation of the results to adopt smaller selections of attributes, grouped by a common characteristic. For example, in Dutch soil taxonomy 'waardveengronden', 'meerveengronden', and 'vlierveengronden' are strictly speaking different soils with different compositions and properties, but they fall under the same main soil type category of 'veen', i.e. peat. Thus, as visualized in Figure 4.13, a selection of 6 representative soil types is used in the nationwide soil deformation analysis in order to obtain a general overview of the deformation behaviour that is observed for each of the 6 classified soil types, i.e. peat, sand, marine clay, river clay, loam, and gravel or 'stone'. Of all the GWT classes in the Netherlands, presented in Table 4.10 and Figure 4.14, the 8 main groups (I – VIII) are considered, thus excluding classes IIb and Vb, as these are expansions to their respective counterparts (II and V). In this way the distinction is made between object-areas in terms of their highest and lowest mean groundwater levels, i.e. GHG and GLG.

As Chapter 6 presents deformation results of smaller case study areas, more attributes are used in the PSI enrichment, providing more detailed contextual deformation analyses. Without the selection of any 'representative' soil types, or the grouping of other attributes as part of 'overarching' classes, the level of detail is kept. This is enabled by a larger variety in contextual information in a more confined

[8] At this stage, track 161 is again left out of the study, considering the slightly superior coverage of track 110 over track 161 and due to data-storage constraints.

environment, which can more easily be managed in terms of the output presentation and the discussion thereof.

4.3.3. Database set-up & visualization

There are several steps involved in setting up a database environment for the main and auxiliary datasets to be stored in. First, the PostgreSQL environment is set up and operated either from the system terminal or with the use of a graphical user interface (GUI). The author opted for pgAdmin 4 (pgAdmin n.d.) (version 4.6) as the administrative GUI front-end tool to manage the database system. As the database used for this study works primarily with spatial data, the open-source GIS support system PostGIS (PostGIS n.d.[d]) is required as a PostgreSQL external extension.
The next steps involve loading in the primary and auxiliary datasets, while accounting for their structures and formats. If necessary, geometry attributes are added to the tables to enable their GIS functionalities. At this stage a connection is maintained between the database and the GIS software, QGIS, which allows for mapped representations of the datasets. Furthermore, in the mapping environment, spatial joins are performed to link the PSI points to their respective external attributes. The resulting joined layers are then used for statistical analysis, of which the set-up is discussed separately.

PSI data storage & inherent attributes

The processed PSI points are stored in a PostgreSQL database in separate tables according to the six different satellite tracks, presented in Table 4.5. Table 4.16 provides an overview of the attributes or 'columns' and their data types. Except for the assigned id code per point, these attributes are considered to be 'inherent', since they have already been assigned to the PSI points prior to their input in the database.

Column	Data Type	Description
id	character varying	PostgreSQL identification key
pnt_id	character varying	Inherent point identification code
pnt_lat	double precision	Point latitude
pnt_lon	double precision	Point longitude
pnt_rdx	double precision	Point x -RD coordinate
pnt_rdy	double precision	Point y -RD coordinate
pnt_demheight	double precision	Point DEM height
pnt_height	double precision	Point height
pnt_quality	real	Point quality
pnt_linear	real	Point linear deformation rate
d_<yyyymmdd>	real	Time series entry: deformation w.r.t. the epoch
pnt_line	double precision	Point line
pnt_pixel	double precision	Point pixel value
pnt_incidence_angle	double precision	Point incidence angle
pnt_seasonal_amp	double precision	Point seasonal amplitude
pnt_seasonal_phase	double precision	Point seasonal phase
graph_00000	text	Processing-specific function, as string code

Table 4.16: Inherent Sentinel-1 PSI track attributes or columns, as provided by SkyGeo.

Spatial Reference

In addition to the epoch (time reference) per track, as initially indicated in Table 4.5 and in Table 4.16, each track has its own spatial reference. Either the spatial reference is set as a selected 'zero point' based on expert knowledge, or it is taken as the mean linear deformation (mm/yr) of all points in the dataset. For this study, the latter approach yields the following spatial references, presented in Table 4.17.

Track	Spatial Reference (track mean) (mm/yr)
Ascending 15	1.16×10^{-1}
Ascending 88	1.10×10^{-1}
Descending 37	4.65×10^{-1}
Descending 110	-4.23×10^{-3}
Descending 139	2.56×10^{-1}

Table 4.17: Spatial reference per track, based on the track-mean linear deformation (mm/yr) between 2015 and 2019 of the PSI datasets from SkyGeo.

LOS linear deformation

After assigning a geometry attribute to the PSI datasets, these can be represented in terms of their linear deformation rates (mm/yr) between 2015 and 2019 in the LOS. The precise begin and end dates for the different S1 PSI datasets are given in Table 4.5 back in chapter 4. As such, Figures 4.16 to 4.20 present the inherent 'pnt_linear' attribute per satellite track. As is clear from these figures, and Figure 4.9, the spatial coverage of these tracks differs. The same color bar settings are applied for all different track datasets. Thus, any points with a LOS linear velocity exceeding the color bar boundaries [-10,10] mm/yr are depicted with the same color 'extreme', i.e. dark red or dark blue respectively. This color setting is selected to obtain better color discrimination for the bulk of the datasets, centered around their respective zero velocity reference.

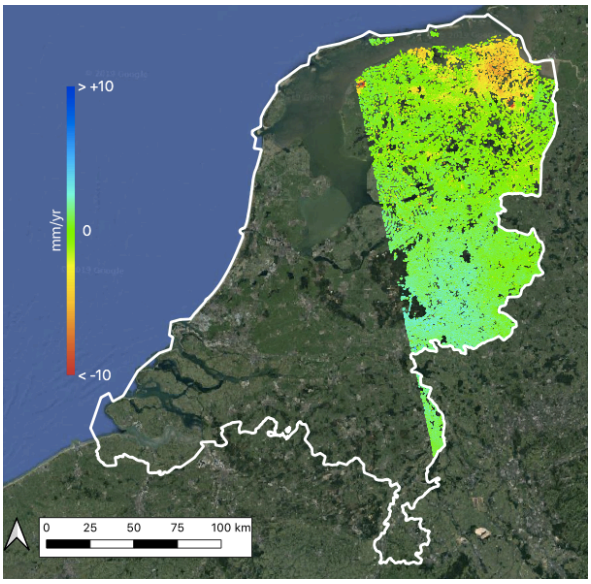

Figure 4.16: S1 Ascending Track 15: Linear LOS deformation rate (mm/yr) for the Netherlands, (data: SkyGeo).

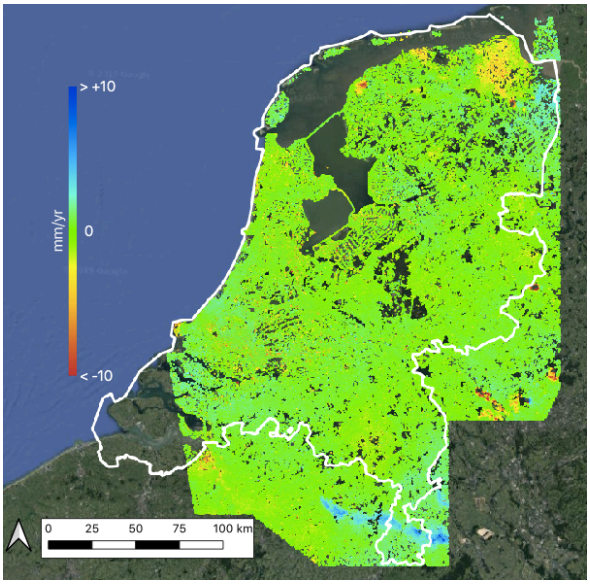

Figure 4.17: S1 Ascending Track 88: Linear LOS deformation rate (mm/yr) for the Netherlands, (data: SkyGeo).

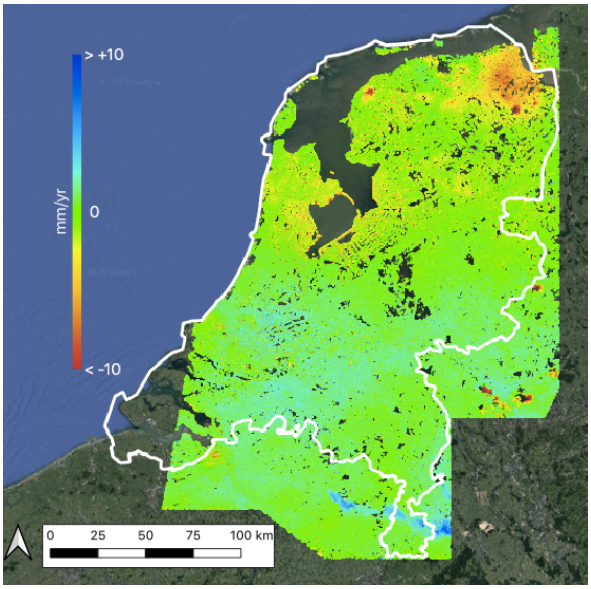

Figure 4.18: S1 Descending Track 37: Linear LOS deformation rate (mm/yr) for the Netherlands, (data: SkyGeo).

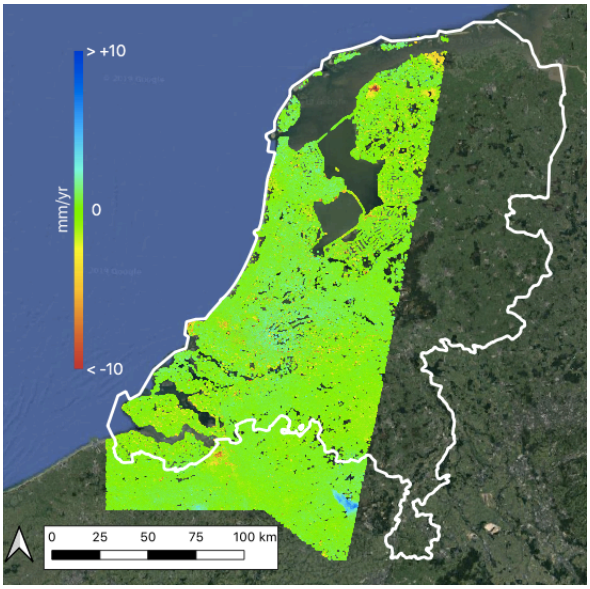

Figure 4.19: S1 Descending Track 110: Linear LOS deformation rate (mm/yr) for the Netherlands (data: SkyGeo).

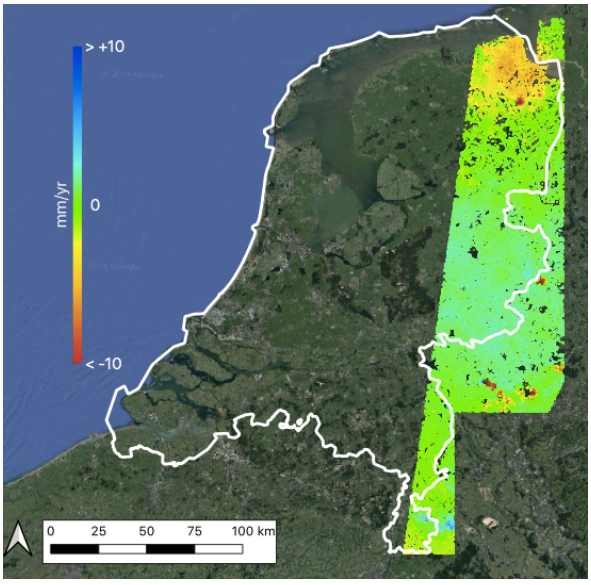

Figure 4.20: S1 Descending Track 139: Linear LOS deformation rate (mm/yr) for the Netherlands (data: SkyGeo).

Auxiliary dataset storage

When the PSI datasets are part of the database, the next step is to add the selection of auxiliary datasets to the same environment. Since most of these are already available in table formats, they can easily be implemented into the system. Similar to the inherent attributes of the PSI datasets, the auxiliary basisregistratie data from BGT and BRO, i.e. the Bodemkaart and GKN, have their own features provided, as indicated in Table 4.15.

Adding geometries

The placement of different datasets together in the same database does not automatically provide any spatial relations between them. Therefore, a 'geometry' is assigned to the PSI points in order for them to be represented in a GIS environment. This is done with the PostGIS function 'AddGeometryColumn', which uses the following arguments: the table name, the column name, the spatial reference system identifier (SRID), the type, and the dimension.
For example, a geometry attribute is added to descending track 110, for it to be used in GIS software, e.g. QGIS. To this end, a new column is added to the already existing table 'nederland_s1_dsc_t110', which is then set in the correct SRID with the code 28992, referring to the RD coordinate system. This would result in the following SQL query;

```
SELECT AddGeometryColumn('nederland_s1_dsc_t110','geom',28992,'POINT',2);
UPDATE nederland_s1_dsc_t110
SET geom = st_setsrid(ST_MakePoint(pnt_rdx,pnt_rdy),28992);
```

4.3.4. Spatial join

Spatial joins are performed on the datasets, meaning that the attributes of one vector layer are copied to another layer. For the nationwide analysis, the soil type and GWT coded attributes in the Bodemkaart are added to the PSI datasets per track, based on their spatial relationship, i.e. a particular PSI point 'inside' of a soil type or GWT polygon, referring back to the topology relations in Table 4.3. The same spatial joins are performed for the separate case studies, but with a larger selection of attributes, including those of BGT and GKN.
In QGIS, the 'Join Attributes by Location' tool is found under the data management tools in the vector directory. The various PSI track-specific datasets are selected as input layers, and the Bodemkaart is selected as the so-called 'join layer'. The option to choose 'selected features only' is available, which is useful as possibly not all attributes from the join layer are of importance for the intended user application. Note that spatial joins of nationwide proportions can be a lengthy process, taking up to several hours. This results in an attribute-enriched PSI dataset, with the additional information stored in separate columns.

4.3.5. Spatial queries

From the enriched PSI datasets, spatial searches or queries are performed to obtain the desired subset from the different tables stored in the database. For the nationwide analysis, the spatial queries are set to extract the following the following;

1. 6 Main soil types – peat, sand, marine clay, river clay, loam, 'stone'[9] – and one class for 'buildings', denoting the entirety of the built environment.

2. 8 Main GWT classes – I, II, III, IV, V, VI, VII, VIII. Thus, this selection excludes the GWT classes IIb and Vb as these serve as extensions to the classes II and V.

In the selection of 8 Main GWT classes, classes IIb and Vb are disregarded, whereas in the selection of 6 main representative soil types, entries are selected based on a shared 'Letter' or soil 'subgroup' (following the terminology used in table 4.8) in their coded notations. This is done with the use of 'AND' and 'OR' statements. For all the case study analyses in Chapter 6, i.e. South Limburg, South

[9]Due to the initial application of an erroneous classification code ('S' instead of 'G' for gravel) prior to the processing of the analysis results, the name 'stone' refers to an alternative soil class, i.e. 'Kalkhoudende bijzondere lutumarme gronden' and 'Kalkhoudende vlakvaaggronden' instead of gravel. For further elaboration on this misinterpretation, the reader is referred back to chapter 4, where the main soil types are introduced in Table 4.9.

Holland and Groningen, the spatial queries are set to extract all individual entries for a particular attribute, listed in Table 4.15, without grouping them under a common characteristic.
As the purpose of these search-queries is to select these subgroups for further statistical analysis, the queries are performed directly from within the computational environment, i.e. Matlab (version 2019a). To this end, a connection is set up between the DBMS (PostgreSQL) and the computational program (Matlab). With this connection, the queries are scripted to perform a cluster of searches instead of manually performing them one at a time. In addition, the repeated or 'automated' queries allow for the data subsets to be stored appropriately for further computational steps involved in obtaining the desired statistics per subset.

Database – Computational environment connection

In Matlab (version 2019a) the 'Database Explorer' application is used to establish the connection with the DBMS, PostgreSQL. Some specifications are needed for this, such as the database name, server, port number, and the driver location. After the connection is established and tested, the retrieval of records or data from within the computational environment is possible.

Automated queries

There are multiple ways to perform search queries and thus to load data subsets onto the computational platform Matlab. Either the queries can be performed with the use of the Database Explorer application from the Matlab command window, or via a Matlab script or function.
The more efficient queries are automated in the sense that these can be performed with the use of iterative commands, written in in either a script or a Matlab function. Thus, no repeated manual queries need to be written for each individual search in the DBMS. Additionally, the iterative commands allow for the user to directly specify the storage options for the data subsets. The coded notations (letters, numbers, symbols, etc.) of the auxiliary datasets are used to specify certain attributes that are to be included in the search operation. To access information from the PostgreSQL database from the Matlab environment, queries are written in SQL as the default language. However, efficient substitutions can be applied in the search parameters, which is in turn implemented in the SQL command.

Example query

As a typical query example, the following SQL query-portion of the script retrieves all PSI points from e.g. track 15 that belong to the different soil type classes for the nationwide analysis.

```
1  % Attribute names & codes
2  code_soil = {'V','Z','M','R','L','S','BE'};
3  code_gwt = {'I','II','III','IV','V','VI','VII','VIII'};
4  ts_15 = {'pnt_linear','d_20150323',...,'d_20190101'}; % lin, timeseries
5  % Query handles
6  name_track = {'nederland_s1_dsc_t15_join'};
7  code_handle = code_soil;
8  query_handle = {'letter'}; % 'letter' for soil type, 'gwt' for GWT.
9  ts_handle = ts_15;
10 % Query
11 query = cell(1,numel(code_handle));
12 for i = 1:numel(code_handle)
13     query{i} = ['SELECT ',ts_handle{1},' FROM ',name_track{1},' WHERE '
           ...  % select column(s)
14     ,query_handle{1},' LIKE ''%',code_handle{i},'%'' OR ' ...
15     ,query_handle{1},' LIKE ''%',code_handle{i},''' OR ' ...
16     ,query_handle{1},' LIKE ''',code_handle{i},'%'' OR ' ...
17     ,query_handle{1},' LIKE ''',code_handle{i},''';'];
18     data{i} = fetch(conn,query{i});
19 end
```

The first 3 commands, i.e. lines 2 to 4, in this example query portion of the script introduce cell arrays, which contain part of the coded notations of the entries that need to be retrieved. These represent the 7 main 'soil type' codes, including the class 'BE', which stands for 'buildings'. The time series string

array for e.g. track 15 consists of the LOS linear velocity, and all date entries, i.e. the deformation with respect to the epoch, here; 2015-03-23. Subsequently, in lines 6 to 9, so-called 'handles' are introduced for the mere purpose of efficient substitution. Thus, the required parameters can be entered once at the beginning of the script, instead of repeatedly redefining the cell array contents for each search through the database. Finally, the query itself is composed by entering the search parameters into the SQL statement (lines 13 to 17). The data is stored in a cell array, of which the size equals the amount of entries in the code handle used for the search.
If alternative storage options are required instead of tables, which are the default in PostgreSQL (e.g. structure or cell arrays), these can be implemented in the query-writing process itself. Note that there is a 'memory limit' (general java heap memory) for the amount of data to be retrieved from the database. For spatially dense observations over a nationwide scale this can result in importation difficulties. Therefore, the java heap size is increased to a maximum, and/or the data import is performed in batches.

4.3.6. Statistical Analysis

The previous sections cover the processes of gathering, sorting, storing, and enriching the PSI datasets with the database approach, as well as retrieval of the necessary selections of data from the database system. This section goes into the statistical analysis of the nationwide selection of datasets, i.e. soil type and GWT -enriched PSI velocity points in the LOS per satellite track and the three separate case study analyses. The goal of the statistical analysis is to provide quantitative contributions to the interpretation of the surface deformation characteristics in terms of the associated classifications.
In most cases, i.e. both nationwide and local studies, the focus is either set on the statistics of the linear deformation trends (mm/yr) or on the time series (mm w.r.t. the epoch) of the estimated deformation per identified class. In this context, deformation is understood in terms of the PSI-derived LOS velocities or the vertical projections thereof. First, the transformation from LOS velocity measures to their vertical projections is discussed, based on the InSAR theory in chapter 3. From these transformed deformation values, the descriptive measures are introduced as part of the statistical analysis. The section concludes with a methodical description of the output computations, leading to the results and discussions in Chapters 5 and 6.

Vertical velocity projection

After querying the appropriate selections from the database into the computational environment, the vertical projection of surface deformation is derived. This step is implemented in the nationwide analysis, as seen in the results of Chapter 5. This derivation uses the conversion of the LOS velocity D_{LOS} directly to a vertical velocity projection D_u, knowing the incidence angle θ_{inc};

$$D_u \approx \frac{D_{\mathrm{LOS}}}{\cos(\theta_{\mathrm{inc}})} \tag{4.2}$$

This goes back to the assumption made in Section 3.3.3. by neglecting the horizontal velocity component in the decomposition of the 3D deformation vector. Eventhough InSAR observations are mostly sensitive to vertical deformation, as recalled from Samieie-Esfahany et al. 2009, this assumption introduces errors. If the horizontal component is perpendicular to the ALD, this implies that $D_{\mathrm{ALD}} = 0$. With an average $\overline{\theta}_{\mathrm{inc}} = 39.4°$ for all tracks, the maximum error follows from a situation in which the horizontal motion is parallel to the ALD, and thus ΔD_u in equation 3.15 becomes

$$\Delta D_u = \tan(39.4°) D_{\mathrm{ALD}} = 0.82 * D_{\mathrm{ALD}} \tag{4.3}$$

or 82% of the horizontal velocity component.
Considering the contribution of the horizontal deformation may differ substantially per location, the results of the localized studies, i.e. presented in Chapter 6, are given in the LOS.

Descriptive & Variability Measures

The statistics applied to the collected nationwide PSI velocity samples include computations of the following descriptive and variability measures of the linear deformation (mm/yr) distributions per track: the mean, median, standard deviation, skewness, minimum, maximum, and the 10th and 90th-percentile deformation values. Thus, based on the prior querying and data selection steps, the statistics apply to

data samples assorted per satellite track (as visualized in Figures 4.9 and 4.16 to 4.20). The results show comparisons for the auxiliary classes of the different attributes, i.e. soil type, GWT, geomorphology and geography classifications.

Output Presentation

The results of the linear deformation analyses in Chapters 5 and 6 are presented visually for the separate satellite tracks. These visual representations include histograms for analyses. Additionally, box plots are included in the nationwide surface deformation results and the main statistics are summarized according to their respective satellite tracks, and attribute-classes in various sets of tables.
The sets of histograms for the different satellite tracks show the normalized distributions of the linear deformation rates for all points assigned to a certain class. In order to present classes together, with vastly differing numbers of observations, the bin selection procedure is set to accommodate for this variety. To this end the Rice rule is applied, which states that the number of bins k equals (Lane n.d.)

$$k = 2 * \sqrt[3]{n} \tag{4.4}$$

in which n represents the total number of observations for a particular class, per satellite track. In a typical histogram the separate bins are shown as bars of a particular bin-width and a height according to the count or probability per bin. Since there are multiple (7 to 8) classes to be compared per sample, individual line plots connect the bin-centers of each distribution, leaving out the bar representations as these may obscure one another. Additionally, the median value of each distribution is represented as a dashed vertical line.
For the nationwide analysis and the South Limburg case study, which have a limited number of classes per attribute, the results of the multiple tracks are summarized in tables. The following descriptive and variability measures are provided, distinguishing between the classes; number of points (-), mean (mm/yr), median (mm/yr), standard deviation (mm/yr), skewness (-), minimum (mm/yr), maximum (mm/yr), 10th-percentile (mm/yr), and the 90th-percentile (mm/yr) of the linear deformation distributions. To highlight the underlying trends of the different samples, a color coding system is applied to the tables in the nationwide analysis. Per track, the highest (most positive) and lowest (most negative) measures are indicated in green and red, respectively. If the same 'highest' or 'lowest' measure applies for the majority of the track, the entries are highlighted in olive or yellow, respectively. The application of the color coding is meant to ease the interpretation of the table results.
In the nationwide analysis, the same distributions are represented in two different box or 'whisker' plots. The first of each set shows the entire deformation rate domain (on the y-axis), and the other is zoomed in on the median linear deformation rate value. In the boxplot representation, the central mark indicates the median of the sample. The top and bottom edges of the box indicate the 75th and 25th percentile values, and the whiskers extend to the extremes of the sample that are not considered outliers (MathWorks n.d.). For Matlab, the default whisker values are taken at approximately 2.7σ (MathWorks n.d.), where σ is the standard deviation of a typical normal distribution. The outliers themselves are indicated with a + sign (MathWorks n.d.).

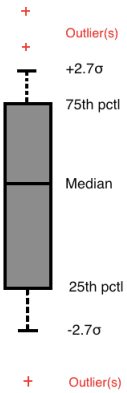

Figure 4.21: Boxplot representation with its default Matlab (MathWorks n.d.) settings.

In addition, the time series for the same points are part of the statistical analysis. Spanning from January 2015 to early January 2019 depending on the satellite track, the individual time series represent the vertical deformation (mm) measured at each acquisition with respect to the epoch.

5

Nationwide Soil Deformation Analysis

This chapter presents the results of a nationwide surface deformation analysis, in which the Sentinel-1 PS-InSAR deformation data acquired between 2015 and 2019 are studied in relation to the available soil datasets of the Netherlands. The PSI signal responses are decomposed into class-partitioned subsets according to (1) the main classified soil types in the Netherlands, and (2) the GWT classifications of the Dutch subsoil, which are both part of BRO. The aim is to obtain an understanding of the relation between the soil composition of the Dutch surface and subsurface, and to assess the rate of deformation of representative sets of points that are attributed to a certain soil characteristics. The results discussed in this chapter, are obtained through the implementation of the database approach, presented in Chapter 4.
As the results in this chapter cover the entirety of the Netherlands, the interpretation thereof also applies to the nationwide scale. The results are presented in various sets of figures and tables, along with their descriptions. At the end of this chapter, a general discussion is given on the results and whether or not these reflect the general deformation background illustrated in Chapters 1 and 2.
The results for the nationwide analysis of the PS-InSAR deformation data are presented according to the contextual datasets that were used to classify them. Following the method presented in Section 5.1, the statistical results are presented and visualized per sample for each of the individual satellite tracks. Descriptions of these results are provided alongside the corresponding histograms, boxplots, time series and tables. The goal of the statistical analysis is to reflect the relations between the nationwide class-partitioned samples and their observed deformation. However, these results do not necessarily predict any type of deformation in particular, without the consideration of any other causal mechanisms. To this end, Chapter 6 involves larger selections of attributes to characterize the deformation behaviour of localized case studies. The presentation and discussion of the nationwide results is divided in sections according to the attributes at hand, i.e. the soil type classes, and the GWT classes.

5.1. Deformation – Soil type

With the selection of the 6 main soil types and the buildings class identified in the Bodemkaart dataset of BRO, the following sets of tables and figures represent the statistical results for the deformation – soil type relation, sampled along each satellite track. These results are presented in the form of histograms and boxplots for the linear deformation trend (mm/yr), and as time series for the deformation measured with respect to the epoch of each sample. Considering the offsets in the spatial reference between the deformation results of the different tracks, Appendix C provides an inter-comparison between the different tracks, with additional visualizations of their deformation results.

5.1.1. Linear deformation

The results of the vertical linear deformation (mm/yr) projections for the satellite track samples (ascending tracks 15 and 88, descending tracks 37, 110 and 139) are first presented as normalized distribution histograms in Figures 5.1 - 5.5. The linear deformation for the same samples are summarized in Table

5.1. Subsequently, the boxplots in Figures 5.6 - 5.15 also provide a structured representation of the linear deformation results, again assorted by track. The discussion of the results follows in sequence of the columns of Table 5.1.
Since the spatial reference point for each track differs to a certain extent, specified in Table 4.17, the scope of the discussion is primarily set on the differences between classes observed within the samples or tracks themselves. Nonetheless, the re-occurrence of similar patterns across the samples, as highlighted in Table 5.1, gives an indication of the deformation pattern per class.

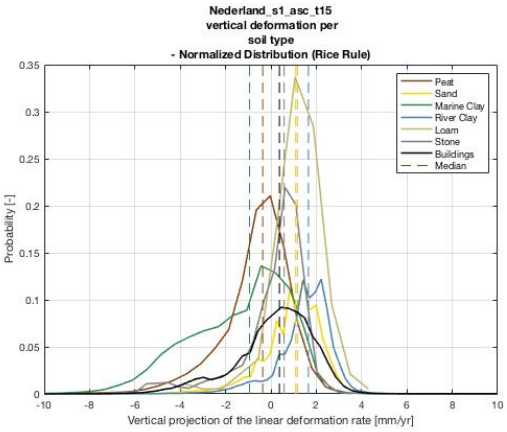

Figure 5.1: Ascending track 15: Normalized distribution & median of vertical linear deformation projections (mm/yr) per soil type class & buildings.

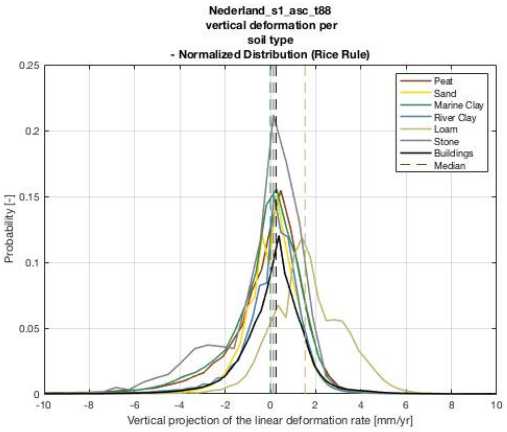

Figure 5.2: Ascending track 88: Normalized distribution & median of vertical linear deformation projections (mm/yr) per soil type class & buildings.

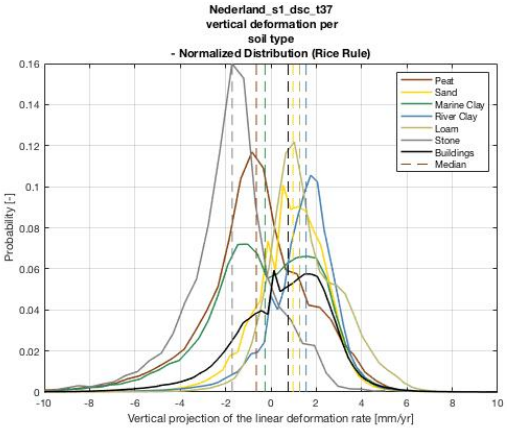

Figure 5.3: Descending track 37: Normalized distribution & median of vertical linear deformation projections (mm/yr) per soil type class & buildings.

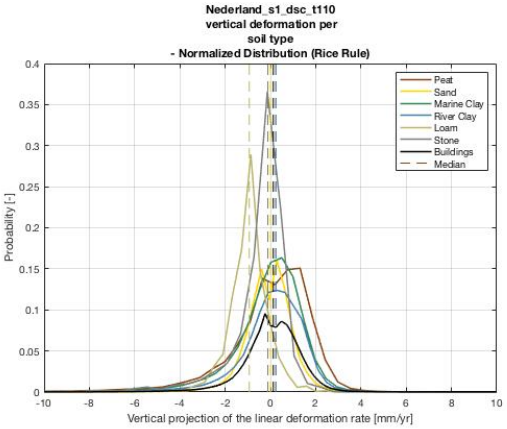

Figure 5.4: Descending track 110: Normalized distribution & median of vertical linear deformation projections (mm/yr) per soil type class & buildings.

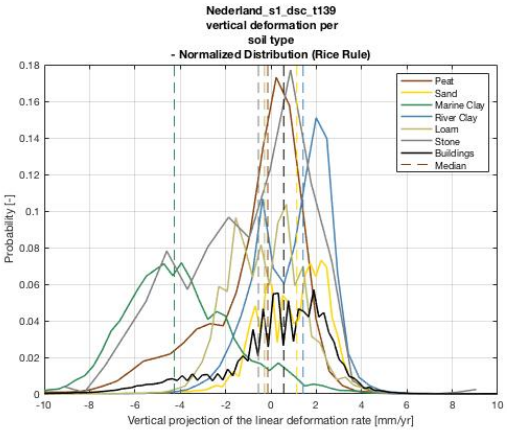

Figure 5.5: Descending track 139: Normalized distribution & median of vertical linear deformation projections (mm/yr) per soil type class & buildings.

Track no.	Soil	No. pnts [-]	Mean [mm/yr]	Med [mm/yr]	Std [mm/yr]	Skew [-]	Min [mm/yr]	Max [mm/yr]	Pctl10 [mm/yr]	Pctl90 [mm/yr]
asc_15	Peat	76 930	−0.64	−0.36	1.57	−1.70	−43.95	7.60	−2.62	0.95
	Sand	171 904	0.91	1.09	1.36	−1.04	−12.53	19.47	−0.73	2.35
	Marine Clay	79 418	−1.41	−0.94	2.25	−0.72	−22.01	31.98	−4.55	1.06
	River Clay	70 615	1.46	1.65	1.26	−1.60	−13.32	8.73	0	2.69
	Loam	190	1.15	1.17	1.16	−0.97	−3.73	4.66	−0.06	2.49
	Stone	2302	0.10	0.58	1.61	−1.83	−7.31	4.55	−1.87	1.44
	Buildings	518 645	0.15	0.37	1.76	−0.90	−20.53	34.67	−2.32	2.11
asc_88	Peat	272 497	−0.25	0.13	2.04	−2.80	−41.56	13.86	−2.38	1.54
	Sand	1 081 513	0.06	0.13	1.19	−0.92	−27.84	38.11	−1.28	1.36
	Marine Clay	669 297	−0.26	0	1.85	−2.08	−44.66	34.38	−2.47	1.49
	River Clay	578 358	0.04	0.25	1.50	−2.43	−35.79	16.23	−1.48	1.45
	Loam	69 858	1.67	1.53	1.62	−0.19	−18.00	11.12	−0.25	3.80
	Stone	5768	−0.33	0.13	1.88	−1.24	−13.46	7.23	−3.11	1.52
	Buildings	3 527 478	0.15	0.25	1.53	−1.43	−42.08	37.45	−1.45	1.66
dsc_37	Peat	252 935	−0.70	−0.65	2.58	−1.42	−43.94	18.87	−3.54	2.35
	Sand	1 210 432	0.86	0.97	1.61	−0.79	−32.44	38.28	−1.09	2.69
	Marine Clay	755 141	−0.36	−0.26	2.56	−1.02	−58.18	20.39	−3.42	2.59
	River Clay	619 884	1.33	1.55	1.66	−2.03	−35.41	14.45	−0.52	2.95
	Loam	86 460	1.50	1.26	1.67	−0.04	−19.95	12.82	−0.26	3.75
	Stone	7783	−1.80	−1.71	2.00	−0.89	−15.16	5.28	−4.08	0.56
	Buildings	3 716 239	0.50	0.76	2.16	−1.02	−44.48	40.21	−2.13	2.85
dsc_110	Peat	125 952	−0.09	0.24	2.14	−2.91	−45.37	9.82	−2.31	1.84
	Sand	526 634	−0.08	0	1.05	−0.83	−22.51	31.78	−1.23	1.08
	Marine Clay	588 999	−0.08	0.23	1.68	−2.34	−45.63	35.66	−1.92	1.51
	River Clay	271 141	0.01	0.23	1.62	−2.49	−34.41	12.91	−1.64	1.58
	Loam	5045	−0.98	−0.94	0.91	−1.03	−10.28	2.27	−1.99	0
	Stone	4127	−0.45	−0.12	1.37	−3.06	−13.89	4.77	−1.76	0.59
	Buildings	2 195 013	0.03	0.12	1.42	−2.49	−45.27	16.88	−1.40	1.46
dsc_139	Peat	66 976	−0.70	−0.14	2.22	−1.45	−37.08	9.88	−3.97	1.41
	Sand	273 617	0.96	1.14	1.59	−0.76	−19.04	12.24	−0.98	2.71
	Marine Clay	57 522	−4.08	−4.26	2.48	0.31	−21.34	8.24	−6.91	−0.85
	River Clay	76 494	1.01	1.41	1.62	−0.62	−19.79	20.15	−1.13	2.72
	Loam	45 712	−0.27	−0.28	1.63	0.13	−12.87	13.83	−2.28	1.71
	Stone	1242	−1.10	−0.56	2.78	−0.37	−9.26	9.43	−5.08	2.11
	Buildings	731 678	0.15	0.57	2.51	−1.20	−28.96	11.05	−3.54	2.69

Table 5.1: Statistics of the vertical linear deformation projections (mm/yr) comparing the different soil type responses per S1 satellite track sample. These statistics include: Number of points, mean, median, standard deviation, skewness, minimum, maximum, 10th-percentile, and 90th-percentile values of the points in a certain satellite track. The colour coding is as follows: Green indicates the highest or 'most positive' statistic found for a certain soil type. Red indicates the lowest or 'most negative' statistic found for a certain soil type. Highlighted green indicates the highest or 'most positive' statistic found for a certain soil type, that re-occurs for the majority of the satellite tracks. Highlighted red indicates the lowest or 'most negative' statistic found for a certain soil type, that re-occurs for the majority of the satellite tracks.

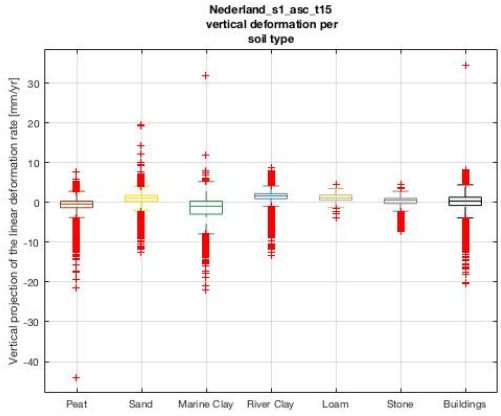

Figure 5.6: Ascending track 15: Boxplot distribution of vertical linear deformation projections (mm/yr) per soil type class & buildings.

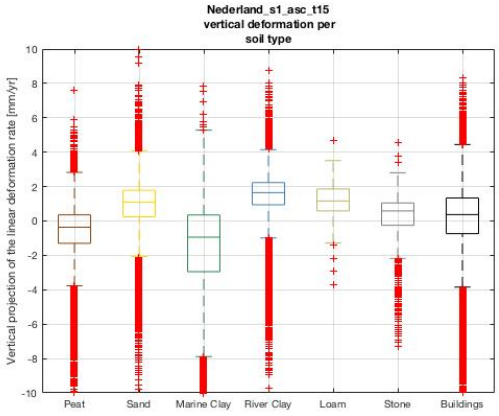

Figure 5.7: Ascending track 15: Boxplot distribution of vertical linear deformation projections (mm/yr) per soil type class & buildings (zoomed in to median).

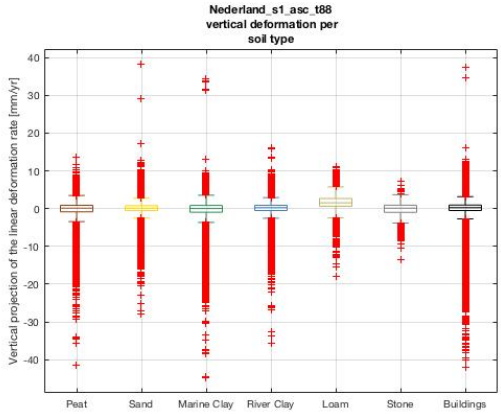

Figure 5.8: Ascending track 88: Boxplot distribution of vertical linear deformation projections (mm/yr) per soil type class & buildings.

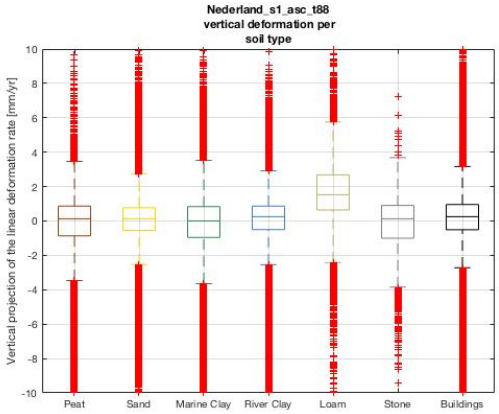

Figure 5.9: Ascending track 88: Boxplot distribution of vertical linear deformation projections (mm/yr) per soil type class & buildings (zoomed in to median).

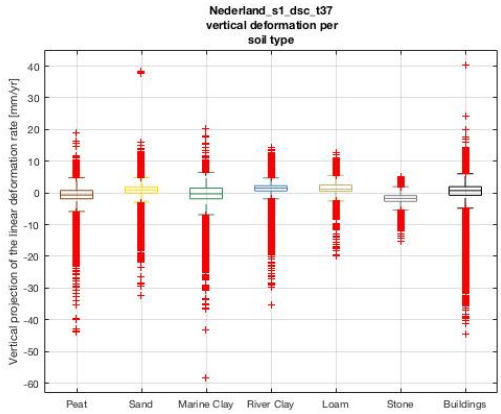

Figure 5.10: Descending track 37: Boxplot distribution of vertical linear deformation projections (mm/yr) per soil type class & buildings.

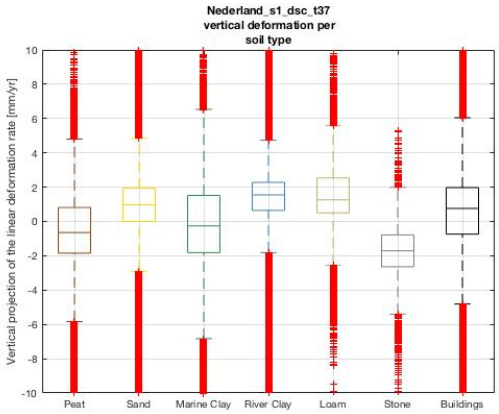

Figure 5.11: Descending track 37: Boxplot distribution of vertical linear deformation projections (mm/yr) per soil type class & buildings (zoomed in to median).

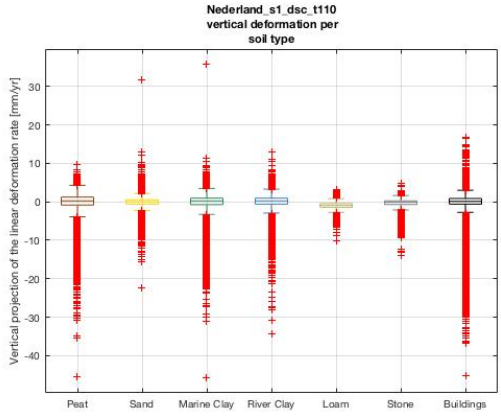

Figure 5.12: Descending track 110: Boxplot distribution of vertical linear deformation projections (mm/yr) per soil type class & buildings.

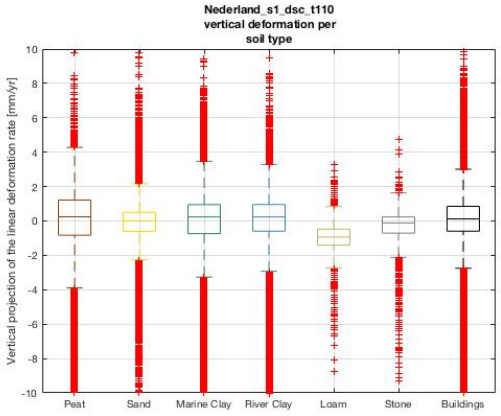

Figure 5.13: Descending track 110: Boxplot distribution of vertical linear deformation projections (mm/yr) per soil type class & buildings (zoomed in to median).

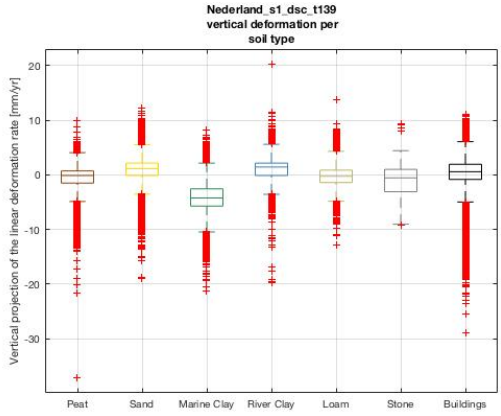

Figure 5.14: Descending track 139: Boxplot distribution of vertical linear deformation projections (mm/yr) per soil type class & buildings.

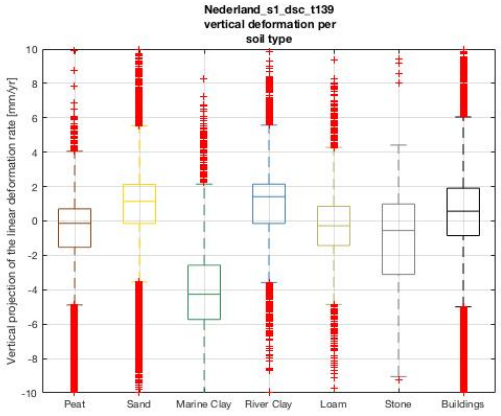

Figure 5.15: Descending track 139: Boxplot distribution of vertical linear deformation projections (mm/yr) per soil type class & buildings (zoomed in to median).

Number of points – Most of the PSI deformation readings are received from areas that contain many stable objects and a high 'surface roughness', primarily found in the built environment. Therefore the buildings class delivers the overall highest number of points in all distributions, followed by sand. Loam and 'stone' appear least frequently in all distributions, as these soil types are present to a relatively lesser amount. In the boxplots, the loam and stone classes also appear to have a narrow range in terms of outliers.

Mean deformation – The mean values per distribution are summarized in Table 5.1. In all samples, peat and marine clay appear to have negative mean values to some extent. 'Stone' also returns mostly negative mean deformation, except in track 15. The sand and loam mean values give more scattered results, showing both positive and negative deformation, depending on the track. Furthermore, the building class shows positive mean deformation in all instances.
Most apparent is track 139, in which the lowest (most negative) mean value identified for marine clay, i.e. -4.08 mm/yr, is almost 4 times the magnitude of the follow-up value (for 'stone'). This is the only mean deformation value that is separated by more than 2 mm/yr from its reference, which is different to all other mean values (across all samples) that remain below this threshold. For track 110, most of the mean values are slightly negative, except for the river clay and buildings classes. However, the range in mean values between the soil types is more significant; For most samples, the highest (most positive) mean deformation appears mostly for river clay (in tracks 15, 37, 110 and 139) and loam (in tracks 88 and 37), whereas the lowest mean values are more scattered, appearing twice for marine clay

(in tracks 15, 139), twice for 'stone' (in tracks 88 and 37), and once for loam (in track 110).

Median deformation – Differences in median linear deformation occur across the sample distributions between the different soil classes. Overall, the median results show similar patterns to the mean results. However, an offset is present between the mean and the median values, where the median deformation entries are slightly more positive than the mean deformation entries.
Even though most median deformation values are centered around their zero-deformation references, there are differences to be seen in the spread of the median deformation the different between soil classes. When comparing the different tracks, especially in the sample tracks 15, 37, and 139, these differences become apparent. River clay shows the most positive median deformation rate in the majority of the tracks, i.e. 15, 37, and 139. The most negative median deformation rates show up for marine clay, 'stone' and loam. The same anomaly is present as for the mean deformation, where the marine clay -mean deformation in track 139 is substantially larger in magnitude, i.e. appearing strongly negative as -4.26 mm/yr, compared to all other median entries.

Standard deviation – The standard deviation serves as a measure of the amount of dispersion (Bland and Altman 1996) present in the different sample distributions. In the histogram figures, the dispersion can be interpreted as the distance between the mean deformation and the other values part of the track distributions. For tracks 88 and 110, depicted in Figures 5.2 and 5.4, a relatively low dispersion is observed with respect to the other sample tracks.
Peat shows the highest dispersion in the majority of the samples, i.e. tracks 88, 37, and 110. In the remaining tracks, i.e. 15 and 139, 'marine clay' and 'stone' show the highest standard deviation values. The trend for lowest standard deviation is observed for sand, referring to the sample tracks 88, 37, and 139.

Skewness – The skewness is interpreted graphically by assessing the level of asymmetry of the different soil distributions per sample. This can be observed by looking at the tail-end of the distribution. Positive skewness appears as a distribution in which the right-hand tail is longest, whereas for negative skew the opposite is true. In the boxplot representations, the level of skewness is observed by comparing the upper and lower parts of the box, whiskers, and outliers with respect to the mean.
By visual inspection of the histograms, the reader is referred to Figures 5.6 - 5.15, where the symmetry is best compared in the normalized distribution plots. At first glance, most of the histogram figures seem to possess longer left tail-ends, resulting in an overall trend towards negative skewness. This trend is confirmed according to Table 5.1, in which all entries show negative levels of skewness, except for the classes marine clay and loam, both in track 139. Generally, the negative skewness implies that more negative deformation or 'subsidence' is observed with respect to the majority (around the mean and median) of the samples than positive deformation or 'uplift'. There is no apparent trend for a dominant positive or negative level of skewness between the soil types, as the results are rather scattered. Stone, in tracks 15 and 110, seems to be at the lower end, whereas marine clay and loam show overall higher skewness results.

Minimum & 10th-percentile deformation – The minimum and 10th-percentile deformation values for the different soil types per track can not be inferred from the histogram plots as they are not explicitly shown. Even though the minima and maxima can be inferred from the boxplot figures, the reader is referred to Table 5.1, as it presents the minimum and 10th-percentile values measured for each track.
The strongest deformation minima belong in all larger samples, i.e. tracks 88, 37, and 110, to marine clay, with peat and 'buildings' as close seconds. Peat shows the strongest negative deformation in tracks 15 and 139. The involvement of the peat class is in line with the author's prior expectations concerning the peat oxidation trend, i.e. 'shallow subsidence' in parts of the Netherlands. The strong surface deformation minima attributed to the marine clay class is not unexpected, considering that the Groningen gas production sites consist of this particular soil type, at least at surface level. The more moderate deformation minima belong to the loam and 'stone' classes.
The 10th-percentile deformation trends do not necessarily coincide with the aforementioned minimum-deformation trends. With a more scattered pattern, the lowest or most negative 10th-percentile results are observed twice for marine clay (in tracks 15 and 139), twice for 'stone' (in tracks 88 and 37) once for peat (in track 110). Sand, river clay, and loam appear at the higher or moderate -end in terms of

their 10th-percentile deformation values.

Maximum & 90th-percentile deformation – As for the minima and the 10th-percentiles, the deformation maxima and 90th-percentile values are best interpreted from Table 5.1.
Generally, the more extreme maximum deformation trends are observed for sand, marine clay and buildings in most tracks. As for the highest 90th-percentile deformation trends, the classes river clay and loam appear to be dominant. Note that for marine clay in track 139, the 90th-percentile deformation value is the only negative entry for all samples and soil classes in the table (even when correcting for the spatial reference).

5.1.2. Time series deformation

Figures 5.16 to 5.20 present the time series results of the median vertical deformation projection with respect to the epoch per track. Due to computational limitations, the time series results for the extensive buildings class is only included in the 'smaller' samples, i.e. tracks 15, and 139.

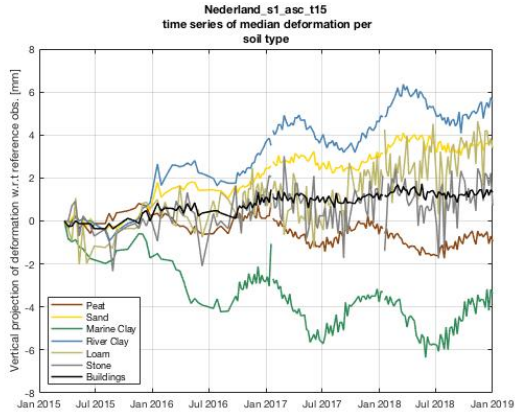

Figure 5.16: Ascending track 15: Time series of median vertical deformation-rate projections (mm) w.r.t the epoch (2015-03-23) per soil type class & buildings.

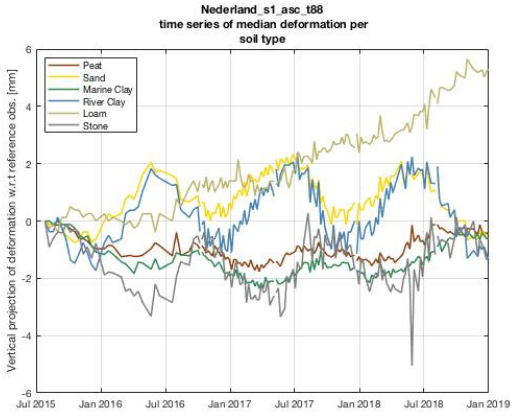

Figure 5.17: Ascending track 88: Time series of median vertical deformation-rate projections (mm) w.r.t the epoch (2015-07-26) per soil type class.

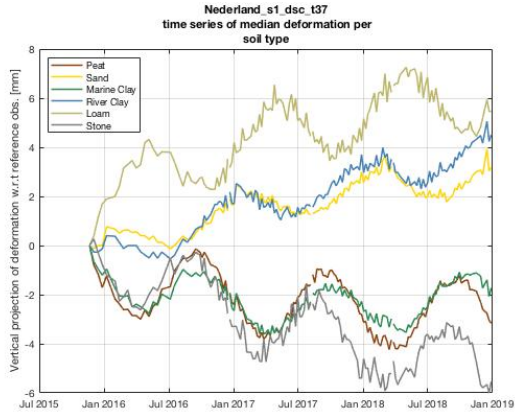

Figure 5.18: Descending track 37: Time series of median vertical deformation-rate projections (mm) w.r.t the epoch (2015-11-20) per soil type class.

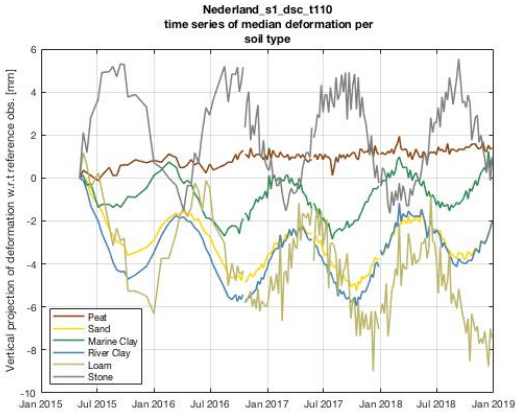

Figure 5.19: Descending track 110: Time series of median vertical deformation-rate projections (mm) w.r.t the epoch (2015-05-05) per soil type class.

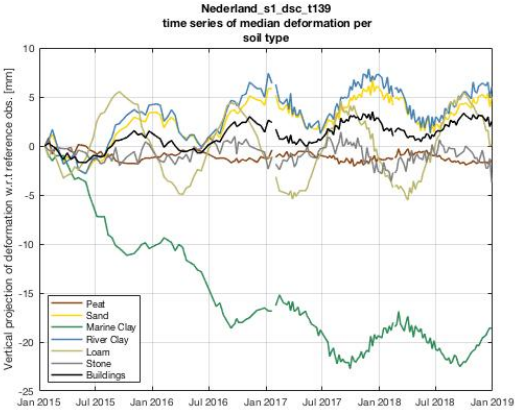

Figure 5.20: Descending track 139: Time series of median vertical deformation-rate projections (mm) w.r.t the epoch (2015-01-19) per soil type class & buildings.

A seasonal deformation pattern is reflected in the median deformation time series, resembling the periodic oscillation of a sinusoid. However, there are differences to be observed in both the amplitude and phase characteristics of the different time series. These 'wave differences' relate to differences in

soil type characteristics and to differences in the satellite track-sample characteristics. This observation is tested by;

1. Differentiating between the soil type classes per satellite track (sample), following the set-up of this chapter.

2. Differentiating between the satellite tracks (samples) per soil type class. The results of this 'reverse' analysis are included in Appendix C.

The median time series profiles are compared in terms of the different soil types per sample. In most cases, the periodic signal characteristics, i.e. the phase and amplitude, are clearly present. The amplitude in most time series appears to be fixed throughout the time series progression. Even if the overall median trend shows an increase or a decrease in time, there seems to be a somewhat fixed amplitude bound to the individual signal. As for the phase characteristics, only some of the profiles within a sample seem to be in phase.
In all track profiles, there are both net increases and decreases to be observed in the profiles. For the majority of the samples the decreasing median profiles belong to: peat, marine clay, and the increasing median profiles belong to: sand and river clay. The profiles for sample track 37 (Figure 5.18) most clearly display these differing trends. The median profiles of loam and 'stone' show more mixed results. Differing across the tracks, these classes show both increasing and decreasing profiles as well as stagnation, e.g. in track 139. The buildings class shows slight increases in its profiles in tracks 15 and 139 (Figures 5.16 and 5.20). Most notable is the decreasing profile of marine clay in track 139 seen in Figure 5.20, which is in line with the observations made for the linear deformation trends in the previous section.
As seen in Figures 5.16 – 5.20, the amplitudes of the profiles differ substantially in each of the track samples. For the majority of the samples, the peat profiles show a relatively low amplitude. The same can be said for the buildings class, present in tracks 15 and 139. The median loam and 'stone' profiles show slightly higher amplitudes compared to the more moderate amplitudes of the sand and clay classes. When it comes to the phase of the sinusoidal median-deformation profiles, some soil types show similar oscillating behavior. Additionally, peat and marine clay are often seen in phase with one another, sometimes with the addition of stone to the group. Noteworthy are the phase similarities between sand and river clay. Apart from their likeness in phase characteristics, the median sand and river clay profiles show many similarities in their increases and amplitudes. Furthermore, the loam and stone median profiles do not resemble the other soil classes in terms of their phase.

5.2. Deformation – GWT

As presented in Chapter 4, the Bodemkaart as part of BRO contains not only a soil type classification of the Netherlands, but also a nationwide GWT classification. This section presents the results of the statistical analysis of the nationwide deformation – GWT relation for the different satellite track samples. The presentation of these results is done in the same order as for the deformation – soil type results, starting with the vertical linear deformation projection (mm/yr) results, followed by the deformation time series (mm) profiles and their discussions.

5.2.1. Linear deformation

The statistical results of the vertical linear-deformation (mm/yr) projections, assorted by their GWT classes in the different sample tracks, are presented in similar histogram plots and boxplots as for the deformation – soil type relations. The histogram plots can be seen in Figures 5.21 - 5.25 and the boxplots in Figures 5.26 - 5.35. Table 5.2 summarizes these results, by stating the following descriptive measures of deformation for the GWT classes per satellite track sample; mean, median, standard deviation, skewness, minimum, maximum, and the 10th and 90th-percentile. The following discussion on the results follows the same order.

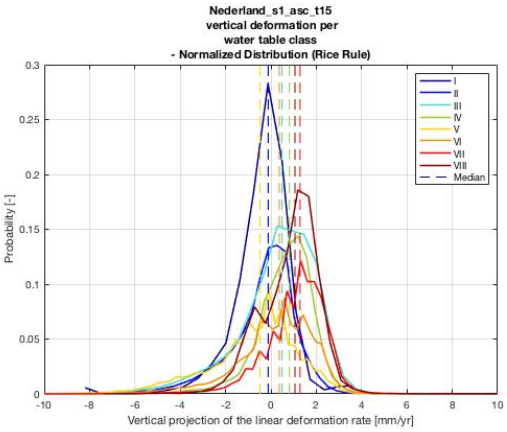

Figure 5.21: Ascending track 15: Normalized distribution & median of vertical linear deformation projections (mm/yr) per GWT class.

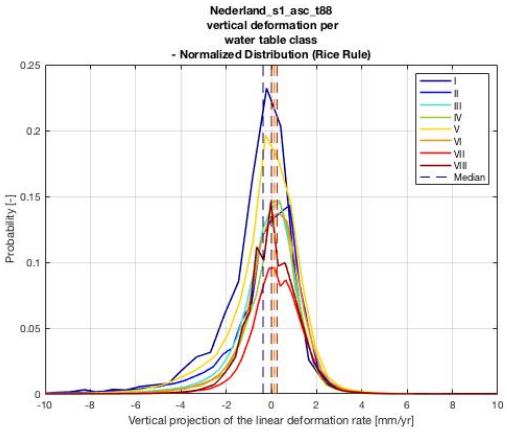

Figure 5.22: Ascending track 88: Normalized distribution & median of vertical linear deformation projections (mm/yr) per GWT class.

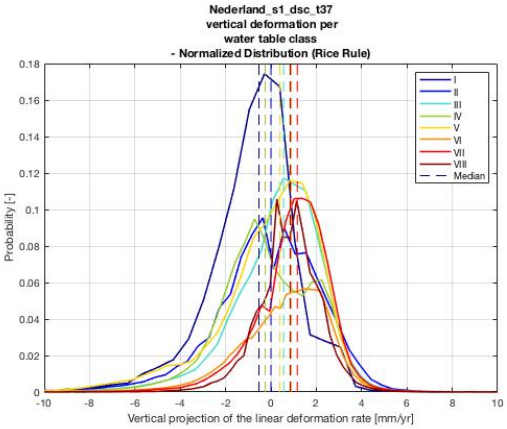

Figure 5.23: Descending track 37: Normalized distribution & median of vertical linear deformation projections (mm/yr) per GWT class.

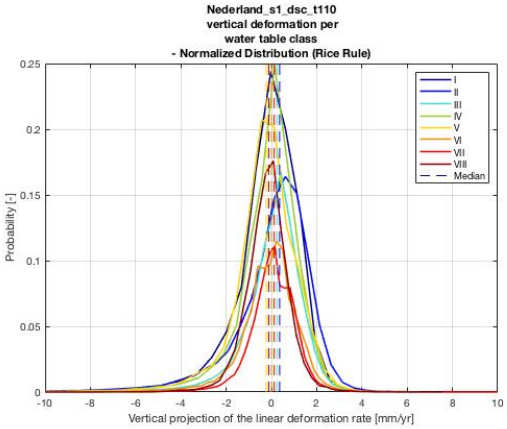

Figure 5.24: Descending track 110: Normalized distribution & median of vertical linear deformation projections (mm/yr) per GWT class.

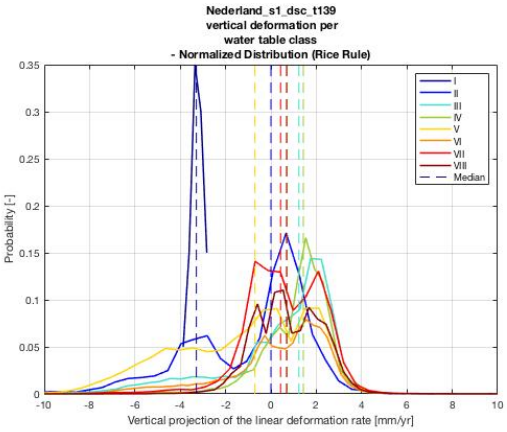

Figure 5.25: Descending track 139: Normalized distribution & median of vertical linear deformation projections (mm/yr) per GWT class.

Track no.	GWT	No. pnts [-]	Mean [mm/yr]	Med [mm/yr]	Std [mm/yr]	Skew [-]	Min [mm/yr]	Max [mm/yr]	Pctl10 [mm/yr]	Pctl90 [mm/yr]
asc_15	I	1061	−0.38	−0.12	1.33	−1.60	−8.04	3.78	−1.84	0.82
	II	50 121	−0.40	−0.12	1.58	−1.47	−21.56	6.03	−2.45	1.19
	III	77 133	0.25	0.48	1.83	−1.35	−17.11	31.98	−2.10	2.16
	IV	36 067	0.61	0.82	1.28	−1.49	−14.64	9.97	−0.86	1.91
	V	87 132	−0.80	−0.48	2.03	−0.89	−16.07	9.54	−3.68	1.52
	VI	186 455	0.18	0.37	1.74	−1.10	−22.17	8.89	−2.00	2.11
	VII	104 514	1.08	1.28	1.39	−1.43	−15.91	12.22	−0.62	2.50
	VIII	22 678	0.82	1.06	1.28	−0.03	−7.54	19.48	−0.87	2.16
asc_88	I	10 615	−0.70	−0.37	1.83	−2.54	−21.11	5.33	−2.72	0.87
	II	280 655	−0.38	0	2.06	−3.02	−41.56	13.63	−2.54	1.34
	III	366 769	−0.20	0	1.50	−2.40	−35.80	18.37	−1.77	1.24
	IV	264 136	−0.07	0.12	1.48	−2.69	−34.72	9.07	−1.57	1.32
	V	310 268	−0.29	0	1.69	−2.10	−44.62	29.06	−2.23	1.35
	VI	1 056 106	0.05	0.13	1.38	−1.40	−38.55	38.11	−1.48	1.47
	VII	536 490	0.18	0.25	1.23	−0.97	−23.44	16.23	−1.18	1.56
	VIII	149 476	0.02	0	1.20	−0.63	−22.94	10.17	−1.34	1.41
dsc_37	I	15 731	−0.81	−0.53	2.07	−1.58	−22.82	9.82	−3.15	1.33
	II	289 988	−0.19	0	2.56	−1.61	−43.93	18.87	−3.03	2.62
	III	388 269	0.30	0.56	2.08	−1.48	−32.44	38.28	−2.11	2.48
	IV	280 611	−0.16	−0.25	2.23	−0.98	−36.57	18.42	−2.62	2.55
	V	320 378	−0.07	0.38	2.39	−1.42	−58.23	14.95	−3.09	2.36
	VI	1 210 196	0.58	0.89	2.03	−1.21	−37.07	15.99	−1.94	2.75
	VII	616 505	0.97	1.17	1.68	−1.04	−23.73	37.61	−1.11	2.74
	VIII	179 543	0.78	0.85	1.40	−0.50	−21.07	11.78	−0.89	2.42
dsc_110	I	9241	−0.16	0	1.54	−2.67	−19.04	7.87	−1.78	1.34
	II	195 556	0.01	0.37	2.02	−2.93	−45.33	12.91	−2.09	1.82
	III	198 223	0.04	0.24	1.48	−2.70	−30.80	12.97	−1.44	1.46
	IV	182 212	−0.16	0	1.55	−2.63	−31.22	31.77	−1.67	1.28
	V	132 197	−0.28	−0.23	1.53	−2.58	−45.66	11.00	−1.76	1.35
	VI	626 850	−0.11	0	1.34	−1.84	−29.92	17.18	−1.53	1.29
	VII	223 077	0.06	0.12	1.06	−0.90	−15.65	11.11	−1.17	1.21
	VIII	37 418	−0.18	−0.12	0.99	−0.87	−14.96	7.65	−1.29	0.85
dsc_139	I	20	−3.27	−3.29	0.30	0.08	−3.86	−2.72	−3.65	−2.79
	II	16 017	−0.98	0	2.78	−1.16	−20.15	8.28	−4.68	1.69
	III	72 093	0.35	1.23	2.68	−1.74	−27.66	11.44	−3.68	2.69
	IV	32 109	1.16	1.43	1.55	−1.76	−14.55	9.72	−0.57	2.57
	V	95 900	−1.27	−0.71	3.08	−0.65	−21.34	34.99	−5.58	2.27
	VI	249 421	0.20	0.71	2.44	−1.51	−24.38	13.91	−3.19	2.55
	VII	192 680	0.56	0.43	1.70	−0.91	−44.47	20.17	−1.14	2.55
	VIII	46 202	0.75	0.69	1.47	−0.19	−15.66	11.30	−1.00	2.60

Table 5.2: Statistics of the vertical linear deformation projections (mm/yr) comparing the different GWT responses per S1 satellite track sample. These statistics include: Number of points, mean, median, standard deviation, skewness, minimum, maximum, 10th-percentile, and 90th-percentile values of the points in a certain satellite track. The colour coding is as follows: Green indicates the highest or 'most positive' statistic found for a certain GWT class. Red indicates the lowest or 'most negative' statistic found for a certain GWT class. Highlighted green indicates the highest or 'most positive' statistic found for a certain GWT class, that re-occurs for the majority of the satellite tracks. Highlighted red indicates the lowest or 'most negative' statistic found for a certain GWT class, that re-occurs for the majority of the satellite tracks.

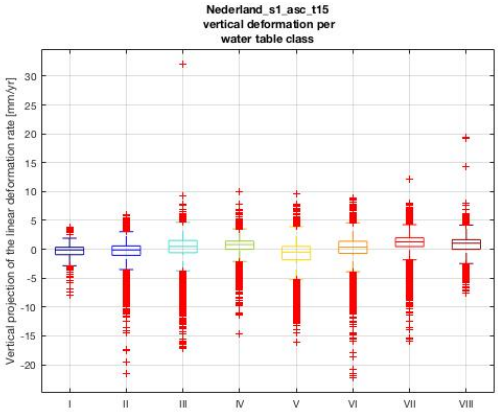

Figure 5.26: Ascending track 15: Boxplot distribution of vertical linear deformation projections (mm/yr) per GWT class.

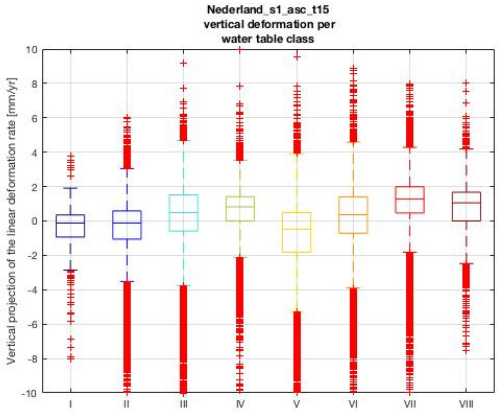

Figure 5.27: Ascending track 15: Boxplot distribution of vertical linear deformation projections (mm/yr) per GWT class (zoomed in to median).

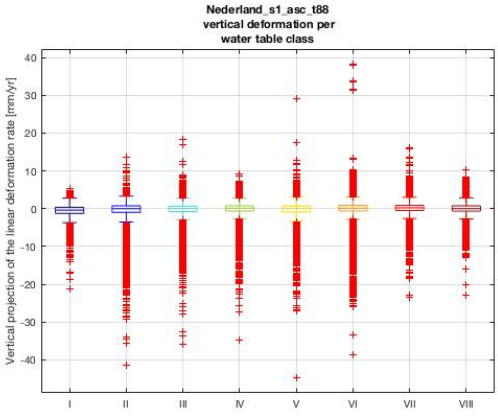

Figure 5.28: Ascending track 88: Boxplot distribution of vertical linear deformation projections (mm/yr) per GWT class.

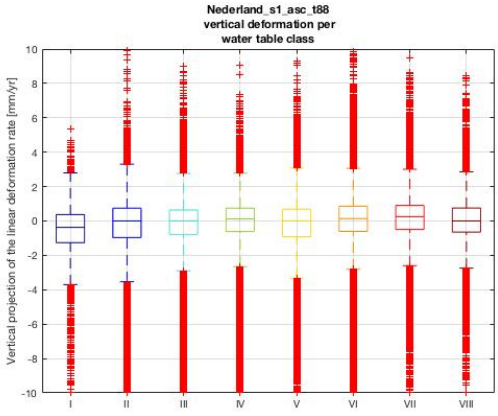

Figure 5.29: Ascending track 88: Boxplot distribution of vertical linear deformation projections (mm/yr) per GWT class (zoomed in to median).

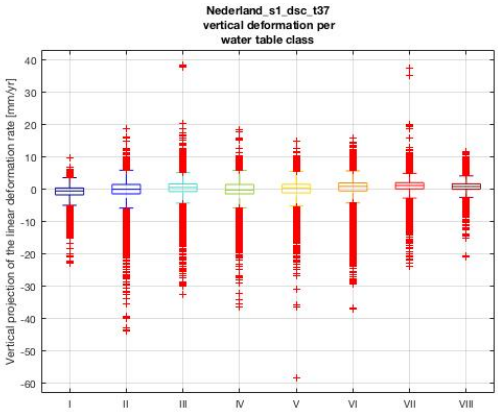

Figure 5.30: Descending track 37: Boxplot distribution of vertical linear deformation projections (mm/yr) per GWT class.

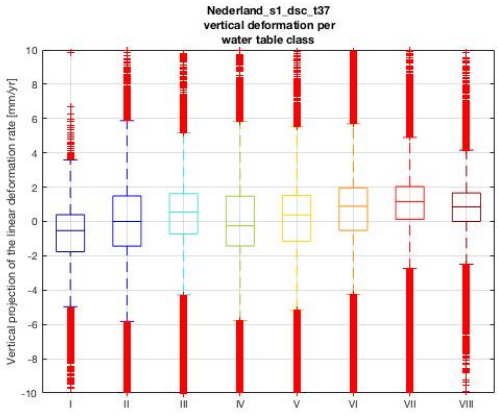

Figure 5.31: Descending track 37: Boxplot distribution of vertical linear deformation projections (mm/yr) per GWT class (zoomed in to median).

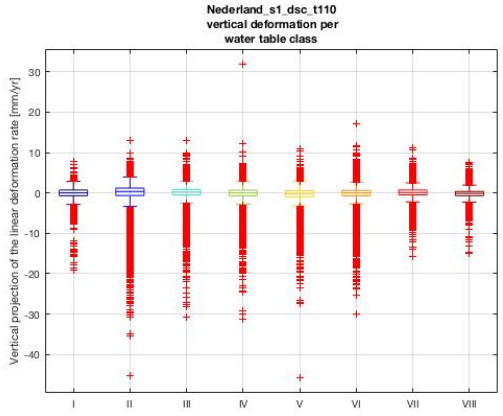

Figure 5.32: Descending track 110: Boxplot distribution of vertical linear deformation projections (mm/yr) per GWT class.

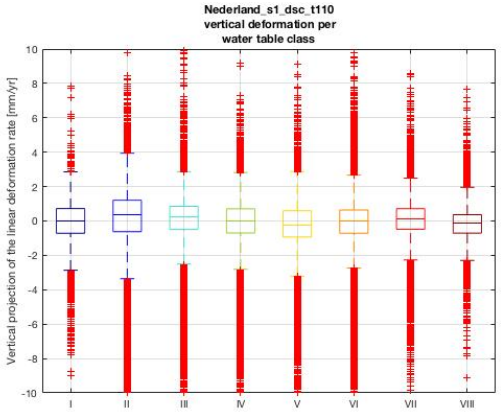

Figure 5.33: Descending track 110: Boxplot distribution of vertical linear deformation projections (mm/yr) per GWT class (zoomed in to median).

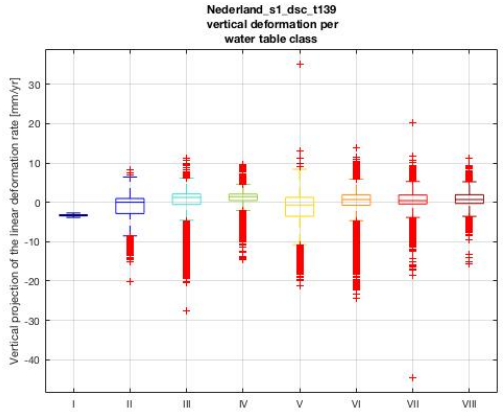

Figure 5.34: Descending track 139: Boxplot distribution of vertical linear deformation projections (mm/yr) per GWT class.

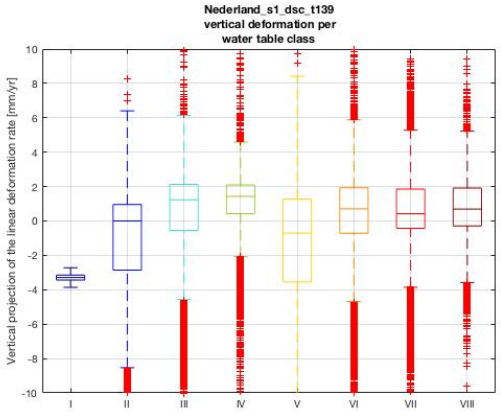

Figure 5.35: Descending track 139: Boxplot distribution of vertical linear deformation projections (mm/yr) per GWT class (zoomed in to median).

Number of points – The frequency distribution histograms and Table 5.2 identify classes VI and I as the GWT classes with, respectively, the highest and lowest number of points across all samples. This in line with the GWT map in Figure 4.14, in which GWT class VI contains large areas all over the country, and class I only appears in a handful of regions, e.g. near Eemdijk and Bunschoten-Spakenburg. Furthermore, class VII contains the second highest number of points in all samples. The other classes (II, III, IV, V and VIII) show mixed results in the amount of points they contain, as this strongly depends on the spatial coverage of the tracks. In sample track 139, class I only contains 20 points, which is an extremely low number compared to the other classes containing at least 16,017 (for class II). This anomaly can additionally be observed in the normalized histogram of Figure 5.25, where the distribution is not well represented following the Rice Rule for the bin selection procedure. The boxplot results in Figures 5.34 and 5.35 also show a very narrow distribution in the leftmost entry. Therefore, the author questions the quality of the statistics associated with class I in track 139.

Mean deformation – Most apparent are the relatively highest mean linear deformation results for class VII in the majority of the samples, except for track 139 where this is true for class IV. As for the lowest mean linear deformation, the results vary between GWT classes I (in tracks 37 and 139), V (in tracks 15 and 110) and II (in track 88). If class I of track 139 is left out of consideration (for the low number of points associated with this entry), class V shows the most negative mean linear deformation in the majority of the tracks.

Median deformation – The trend for highest median linear deformation is attributed again to class VII, which is in line with the mean linear deformation results. This result holds for the samples of tracks 15, 88 and 37, whereas in tracks 110 and 139; the classes II and IV (respectively) show the highest median linear deformation. If class I for sample track 139 is considered, class I shows the lowest entries for the median linear deformation (mm/yr) in a majority of the samples with the addition of tracks 37 and 88. Without the inclusion of class I in track 139, class V takes the place for GWT class with the most lowest median linear deformation entries, thus observed for tracks 15 and 110 as well.

Standard deviation – With its distribution closest to the median, class VIII shows the lowest linear deformation standard deviation entries across all samples, except for track 139 in which GWT class I has the lowest standard deviation. As the latter results from an anomaly in its sample size, class VIII is again considered for its low standard deviation. With this trend it is kept in mind that class VIII contains ta relatively low number of points besides class I. In the majority of the samples, class II shows the highest standard deviation for its vertical linear-deformation projection results, except in tracks 15, and 139 where this is the case for class V.

Skewness – Aside from the positive entry of class I in sample track 139, all classes across all samples have distributions with a negative skewness. This is also observed in the histogram plots, showing what appears to be left-hand tails in their distributions. In the majority of the samples, the strongest negative skewness of the linear deformation is attributed to class II, except in tracks 15 and 139, with classes I and V, respectively having the strongest negative levels of skewness in their distributions.

Minimum & 10th-percentile deformation – At the lower end of the distribution, the minimum and 10th-percentile values are computed for the linear deformation results in relation to the GWT classifications per sample. Class V has the most negative linear deformation minima, as observed in tracks 88, 37 and 110. In the other cases, class vI in track 15 and class VII in track 139 contain the lowest minima. The minimum results are not directly reflected in the 10th-percentile values of the linear deformation results. Although, the strongly negative 10th-percentile values appear twice for class I and twice for class V. The 'moderate' (least negative) minimum deformation values across the samples are observed for class VIII and I (in tracks 88 and 139).

Maximum & 90th-percentile deformation – The most positive maximum values of the linear deformation are scattered across the samples, with at most two strongly positive maxima for class III in tracks 15 and 37. A similar pattern is observed for the 90th-percentile values. Only class VII, in tracks 15 and 88, gives the most positive 90th-percentile values. Most apparent is that class I, for almost all samples (except for track 110), appears to have both the weakest maximum and 90th-percentile values compared to the other classes. In track 139, which has the lowest number of points (20) attributed to class I, the minimum and 90th-percentile are negative.

5.2.2. Time series deformation

The median time series profiles of the deformation w.r.t. the epoch of the different sample tracks in relation to the GWT classes are shown in Figures 5.36 to 5.40.

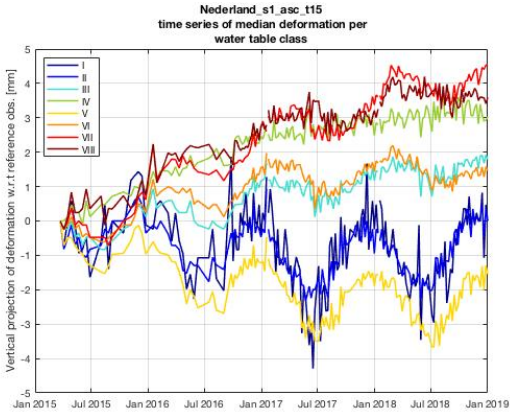

Figure 5.36: Ascending track 15: Time series of median vertical deformation-rate projections (mm) w.r.t the epoch (2015-03-23) per GWT class.

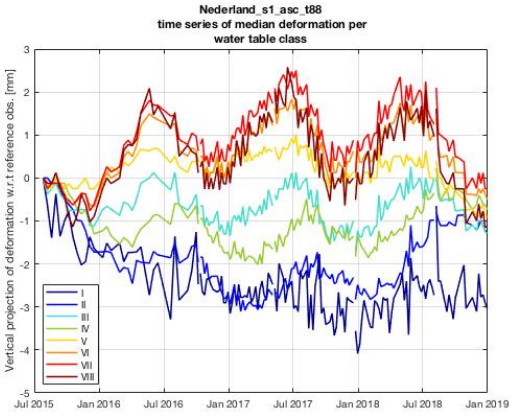

Figure 5.37: Ascending track 88: Time series of median vertical deformation-rate projections (mm) w.r.t the epoch (2015-07-26) per GWT class.

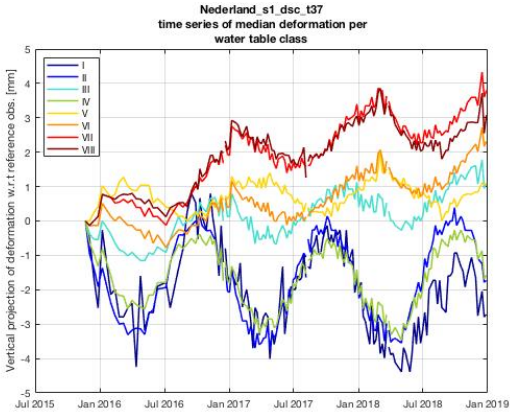

Figure 5.38: Descending track 37: Time series of median vertical deformation-rate projections (mm) w.r.t the epoch (2015-11-20) per GWT class.

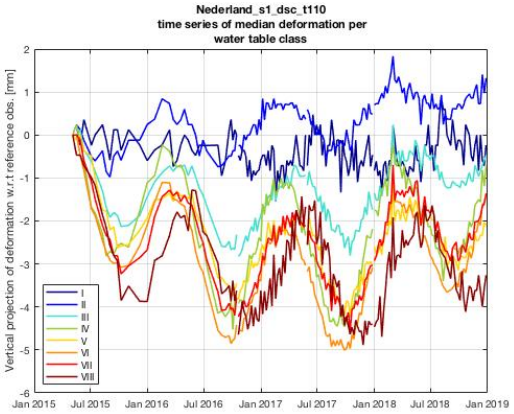

Figure 5.39: Descending track 110: Time series of median vertical deformation-rate projections (mm) w.r.t the epoch (2015-05-05) per GWT class.

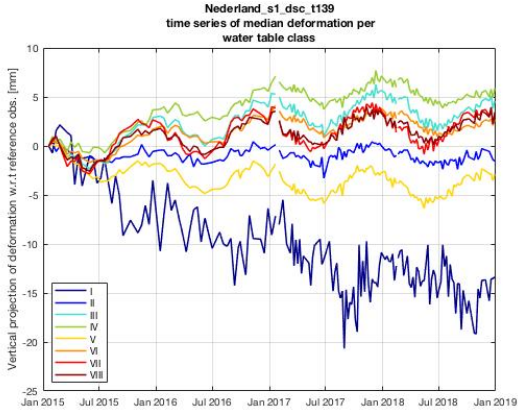

Figure 5.40: Descending track 139: Time series of median vertical deformation-rate projections (mm) w.r.t the epoch (2015-01-19) per GWT class.

The seasonal pattern is present in the median deformation profiles, following a trend of periodic oscillation seen in a typical sinusoid. Differences in the wave characteristics in terms of amplitude, phase are present between the different GWT profiles for all samples.

In most samples, the classes I and II show negative deformation profiles, except in track 110 where the profile of I and II show stagnation and a slight increase (respectively). As seen in the linear deformation results, the median time series of class I in sample track 139, with the low sample size of 20 points, shows a steep decrease in Figure 5.40. The profiles of classes III to VI show mixed median deformation profile results, with increases, decreases and stagnation across all samples.
The deepest GWT classes, i.e. VII and VIII often show similar profiles in terms of their overall increase, medium-to-high amplitudes, and 'in phase' behaviour. As a result, their median profiles nearly coincide in all tracks. In terms of their positive or negative median profiles, classes I and II appear at the lower (negative) end, and classes VII and VIII at the higher (positive) end. The 'middle' GWT class profiles (III-VI) show more 'stable' profiles. This observation does not strictly hold for all samples, especially in descending sample tracks 110 where the profiles appear to be inversely 'stacked'. In general, the shallow water level classes (I and II) show the more extreme amplitudes in their profiles compared to those of the other classes. Class I, with its relatively low number of points in the samples, oscillates with a different phase compared to the other classes in the sample.

5.3. Discussion

The nationwide soil deformation analysis, presented and discussed in this chapter, focuses on the relation between large spatial-scale deformation trends of the Dutch surface and the country's soil characteristics. The selection of soil characteristics is focused on soil type and groundwater level classifications of the Netherlands, as presented in the Bodemkaart dataset of BRO.
The database approach is implemented to enrich the PSI deformation points on a nationwide scale with soil-specific classifications, including;

1. 7 main soil type classes, i.e. peat, sand, marine clay, river clay, loam, 'stone' and 'buildings'.
2. 8 main GWT classes based on their different highest and lowest mean water levels (as summarized in Table 4.10), i.e. I – VIII.

A spatial join is performed on the primary PSI deformation measurements, adding contextual soil class and GWT attributes to the points. Based on this added contextual information, queries are performed to separate and store the deformation points in groups according to their common soil types and GWT classes. This process is repeated for the different S1 satellite acquisition tracks, which make up the different samples for the statistical analysis. The deformation behaviour of a certain group is studied by computing and analyzing their deformation statistics, i.e. descriptive measures, such as the mean, median, standard deviation, skewness, minimum, maximum, 10th and 90th-percentile. The results of the statistical analysis, presented in this chapter (and partially in Appendix B), allow for a characterization of the deformation of the Dutch surface in relation to its main soil types and GWT classes.

5.3.1. Deformation – Soil type results

The PSI points, assorted by soil type in their sample tracks 15, 88, 37, 110, and 139, have shown multiple differences in terms of their descriptive measures. The most relevant findings are discussed in the following sections, presented according to the soil classes and their general deformation trends, i.e. subsidence or uplift.

Subsidence

In general, the marine clay and peat classes show the most negative mean and median deformation trends across the different tracks. This is reflected in both their linear deformation representations, as shown in the various sets of histograms and boxplots, as well as in their time series profiles. The negative median deformation trends are more subtle for the peat class, as opposed to the marine clay class, which shows generally higher rate of subsidence, e.g. for sample tracks 15 and 139. This overall negative deformation trend is expected in the track samples with coverage of the peatlands in the western parts of the Netherlands, i.e. tracks 88, 37 and 110, and of the hydrocarbon extraction areas in Groningen, i.e. tracks 15, 88, 37 and 139, consisting of mainly marine clay and peat soils. However for track 110, covering the west-to-middle parts of the Netherlands the opposite is true. The median linear deformation of peat and marine clay (along with river clay) in this sample are highest w.r.t. the other soil classes.

For the eastern part of the Netherlands, track 139 forms an interesting case, since all the marine clay covered in this track is situated mostly in the province of Groningen where the strongest 'deep' subsiding motion has been estimated. Thus, in sample track 139 the results for marine clay in particular, which contains a lower number of PSI points, show extreme mean and median subsiding motion (-4.1 mm/yr) compared to the other soil types covered by this track, as these remain close to the zero-deformation mark. This observation highlights the need for additional classifications to be included in the study, e.g. subsurface information, which (combined) would provide more accurate explanations.
Furthermore, in a selection of tracks, most notably in descending tracks 110 and 139, the loam and 'stone'[1] classes show general trends of subsidence, along with peat and marine clay.
Negative skewness is identified in all linear deformation distributions, except for the marine clay and loam classes in sample track 139, where the skewness is slightly positive (0.3 mm/yr). The distributions of peat and 'stone' tend to be the most negatively skewed, which means that, regardless of their median observed deformation, these soil types show the most cases of subsidence. This is in line with the high standard deviation observed for peat soils (followed by marine clay and 'stone'), showing relatively high dispersion in its deformation.
Furthermore, peat and marine clay both show strong deformation minima, e.g. down to -58.2 mm/yr as identified for marine clay in sample track 37.

Uplift

River clay and sand, to a lesser extent, mostly show the highest median deformation trends in their linear and time series profile results. In most cases a net uplift is observed for sand and river clay, even after correction for the spatial reference in table 4.17. Although the skewness of nearly all samples is negative, more moderate negative skewness is observed for the sand class, indicating fewer cases of subsidence compared to most soil types.
In terms of extremes, marine clay shows strong deformation maxima (aside from its strong minima) along with sand and 'buildings'. The latter two classes have recorded positive deformation maxima of up to 40 mm/yr. The buildings class, with its large number of PSI points per sample, shows high standard deviations with relatively strong linear deformation minima and maxima (in most samples).

Time Series – Ascending vs. Descending

In the track-overlap analysis, presented in Appendix C, the focus is set on the deformation profiles compared for the different tracks. Here, the oscillating nature of the deformation profiles displays similar phase behaviour between the ascending tracks themselves, i.e. tracks 15 and 88, and the descending tracks themselves, i.e. tracks 37 and 110. When comparing the ascending tracks with the descending tracks, for the most part, the two groups seem to be out of phase with one another. The reason for this apparent phase delay might be the difference in time between the acquisitions of the ascending and descending tracks, i.e. ±7:30 p.m. and ±8:00 a.m. local time (respectively), leading to different physical conditions, e.g. weather, moisture, temperature, ground swelling, etc.

5.3.2. Deformation – GWT results

Similar to the discussion of deformation in the context of soil type behaviour, there are several points of discussion to be addressed regarding deformation in the context of groundwater-level behaviour. As the GWT classes indicate the highest and lowest mean water levels (mm -mv), known as GHG and GLG, the relation with deformation may be better understood.

Shallow GWT

Where the deep GWT class VII shows the overall highest (most positive) mean and median linear deformation, the lowest mean and median deformation is observed for the shallow GWT classes I and II, as well as class V. Therefore it subsidence is more likely to be observed for the shallow GWT classes. The shallow GWT classes I and II mostly coincide with the Dutch peatlands, (not coincidentally) referred to as 'wetlands'. As such, these observed subsidence trends in classes I and II reflect the same

[1] As stated in the earlier parts of this chapter and Chapter 4, the 'stone' class no longer refers to 'gravel' soils but rather to 'Kalkhoudende bijzondere lutumarme gronden' and 'Kalkhoudende vlakvaaggronden'. For further elaboration on this erroneous classification, the reader is referred to the presentation of the 'main' soil types in the discussion of Table 4.9. However, the erroneous stone class does not affect the validity of the results for the other soil classes, i.e. peat, sand, marine clay, river clay, loam, and the buildings class, which are of higher relevance for the nationwide study.

estimated subsidence of the peatlands, as a supposed product of peat oxidation.
In addition, GWT class II shows the highest level of dispersion with its standard deviation results, followed by class V. Besides its relatively large standard deviation results, class II for the most part exhibits the stongest levels of negative skewness across the majority of the samples, often followed by the other shallow GWT class I. Additionally, shallow GWT class I shows the lowest linear deformation maxima and 90th-percentile values across the majority of the tracks.

Middle – Deep GWT

Generally, the middle to deep GWT classes, i.e. V – VIII, either show stronger positive and weaker negative deformation than their shallow counterparts. Specifically, class VII shows the highest deformation on average. The GWT class VIII distributions have the lowest standard deviation, also showing the least negative skewness.
As an mid-level GWT class, V contains the strongest negative deformation minima in the majority of the samples. In contrast, the more least negative minima are found for deep GWT class VIII. Thus keeping in mind the low deformation maxima observed for class I, the 'boundary' classes (I and VIII) show the more moderate deformation extremes.

6

Localized Deformation Analyses

In the previous chapter the nationwide deformation trends are analyzed in relation to the different soil type and GWT classifications from Bodemkaart. This chapter focuses on three separate case studies for which the deformation is analyzed with a larger selection of auxiliary attributes compared to the nationwide analysis. The three case studies are focused on different parts of the Netherlands, presumed to show different soil deformation regimes. The first case study focuses on Limburg, where upward deformation is observed. This upward deformation is caused by inflowing groundwater in abandoned mines. Additionally, particular areas in South Limburg are at risk of subsidence and sinkholes due to old shafts and shallow mining. The second case study focuses on an area in South Holland comprising Delft and the northern parts of Rotterdam and Schiedam, characterized by peat soils with shallow groundwater levels. The third and final case study focuses on the hydrocarbon extraction areas in Groningen. The methods and results are specific to the individual case studies, and are therefore discussed accordingly in their respective sections. General remarks on the deformation patterns observed in these case studies are provided in the discussion at the end of this chapter.

6.1. South Limburg – Coal Mining After-Effects

For an investigation on the risk of sinkhole occurrence in the southern part of Limburg, the surface deformation is analyzed for the concerned areas. The after-effects from mining in South Limburg involve three main processes. The first process is the differential ground heave and the development of discontinuities, induced by rising mine water (Heitfeld, Klunker, et al. 2016). Secondly, potential problems concerning ground stability in the affected area could occur, as the failure of a shaft may cause subsidence or sinkhole formation (Heitfeld, Klunker, et al. 2016). In the context of the risk analysis study in Heitfeld, Klunker, et al. 2016, a distinction is made between shallow 'historical' and 'industrial' mines, which is elaborated on in further sections. Lastly, Heitfeld, Klunker, et al. 2016 define so-called impact areas close to near-surface mine voids. Since the mine workings were not backfilled after the mining of a coal seam, the hanging wall was allowed to collapse into the mined seam (Heitfeld, Klunker, et al. 2016). If the hanging wall has not entirely collapsed, there might still be underground voids present (Heitfeld, Klunker, et al. 2016).
The Limburg case study is set up with a general background of the former mining activities, followed by a discussion of the after-effects and their potential impact classifications. As these impact classifications serve as the auxiliary information in this case study, their associated deformation is analyzed and discussed.

6.1.1. Mining history

The Limburg mining activities in the last two centuries are divided in two main groups. One group of mines was state owned, operated by the former state company the 'Dutch State Mines' (DSM), from which a Dutch chemistry company has emerged by the same name. This mine group counted four different mines, active from 1906 until the last one closed in 1973. Furthermore, nine privately owned coal mines were in operation between 1815 and 1974 in the 'Oostelijke Mijnstreek' or the 'Eastern Mine Region' (TU Delft 2014). Table 6.1 provides an overview of the four state owned and nine privately

owned coal mines, their location (within the project area), operation time, production, and number of shafts.

Project area	Mine	S/P	Location	Operation	Production (t)	No. shafts
3	Maurits	S	Lutterade/Geleen	1926 - 1967	96.214.000	3
3	Emma	S	Hoensbroek	1911 - 1973	109.032.000	4
3	Hendrik	S	Rumpen, Brunssum	1915 - 1963	61.203.000	4
2	Oranje Nassau I	P	Heerlen	1899 - 1974	31.978.000	3
2	Oranje Nassau II	P	Landgraaf (Schaesberg)	1904 - 1971	34.064.000	2
2	Oranje Nassau III	P	Heerlerheide, Heerlen	1914 - 1973	38.265.000	1
2	Oranje Nassau IV	P	Heksenberg, Heerlen	1927 - 1966	13.754.000	1
2	Wilhelmina	S	Terwinselen, Kerkrade	1906 - 1969	59.235.000	2
2	Laura	P	Eygelshoven	1905 - 1968	31.885.000	2
2	Julia	P	Eygelshoven	1927 - 1974	31.963.000	2
2	Willem-Sophia	P	Spekholzerheide, Kerkrade	1902 - 1970	22.678.000	5
1 & 2	Domaniale	P	Kerkrade	1815 - 1969	37.990.000	6
1 & 2	Neuprick	P	Kerkrade	1852 - 1904	n/a	1

Table 6.1: Overview of the four state owned (S), and nine privately owned (P) coal mines in South East Limburg. Information is provided about their location, lifetime, production (tonne), and number of shafts, based on TU Delft 2014. Additionally, the project area number is stated for each mine, as depicted in Figure 6.1.

A mapped representation of the Dutch mines in South Limburg is provided in Figure 6.1, taken from Heitfeld, Klunker, et al. 2016, dividing the South Limburg area into three different project areas.

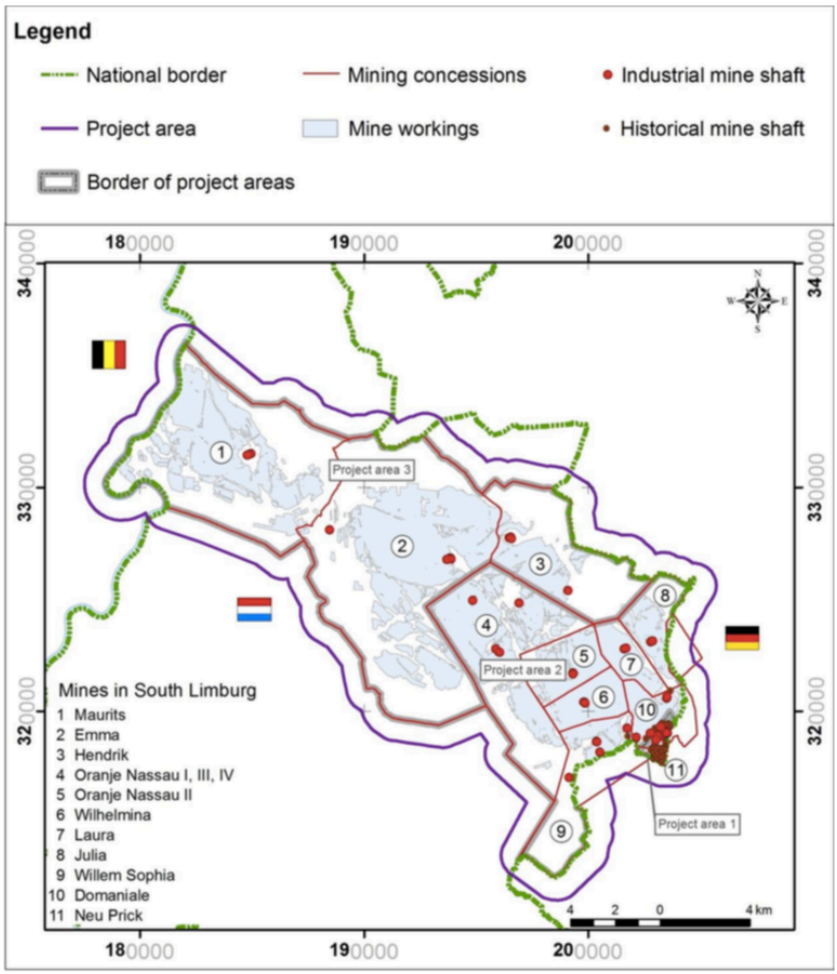

Figure 6.1: Map of the 'historical' mines and the 'industrial' private and state owned mines in South Limburg, divided into 3 project areas (Source: Heitfeld, Klunker, et al. 2016).

6.1.2. Risk Analysis

Based on the risk analysis, presented in Heitfeld, Klunker, et al. 2016 on the after-effects of former coal mining activities in South Limburg, the observed and potential deformation risks are identified and classified. The risk analysis is divided in three parts, addressing the differential ground heave, the mine shafts, and the near-surface mining activities.

Differential Ground Heave

With the closure of the last industrial mine Julia in Eygelshoven in 1974, dewatering measures were maintained to protect the German mines that were still active until 1994. Since then, due to halting of the dewatering processes, the mine water has been rising in the South Limburg region and has yet to reach hydraulic equilibrium (Heitfeld, Klunker, et al. 2016). The mine water rise and resulting ground heave are consequences of 'the decompaction of the broken coal-bearing bedrock due to increased pore water pressure' (Heitfeld, Klunker, et al. 2016). Due to the rise in mine water, problems have emerged relating to upward ground movement or 'heave', risks from the abandoned mine shafts, the release of mine gas, and from small earthquakes. The groundwater quality in these areas has also been affected. Since hydraulic equilibrium is not yet reached, this process is still ongoing. Following Heitfeld, Klunker, et al. 2016, it will take at least 10 to 15 years until hydraulic equilibrium is reached[1]. Due to differential ground heave, damage to buildings and infrastructure may be expected at certain locations in the study area. Based on the developments of ground heave in the period from 1974 to 2014 documented in Heitfeld, Klunker, et al. 2016 estimated with the use of integrated InSAR and levelling data, three major ground heave zones have been identified;

1. Ground heave zone 1 – situated in Geleen, at the northeastern edge of the Maurits coal mine, along the Heerlerheide fault.
2. Ground heave zone 2 – situated in Brunssum, at the northeastern edge of the Emma and Hendrick coal mines, along the Feldbiß fault.
3. Ground heave zone 3 – situated in Eygelshoven, near the Julia coal mine, along the Feldbiß fault.

The ground movement in the period between 1974 and 2014 is mapped in Figure 6.2, as a product of levelling and InSAR data. The map indicates the three major ground heave zones, with significant gradients or 'discontinuities' (Heitfeld, Klunker, et al. 2016).

[1] As of December 2019.

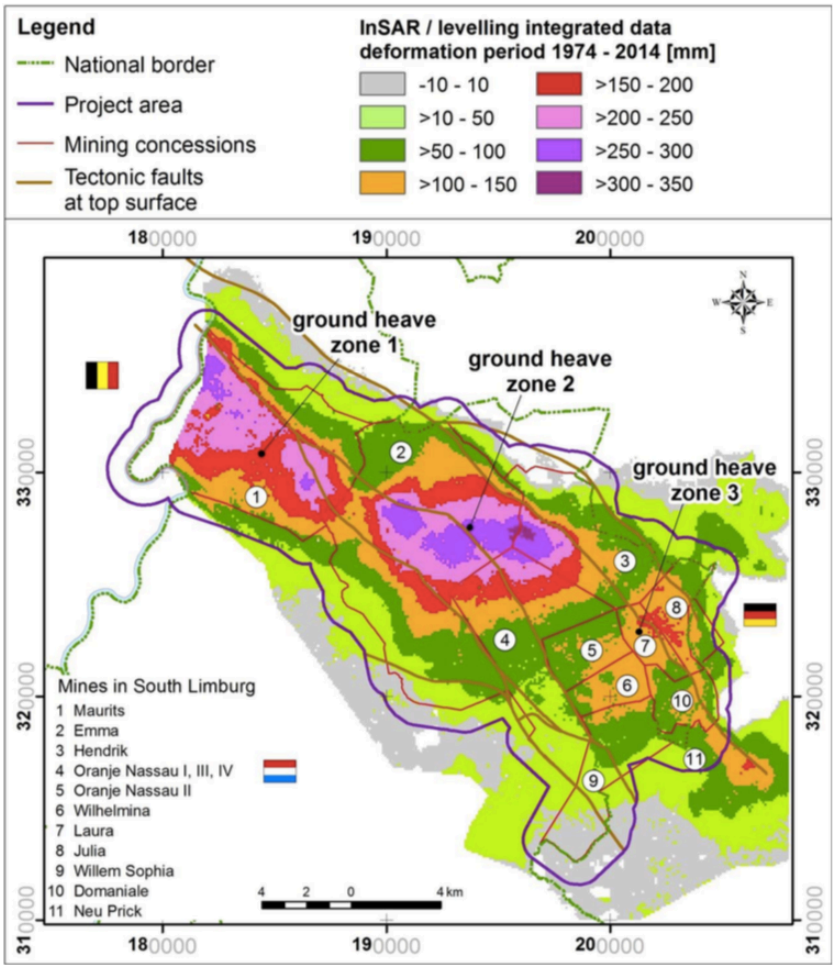

Figure 6.2: Surface deformation in the South Limburg mining district for the period 1974 – 2014, from InSAR / levelling integrated data (Source: Heitfeld, Klunker, et al. 2016).

The ground heave zones in Figure 6.2 are assigned impact category (EK) classifications, defined as having a high (EK 1), medium (EK 2) or low (EK 3) 'probability of occurrence of significant differences in ground heave and the development of discontinuities' (Heitfeld, Denys, et al. 2015). None of the ground heave zones in the study area are attributed an EK 1 classification.
The spatial extent of the potential impact areas are illustrated in Figure 6.3, where they are clearly observed along the different faults. Figure 6.3 also indicates the positions of several cross-sections or 'monitoring profiles' by leveling, proposed in Heitfeld, Klunker, et al. 2016 to detect any further discontinuities.
The discontinuities appear along three major SW-NE oriented faults at the top surface, namely the Benzenrade fault, the Heerlerheide fault, and the Feldbiß fault. Appendix D provides a mapped representation of these faults and the main hydrogeological units (HY) in the former mining concessions, along with cross-sections to illustrate these (Heitfeld, Klunker, et al. 2016; Rosner 2011). The differentiation in hydrogeological units is made based on the hydrogeological characteristics in the level of overburden (HY I – HY IVb) (Heitfeld, Klunker, et al. 2016). Cretaceous sediments appear predominantly in HY I and in the northwestern part of HY II, while mostly Tertiary sediments appear in the remaining hydrogeological units.

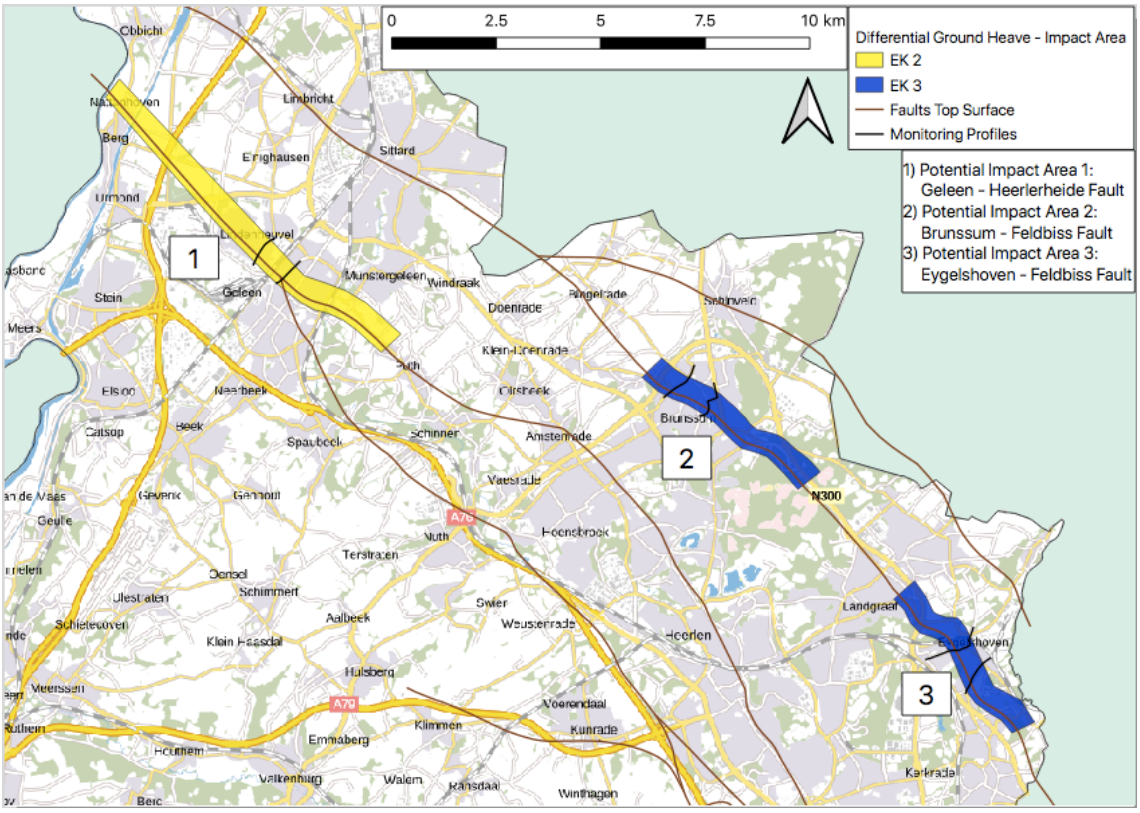

Figure 6.3: Potential impact areas EK 2-3 for the South Limburg region due to differential ground heave, with the faults at top surface and the associated cross-sectional monitoring profile locations. The fault and cross-section shape files originate from the risk analysis performed in Heitfeld, Klunker, et al. 2016. The potential impact area shape files were constructed based on Heitfeld, Klunker, et al. 2016.

Mine Shafts

The potential risks involved with the failure of mine shafts can lead to subsidence or sinkholes (Heitfeld, Klunker, et al. 2016). In their risk analysis study on the delayed effects of the South Limburg coal extractions, Heitfeld, Klunker, et al. 2016 make the distinction between a total of 59 shallow 'historical' mine shafts and a total of 39 deep 'industrial' mine shafts. The historical shafts refer to the pre-industrial shafts that were constructed and operated before industrial mining took place. These shafts are traced back to even the Middle Ages. The more recent industrial shafts involve all the mines introduced in Table 6.1, during the industrial mining period ranging from the early 19th century until the late 20th century. Both mine shaft categories are provided their own safety level assessments consisting of different 'impact categories' (EK). These are based on the German concept of 'Shaft-Protection-Zones' (SPZ), which refer to 'the area that is potentially affected owing to failure of a shaft' (Heitfeld, Klunker, et al. 2016).
Four EKs are to be distinguished in the risk assessment of the different mine shafts, describing the relative probability of the occurrence of a collapse, subsidence or sinkhole (Heitfeld, Klunker, et al. 2016). However, since the characteristics and levels of safety differ between the historical and industrial mines, they are assigned different EK classifications.

Historical Shafts EK – Following the procedure of a prior case study in North Rhine-Westphalia, all historical shafts are assigned to impact category EK 1 (red) (Heitfeld, Klunker, et al. 2016). The reason for this is that the probability of occurrence of a collapse, sinkhole or subsidence increases in time due to degradation, weathering processes and the added destabilizing effect of rising mine water (Heitfeld, Klunker, et al. 2016). The set-up of a prioritization system and 'refinement' of the SPZs for historical shafts has been set in place, since these are all located in the urbanized area of Kerkrade. Classified on the basis of the vulnerability of the specific land use, the three EK categories are defined in terms of the level of protection the buildings and infrastructure in the vicinity of the shafts need: 1 –

'high' for shafts under or very close to buildings, 2 – 'medium' for shafts near buildings or other forms of built property, and 3 – 'low' for forests, grasslands, etc. (Heitfeld, Klunker, et al. 2016).

Industrial Shafts EK – The 39 industrial shafts from the mines in Table 6.1 are given an indication of their safety level as part of their EK classifications. Here, an extra category EK 4 (green) is added which denoted a 'high' or 'permanently' safe level. Three industrial shafts are attributed to this group. Thirty industrial shafts are indicated to have a 'medium' or 'low' safety level (EK 3), whereas six industrial shafts are attributed a 'very low' safety level, or 'not yet treated' (EK 2) (Heitfeld, Klunker, et al. 2016). Thus, none of the industrial mine shafts have been given the EK 1 safety classification.

Near-surface Mining

As one of the mentioned after-effects, the former underground mine workings affect the ground surface stability. Project areas 2 and 3 of the South Limburg mining area are characterized by industrial deep mining, which are mainly situated below a thicker overburden (Heitfeld, Klunker, et al. 2016). As opposed to project area 1, the stopes close to the top of the Carboniferous bedrock were excavated under preservation of a thicker crown pillar[2] (Heitfeld, Klunker, et al. 2016).
Since 1939, the crown pillar heights could be reduced from 50 m to 10 m, or even 3 m if the overlying strata was investigated by means of upward drillings. In the presence of strongly-water bearing layers or quicksands, the layers were dewatered (de Man 1988; Heitfeld, Klunker, et al. 2016). Since it was common for the mine workings not to be backfilled, after mining of the coal seam, the hanging wall was allowed to collapse into the mined seam (Heitfeld, Klunker, et al. 2016). However, since there are cases in which the hanging wall rocks did not collapse, subsurface mine voids are present in the area (Heitfeld, Klunker, et al. 2016).
As an after-effect of the remaining subsurface mining voids, sudden collapse might occur, potentially leading to infrastructural damage. For example the case of shopping centre 't Loon in Heerlen, which was partly damaged on 3 December 2011. The occurrence of a sinkhole beneath one of the columns, lead to its detachment from the building's supporting structure. The local carrying capacity of the structure was hampered, but due to the second load path of the structure, no collapse occurred (van Waning 2014).
Following the risk categorization of the mine shafts, the risk assessment for near-surface mining distinguishes between historical near-surface mining (project area 1) and industrial near-surface mining (project areas 2 and 3).

Historical Near-Surface Mining EK – For the historical near-surface mining, the risk analysis makes use of the mining documents and maps to construct the outcrop lines of all coal seams (Heitfeld, Klunker, et al. 2016). Both the tectonic conditions and the mining situation, i.e. regional significance of each coal seam (the presence of 'main' or 'mineable' seam), the dip of the coal seam ($< 36°$ or $\geq 36°$) and the knowledge from mining documents, are the basis for the assignment of the impact categories EK (Heitfeld, Klunker, et al. 2016).
As a result, the assigned impact category EK gives the estimated relative probability for future sinkholes and/or subsidence, as being either 'high' (EK 1, red), 'medium' (EK 2, yellow), 'low' (EK 3, blue) or 'none' (EK 4, green) (Heitfeld, Klunker, et al. 2016). For a full overview of the historical near-surface mining EK classification criteria, the reader is referred to Table D.1 in Appendix D.

Industrial Near-Surface Mining EK – For the risk assessment of the industrial near-surface mining activities, all stopes located in the range between 0 and 20 m below the top of the Carboniferous bedrock are taken into consideration, based on their rock mechanical properties and the uncertainty in their historical documentation (Heitfeld, Klunker, et al. 2016).
The categories for the ground level impact areas from near-surface mining are based on the geotechnical approach applied in the mining areas in Nordrhein-Westfalen (NRW), Germany. Additionally, the geologic-tectonical settings of South Limburg and the investigations of the incident at Winkelcentrum 't Loon in Heerlen are taken into account (Heitfeld, Klunker, et al. 2016). The impact areas around a ground segment are defined, with a safety margin of 10m and a width resulting from impact of the overburden (Heitfeld, Klunker, et al. 2016), as illustrated in Figure 6.4.

[2]The crown pillar is defined as the rock mass situated above the uppermost stope of the mine, which is designed to protect the surface land and the underground mine (Bakhtavar 2010).

The impact category EK 1 includes areas above the 'not-fallen-in' voids, enabled by a special type of stress-strain distribution under the conditions of stopes that are characterized by a 'tri-angle-shaped/acute-angled' geometry (Heitfeld, Klunker, et al. 2016), e.g. in the case of Winkelcentrum 't Loon. The existence of not-fallen-in voids is also assumed to be more likely at 'room and pillar' mining systems between 0 and 20 m below the top of the Carboniferous bedrock (Heitfeld, Klunker, et al. 2016). For illustration, the potential failure in a room and pillar mining system is shown in Figure 6.5. Based on an AHN2 DTM and upward drillings documented in the mining maps, EK 2 is delimited by the thickness of the overburden with a 45° angle of repose (Heitfeld, Klunker, et al. 2016). Any stope in the range between 0 and 20 m below the top level of the Carboniferous bedrock is implemented into the risk assessment and assigned to EK 3. Following the same principle for EK 3, the stopes' impact area is extended by 10m at each side and its overburden thickness is taken into account by taking a 45° angle of repose (Heitfeld, Klunker, et al. 2016).

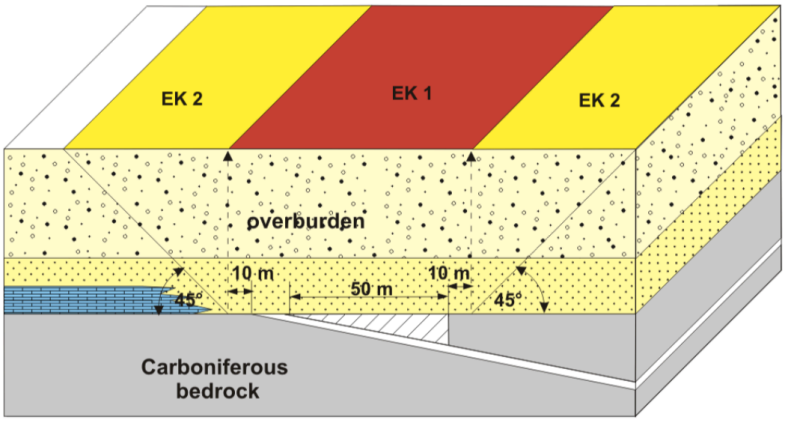

Figure 6.4: Illustrative definition of the impact categories EK 1 and 2 in project areas 2 and 3 of a segment with 10m safety margins around the acute-angled (45°) open area or 'stope' and delimited by the impact of the overburden (Source: Heitfeld, Klunker, et al. 2016).

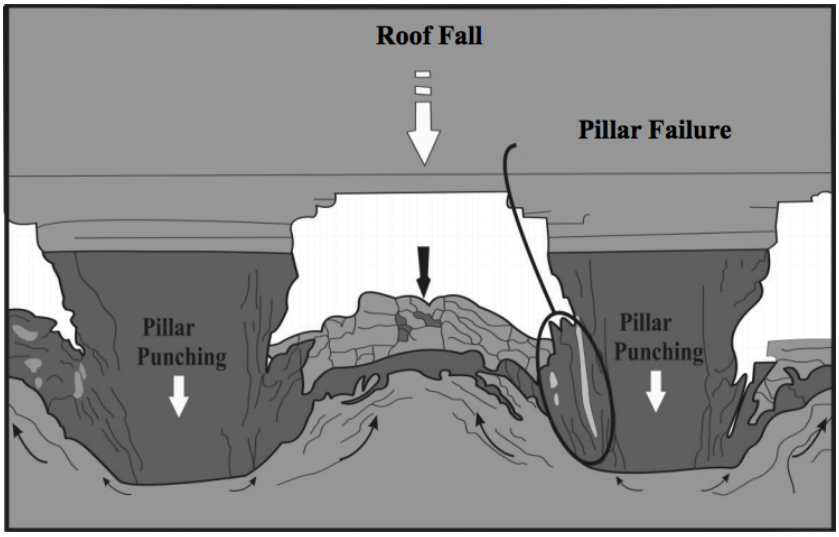

Figure 6.5: Simplified representation of roof fall and pillar failure in a typical room and pillar mining system (Source: Fathi 2016).

The impact areas of the industrial and historical near-surface mining in the different project areas (1 to 3) are visualized in Figure 6.6, where the historical near-surface mining EK are shown in greater detail.

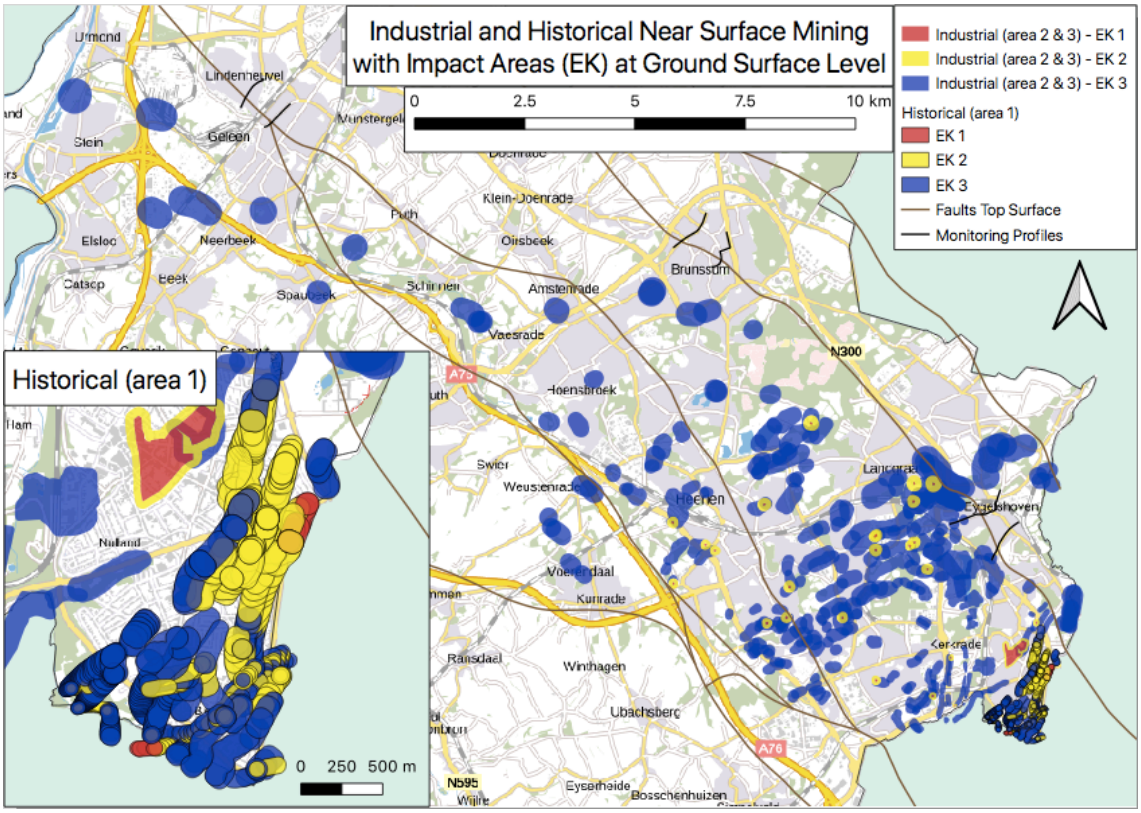

Figure 6.6: Potential impact areas at ground surface level from historical (project area 1, zoomed-in) and industrial (project areas 2 and 3) near-surface mining, with the faults at top surface and the associated cross-sectional monitoring profile locations. The shapefiles originate from Heitfeld, Klunker, et al. 2016.

6.1.3. Deformation Analysis – Spatial Representation

A localized deformation analysis is performed on the study area in South Limburg containing the different mines and associated impact categories, faults of the top surface and their suggested cross-sectional monitoring profiles. In specific, the measurement points from two Sentinel-1 tracks, one ascending (i.e. track 88) and one descending (i.e. track 37), are used in this analysis. From the provided datasets, as presented in chapter 4, the two tracks cover the South Limburg mining areas. First, the spatial representations of the linear deformation are provided per track in the form of maps with associated histograms, showing the applied color classifications. In further sections, the results of two localized deformation analyses are presented. The first analysis focuses on the differential ground heave, and the second analysis focuses on the deformation related to near-surface mining. In each case, the deformation is studied in relation to the previously determined EK classifications. The output is presented in the form of histograms of the linear deformation in the period 2015-2019, as well as their respective time series, per EK category.

Spatial Representation

The linear deformation for the periods 2015-2019 in the study area is shown for tracks 88 and 37 in Figures 6.7 and 6.9 respectively. The color ramp used in these figures is non linear, as it uses 'natural breaks', based on the Jenks optimization method which is designed to determine the best arrangement of values into different classes. This is done by 'minimizing each class's average deviation from the class mean, while maximizing each class's deviation from the means of the other groups' (Chen et al. 2013). The distributions of the linear deformation points, according to their respective classes or 'color groups', can be observed for tracks 88 and 37 in Figures 6.8 and 6.10 respectively. Both distributions have the same classes, namely the natural breaks found for track 88 as these also enclose and decently characterize the measurements of track 37.

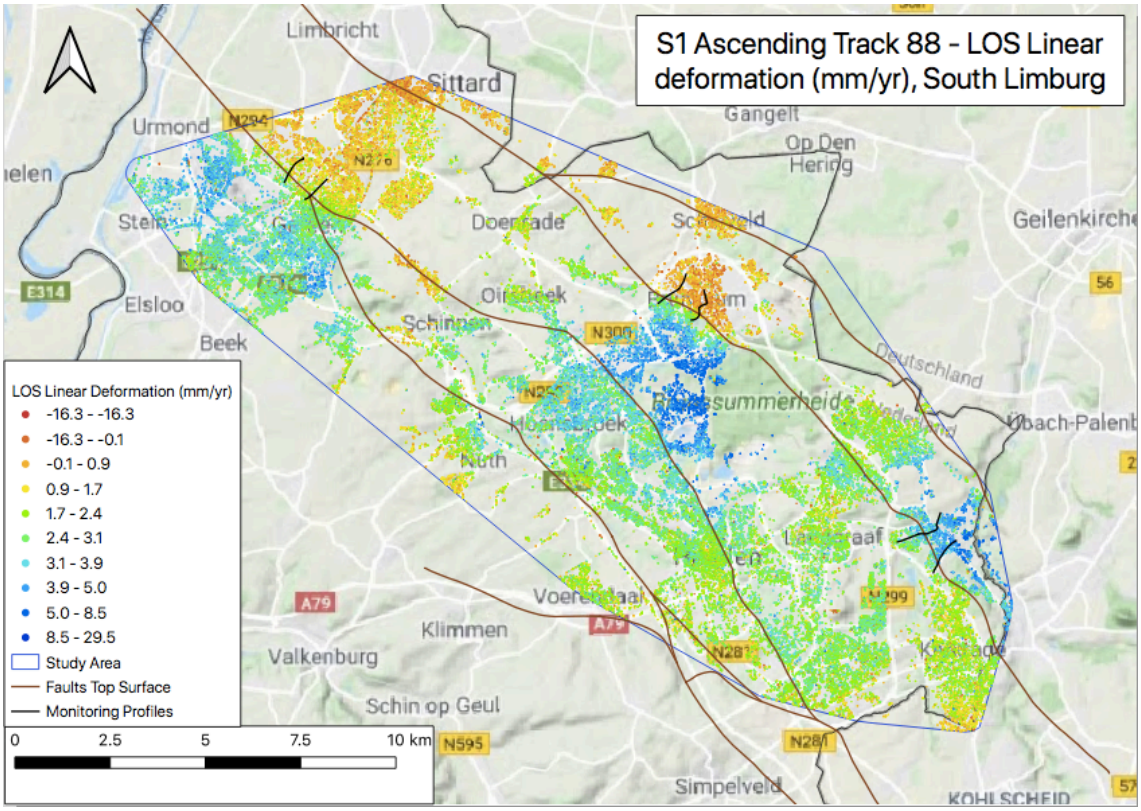

Figure 6.7: S1 Ascending Track 88: Linear LOS deformation rate (mm/yr) in the period 2015-2019 for the South Limburg study area, with the faults at top surface and the associated cross-sectional monitoring profile locations (PSI data: SkyGeo). The latter shapes originate from the risk analysis performed in Heitfeld, Klunker, et al. 2016.

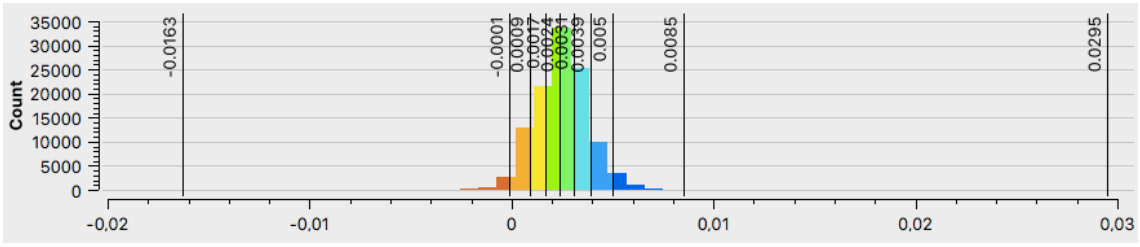

Figure 6.8: S1 Ascending Track 88: Linear LOS deformation rate (m/yr) frequency histogram (count) for the South Limburg area. The color classification relies on the natural breaks optimization method (data: SkyGeo).

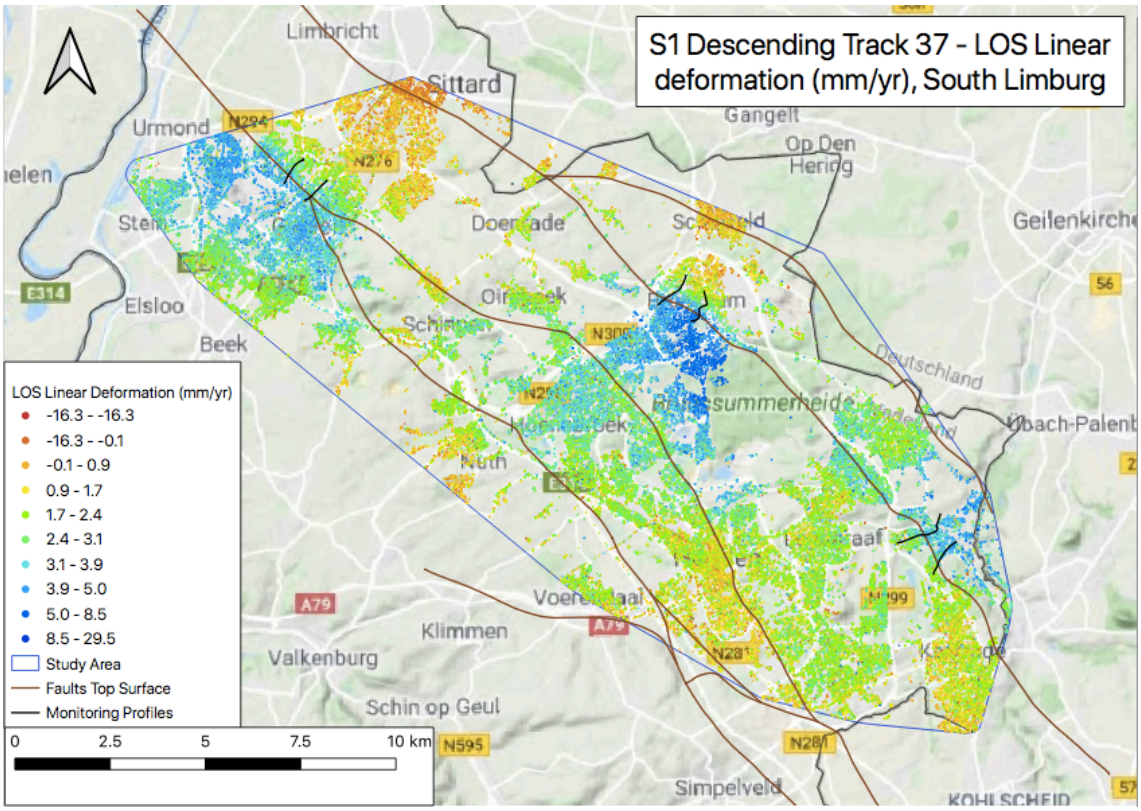

Figure 6.9: S1 Descending Track 37: Linear LOS deformation rate (mm/yr) in the period 2015-2019 for the South Limburg study area, with the faults at top surface and the associated cross-sectional monitoring profile locations (PSI data: SkyGeo). The latter shapes originate from the risk analysis performed in Heitfeld, Klunker, et al. 2016.

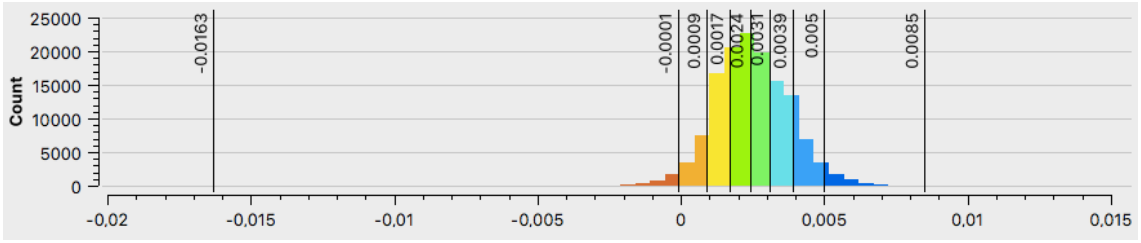

Figure 6.10: S1 Descending Track 37: Linear LOS deformation rate (m/yr) frequency histogram (count) for the South Limburg area. The color classification relies on the natural breaks optimization method (data: SkyGeo).

Spatial Reference

With the comparison of the different ground heave and near-surface mining impact areas (EK) in terms of their deformation, differences between the two tracks (88 and 37) are apparent. Here, the spatial reference should be kept in mind, as presented in Table 4.17 of the database implementation in Chapter 4, showing a 0.110 mm/yr and a 0.465 mm/yr difference for tracks 88 and 37 (respectively) with respect to the nationwide zero-deformation reference. Additionally, since the deformation from both tracks is expressed in the line-of-sight (LOS) as opposed to their vertical projections, the EK comparisons should be considered in the context of their respective tracks.

6.1.4. Deformation Analysis – Differential Ground Heave

As one of the mining after-effects in the South Limburg study area, differential ground heave is analyzed with the use of Sentinel-1 InSAR datasets. Through the attribution of the previously determined ground heave EK classes to the PSI points of ascending track 88 and descending track 37, the observed deformation can be better understood. The PSI datasets used in this study, spanning from 2015 to 2019, follow upon the ground heave results in Heitfeld, Klunker, et al. 2016, acquired between 1974 and 2014, as presented in Figure 6.2. This helps in the interpretation of the deformation results, either showing a smooth continuation of the observed deformation or any inconsistencies therein.

First, the three ground heave potential impact areas are split in northern and southern components (1N, 1S, 2N, 2S, 3N and 3S) along their respective faults at the top surface. The resulting polygon areas are represented in Figure 6.11. Subsequently, the deformation points of tracks 88 and 37 corresponding to the potential impact areas are enriched with the EK North-South classes.

For all three potential impact areas the northern polygon (with respect to the fault) is wider than the southern one, as it follows the northern ground heave gradient directed in the cross sectional (SW – NE) direction. For example, at the most probable location of the Heerlerheide fault, shown (in brown) in Figures 6.7, 6.9 and 6.11, there are no indications of the development of a significant discontinuity. This means that the Heerlerheide Fault (EK 2 – yellow) has not yet been activated as a major movement path because of ground heave due to rise in mine water (Heitfeld, Klunker, et al. 2016). The same observation is made for the other two (EK 3 – blue) areas along the Feldbiß fault.

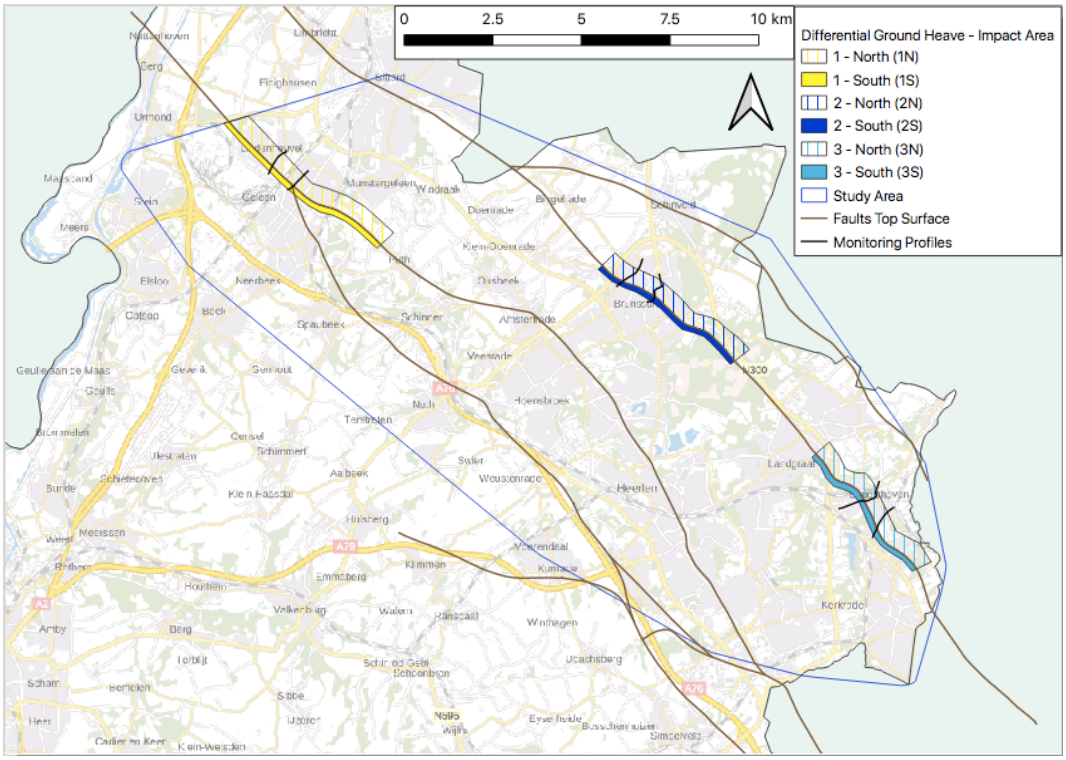

Figure 6.11: Three potential ground heave impact areas for the South Limburg region, (1) Geleen, (2) Brunssum and (3) Eygelshoven, split along their respective faults into a North (N) and South (S) component for deformation analysis. The fault and cross-section shape files originate from the risk analysis performed in Heitfeld, Klunker, et al. 2016. The potential impact area shape files were constructed based on Heitfeld, Klunker, et al. 2016.

Linear Deformation

First, the results are presented as histograms showing the normalized distribution of the linear deformation (2015 - 2019) of the potential impact areas per sample track (88 and 37) in Figures 6.12 and 6.13. Table 6.2 summarizes the statistical results of these distributions.

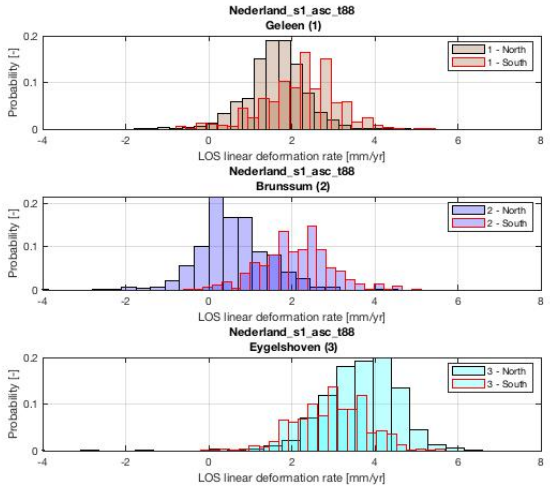

Figure 6.12: S1 Ascending Track 88: Normalized distribution (25 bins) of the LOS linear deformation rates (mm/yr) from 2015 to 2019 of the three potential ground heave impact areas in South Limburg.

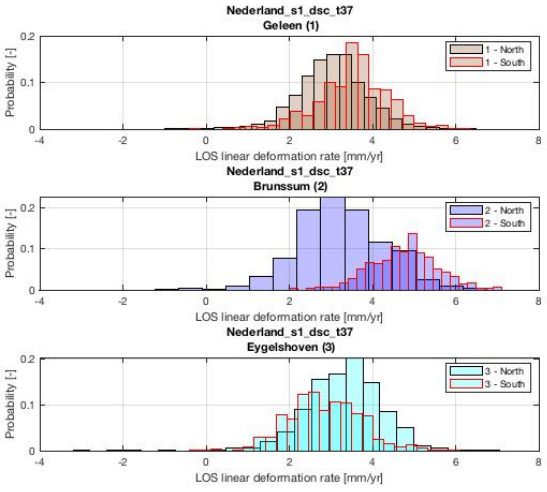

Figure 6.13: S1 Descending Track 37: Normalized distribution (25 bins) of the LOS linear deformation rates (mm/yr) from 2015 to 2019 of the three potential ground heave impact areas in South Limburg.

Track no.	IA	No. pnts [-]	Mean [mm/yr]	Med [mm/yr]	Std [mm/yr]	Skew [-]	Min [mm/yr]	Max [mm/yr]	Pctl10 [mm/yr]	Pctl90 [mm/yr]
asc_88	1N	2063	1.61	1.60	0.70	−0.02	−1.80	5.30	0.80	2.40
	1S	645	2.21	2.30	0.88	−0.44	−0.80	5.40	1.10	3.20
	2N	1248	0.56	0.50	0.84	−0.10	−4.00	4.40	−0.30	1.70
	2S	482	2.12	2.10	0.83	0.10	−0.50	5.10	1.10	3.10
	3N	1498	3.65	3.70	0.92	−1.40	−4.40	6.40	2.60	4.70
	3S	450	2.97	3.05	0.88	−0.19	−0.10	5.70	1.90	4.10
dsc_37	1N	2462	2.99	3.00	0.82	−0.07	−1.00	6.40	2.00	4.00
	1S	779	3.54	3.60	0.82	−0.43	−0.40	6.20	2.40	4.50
	2N	1240	3.24	3.20	1.09	−0.64	−7.10	6.50	2.00	4.65
	2S	300	4.76	4.80	0.78	−0.11	2.00	7.10	3.80	5.70
	3N	1763	3.32	3.40	0.92	−0.82	−3.20	6.90	2.30	4.40
	3S	535	2.84	2.80	0.89	0.10	−0.40	5.90	1.80	3.90

Table 6.2: Statistics of the LOS linear deformation rate (mm/yr) comparing the three different potential ground heave impact areas (IA), (1) Geleen, (2) Brunssum and (3) Eygelshoven divided in a northern and southern component, for S1 sample tracks 88 and 37 in the period 2015-2019. These statistics include: Number of points, mean, median, standard deviation, skewness, minimum, maximum, 10th-percentile, and 90th-percentile values of the points in the study area, observed along the satellite track. Additionally, the lowest value in the sample is indicated in red and the highest value in green.

The difference in size between the northeastern parts (1N, 2N and 3N) and the southwestern parts (1S, 2S and 3S) of the EK areas is reflected in the amount of PSI points attributed to these areas, as confirmed in Table 6.2. The mean and median deformation values of all six individual areas show an overall net linear increase. However, as it appears from Figures 6.12 and 6.13, the magnitude of this 'average' upward deformation differs between the different potential impact areas (1 – 2 – 3) and between the northeastern and the southwestern parts of thereof (N – S). The southern parts of the impact areas of Geleen (1) and Brunssum (2) show, on average, more positive deformation than their northern counterparts. The largest difference between the northern and southern parts is found for the EK area in Brunssum (2), i.e. ±1.6 mm/yr as opposed to ±0.7 mm/yr for the other two EK areas. This can also be seen in Figures 6.7 and 6.9, when comparing both sides in the different impact areas. Furthermore, two opposing deformation trends are observed along the Feldbiß fault. Where the northern part of the Brunssum area (2) shows less positive deformation than its southern counterpart, the northern part of the Eygelshoven area (3) deforms at a higher rate than the southern part.
Similar trends are seen when comparing the northern and southern parts for each of the three impact areas in terms of their 90th-percentile linear deformation values. For the EK areas of Geleen (1) and Brunssum (2), the 90th-percentile of linear deformation is lower for their northern parts compared to their southern parts, and vice versa for the EK area of Eygelshoven (3). However, the same trend is not necessarily observed in the maximum linear deformation values, which are quite close together in magnitude. On the other hand, relatively strong minima are observed for both tracks in the northern parts of potential impact areas 2 and 3.
Overall, the linear deformation distributions of all individual areas show similar values in terms of their standard deviations. The level of skewness is mostly negative across all samples, except in track 88 for EK area 2S, and in track 37 for EK area 3S. For the Brunssum and Eygelshoven EK areas (2 and 3), both situated along the Feldbiß fault, their northern parts show stronger negative skewness than their southern parts, whereas the opposite is true for the Geleen EK area (1).

Time Series Deformation

The time series of the median deformation in the northern (1N, 2N and 3N) and southern (1S, 2S and 3S) parts of the potential ground heave impact areas EK are presented for tracks 88 and 37 in Figures 6.14 and 6.15 respectively. Since a phase unwrapping error of 28 mm affects the interpretation of the extreme deformation results, i.e. maximum and minimum profiles, these are included as an example for tracks 88 and 37 in Figures D.5 and D.6 of Appendix D.

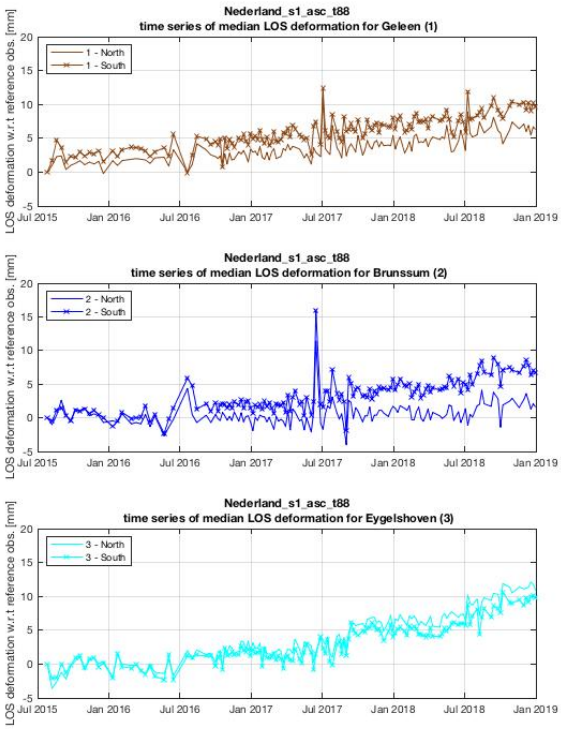

Figure 6.14: S1 Ascending Track 88: Time series of the median LOS deformation (mm) w.r.t. the epoch (2015-07-26) of the three potential ground heave impact areas in South Limburg.

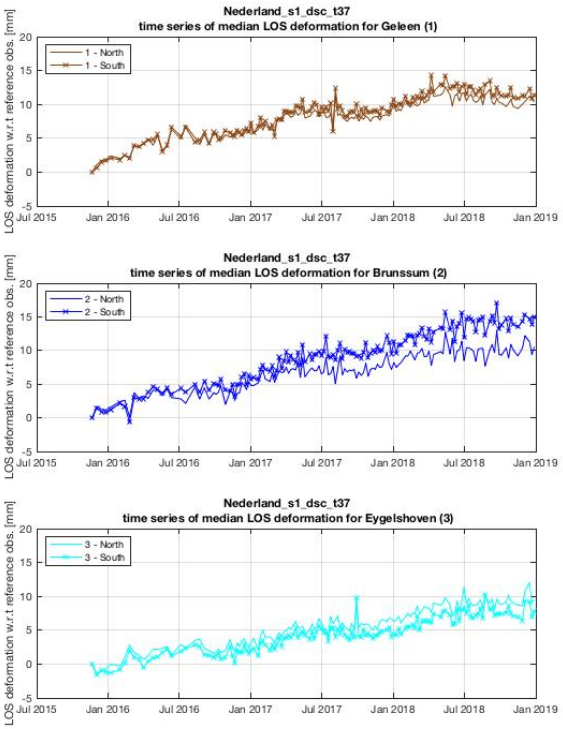

Figure 6.15: S1 Descending Track 37: Time series of the median LOS deformation (mm) w.r.t. the epoch (2015-11-20) of the three potential ground heave impact areas in South Limburg.

In general the deformation time series results (between 2015 and 2019) confirm the separation between the northeastern and southwestern potential ground heave EK areas with respect to the major top surface faults. The northeastern parts of the Geleen and Brunssum impact areas (1 and 2) show higher upward motion than their southwestern counterparts, whereas the opposite trend is observed for the Eygelshoven potential impact area (3). The largest difference in deformation between the northern and southern counterparts is found in Brunssum (area 2), i.e. ±5mm in 4 years (2015-2019) for both tracks. This observation is in line with the linear deformation trends in Table 6.2, even indicating a difference of 1.6mm/yr.

6.1.5. Deformation Analysis – Near-Surface Mining

Aside from ground heave in the South Limburg area, other local after-effects are the consequence of near-surface mining. With the risk assessment of near-surface mining in Section 6.1.2, potential impact areas EK (1 – 3) are defined for both the historical (project area 1) and the industrial near-surface mining areas (project areas 2 and 3), related to the 'not-fallen-in' voids of their respective coal seams. These voids can potentially lead to subsidence or sinkholes, in turn causing damage to buildings and local infrastructure.

As with the ground heave deformation analysis, the results of the deformation analysis concerning the after-effects of near-surface mining are divided in two parts. First, the linear deformation results are presented and discussed, followed by the presentation of the deformation time series results for the same EK classifications.

Linear Deformation

The results of the localized deformation analyses are presented with respect to the impact areas EK 1 to 3 at ground level from near-surface mining. The normalized distributions of the linear deformation (mm/yr) measurements per EK class, are shown for tracks 88 and 37 for the historical mining areas in

Figures 6.16 and 6.17, and for the industrial mining areas in Figures 6.18 and 6.19. In addition, the descriptive statistics per distribution can be found for the historical mining areas in Table 6.3 and for the industrial mining areas in Table 6.4.

Historical Near-Surface Mining EK –

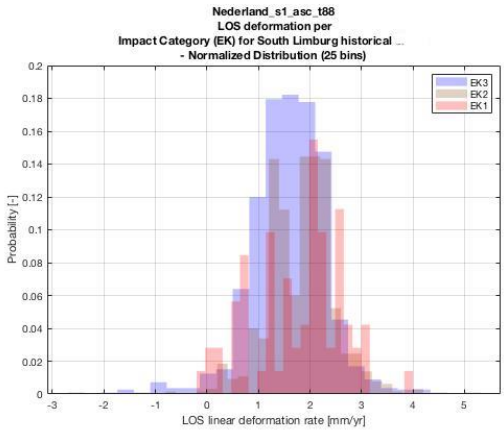

Figure 6.16: S1 Ascending Track 88: Normalized distribution of the LOS linear deformation rate (mm/yr) per impact category class (EK) of the historical near-surface mining areas in South Limburg.

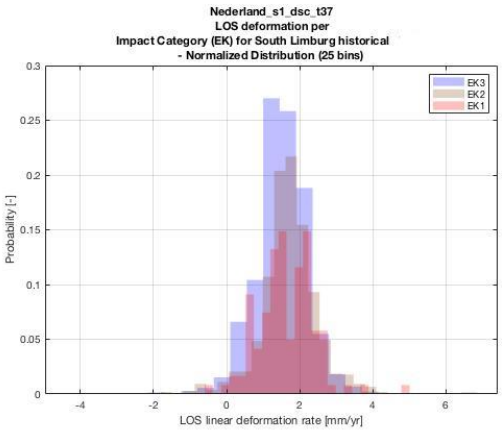

Figure 6.17: S1 Descending Track 37: Normalized distribution of the LOS linear deformation rate (mm/yr) per impact category class (EK) of the historical near-surface mining areas in South Limburg.

Track no.	EK	No. pnts [-]	Mean [mm/yr]	Med [mm/yr]	Std [mm/yr]	Skew [-]	Min [mm/yr]	Max [mm/yr]	Pctl10 [mm/yr]	Pctl90 [mm/yr]
asc_88	1	71	1.78	2.00	0.85	−0.26	−0.20	4.00	0.60	2.74
	2	650	1.82	1.80	0.63	−0.06	−0.80	4.20	1.10	2.60
	3	1125	1.58	1.60	0.73	−0.51	−2.70	5.10	0.80	2.40
dsc_37	1	121	1.63	1.60	0.78	0.49	−0.60	5.00	0.60	2.50
	2	1074	1.72	1.70	0.79	−0.10	−1.80	5.80	0.80	2.60
	3	1440	1.47	1.50	0.78	−0.19	−4.10	6.70	0.60	2.30

Table 6.3: Statistics of the LOS linear deformation rate (mm/yr) comparing the different impact categories (EK 1 – 3) of the South Limburg historical near-surface mining areas for Sentinel-1 tracks 88 and 37 in the period 2015-2019. These statistics include: Number of points, mean, median, standard deviation, skewness, minimum, maximum, 10th-percentile, and 90th-percentile values of the points in the study area, observed along the satellite track. Additionally, the lowest value in the sample is indicated in red and the highest value in green.

With the historical near-surface mining EK 3 areas covering the largest part of project area 1, compared to EK 2 and (lastly) EK 1, the EK 3 classification contains the most PSI points. However, since the historical near-surface mining affects a smaller area in general (project area 1), as opposed to project areas 2 and 3, all of the historical mining samples are smaller than the industrial mining samples. Additionally, the historical mining EK 2 and 3 samples are similar in size, i.e. number of points, as opposed to those of EK 2 and 3 in the industrial mining analysis.
On average, considering the mean and median deformation values in Table 6.3, the most positive (upward) deformation is observed for historical EK class 2, followed by EK class 1 and lastly EK class 3. No clear trend is observed for the standard deviation of the linear deformation between the different historical EK classes, as for track 88 these are all ±0.78 mm/yr. In track 37, EK 1 shows the highest standard deviation in its distribution, followed by EK 3.
In all cases, the assessed skewness levels are negative to a certain extent (down to -0.5), except for the positive skewness identified for the distribution of EK 1 in track 37 of about 0.5. With its relatively large sample size, EK 3 shows the strongest linear deformation extremes both in its minima and maxima in both tracks 88 and 37. However, this trend appears to be more subtle than for the industrial shafts, in which the sample sizes for EK 3 are vastly larger than the remaining impact category classes. The percentile deformation results for the historical EK 3 class do not necessarily follow the extreme

deformation trends observed for the same class.

Industrial Near-Surface Mining EK –

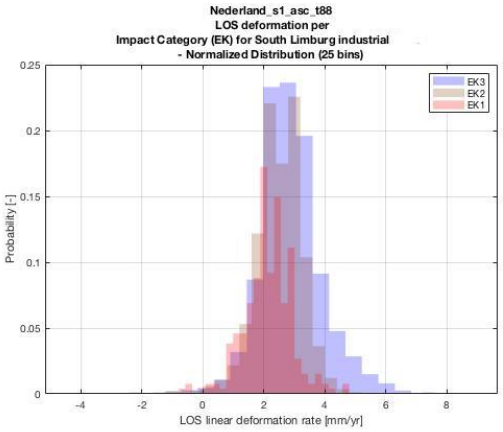

Figure 6.18: S1 Ascending Track 88: Normalized distribution of the LOS linear deformation rate (mm/yr) per impact category class (EK) of the industrial near-surface mining areas in South Limburg.

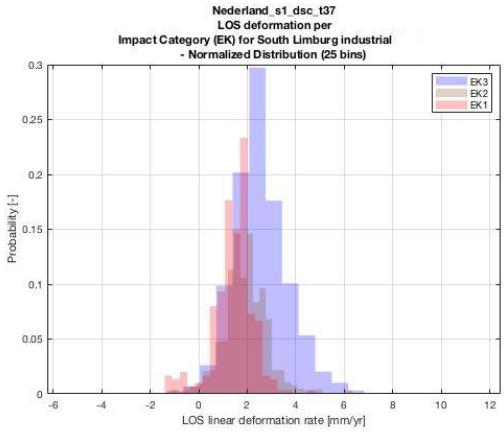

Figure 6.19: S1 Descending Track 37: Normalized distribution of the LOS linear deformation rate (mm/yr) per impact category class (EK) of the industrial near-surface mining areas in South Limburg.

Track no.	EK	No. [-]	Mean [mm/yr]	Med [mm/yr]	Std [mm/yr]	Skew [-]	Min [mm/yr]	Max [mm/yr]	Pctl10 [mm/yr]	Pctl90 [mm/yr]
asc_88	1	261	2.13	2.20	0.80	−0.15	−0.70	4.80	1.20	2.90
	2	829	2.48	2.50	0.80	−0.54	−2.30	7.50	1.60	3.30
	3	15 160	2.90	2.80	1.05	0.25	−4.40	9.00	1.80	4.20
dsc_37	1	300	1.43	1.50	0.89	−0.05	−1.40	6.10	0.50	2.40
	2	1246	1.90	1.90	0.88	0.08	−1.40	5.10	0.80	2.90
	3	20 644	2.54	2.40	1.14	0.38	−5.20	11.40	1.30	4.10

Table 6.4: Statistics of the LOS linear deformation rate (mm/yr) comparing the different impact categories (EK 1 – 3) of the South Limburg industrial near-surface mining areas for Sentinel-1 tracks 88 and 37 in the period 2015-2019. These statistics include: Number of points, mean, median, standard deviation, skewness, minimum, maximum, 10th-percentile, and 90th-percentile values of the points in the study area, observed along the satellite track. Additionally, the lowest value in the sample is indicated in red and the highest value in green.

As expected from the number of different industrial EK polygons and their sizes (Figure 6.6), most of the PSI points belong to EK 3, followed by EK 2 and lastly EK 1. On average, the linear deformation trends are highest for the industrial EK 3 classes and lowest for EK 1. Note this observation differs from the comparison of the historical EK classes, where EK 3 shows the lowest upward deformation on average, i.e. mean and median. Furthermore, the mean and median linear deformation results of the different industrial near-surface mining EK classes are further apart (between ±1.5 to ±2.5 mm/yr) compared to the average linear deformation results of the historical near-surface mining (between ±1.5 to ±2.0 mm/yr).
The standard deviation of the EK 3 classified points is higher than that of the remaining near-surface mining EK classes, which are close together in magnitude. Additionally, in both tracks the EK 1 distribution shows negative skewness, while the skewness is positive (and highest) for the EK 3 - attributed points.As expected from its largest sample size, EK 3 shows the strongest extremes both in its minimum and maximum linear deformation values. However, when considering the 10th and 90th-percentiles, EK 1 and EK 3 consistently shows the least and most positive deformation (respectively).

Time Series Deformation

Figures 6.20 and 6.21 show the median deformation time series of tracks 88 and 37, comparing the historical near-surface mining impact categories EK 1 – 3. The same approach is used to characterize the industrial near-surface mining potential impact zones, of which the time series are presented in

Figures 6.22 and 6.23.

Historical Near-Surface Mining EK –

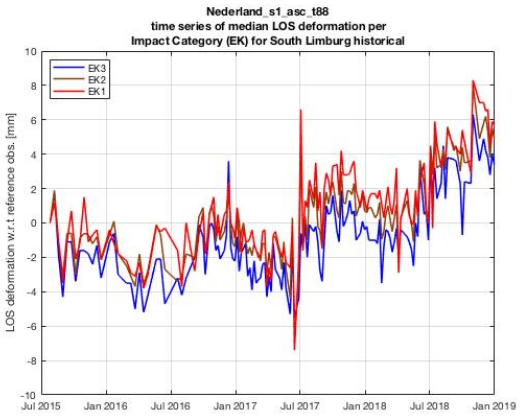

Figure 6.20: S1 Ascending Track 88: Time series of the median LOS deformation (mm) w.r.t. the epoch (2015-07-26) per impact category class (EK) of the historical near-surface mining areas in South Limburg.

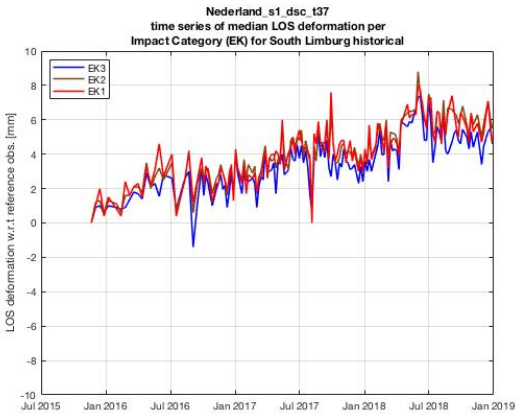

Figure 6.21: S1 Descending Track 37: Time series of the median LOS deformation (mm) w.r.t. the epoch (2015-11-20) per impact category class (EK) of the historical near-surface mining areas in South Limburg.

The median deformation profiles of the historical near-surface mining areas show near-identical trends toward net uplift, aside from any differences between ascending track 88 and descending track 37. All three profiles follow the same seasonality pattern, resembling that of a sinusoid. The median deformation profiles of near-surface mining class EK 1 are situated slightly above those of EK 3. The EK 2 profiles stay relatively centered in between the two others, although these seem to lean closer to the EK 2 profiles.
Note that the deformation time series of the industrial near-surface mining EK classes, in Figures 6.22 and 6.23, show the opposite sequence, i.e. with EK 3 remaining at the stronger positive end, followed by EK 2 and lastly EK 1. Furthermore, if the results are compared for both tracks, it can be seen that track 37 tends to show a direct uplift in all its median deformation profiles (starting from the epoch), whereas the net uplift in the track 88 profiles seems to be 'delayed' by roughly one seasonal cycle.

Industrial Near-Surface Mining EK –

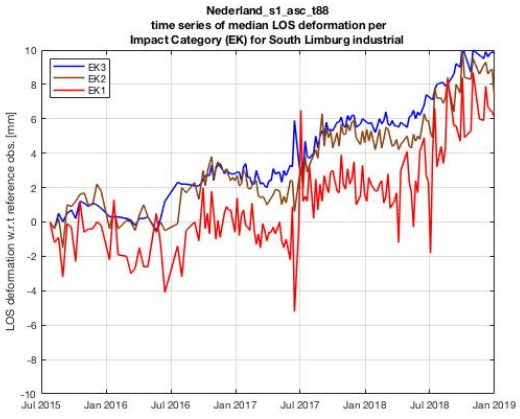

Figure 6.22: S1 Ascending Track 88: Time series of the median LOS deformation (mm) w.r.t. the epoch (2015-07-26) per impact category class (EK) of the industrial near-surface mining areas in South Limburg.

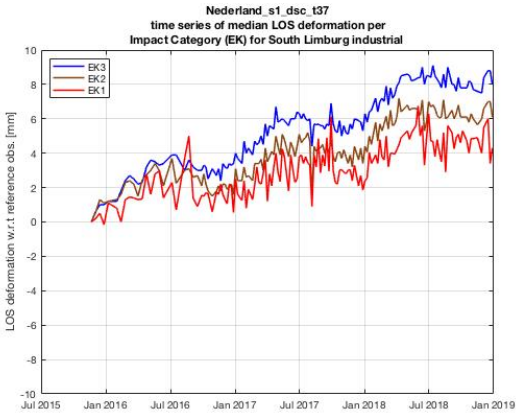

Figure 6.23: S1 Descending Track 37: Time series of the median LOS deformation (mm) w.r.t. the epoch (2015-11-20) per impact category class (EK) of the industrial near-surface mining areas in South Limburg.

As with the deformation of the historical near-surface mining EK classes, a net increase is observed

for the industrial EK classes. In general, the spread in profiles between the three classes is larger than for the historical near-surface EK classifications. In ascending track 88 the deformation profiles of EK 3 and EK 2 remain relatively close together, with the profile of EK 1 remaining at the bottom-end and showing larger fluctuations. In track 37, this effect is observed to a lesser degree, with the profile of EK 2 being centered between the other two profiles. Regarding the seasonality, the different profiles seem to be in phase with one another, showing quite similar oscillating behaviour in terms of their amplitudes.

6.1.6. Discussion

In the South Limburg case study, comparisons are made in terms of the observed deformation between the risk-based classifications of two different mining after-effects, i.e. differential ground heave and near-surface mining. In recent study by Heitfeld, Klunker, et al. 2016, among other identified after-effects, the two processes implemented in this study have shown to be potential threats to the South Limburg environment. This involves the risk for subsidence and sinkholes, in turn causing damage to the in situ and surrounding buildings and infrastructure, e.g. the case of Winkelcentrum 't Loon in Heerlen. For this case study the database approach of Chapter 4 is implemented as a framework to assign the different impact category EK classifications as attributes to the PSI points of two tracks, i.e. ascending track 88 and descending track 37.

Differential Ground Heave

For the differential ground heave, deformation differences are observed between the northern and southern parts of the three impact areas with respect to their fault lines. For Geleen and Brunssum (impact areas 1 and 2), the northern sections of their EK areas show slower ground heave compared to their southern counterparts with, on average, differences of about 0.7 mm/yr and 1.6 mm/yr respectively. In Eygelshoven (impact area 3), the opposite deformation trend is observed, with the northern section showing faster ground heave than the southern section, along the Feldbiß fault. Here, a difference of about 0.7 mm/yr is observed, which is about the same in magnitude as in the area of Geleen (1). Based solely on this case study's deformation results, it would seem that the Brunssum potential impact area (2) requires the assignment of differential ground heave class EK 2, as the difference is largest between its northern and southern sections. Following the same reasoning, the Geleen and Eygelshoven areas (1 and 3) should be classified under the same category, i.e. EK 3. However, the assignment of potential ground heave EK classes is also based on further basic risk factors, such as the rise in groundwater levels in the overburden, the presence of 'Drempels' (or 'sills') from active mining along the fault zone, or damage to buildings or infrastructure in that area (Heitfeld, Klunker, et al. 2016).
Since the 1980s up until 2014, ground heave up to a maximum of about 0,35 m has been observed. Heitfeld, Klunker, et al. 2016 expect a maximum of further 0,10 to 0,17 m in the future. In the context of the deformation between 1974 and 2014 as shown in Figure 6.2, the overall rate of ground heave in the study EK areas shows an overall slowing trend between 2015 and 2019, as it appears from Figures 6.7 and 6.9 and the results in Table 6.2. Note that the rising mine water profiles in (Heitfeld, Klunker, et al. 2016) (between 1974 and 2014) do not necessarily show linear progression in time. In most cases, a gradual slowing trend is already observed towards the later end of the mine water monitoring records in (Heitfeld, Klunker, et al. 2016). Additionally, based on Figure 6.2, the difference in ground heave from 1974 to 2014, between the northern and southern sections of the potential impact areas, is approximately 100mm in Geleen (2.5 mm/yr), 125mm in Brunssum (3.1 mm/yr) and 50mm in Eygelshoven (1.3 mm/yr). These prior (1974 – 2014) differences are high compared to the linear deformation differences observed in 2015 to 2019, i.e. 0.7 mm/yr in Geleen, 1.6 mm/yr in Brunssum and 0.7 mm/yr in Eygelshoven.

Near-Surface Mining

The potential risk of near-surface mining relates to the not-fallen-in subsurface mining voids. Their presence is due to the hanging wall rocks not collapsing after the seam was mined out. The analysis of deformation related to near-surface mining activities follows the risk-based distinction between historical and industrial mining. The deformation results, presented both linearly and as time series profiles, reflect this distinction, as well as the overall differences between the different EK classes (1 – 3).
As the historical near-surface mining took place in a relatively confined area (project area 1) compared to the industrial mining areas (project areas 2 and 3), the historical EK polygons contain less points, which show more homogeneous deformation. This is reflected in the linear deformation, where the

distributions of the different classes are close together, based on their deformation averages, extremes and low standard deviations. The same observation is made, based on the median time series profiles of the historical EK classes, which are very similar as opposed to the deformation profiles of the industrial EK classes. This might be explained by the relatively few historical EK points being concentrated in a smaller area (project area 1), compared to the larger industrial EK sample sizes, which are spread out over the entire study area (including project areas 2 and 3). This spread of industrial near-surface mining areas, and the points these contain, is most apparent for its EK 3 category, as seen in Figure 6.6.

Nonetheless, the historical near-surface mining EK 2 class shows on average the most positive deformation, whereas the EK 3 class shows the least positive deformation. However, for the industrial near-surface mining, EK 1 shows the least positive deformation, whereas EK shows the most positive (upward) surface deformation, based on the mean, median and maximum linear deformation values. The median linear deformation of the historical EK classes range from 0.1 mm/yr to 0.4 mm/yr (observed in track 88). In contrast, for the industrial near-surface mining analysis, this difference in median deformation between the EK classes ranges from 0.3 mm/yr to 0.9 mm/yr (in track 37). Considering adjacent polygons of different EK categories (e.g. 2 next to 1), the resulting differential deformation can be quite substantial for the industrial near-surface mining areas, potentially leading to damage of the surrounding buildings and infrastructure. The same is true for the extreme deformation, i.e. minima and maxima, which show a wider range for the indusrial near surface mining areas. However, the difference in sample sizes between the industrial and historical areas should be kept in mind[3].

Considering the median time series profiles for the different EK-attributed points, the largest and most frequent 'spikes' are observed for EK class 1 for both the historical and industrial near-surface mining. Apart from any direct implications of this observation for the EK 1 potential impact areas, this observation is to a certain extent explained by the fact that the EK classes 1 contain the lowest number of points in every case.

[3]For larger sample sizes, the likelihood of finding a stronger extreme or outlier increases.

6.2. South Holland – Subsiding Peatlands

With the general focus of this study centered on the differentiation between deep and shallow subsidence, the second case study focuses on a particular area in the province South Holland where shallow subsidence is presumably the case. Following the Bodemdalingskaart 2018 terminology, the three types of subsidence, i.e. 'total', 'deep' and 'shallow', are represented by a set of statistical descriptors that apply to 2 ×2 km grid cells covering the Netherlands. For each individual grid cell the deep subsidence is set as the median of its linear deformation distribution and total subsidence as the 10th-percentile. The difference between the total and the deep subsidence is taken as the shallow subsidence. The reasoning behind the assignment of 'deep' subsidence to the median value is that deep subsidence is generally observed for objects (e.g. buildings) that are founded on stable 'deep' underground layers. This is mostly the case in the Netherlands, where the foundation of buildings consist of wooden or concrete piles driven on a deep sandstone layer, sometimes extending to depths of more than 20m (Coevert 2019).
First, the study area is introduced in terms of its extent and characteristics. A brief overview is given of the selected PSI datasets, presented in Chapter 4, that cover the South Holland study area. Subsequently, a grid representation of this area is presented following the statistically-based method used to represent subsidence in Bodemdalingskaart 2018. An in-depth overview is provided of the auxiliary datasets and their features, which are selected for attribute-enrichment of the grid cells covering region. This approach is similar to the one applied in the nationwide analysis, in which the main statistical descriptors are used to characterize the deformation of a particular area. However, this case study and the Groningen case study makes use of grid cells, as implemented in Bodemdalingskaart 2018, to study the statistical distinction between total, deep and shallow subsidence in their 'contextual' environment.

6.2.1. Background

The province of South Holland, situated in the western part of the Netherlands, is characterized by a typical Dutch landscape of fen-meadows and polders below sea level. These fen-meadows consist of wet pasture lands, drained with peat soils, alternated by lakes, ditches, reed swamps and quaking fens (Cuenca, van Leijen, and Hanssen 2010). The water levels in the area are artificially controlled by water management authorities for agricultural, residential and recreational purpose, as well as the conservation of the natural environment (Cuenca and Hanssen 2008). Extraction of groundwater in the western peat areas, used in dairy farming, leads to the oxidation of peat. In turn, the process of peat oxidation leads to subsidence rates of up to 13 mm/yr and CO_2 emissions to approximately 27 $t \cdot ha^{-1} \cdot yr^{-1}$ (van den Akker and Hendriks 2017). Since approximately 26% of the land surface of the Netherlands is already situated below mean sea level (MSL) (Schiermeier 2010), the ongoing subsidence trend of the peat areas increases the local vulnerability to flood events.

6.2.2. PSI Datasets

As with the nationwide analysis, the South Holland case study makes use of the Sentinel-1 PSI datasets, presented in Chapter 4, to analyze the deformation in the case study area. First, the PSI data selection is discussed in terms of the different available Sentinel-1 tracks, which contain the deformation data collected between 2015 and 2019. Furthermore, the grid cell representation of the study area is introduced, which makes use of the selected PSI datasets.

Track Selection

The PSI data used in the South Holland case study include Sentinel-1 descending tracks 37 and 110. The reasoning behind the selection of these particular tracks is based on the following considerations. The first consideration is, of course, whether or not a particular track covers the region of interest. Of the selection of available tracks, presented in Chapter 4, tracks 88, 37 and 110 cover the province of South Holland. The second consideration in the selection of tracks for the South Holland and Groningen case studies is that at least one of the tracks should be used twice. This is done for the purpose of having the ability to make direct comparisons between the two case studies (South Holland and Groningen) for the same track. The reasoning for this is that any track-specific differences in the deformation results can be neglected, e.g. differences in terms of the spatial reference between tracks. For this reason, descending track 37 is included in both the Groningen and South Holland case studies, as it covers

both study areas.[4] Finally, descending track 110 was opted for as the second PSI dataset in the South Holland case study, for its coverage of the study area and its relatively low deviation from the spatial reference (taken as the track mean, listed in Table 4.17), i.e. $-4.23 \cdot 10^{-3}$ mm/yr.

Grid Representation

Since the peat oxidation and the related subsidence affect extensive parts of South Holland, the study area is set to capture these processes. Even though the areas of interest for this case study are mostly found in rural environments, i.e. pastures, the extent of the study area should also include enough measurements. Therefore, the extent of the study area covers the PSI point-dense urban environments as well, i.e. Rotterdam, Delft and part of The Hague. Additionally, the non-subsiding 'stable' areas are included in order to have a certain level of heterogeneity in the samples, which aids in the interpretation of the results. Based on this mix of differing areas, in terms of their geomorphological and geographical characteristics, the extent of the South Holland study area can be observed in Figure 6.24, showing the grid cell representation.

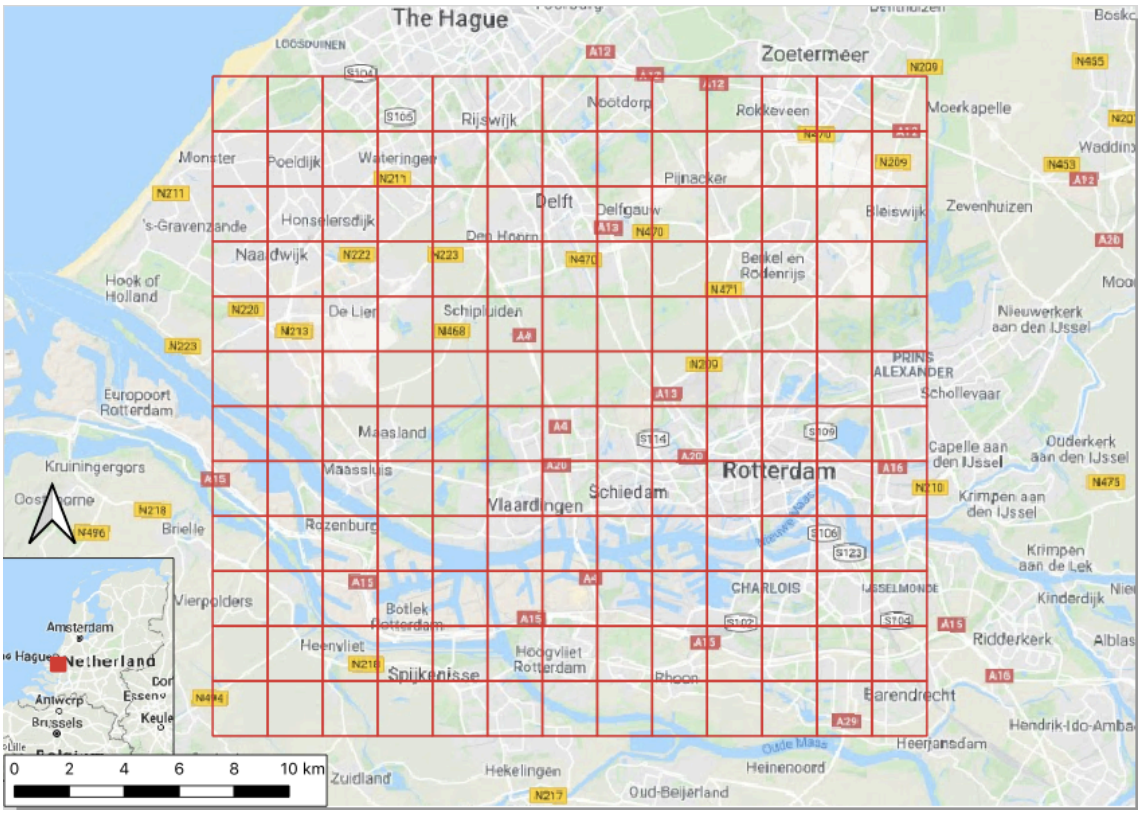

Figure 6.24: Grid of the South Holland study area composed of 156 grid cells (2 ×2km), based on the grid cells implemented in Bodemdalingskaart 2018

Prior to their inclusion within grid cells, the PSI derived linear deformation points that are part of the study area are shown in the LOS of two S1 acquisition tracks. Figures 6.25 and 6.26 show their distributions for S1 descending tracks 37 and 110 respectively in the South Holland study area.

[4]Note that ascending track 88 also covers both study areas and could be implemented as well in further research. However, in consideration of processing and time restrictions, in this study it was opted for to only include a maximum of 2 tracks per case study.

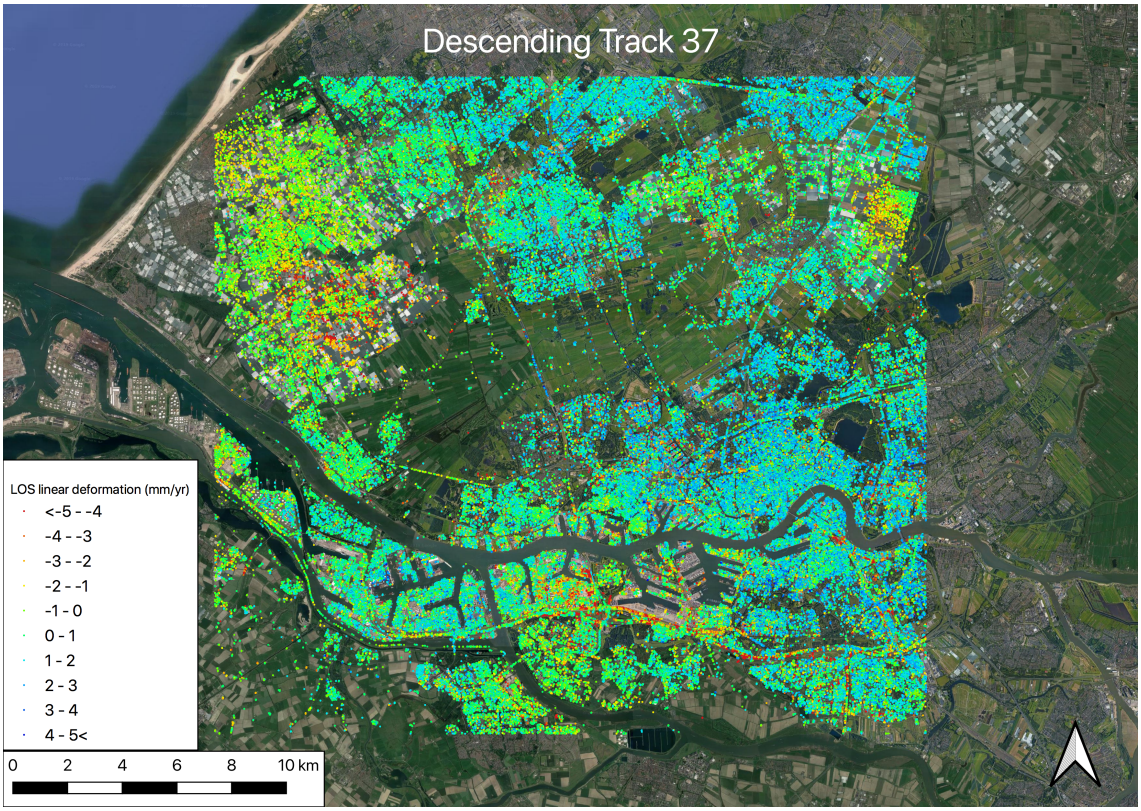

Figure 6.25: S1 Descending Track 37: LOS linear deformation (mm/yr) in the South Holland study area (data: SkyGeo).

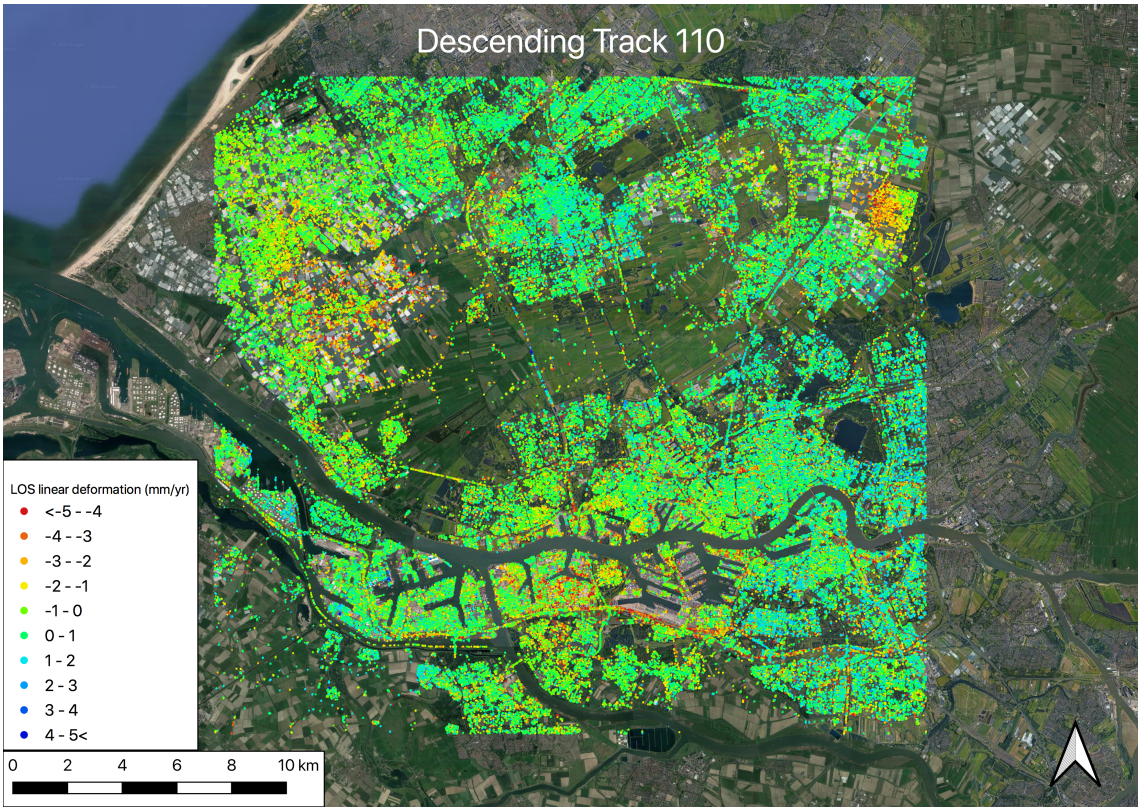

Figure 6.26: S1 Descending Track 110: LOS linear deformation (mm/yr) in the South Holland study area (data: SkyGeo).

Most of the measurement points in Figures 6.25 and 6.26 originate from persistent scatterers, mainly concentrated in the city areas where the landscape consists of buildings and infrastructure. Outside of the urban areas, the reflections are mainly from similar objects of which these are present to a lesser extent. Therefore, these rural areas are more difficult to interpret. Since the response of these areas is especially relevant for the distinction between shallow and deep subsidence, the 'gaps' in data from these areas needs to be 'filled in' for further interpretation.

Total, Deep and Shallow Deformation

As mentioned at the beginning of this study, Bodemdalingskaart 2018 applies a grid cell representation to assess the nationwide subsidence. This allows for interpretations to be made over the entire surface of the Netherlands, including the pastures with an overall low point density. The South Holland and Groningen case studies provide similar grid representations of their surface deformation, as shown in Figure 6.24. To this end, several steps are to be undertaken;

1. The first step is to assign the deformation points to their respective grid cells. This is done by loading the necessary PSI point measurement in the same spatial environment as the 'empty' grid cell structure, which covers the entire study area. A crop is made of the PSI datasets in order to remove the points that are situated outside of the area of interest.

2. The second step involves a spatial join between the target grid vector layer and the join layers, which are the PSI points themselves. As such, the PSI points are coupled to their respective grid cells, based on their topological relation, i.e. points 'inside' polygons. In this case, the target attribute is the linear deformation (mm/yr) of each individual point.

3. Subsequently, the 'total' and 'deep' linear deformation are derived for each grid cell from the 10th-percentile and the mean values respectively. Whereas the median can be computed directly in the mapping environment itself, i.e. QGIS, the 10th percentile for each grid is computed in the database environment through queries. After both values are stored as attributes per grid cell, the 'shallow subsidence' is computed in QGIS as the difference between both attributes, i.e. 'total' (10th PCTL) - 'deep' (median) = 'shallow'.

The resulting deformation grids are presented in the following sets of figures. For descending tracks 37 and 110, Figures 6.27 and 6.28 show the total linear deformation, Figures 6.29 and 6.30 show the deep linear deformation, and lastly Figures 6.31 and 6.32 show the shallow deformation per individual grid cell.

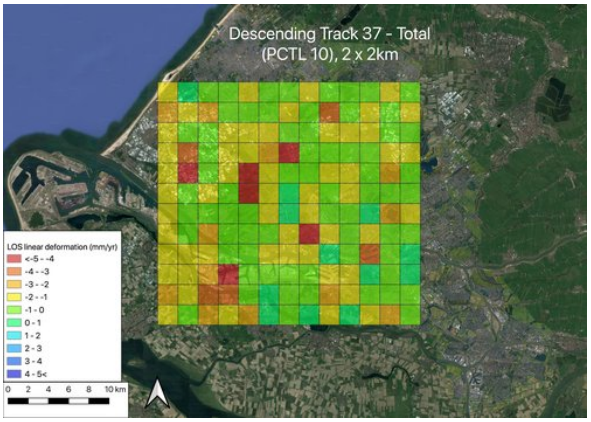

Figure 6.27: S1 Descending Track 37: Grid of the 'total' (10th-percentile) Linear LOS deformation (mm/yr) within 2 ×2 km grid cells covering part of South Holland (data: SkyGeo).

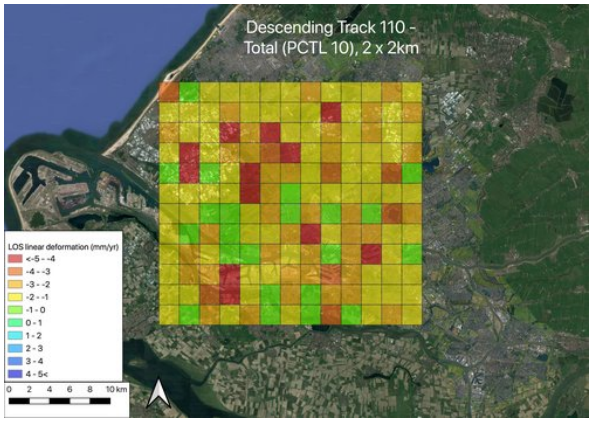

Figure 6.28: S1 Descending Track 110: Grid of the 'total' (10th-percentile) Linear LOS deformation (mm/yr) within 2 ×2 km grid cells covering part of South Holland (data: SkyGeo).

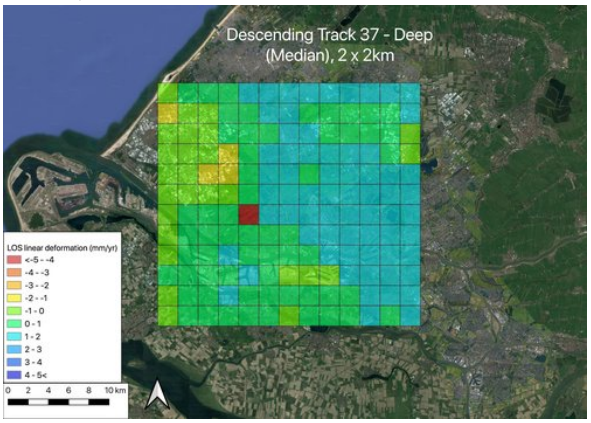

Figure 6.29: S1 Descending Track 37: Grid of the 'deep' (median) Linear LOS deformation (mm/yr) within 2 ×2 km grid cells covering part of South Holland (data: SkyGeo).

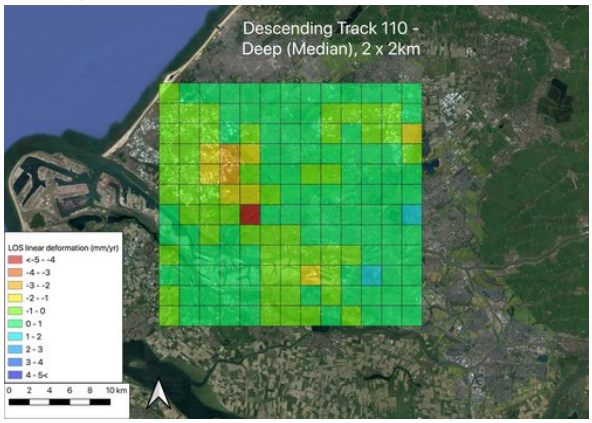

Figure 6.30: S1 Descending Track 110: Grid of the 'deep' (median) Linear LOS deformation (mm/yr) within 2 ×2 km grid cells covering part of South Holland (data: SkyGeo).

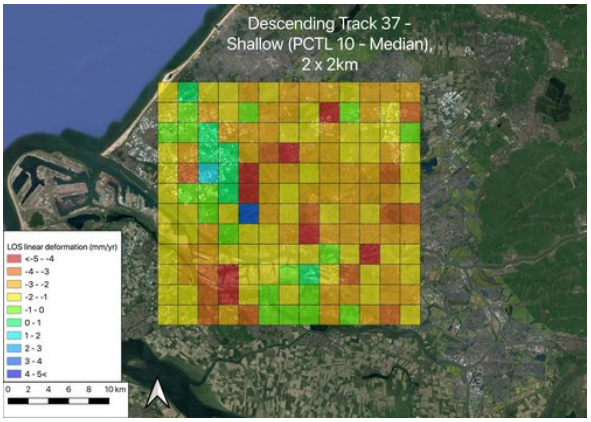

Figure 6.31: S1 Descending Track 37: Grid of the 'shallow' (10th-percentile - median) Linear LOS deformation (mm/yr) within 2 ×2 km grid cells covering part of South Holland (data: SkyGeo).

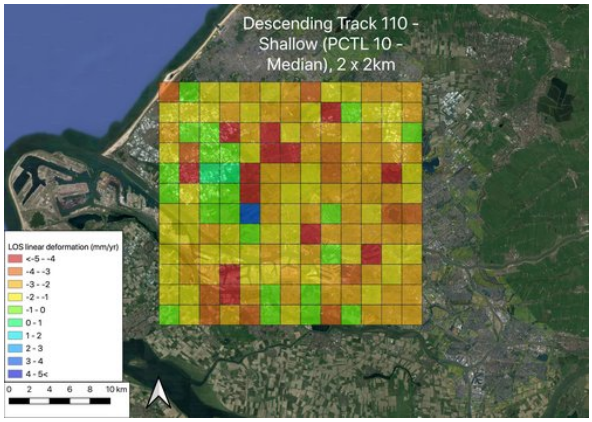

Figure 6.32: S1 Descending Track 110: Grid of the 'shallow' (10th-percentile - median) Linear LOS deformation (mm/yr) within 2 ×2 km grid cells covering part of South Holland (data: SkyGeo).

6.2.3. Auxiliary Datasets

Where the statistical approach of interpreting total, deep and shallow subsidence relies on internal measures of the deformation datasets, the attribute-enrichment approach focuses on external information to be used in this distinction. In Chapter 4, Table 4.15 provides an overview of the different datasets

and their implementations in the different analyses. Where the nationwide deformation analysis solely uses Bodemkaart attributes and objects, the South Holland and Groningen case studies also implement geographical attributes from BGT and geomorphology attributes from GKN. Following Table 4.15, the selected Bodemkaart attribute is the soil type and from GKN (Dutch geomorphology map) the 'form subgroup' attribute is selected. Additionally, different BGT objects and attributes are selected to characterize the built environment and infrastructure, i.e. road sections, buildings, non-vegetated terrain and vegetated terrain.

Soil Type

Figure 6.33 presents the soil type classifications in the South Holland area, of which an overview is given in Table 6.5[5]. Since there are 130 individual soil types to be identified within the South Holland study area, a selection is made to extract 30 representative soil types, which are presented in Table 6.5 and in Figure 6.33. The selection of these 30 representative soil types is based on the number of spatial joins that is obtained for each of these, and on their location with respect to the areas of expected shallow subsidence. In turn, the expected shallow subsidence is based on the grid cells classified with strong 'shallow' subsidence, i.e. colored as 'orange-to-red' (or $<$ -3 mm/yr), in Figures 6.31 and 6.32.
Note that in Table 6.5 the full soil names are only provided in Dutch, since these are specific to the country's geological setting. From the coded notation, provided in he first column, the capital letter denotes the main soil code, as listed in Table 4.9 of Chapter 4. As recalled from Chapter 4, the letter denoting the main soil code appears in various combinations with other attachments or prefixes and suffixes. These attachments elaborate on the soil properties, indicating for example the limestone content or information on the topsoil.
Aside from the first three non-soil type classes in Table 6.5, i.e. 'raised' (|c), 'buildings' (|h) and 'overland strip' (|i), the main soils are; 'swampy soils' (W), 'mollisol soils' (EK), 'marine clay' (M) and 'peat' (V). These are written in combination with various prefixes and suffixes. Locally dried layers in the upper soil layers are represented with the 'd' prefix. The suffixes 'g' (ripened) or 'o' (non-ripened) are used to further describe the swampy soils (W).
For the marine clay soils (M), the combination 'Mn' denotes the 'poldervaaggronden', which translates to clay soils in which periodically high groundwater levels occur (Wikipedia contributors 2019a). Additionally, Mn does not contain any peat within the upper 80 cm, nor any dark material in the topsoil (Wikipedia contributors 2019a). On the other hand, the suffix 'v' for marine clay soils indicates the presence of swampy material, deeper than 80 cm (de Vries, de Groot, et al. 2003). The marine clay soils (M) are often seen in combination with the prefix 'g', which indicates a low calcium-magnesium ratio ($<$10) (STIBOKA 1964), or the prefix 'p', which indicates a humus-rich topsoil. Furthermore, the suffixes 'A' and 'C' denote high and low limestone contents (respectively), as discussed in Chapter 4.
Lastly, the peat soils also show various combinations. The combination 'hV' refers to peat soils that have a topsoil with a maximum thickness of 50 cm, which contain 'clayey peat' or 'peaty clay' (Wikipedia contributors 2019a). The other combination 'kV' or 'waardveengronden' are peat soils with a shallow layer of heavy, limestone-poor clay with a maximum thickness of 40 cm (Wikipedia contributors 2019a). One instance of 'pV' is present in Table 6.5, which has a clay layer in combination with a $>$20 cm thick, dark humus-rich topsoil (Wikipedia contributors 2019a). The suffixes for peat represent the underlying peat layers and the vegetation from which these originate. The suffix 'c' denotes and underlying sedge-speat[6], reed-sedgespeat or mesotrophic (medium nutrient-rich) peat. For the suffix 'r', the underlying peat layer is a composed of reedpeat or sedges-reedpeat. Finally, for the suffix 'd', the underlying peat originates from 'bagger' (dredge material) and/or gyttja.

[5] The Bodemkaart includes combinations of the 'main' soil types (i.e. peat, sand, marine clay, river clay, loam, gravel, etc.) with other attributes, for example the limestone content, texture, etc. Additionally, a 'buildings' class is included, as seen in the nationwide results of Chapter 5.
[6] Sedges or 'carex' is a genus of grass-like plants, most commonly found in wetlands and marshes (Wikipedia contributors 2019b).

Soil Code	Meaning (NL)
|c OPHOOG	Opgehoogd of opgespoten
|h BEBOUW	Bebouwing
|i BOVLAND	Bovenlandstrook
AK	Kreekbeddingen
AWg	Warmoezerijgronden (gerijpt)
AWo	Warmoezerijgronden (ongerijpt)
dWo	Moerige eerdgronden (ongerijpt), (Plaatselijk verdrogende lagen in de bovengrond)
dWol	Moerige eerdgronden (ongerijpt), (Plaatselijk verdrogende lagen in de bovengrond) (Plaatselijk katteklei binnen 80 cm beginnend en tenminste 10 cm dik)
Wo	Moerige eerdgronden (ongerijpt)
EK19	Tuineerdgronden; lichte zavel, profielverloop 5, of 5 en 2, of 2
hVc	Koopveengronden op zeggeveen, rietzeggeveen of (mesotroof) broekveen
hVd	Koopveengronden op bagger, verslagen veen, gyttja of andere veensoorten
hVr	Koopveengronden op rietveen of zeggerietveen
kVc	Waardveengronden op zeggeveen, rietzeggeveen, of (mesotroof) broekveen
kVr	Waardveengronden op rietveen of zeggerietveen
pVc	Weideveengronden op zeggeveen, rietzeggeveen,of (mesotroof) broekveen
pVr	Weideveengronden op rietveen of zeggerietveen
Mn15A	Kalkrijke poldervaaggronden; lichte zavel, profielverloop 5
Mn25A	Kalkrijke poldervaaggronden; zware zavel, profielverloop 5
Mn35A	Kalkrijke poldervaaggronden; lichte klei, profielverloop 5
Mn35Av	Kalkrijke poldervaaggronden; lichte klei, profielverloop 5 Moerig materiaal beginnend dieper dan 80 cm en doorgaand tot dieper dan 120 cm
Mn45A	Kalkrijke poldervaaggronden; zware klei, profielverloop 5
Mn85C	Kalkarme poldervaaggronden; klei, profielverloop 5
Mv41C	Kalkarme drechtvaaggronden; zware klei, profielverloop 1
gMn83C	Knippige poldervaaggronden; klei, profielverloop 3
gMn83Cv	Knippige poldervaaggronden; klei, profielverloop 3 (Moerig materiaal beginnend dieper dan 80 cm en doorgaand tot dieper dan 120 cm)
pMn85A	Kalkrijke leek-/woudeerdgronden; klei, profielverloop 5
pMn85C	Kalkarme leek-/woudeerdgronden; klei, profielverloop 5
pMn86C	Kalkarme leek-/woudeerdgronden; klei, profielverloop 3, of 3 en 4 of 4
pMo80	Tochteerdgronden; klei

Table 6.5: Overview of the 30 soil type classifications representative of the South Holland study area. The listing of features presented in this table is based on de Vries, de Groot, et al. 2003.

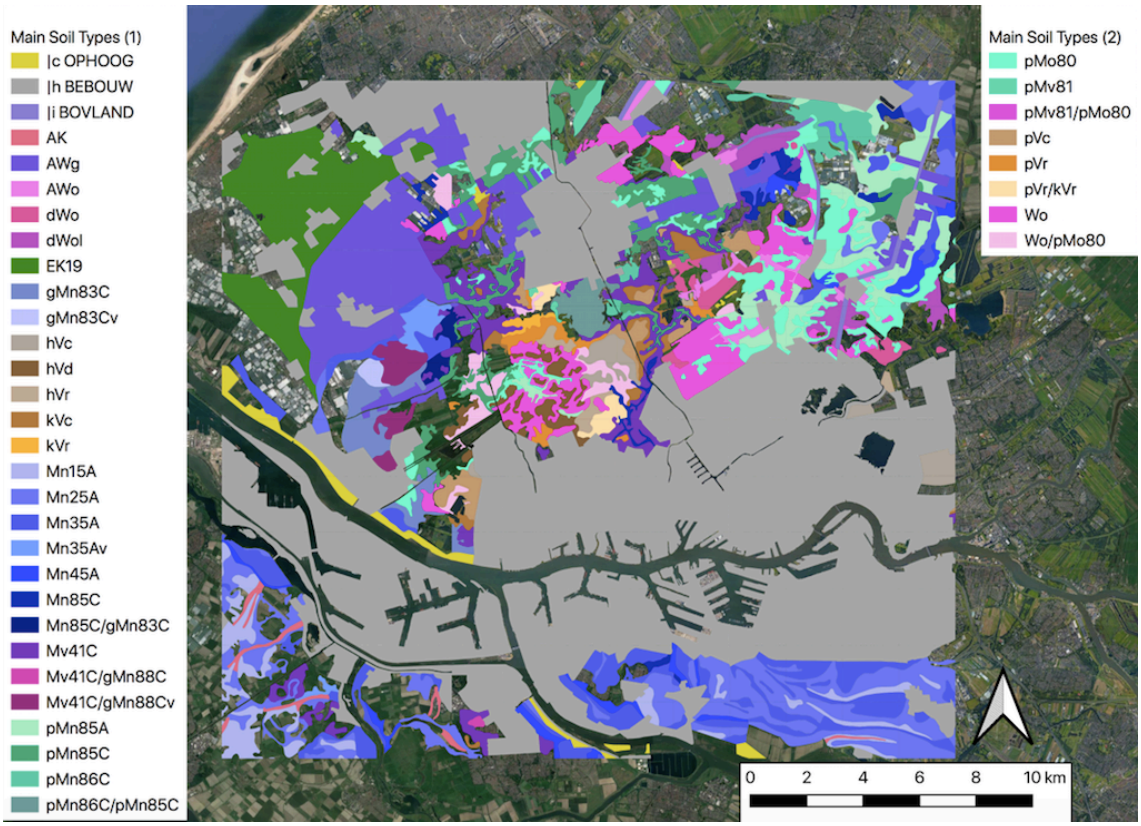

Figure 6.33: Map of the representative soil type classifications present in the South Holland study area. The listing of features presented in this map is based on de Vries, de Groot, et al. 2003.

Geomorphology

In addition to the various soil types in the South Holland, the area's geomorphology is used as contextual information. The geomorphology classifications originate from GKN, as presented in section 4.2.2. of Chapter 4. The 'form subgroup' attribute is used in this analysis, of which the different classes[7] are presented in Table 6.6 that are present in the South Holland study area (mapped in Figure 6.34).
All of the form subgroups are part of their respective 'form groups'. These are represented by the first letter of their codes in Table 6.6. For the South Holland study area, the form groups include isolated hills and ridges (B), plateau-like forms (F), non-fan-shaped slopes (H), hills and ridges with associated plains and lows (L), plains (M), and valley-shaped lows (R). For a full overview of all GKN form groups, the reader is referred to table 4.14 in Chapter 4.

Form Subgroup	Meaning (NL)	Meaning (EN)
B59	Stuifdijk	Drift dike
B71	Getij-inversierug	Tide-inversion ridge
B72	Getij-oeverwal	Tidal bank
B76	Strandwal	Coastal wall
B81	Veenrest-dijk	Peat-dike
B91	Terp of hoogwatervluchtplaats	Mound or high-tide refuges
B92	Storthoop	Landfill
F91	Plateau-achtige storthoop, opgespoten terrein of kunstmatig eiland	Plateau-like landfill, raised terrain or artificial island
H71	Zeestrandglooiing	Beach acclivity
L53	Kustduinen met bijbehorende vlakten en laagten	Coastal dunes with associated plains and lows
L72	Welvingen in plaatselijk gemoerde getij-afzettingen	Curvatures in locally moored tidal deposits
L74	Welvingen in getij-afzettingen	Curvatures in tidal deposits
L92	Kunstmatig gecreëerd reliëf voor recreatiedoeleinden	Artificial relief for recreational purposes
M72	Vlakte van getij-afzettingen	Plain of tidal deposits
M73	Vlakte van getij-riviermondafzettingen	Plain of tidal-delta deposits
M76	Ingesloten strandvlakte	Enclosed beach plain
M79	Aanwasvlakte	Accretion plain
M81	Ontgonnen veenvlakte	Reclaimed peat plain
M82	Ontgonnen veenvlakte met petgaten	Reclaimed peat plain with pits
M83	Veenrestvlakte	Peat-remain plain
M84	Boezemland, vlietland e.d.(moerassige vlakte)	Swampy plain (between flood defence & surface water)
M92	Vlakte ontstaan door afgraving en/of egalisatie van duinen of strandwallen	Plain originating from excavation and/or levelling of dunes or coastal walls
M93	Vlakte ontstaan door afgraving of egalisatie	Plain originating from excavation or levelling
R71	Getij-kreekbedding, zee-erosiegeul	Tide-creek bed, sea-erosion gully

Table 6.6: Overview of the GKN form subgroup classifications present in the South Holland study area. The listing of features presented in this table is based on WUR 2017.

[7] Note that the English translations of the Dutch GKN classifications are interpreted by the author. In some cases, the nuance or the exact meaning of the Dutch term is lost in translation. Therefore, the English translations are not fixed by any means, but rather interpretations of the Dutch term.

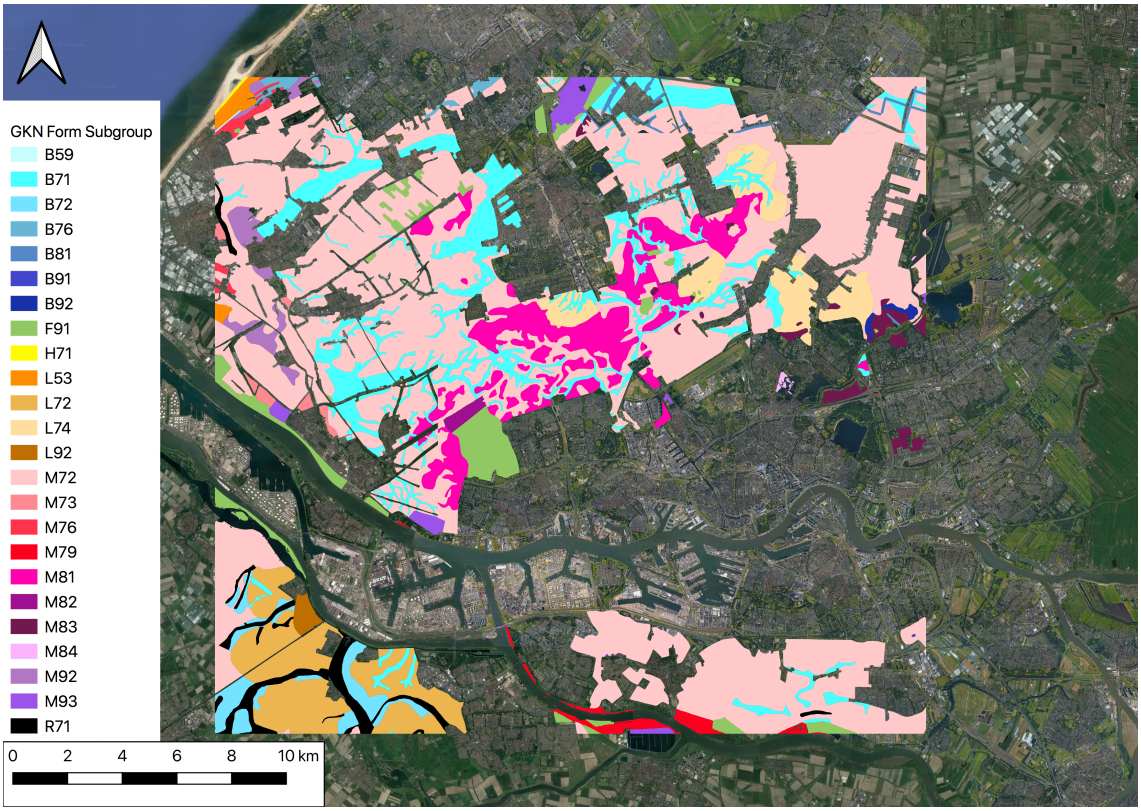

Figure 6.34: Map of the GKN form subgroup classifications present in the South Holland study area. The listing of features presented in this map is based on WUR 2017.

Buildings & Infrastructure

Information on the local buildings and infrastructure is provided in this case study from the Dutch BGT dataset, presented in Chapter 4. The BGT classifications include the basic objects and attributes that characterize the built environment, including the classes 'buildings', 'roads' (here, divided into 'road sections'), 'non-vegetated terrain' and 'vegetated terrain'.

Since most of the PSI points originate from buildings and infrastructure, a more local area is selected based on the results of the soil type and geomorphology analysis, presented later in this chapter. The extent of the South Holland study area shown in Figure 6.24 is useful for the analysis of the deformation with respect to the BRO soil type and geomorphology classifications, which are represented by large polygons. However for this study, it is too extensive for a complete deformation analysis of the BGT classifications. Therefore, a single 2 $\times$2 km grid cell is selected for further analysis. Grid cell F5, presented in Figure 6.35, is selected, because it contains a wide range of soil type and geomorphological landform (sub group) classes. In Figure 6.35, grid cell F5 is located to the west of Schipluiden and contains part of the A4 highway between Delft and Schiedam/Vlaardingen.

Some of the soil types in the South Holland study area show substantial differences in their total, deep and shallow deformation results. These soil types are of interest in the selection of a more confined study area for the inclusion of BGT classifications. For example the soil type 'kVr', which stands for 'Waardveengronden op rietveen of zeggerietveen' (peat soils with a shallow clay layer on reedpeat or sedges-reedpeat'), shows strong shallow subsidence. Thus, grid cell F5 is selected for the presence of shallow-subsiding soils (among others), and for its inclusion of stable infrastructure, which provide persistent scatterers.

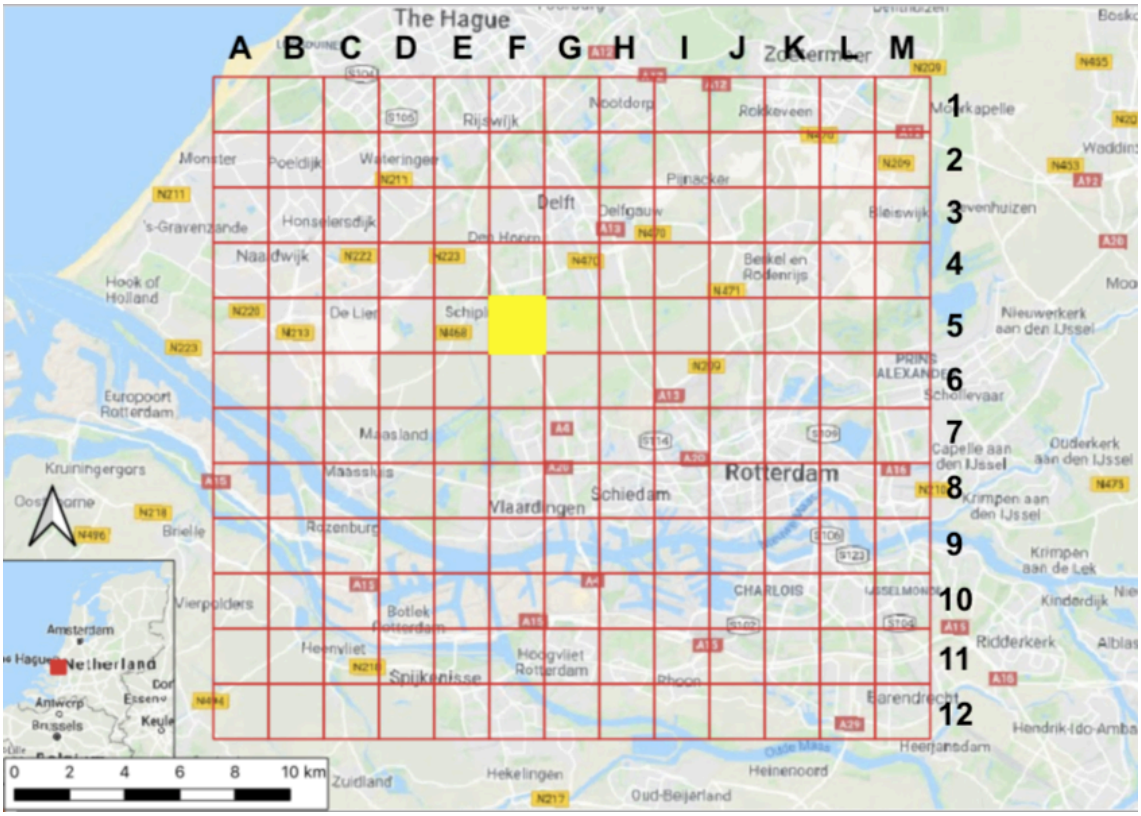

Figure 6.35: Selection of the grid cell F5 (yellow) for the buildings & infrastructure analysis, as part of the South Holland grid of the entire study area, composed of 156 grid cells (2 ×2 km) based on the grid cells implemented in Bodemdalingskaart 2018.

Most of the BGT objects are further categorized into different classes, with the exception of the buildings class. The classes that are identified in the F5 grid cell of the South Holland study area are summarized in Table 6.7. The BGT objects, i.e. the buildings, roads, non-vegetated and vegetated terrains, are mapped for grid cell F5 in Figure 6.37, covered by the linear deformation points of descending track 37. Additionally, the extent of the selected grid cell is shown in Figure 6.36 along with the soil type and geomorphology classifications within grid cell F5, shown respectively in Figures 6.38 and 6.39.

Object	Class (NL)	Class (EN)
Road section	Voetpad	Sidewalk
	Transitie	Transition
	Rijbaan lokale weg	Local roadway
	Rijbaan autoweg	Roadway
Rijbaan autosnelweg	Highway	
	Parkeervlak	Parking space
	OV-baan	Public transportation road
	Fietspad	Bike lane
Building	-	-
Non-vegetated terrain	Open verharding	Open pavement, e.g. tiles
	Gesloten verharding	Closed pavement, e.g. asphalt or concrete
	Erf	Property, e.g. yardland, courtyard, curtilage
Vegetated terrain	Groenvoorziening	Green spaces, e.g. parks
	Grasland (overig)	Grassland (other)

Table 6.7: Overview of the BGT classifications present in the F5 study area of the South Holland case study. The listing of features presented in this table is based on Ministerie van Infrastructuur en Milieu 2013.

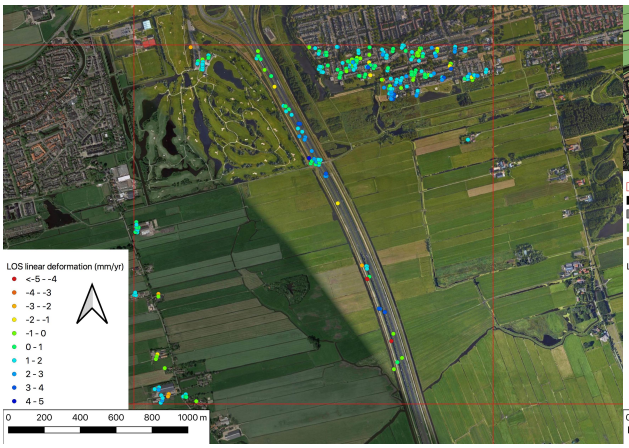

Figure 6.36: Extent of the F5 grid cell.

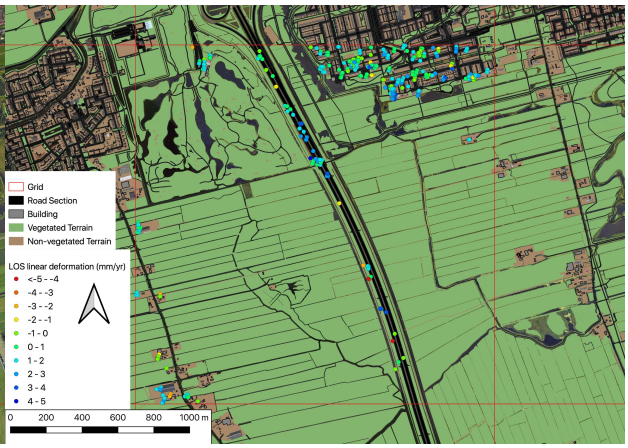

Figure 6.37: Geography classification of the F5 grid cell.

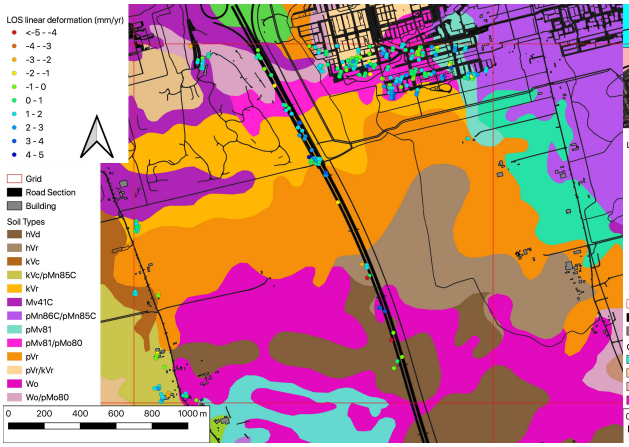

Figure 6.38: Soil type classification of the F5 grid cell.

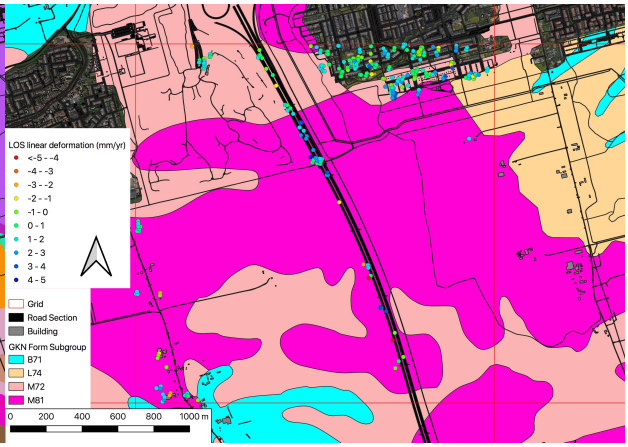

Figure 6.39: Geomorphology classification of the F5 grid cell.

6.2.4. Method

The deformation analysis of the South Holland case study is divided in two parts with different results. The first part of the deformation analysis uses the grid cell representation from Bodemdalingskaart 2018 and its definition of 'total', 'deep' and 'shallow' deformation (from tracks 37 and 110) within the study area, as presented in Figures 6.27 to 6.32. The soil type and geomorphology classes are used as

auxiliary information to enrich the grid cells. Subsequently, the deformation statistics for each of these classes are presented and compared in Section 6.2.5. in terms of their corresponding 'total', 'deep' and 'shallow' components.
For the second part of the South Holland deformation analysis, grid cell F5 is selected for further study with the geography datasets from BGT alongside the soil type and geomorphology classes. As opposed to the first part of the South Holland deformation analysis, the attribute enrichment and output presentation in the second part of the analysis use the PSI points themselves (as in the nationwide and South Limburg analyses) instead of the Bodemdalingskaart 2018 statistical definitions of total, deep and shallow subsidence. The deformation results are presented in relation to the the buildings (and infrastructure) (Figure 6.37), the soil type (Figure 6.38) and the geomorphology (Figure 6.39) of the area represented by grid cell F5.
The attribute-enrichment and output presentation procedures for both parts of the deformation analysis are discussed in the following subsections.

Attribute-Enrichment

The attribute-enrichment, as implemented with the database approach discussed in Chapter 4, is performed in the mapping environment, i.e. QGIS for this study, by means of spatial joins. As recalled from Chapter 4, the process of spatial join relies on the definition of the topological relation between the two vector layers that are to be joined.
For the first part of the South Holland deformation analysis, spatial joins are performed between entire grid cells and the soil type and geomorphology polygons. For the linking between polygons, i.e. the grid cells and the auxiliary vector 'join' layers, the geometric predicate specifies that the join layer 'intersects' with, 'contains' or is situated 'inside' the target layer. For a spatial join between a line and a polygon, the line is required to overlap with the polygon or to be situated fully inside of it.
In the second part of the South Holland deformation analysis, the spatial joins involve the topological relations of points, i.e. the PSI data, 'inside' of a polygon, i.e. the auxiliary classifications. The extent of the F5 grid cell has no further influence on this part of the study, aside from serving as a clipping vector layer to define the area of interest.

Deformation Analysis

The output presentation in both parts of the South Holland deformation analysis relies on the the linear deformation (mm/yr) of descending tracks 37 and 110.
In the first part of the deformation analysis, after the attribute-enrichment of the grid cells themselves, the total, deep and shallow deformation are presented per contextual soil type and geomorphology class in a sequence of bar graphs (with the deformation shown along the y-axis). This is repeated for both samples, i.e. tracks 37 and 110. Note that in the output presentation, the deep deformation (median) and shallow deformation (10th percentile - median) per class do not necessarily add up to the total deformation (10th percentile) per class. The reason for this is that the different polygons of a particular class, e.g. the soil type 'kVr', can be present within different grid cells, each having different values for their total, deep and shallow deformation. Since every spatial join is stored in the database, there is no single value to be shown per class in the output presentation. Rather the median of the stored deformation values is computed separately for the total (10th percentile), deep (median) and shallow (10th percentile - median) components per class.
The second part of the deformation analysis makes use of the descriptive statistics of the PSI points, i.e. linear deformation (mm/yr) that are classified under the same category, e.g. 'kVr', within the selected grid cell (F5). This approach is the same as the one used in the nationwide analysis and the South Limburg case study. The output presentation is also resembles the output of the nationwide analysis, as a sequence of boxplot or 'whisker plots', computed per class, i.e. of the Bodemkaart, GKN an BGT datasets. For an in-depth overview of the whisker plot output presentation, the reader is referred to Section 4.3.6.

6.2.5. Deformation Analysis 1 – South Holland

The first part of this case study's deformation analysis provides the results of the linear deformation in the context of the representative soil type and geomorphology classifications, as presented in Tables 6.5 and 6.6 and Figures 6.33 and 6.34.

Soil Type

The deformation results of the 30 representative soil types, identified in the full extent of the South Holland case study area, are presented (in sequence) in Figure 6.40 for descending track 37 and in Figure 6.41 for descending track 110. For the total, deep and shallow LOS linear deformation results (in track 37) of the full list of soil type classes identified in the South Holland case study area, the reader is referred to Figure E.1 in Appendix E.

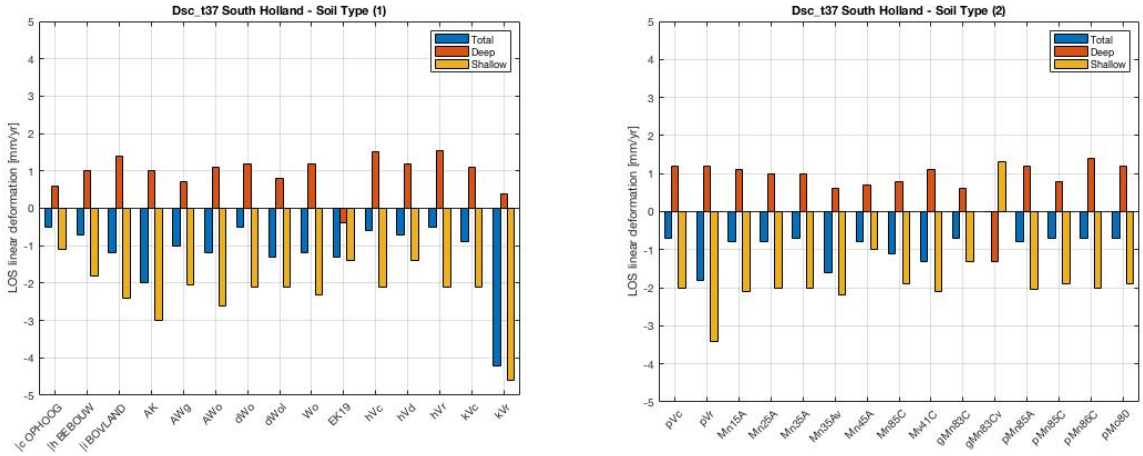

Figure 6.40: Descending track 37: Total, deep and shallow LOS linear deformation of the 30 representative South Holland soil types (data: SkyGeo).

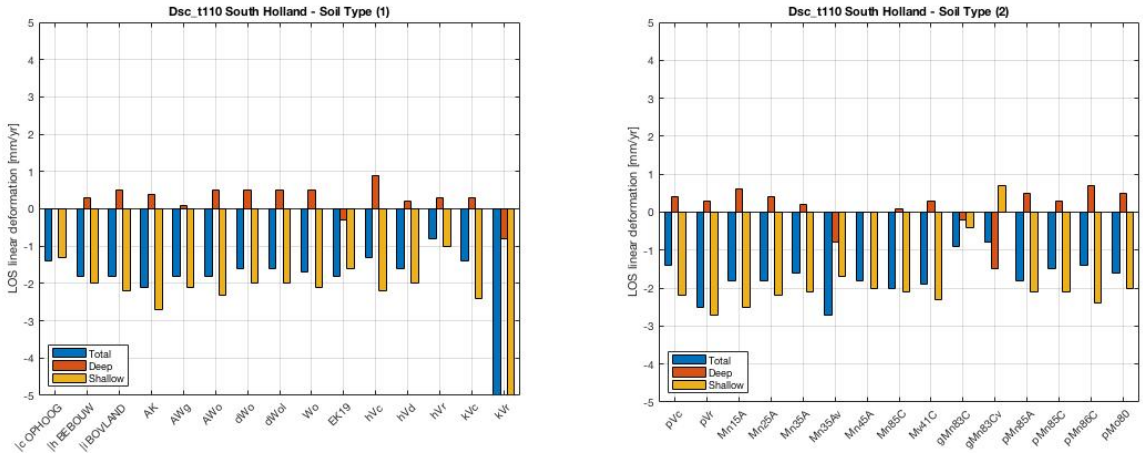

Figure 6.41: Descending track 110: Total, deep and shallow LOS linear deformation of the 30 representative South Holland soil types (data: SkyGeo).

The linear deformation results of the South Holland study area show for nearly all soil types the same general pattern of negative total deformation, negative shallow deformation and positive deep deformation. Only the soil gMn83Cv (low-calcium marine clay soil with high GWT and swampy material) shows positive shallow deformation. Combined with its negative deep deformation, this results in slightly negative-to-zero total deformation. Additionally, the soil EK19 (finesand-to-clay soils with a thick humusrich topsoil) shows slightly negative deep deformation, considering its total deformation slightly exceeds its shallow deformation response, as seen in track 110. Similar (slightly) negative deep deformation is observed in track 110 for the soils kVr (peat soils with a shallow layer of heavy, limestone-poor clay, and an underlying sedges-reedpeat layer), Mn35Av (lime-rich clay soils with occasional high groundwater levels), gMn83C (low-calcium marine clay soil), and its variant gMn83Cv (low-calcium marine clay soil with high GWT and swampy material).
No clear differences are observed between the 'main' soil groups, i.e. swampy soils (W), marine clay (M) and peat (V) in the magnitude of their total, deep and shallow deformation responses. Overall, peat shows the highest level of heterogeneity in the deformation of its sub-classifications. In two instances

the 'Vr' soil types (peat with an underlying layer of reedpeat or reed-sedgespeat), i.e. pVr and kVr, show the highest level of shallow subsidence. Observed in track 110, kVr shows shallow subsidence of -8.9 mm/yr and total subsidence of -9.7 mm/yr[8]. The validity of the kVr deformation results are questionable. From a posterior check in the mapping environment, the kVr classification only appears as a relatively small polygon, overlapping only with two grid cells, i.e. E5 and F5, thus negatively skewing its deformation distribution.
Furthermore, the deformation of the buildings class, which has the largest sample size, is in line with the other deformation results in terms of its magnitude and the relation between its total, median and shallow deformation.

Geomorphology

Similar to the soil type classes, the GKN landform subgroup classes are attributed to the grid cells of the South Holland area. The results of the total, deep and shallow deformation results linked to the geomorphology classes of the South Holland case study area can be found in Figure 6.42 for descending track 37 and in Figure 6.43 for descending track 110.

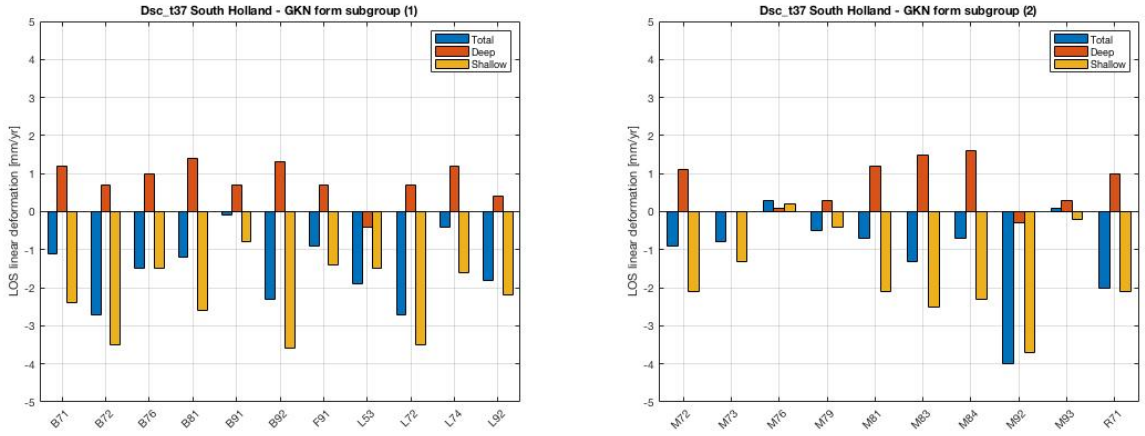

Figure 6.42: Descending track 37: Total, deep and shallow LOS linear deformation of the South Holland geomorphology landform subgroups (data: SkyGeo).

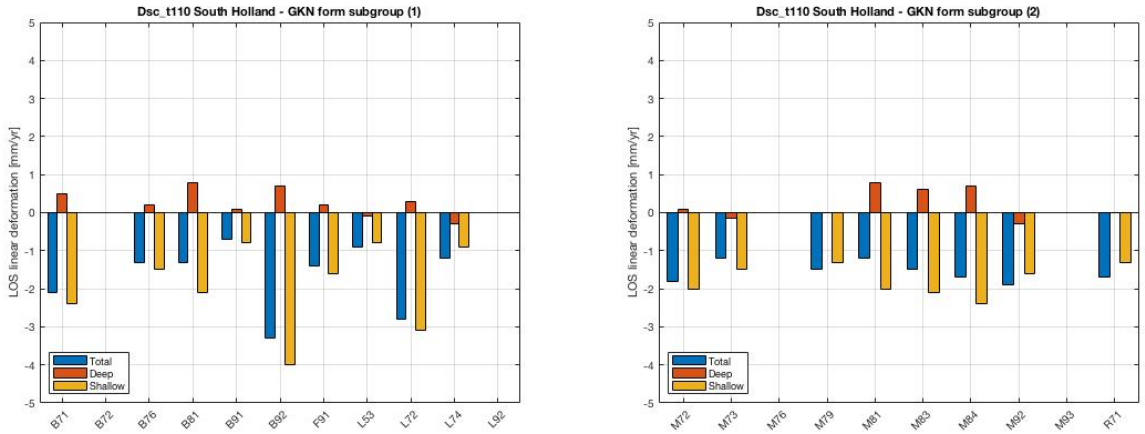

Figure 6.43: Descending track 110: Total, deep and shallow LOS linear deformation of the South Holland geomorphology landform subgroups (data: SkyGeo).

The overall trend of negative total deformation, positive deep deformation and negative shallow deformation is present for most of the geomorphology classes. However, there are some exceptions to this trend. For example, in the form subgroup M76 (enclosed beach plain) slight positive deformation

[8]For this single instance, the y-axis was not adjusted to this extent to keep the current (uniform) level of detail for the majority of the deformation results.

is observed for the total and shallow deformation components (in track 37). Positive total deformation is also observed for M93 (Plain originating from excavation or levelling).
There are no clear differences observed in terms of the deformation between the different form groups (which contain the form subgroups), i.e. B, F, L, M and R. Within the frequently recurring form groups, i.e. B (isolated hills and ridges), L (hills and ridges with associated plains and lows) and M (plains), the form subgroups vastly differ from each other in the magnitude and ratio between deep and shallow deformation. For example, the form subgroup B92 (landfill) behaves more extremely in its negative shallow deformation (-3.5 to -4 mm/yr) and positive deep deformation (+0.8 to +1.2 mm/yr) compared to the form subgroup B91 (Mound or high-tide refuges), of which both deformation trends are close to zero. In the form group L (hills and ridges with associated plains and lows), the form subgroup L72 (curvatures in locally moored tidal deposits) shows the strongest negative shallow deformation in both tracks. In descending track 37 the form subgroup M92 (Plain originating from excavation and/or levelling of dunes), as part of form group M (plains), shows the strongest negative shallow deformation (-3.7 mm/yr). However, this shallow deformation 'extreme' is not observed in descending track 110. The cluster of peat and swampy plains, i.e. M81, M83 and M84, show similar behaviour in their deformation, with their shallow components between -2 and -2.5 mm/yr.

6.2.6. Deformation Analysis 2 – Grid Cell F5

The second part of the deformation analysis presents the results of the deformation per attribute, i.e. soil type, geomorphology, buildings and infrastructure, within the extent of grid cell F5, as depicted in Figure 6.36. Similar to the nationwide analysis, the linear deformation results stem from the relations between the individual PSI points and the auxiliary polygons and these are presented (for all classes) in a sequence of boxplots, presented in Figure E.2 for descending track 37 and in Figure 6.45 for descending track 110.

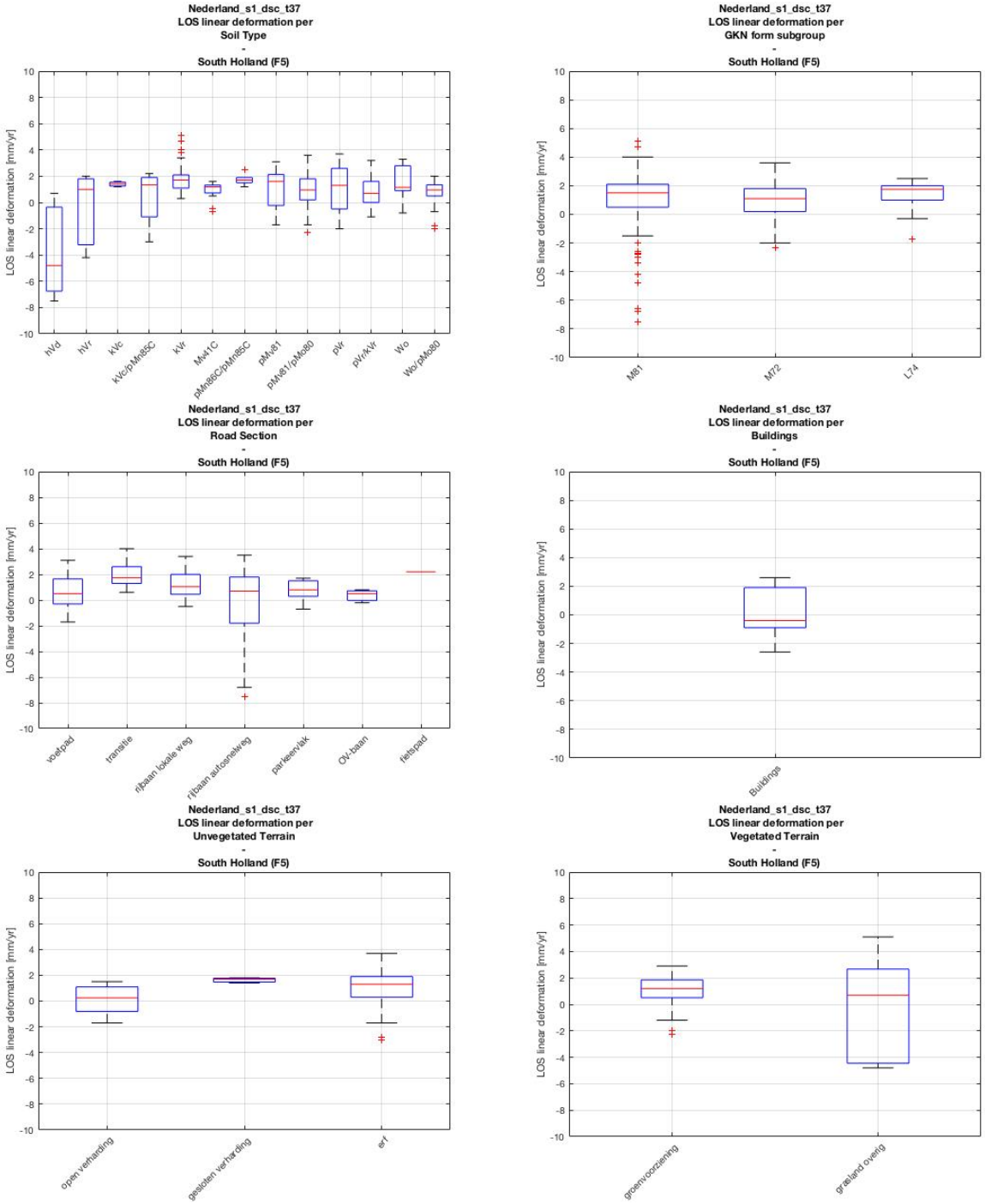

Figure 6.44: Descending track 37 for the South Holland case study area F5: LOS linear deformation (mm/yr) of the following classes: soil type, GKN form subgroup, road section, buildings, non-vegetated terrain, and vegetated terrain (data: SkyGeo).

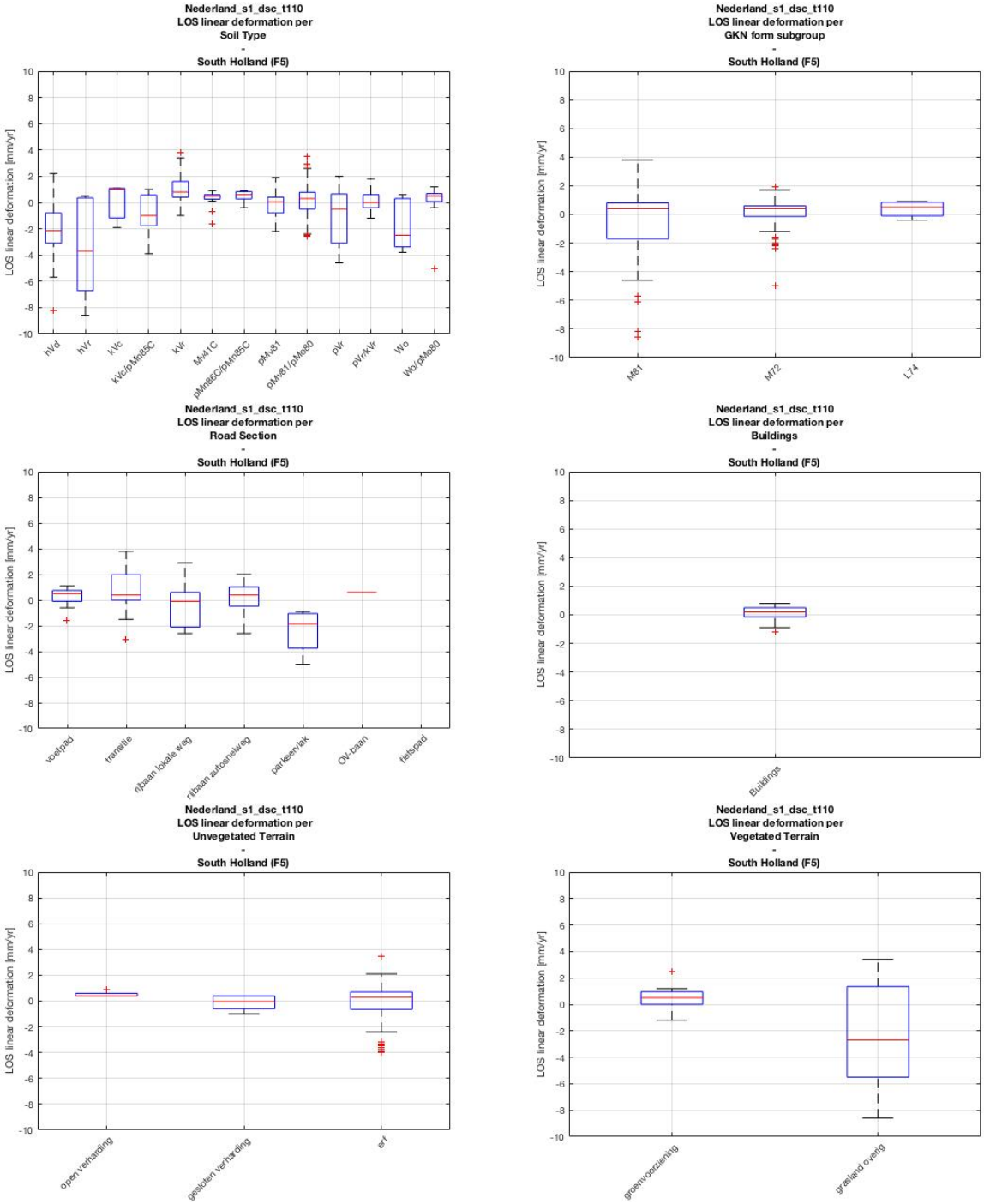

Figure 6.45: Descending track 110 for the South Holland case study area F5: LOS linear deformation (mm/yr) of the following classes: soil type, GKN form subgroup, road section, buildings, non-vegetated terrain, and vegetated terrain (data: SkyGeo).

Of all the different soil types identified in grid cell F5, hVd (peat with a 'clayey peat' or 'peaty clay' topsoil and an underlying layer of peat that originates from 'bagger' (dredge material) and/or gyttja) shows the strongest subsidence in track 37 with a median of about -4.8 mm/yr, and the lower edge of the distribution around -7.5 mm/yr. In descending track 110 the soil type that shows the strongest subsidence in grid cell F5 is hVr (peat with a 'clayey peat' or 'peaty clay' topsoil and an underlying layer of reedpeat or sedges-reedpeat) with its median at about -3.8 mm/yr and its lower edge at about -8.6 mm/yr. In Figure 6.38 the PSI points contained by the hVd and hVr soil polygons originate from a road section, i.e. the A4 highway, in the southern part of grid cell F5. This is in line with the deformation results of track 37, classified under 'highway' in the road section attributes of BGT. Even though the part of the A4 highway in grid cell F5 shows slightly positive median linear deformation, its track 37 distribution is negatively skewed, with the bottom-end reaching about -6.7 mm/yr (not considering the outlier at about -7.5 mm/yr). However, in track 110 the distribution of the deformation for the highway stays centered around 0 mm/yr.
Furthermore, most of the highway in grid cell F5 and the associated PSI points are classified under the geomorphology form subgroup M81 (reclaimed peat plain) in Figure 6.39. This is reflected in the distribution of M81, which shows the most negative outliers in both tracks. Many PSI points originate from many buildings and infrastructure in the northeastern part of grid cell F5, i.e. Tanthof-West. The 'buildings' and 'non-vegetated terrain' distributions of the deformation, containing most of the northeastern 'cluster' of points, are centered around 0 mm/yr and lean slightly more towards positive deformation in track 37, while showing mostly negative outliers in track 110.

6.2.7. Discussion

The deformation analysis of the South Holland case study is performed in two parts, resulting in different types of output. The first part of the deformation analysis focuses on the distinction between the Bodemdalingskaart 2018 statistical definition of total, deep and shallow deformation. These definitions are implemented in a grid cell representation to characterize the deformation within the defined study area. The grid cells are enriched with their coinciding soil type and geomorphology attributes. Subsequently, the soil type and geomorphology classifications are compared in terms of their coupled deformation, i.e. divided in the total, deep and shallow components. In the second part of the South Holland deformation analysis, the PSI points within grid cell F5 are attribute-enriched with buildings and infrastructure attributes, as well as (again) soil type and geomorphology attributes. Grid cell F5 is of selected for its heterogeneity in soil types (without 'buildings' classes), landforms, buildings and infrastructure.

Deformation Analysis 1 – South Holland

The soil types and landforms in South Holland are characterized by strong shallow subsidence and slight upward deep deformation. This results in total subsidence, which is generally lower in magnitude than its shallow component, due to the mild upward deep deformation component. However, since the PSI points in track 37 deviate from the spatial reference (taken as the track mean) by +0.47 mm/yr (based on table 4.17), there is an offset in the positive LOS direction (towards the satellite). If corrected for, the upward total deformation would still be observed, but to a lesser extent. Additionally, this means that the estimated shallow and deep subsidence are actually slightly underestimated. Since track 110 has an offset from the spatial reference of only -4.23 $\times 10^{-3}$, it provides a more accurate representation of the total, deep and shallow subsidence in the South Holland study area.
Furthermore, no major differences are observed between the most identified main soil groups, i.e. swampy soils (W), marine clay (M) and peat (V), and between the most identified landform groups, i.e. isolated hills and ridges (B), hills and ridges with associated plains and lows (L) and plains (M), in terms of one group showing (on average) more or less subsidence compared to the other. Differences in deformation are rather observed in the variability within these groups. The most difference in deformation is observed in terms of their 'sub-characteristics', i.e. the topsoil and underlying soil characteristics, the lime content, any GWT fluctuations and the overall deposition environments. Note that this part of the deformation analysis has not yet taken into consideration any other contextual characteristics, such as the buildings and infrastructure attributes. Therefore, the more localized deformation analysis for a particular grid cell, i.e. grid cell F5, aims to include a wider variety of attributes.

Deformation Analysis 2 – Grid Cell F5

Within grid cell F5, shown in Figures 6.36 to 6.39, the different attributes, i.e. buildings, infrastructure, soil type and geomorphology, are directly compared in terms of their deformation and their location. For example, knowing that the polygons of the road section, e.g. the A4 highway, intersects with the polygons of the peat soils hVd and hVr, and the polygon for the reclaimed peat plain landform subgroup M81, their deformation distributions can directly be compared. Roads are in general very useful for the analysis of deformation in the more 'remote' areas with little to no buildings. The 'road'-classified PSI points reflect the deformation of the different soil types present in these areas, without being given the Bodemkaart label 'buildings'. This, in part, motivates the location of the selected grid cell F5 and the selection of any (future) research area. The characterization of urban areas, represented in the Bodemkaart with 'bebouwing' (built environment) polygons, require more in-depth classifications in order to accurately distinguish between the different reflection objects. The inclusion of elevation data from AHN and the BAG (address) registry would be useful for this distinction.
As an alternative type of output presentation, Appendix E.2. presents an overview of the deformation observed in track 37 for all the combinations of overlapping polygons of the attributes identified in grid cell F5. This brings the advantage of more direct comparisons to be made between the classes of 'clustered' or grouped attributes. However, already for a relatively confined area, i.e. 2 $\times$2 km for a typical grid cell, this leads to an extensive set of results, e.g. 84 identified class-combinations in grid cell F5. The number of combinations depends on the number of datasets used, the number of attributes within a dataset, the number of possible classifications for a particular attribute, and the extent of the study area. This makes the interpretation of the results quite difficult, and requires a lot of repetition. This could alternatively be dealt with by sorting the combinations based on the magnitude of their observed deformation. Ideally, the process of identifying and extracting the 'relevant' combinations would be automated in a script or function.

6.3. Groningen – Natural Gas Extraction

Similar to the South Holland case study, the Groningen case study focuses on the differentiation between total, shallow and deep subsidence. As predominantly shallow subsidence is observed in the South Holland case study, deep subsidence is presumed to be the abundant in the Groningen case study. Again, the statistical Bodemdalingskaart 2018 terminology is used for the grid representation of deformation in the area. In the first part of the Groningen deformation analysis, deep subsidence is described by the median per grid cell, total subsidence by the 10th-percentile, and shallow subsidence by the difference between the two. In the second part of the Groningen deformation analysis the statistics of the PSI points distributions themselves are presented in the context of all three auxiliary sources, i.e. soil type, geomorphology and geography (buildings and infrastructure).
First, a short background is given on the Groningen case study area. Subsequently, the selected Sentinel-1 PSI datasets are introduced along with the grid cell representation of the study area, based on Bodemdalingskaart 2018. The corresponding auxiliary datasets for the case study area are introduced as well. Since the same methods are applied in the attribute-enrichment and the deformation analyses as in the South Holland case study, these are discussed in lesser detail. Finally, the deformation results of the two analyses are presented and discussed.

6.3.1. Background

As mentioned in Chapter 2, the natural gas reserves of the Netherlands are mainly situated in the province of Groningen, and partly below the North Sea. The gas is stored in porous source rocks from the Permian Rotliegend, some 3 to 4 km below the surface (TU Delft 2014). Since the NAM started production in 1959, approximately 3582 billion m^3 (80%) of the gas has been extracted in the Netherlands, with approximately 940 billion m^3 left by 2015. This could potentially provide the country for another 17 years, assuming the same rate of extraction (CBS 2016).
In Bodemdalingskaart 2018 the bowl of deep subsidence is clearly present in the Groningen case study area. The prognosis by NAM n.d.(b) is that the subsidence by 2050, as a consequence of gas extraction, will amount to maximally 40 to 50 cm in Loppersum. In the period of 1972 to 2013, the total amount of subsidence extended up to 30cm in the same area (NAM n.d.[b]). In addition to the deep subsidence, the gas extraction leads to earthquakes. Of the 1369 earthquakes recorded in the Groningen gas field between 1986 and 2020, 40 had a magnitude of more than 3 on Richter's scale (NAM n.d.[a]).

6.3.2. PSI Datasets

The Groningen case study uses the Sentinel-1 PSI datasets, presented in Chapter 4, as the primary dataset in the implementation of the database approach, also presented in Chapter 4. First the PSI track selection is discussed, followed by the presentation of the grid cell representation of total, deep and shallow deformation.

Track Selection

Following the motivation for the selection of two Sentinel-1 PSI tracks (between 2015 and 2019) in the South Holland case study (Section 6.2.2), the selection of PSI data for the Groningen case study includes ascending track 15 and descending track 37. The latter is used in the South Holland case study, and once again selected in this study for direct comparison between the two areas, thus excluding any inconsistencies between the tracks, i.e. in terms of spatial reference, ascending/descending orbits, etc. Furthermore, the PSI data from ascending track 15 is selected as the second primary dataset for its coverage of the Groningen and its relatively low deviation, i.e. 1.16 $\times 10^{-1}$ mm/yr in Table 4.17, from the spatial reference (computed as the mean of all PSI points in a particular track).

Grid Representation

As seen from the grid representation of the study area in Figure 6.46, the study area is set to include various classes, responding differently to any type of deformation in the area, referred to as the 'subsidence bowl'. The city of Groningen provides a high point density, while being situated within the affected area, i.e. the subsidence bowl, and is therefore include in the study area. The linear deformation points of the Groningen study area are presented in Figure 6.47 for ascending track 15 and in Figure 6.48 for descending track 37.

The Groningen study area contains less points compared to the South Holland project area. This is influenced by the precise delimination of the study area. However, the main reason for the lower number points is the overall lower population density in the Groningen province, i.e. 583,990 over 2960 km^2 (CBS 2019), compared to the province of South Holland, i.e. 3.67 million over 3403 km^2 (CBS 2019). Therefore, less buildings and infrastructure are present over a comparable area. Most of the PSI points in the study area originate from buildings and infrastructure in the city of Groningen and a number of smaller communities, which are situated closer to the subsidence bowl. Even though these areas have a lower point density, they are essential for the study of the deep subsidence taking place at the gas fields.

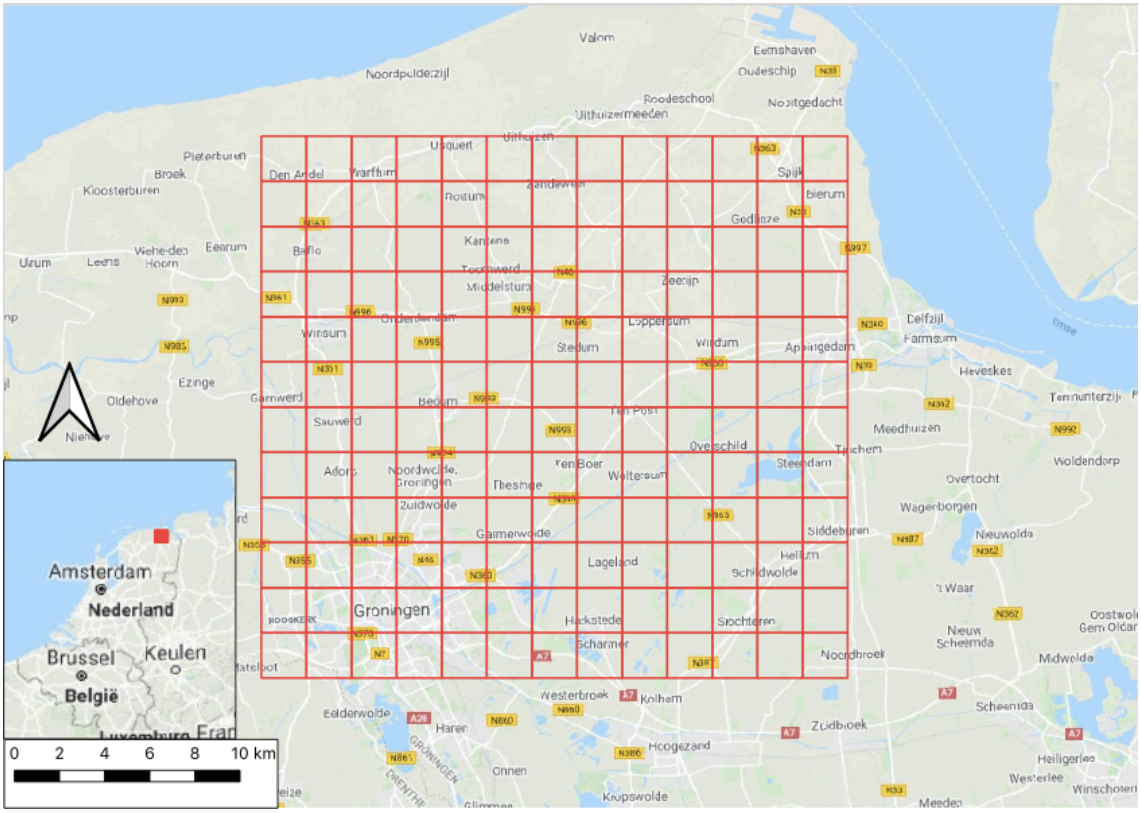

Figure 6.46: Grid of the Groningen study area composed of 156 grid cells (2 ×2 km), based on the grid cells implemented in Bodemdalingskaart 2018

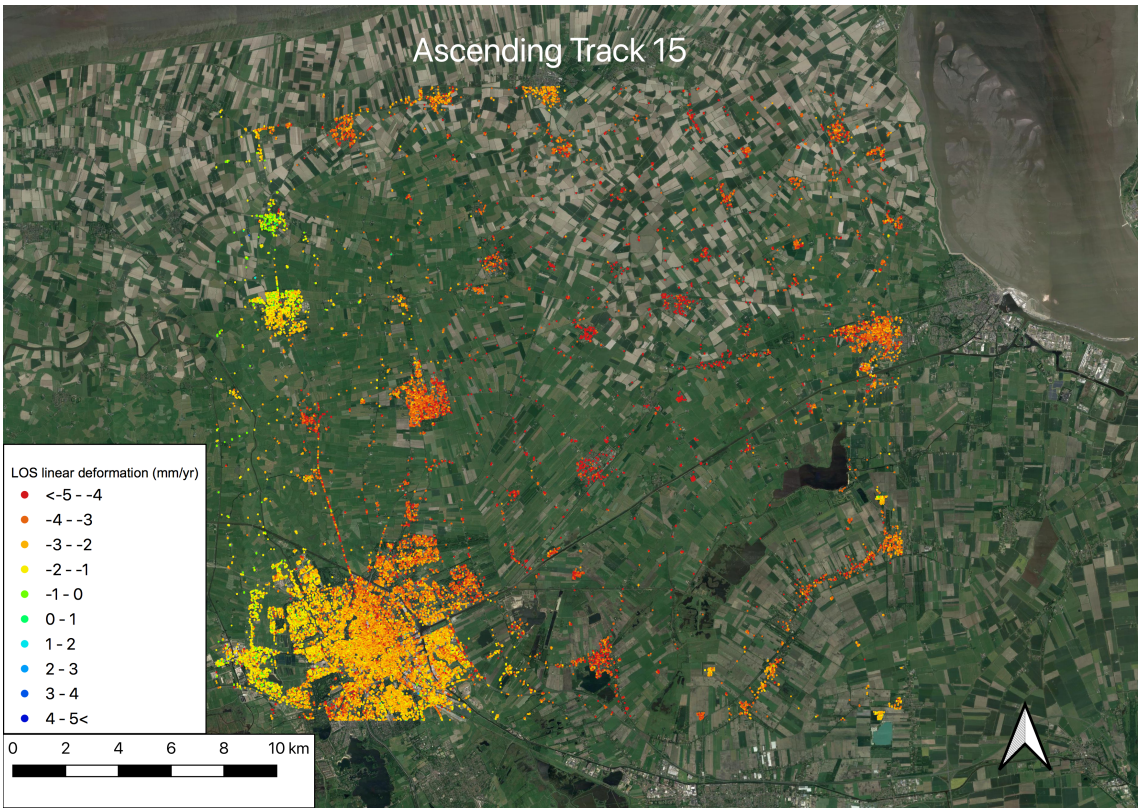

Figure 6.47: S1 Ascending Track 15: LOS linear deformation (mm/yr) in the Groningen study area (data: SkyGeo).

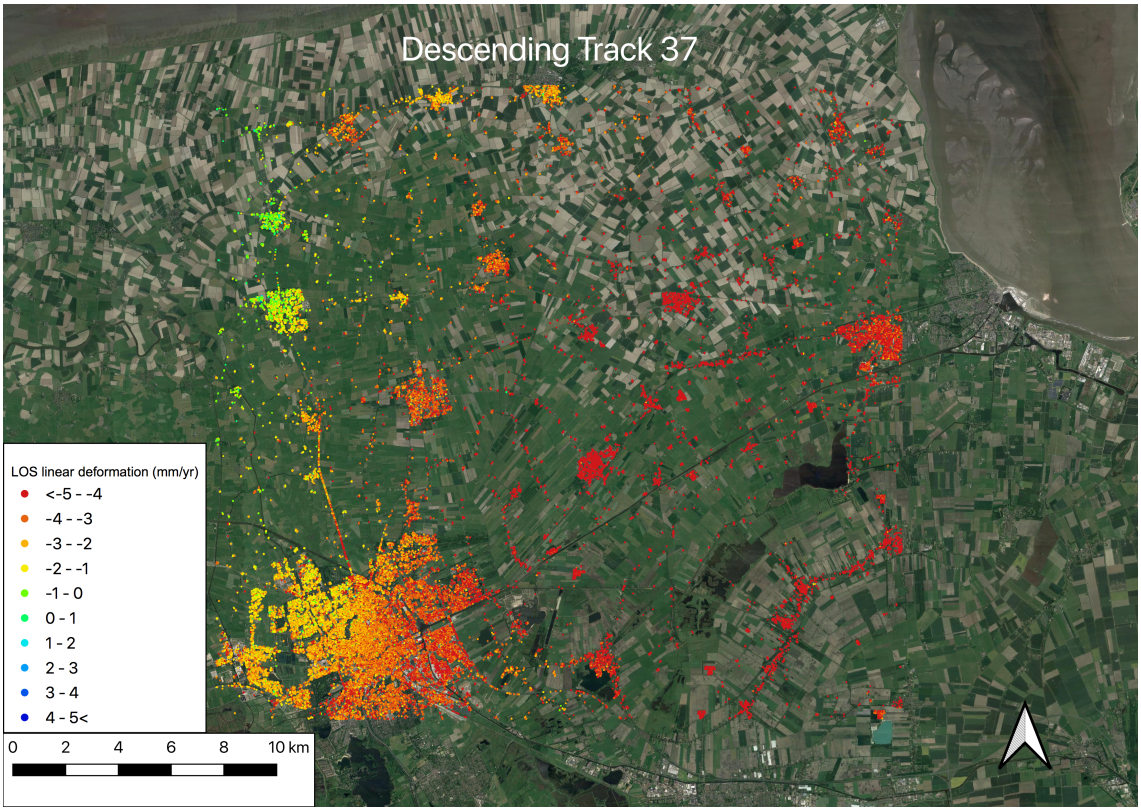

Figure 6.48: S1 Descending Track 37: LOS linear deformation (mm/yr) in the Groningen study area (data: SkyGeo).

Total, Deep and Shallow Deformation

Following the grid cell approach in Bodemdalingskaart 2018, the deformation in the Groningen study area can be interpreted over low point-density areas. The heterogeneity in the point density of the case study area is reflected in the positions of the scatterers in Figures 6.47 and 6.48. The same method is implemented as for the South Holland case study to obtain the total, deep and shallow deformation values per grid cell, computed as the 10th-percentile, the median, and the difference between these.
The resulting deformation grids are presented in the following sets of figures. For descending tracks 37 and 110, Figures 6.49 and 6.50 show the total linear deformation, Figures 6.51 and 6.52 show the deep linear deformation, and lastly Figures 6.53 and 6.54 show the shallow deformation per individual grid cell.

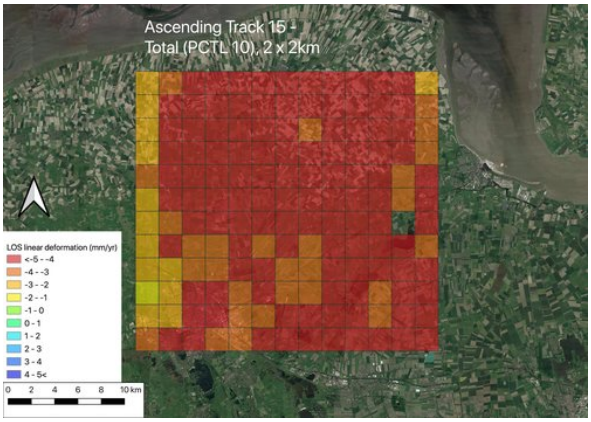

Figure 6.49: S1 Ascending Track 15: Grid of the 'total' (10th-percentile) Linear LOS deformation (mm/yr) within 2 ×2 km grid cells covering part of Groningen (data: SkyGeo).

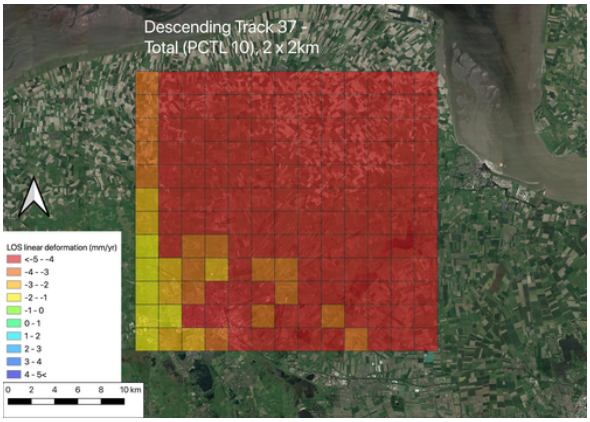

Figure 6.50: S1 Descending Track 37: Grid of the 'total' (10th-percentile) Linear LOS deformation (mm/yr) within 2 ×2 km grid cells covering part of Groningen (data: SkyGeo).

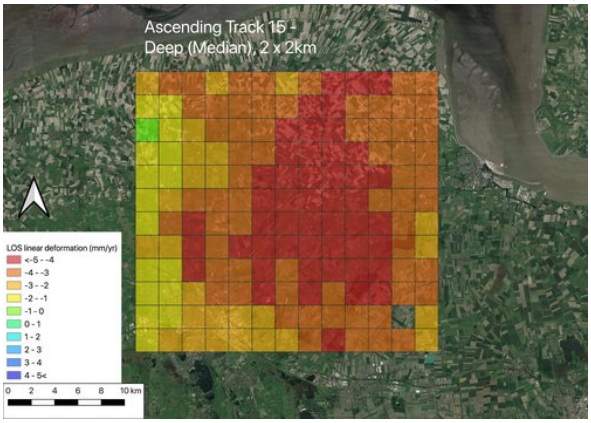

Figure 6.51: S1 Ascending Track 15: Grid of the 'deep' (median) Linear LOS deformation (mm/yr) within 2 ×2 km grid cells covering part of Groningen (data: SkyGeo).

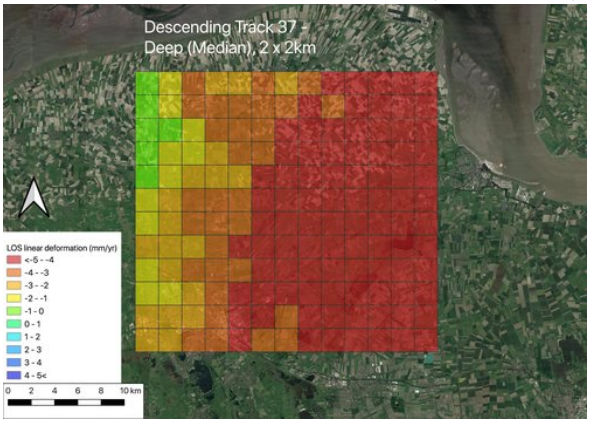

Figure 6.52: S1 Descending Track 37: Grid of the 'deep' (median) Linear LOS deformation (mm/yr) within 2 ×2 km grid cells covering part of Groningen (data: SkyGeo).

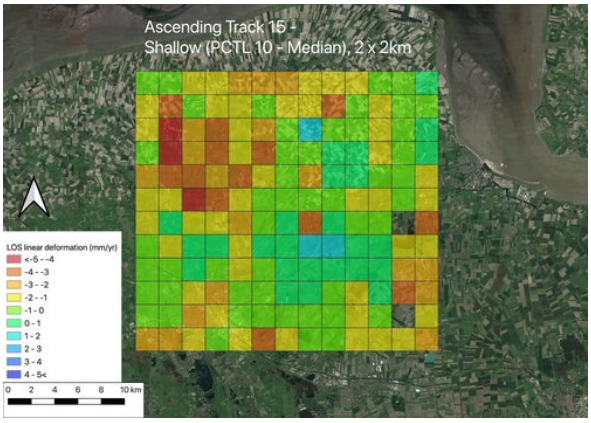

Figure 6.53: S1 Ascending Track 15: Grid of the 'shallow' (10th-percentile - median) Linear LOS deformation (mm/yr) within 2 ×2 km grid cells covering part of Groningen (data: SkyGeo).

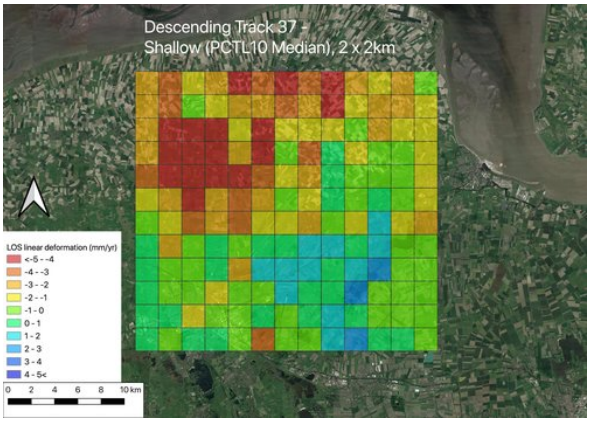

Figure 6.54: S1 Descending Track 37: Grid of the 'shallow' (10th-percentile - median) Linear LOS deformation (mm/yr) within 2 ×2 km grid cells covering part of Groningen (data: SkyGeo).

6.3.3. Auxiliary Datasets

The deformation grids and points are enriched in the same manner as in the South Holland case study with auxiliary information from the Bodemkaart, GKN and BGT datasets. As such, their respective soil type, geomorphology and building (and infrastructure) classifications are introduced in the following (sub)sections.

Soil Type

Based on the soil type classes with the most spatial joins (relations) to the grid cells in Figure 6.46 and their location with respect to the deep subsidence bowl, the representative soil type classes in the Groningen study area are listed in Table 6.8. Additionally, the different soil type classes are mapped in Figure 6.55.

Aside from the first three entries in Table 6.5 that are not soil types, i.e. 'raised' (|c), 'mound' (|f) and 'buildings' (|h), the main soils are; 'peat' (V), 'podzolic soils' (H), 'marine clay' (M), 'swampy soils' (W) and 'sand' (Z). As in the South Holland case study, these main soil types are written in combination with various prefixes and suffixes.

As mentioned in Chapter 4, the A or C suffixes indicate high and low levels of limestone in the soil. One instance of the 'c' prefix is found for the podzolic soils (H), which indicates that the soil is hydromorphic, with a 30 to 50 cm thick, often fertilized topsoil. The 'n' suffix for H indicates the presence of a mineral-poor topsoil (A-horizont) with sand grains. Most of the prefixes and suffixes for the marine clay (M) soils are already discussed in the South Holland case study (Section 6.2.3.), i.e. gM, pM, Mv, Mn and Mo. However, the new combination 'kM' observed in the Groningen case study area, translates to 'Knippoldervaaggronden'. The Friesian word 'knip' is used to describe the 'grayish and spotty'(STIBOKA 1964) rust patches in the topsoil.

Similar to the marine clay soils, most of the peat combinations are also described in Section 6.2.3. of the South Holland case study. New in the Groningen case study are the combinations 'aV' and 'Vz'. The first combination 'aV' is used for 'madeveengronden', which are peat soils with a thin settled topsoil composed of peaty-sand, sandy-peat or peat (Wikipedia contributors 2019a). The second combination 'Vz' refers to the underlying sand layer of the peat soil.

As opposed to marine clay (M) and peat (V), all the new swampy soil (W) combinations have not yet been identified in the South Holland area. The prefixes 'k', 'v' and 'z' respectively refer to the clayey, swampy or sandy topsoil of the swampy soils (W) themselves. Furthermore, the combination 'Wg' refers to a swampy soil with a swampy topsoil or inner layer on ripened finesand or clay. The combination 'Wp' refers to a swampy soil with a finesand or clay cover and a swampy inner layer on non-ripened finesand or clay. Lastly, the combination 'Wz' refers to swampy soils with a swampy inner layer on sand (de Vries, de Groot, et al. 2003). The only occurrence of sand (Z) is the code 'pZn', which refers to loamy fine sands with little to no rust patches (de Vries, de Groot, et al. 2003; Wikipedia contributors 2019a).

Soil Code	Meaning (NL)
|c OPHOOG	Opgehoogd of opgespoten
|f TERP	Oude bewoningsplaatsen
|h BEBOUW	Bebouwing
cHn21	Laarpodzolgronden; leemarm en zwak lemig fijn zand
Hn21	Veldpodzolgronden; leemarm en zwak lemig fijn zand
Hn23	Veldpodzolgronden; lemig fijn zand
gMn15C	Knippige poldervaaggronden; lichte zavel, profielverloop 5
gMn25C	Knippige poldervaaggronden; zware zavel, profielverloop 5
gMn53C	Knippige poldervaaggronden; zavel, profielverloop 3
gMn58C	Knippige poldervaaggronden; zavel, profielverloop 4, of 4 en 3
gMn83C	Knippige poldervaaggronden; klei, profielverloop 3
gMn85C	Knippige poldervaaggronden; klei, profielverloop 5
gMn88C	Knippige poldervaaggronden; klei, profielverloop 4, of 4 en 3
kMn43C	Knippoldervaaggronden; zware klei, profielverloop 3
kMn48C	Knippoldervaaggronden; zware klei, profielverloop 4, of 4 en 3
kMn63C	Knippoldervaaggronden; zavel en lichte klei, profielverloop 3
kMn68C	Knippoldervaaggronden; zavel en lichte klei, profielverloop 4, of 4 en 3
Mn15A	Kalkrijke poldervaaggronden; lichte zavel, profielverloop 5
Mn15C	Kalkarme poldervaaggronden; lichte zavel, profielverloop 5
Mn25A	Kalkrijke poldervaaggronden; zware zavel, profielverloop 5
Mn25C	Kalkarme poldervaaggronden; zware zavel, profielverloop 5
Mn35A	Kalkrijke poldervaaggronden; lichte klei, profielverloop 5
Mn45A	Kalkrijke poldervaaggronden; zware klei, profielverloop 5
Mn85C	Kalkarme poldervaaggronden; klei, profielverloop 5
Mo80A	Kalkrijke nesvaaggronden; klei
Mo80C	kalkarme nesvaaggronden; klei
Mv41C	Kalkarme drechtvaaggronden; zware klei, profielverloop 1
pMn55C	Kalkarme leek-/woudeerdgronden; zavel, profielverloop 5
pMn85C	Kalkarme leek-/woudeerdgronden; klei, profielverloop 5
pMn86C	Kalkarme leek-/woudeerdgronden; klei, profielverloop 3, of 3 en 4 of 4
pMo80	Tochteerdgronden; klei
pMv81	Liedeerdgronden; klei, profielverloop 1
aVp	Madeveengronden op zand met humuspodzol, beginnend ondieper dan 120 cm
aVz	Madeveengronden op zand zonder humuspodzol, beginnend ondieper dan 120 cm
hVc	Koopveengronden op zeggeveen, rietzeggeveen of (mesotroof) broekveen
hVz	Koopveengronden op zand, beginnend ondieper dan 120 cm
kVc	Waardveengronden op zeggeveen, rietzeggeveen of (mesotroof) broekveen
kVz	Waardveengronden op zand, beginnend ondieper dan 120 cm
pVc	Weideveengronden op zeggeveen, rietzeggeveen of (mesotroof) broekveen
pVs	Weideveengronden op veenmosveen
pVz	Weideveengronden op zand, beginnend ondieper dan 120 cm
Vp	Vlierveengronden op zand met humuspodzol, beginnend ondieper dan 120 cm
kWp	Moerige podzolgronden met een zavel- of een kleidek en een moerige tussenlaag
kWz	Moerige eerdgronden met een zavel- of kleidek en een moerige tussenlaag op zand
vWp	Moerige podzolgronden met een moerige bovengrond
vWz	Moerige eerdgronden met een moerige bovengrond op zand
Wg	Moerige eerdgronden met een moerige bovengrond of moerige tussenlaag op gerijpte zavel of klei
Wo	Moerige eerdgronden (ongerijpt)
zWp	Moerige podzolgronden met een humushoudend zanddek en een moerige tussenlaag
zWz	Moerige eerdgronden met een zanddek en een moerige tussenlaag op zand
pZn23	Gooreerdgronden; lemig fijn zand

Table 6.8: Overview of the main soil type classifications present in the Groningen study area. The listing of features presented in this table is based on de Vries, de Groot, et al. 2003.

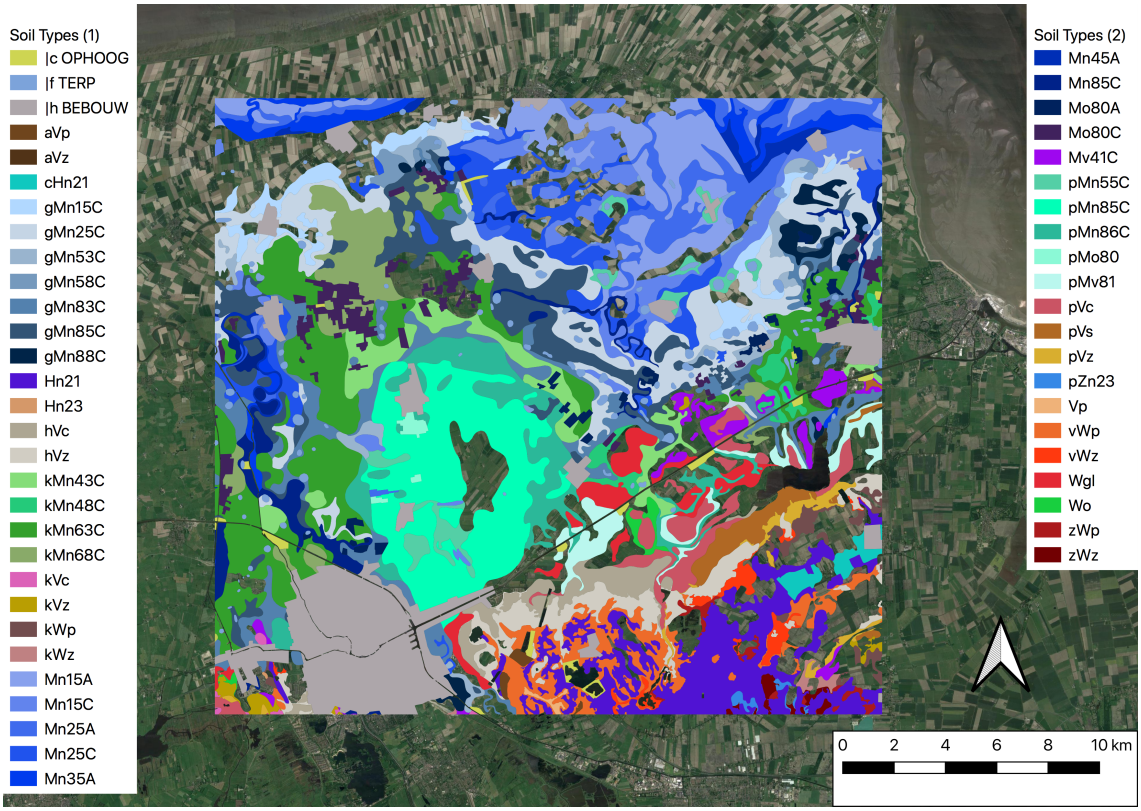

Figure 6.55: Map of the main soil type classifications present in the Groningen study area. The listing of features presented in this map is based on de Vries, de Groot, et al. 2003.

Geomorphology

The GKN, as part of BRO, describes the geomorphology of the Netherlands. As one of the GKN attributes, the 'landform subgroup codes' -attribute is selected, as it provide information on the basic formation group (e.g. plateaus, terraces) of the study area (letter), as well as their genesis (number). For the Groningen study area, the identified GKN landform subgroups are summarized in Table 6.9, and mapped in Figure 6.56.

The form subgroup classes in Table 6.9 belong to the following main form groups, i.e. isolated hills and ridges (B), plateau-like forms (F), hills and ridges with associated plains and lows (L), plains (M), non-valley-shaped lows (N) and valley-shaped lows (R). The full list of GKN form groups is available in Table 4.14 and for a complete overview of the form subgroups, the reader is referred to WUR 2017. Note that the translations of the Dutch terminology used in Table 6.9 are interpreted by the author.

Form Subgroup	Meaning (NL)	Meaning (EN)
B13	Grondmorenerug	Soilmorene ridge
B53	Dekzandrug	Cover-sand ridge
B71	Getij-inversierug	Tide-inversion ridge
B73	Getij-riviermondrug	Tide-delta ridge
B75	Kwelderwal	Salt marsh
B91	Terp of hoogwatervluchtplaats	Mound or high-tide refuges
F91	Plateau-achtige storthoop, opgespoten terrein of kunstmatig eiland	Plateau-like landfill, raised terrain or artificial island
L11	Grondmorenewelvingen	Soilmorene curvatures
L51	Dekzandwelvingen	Cover-sand curvatures
M48	Rivierkom- en oeverwalachtige vlakte	River-'bowl' and tidal bank-like plain
M51	Dekzandvlakte	Cover-sand plain
M53	Vlakte van ten dele verspoelde dekzanden of löss	Plain of partly washed up cover-sand or loess
M62	Vlakte van zee-of meerbodemafzettingen	Plain of sea-or-lakebed deposits
M72	Vlakte van getij-afzettingen	Plain of tidal deposits
M73	Vlakte van getij-riviermondafzettingen	Plain of tidal-delta deposits
M75	Zeeboezemvlakte	Sea-bay plain
M81	Ontgonnen veenvlakte	Reclaimed peat plain
M82	Ontgonnen veenvlakte met petgaten	Reclaimed peat plain with pits
M84	Boezemland, vlietland e.d.(moerassige vlakte)	Swampy plain (between flood defence & surface water)
M93	Vlakte ontstaan door afgraving of egalisatie	Plain originating from excavation or levelling
N51	Laagte zonder randwal	Low without sideshore
N94	Laagte ontstaan door afgraving	Low originating from excavation
R43	Restgeul	Restgully
R71	Getij-kreekbedding, zee-erosiegeul	Tide-creek bed, sea-erosion gully

Table 6.9: Overview of the GKN form subgroup classifications present in the Groningen study area. The listing of features presented in this table is based on WUR 2017.

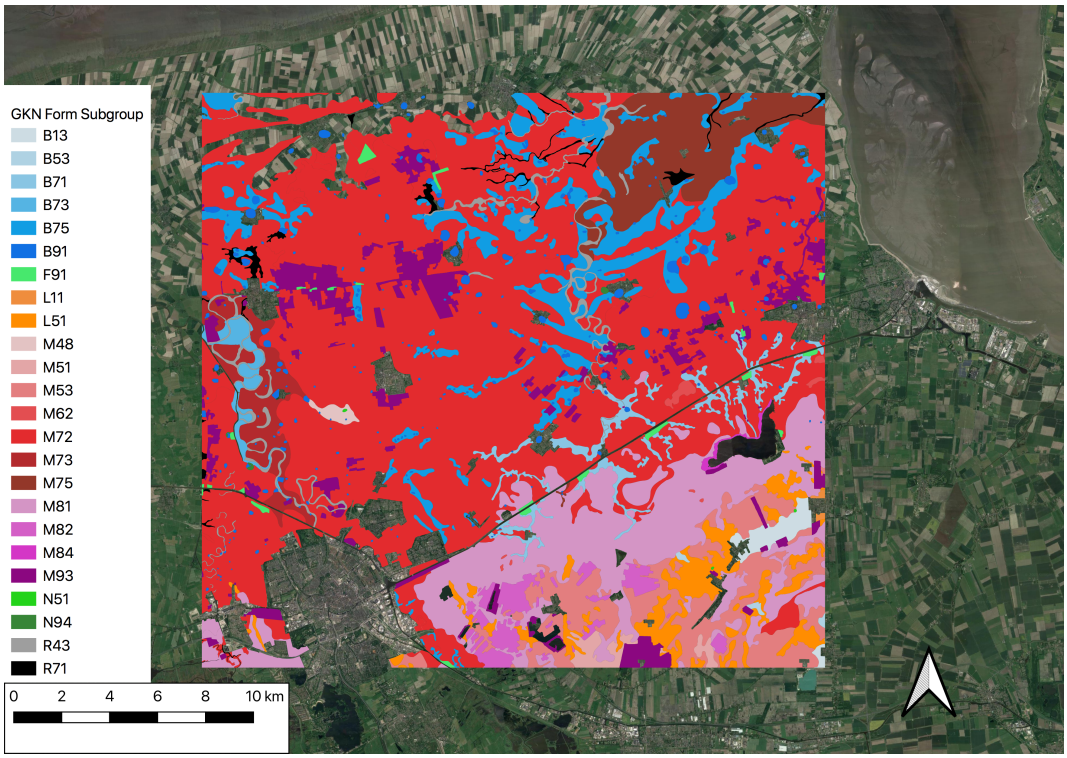

Figure 6.56: Map of the GKN form subgroup classifications present in the Groningen study area. The listing of features presented in this map is based on WUR 2017.

Buildings & Infrastructure

The buildings and infrastructure classifications used in this case study originate from the BGT dataset, presented in Chapter 4. In this way, the built environment is characterized with four types of attribute or object classes, i.e. 'buildings', 'road (sections)', 'non-vegetated area' and vegetated area. As in the South Holland case study, a single grid cell is selected for the deformation analysis in the context of building and infrastructure, which contain most of the PSI points within the track datasets. However, the localized study extent also requires the presence of enough soil type and geomorphology classes which have a lower point density. Therefore, the grid cell, for further analysis, is selected based on its coverage of both high and low point density areas. Following this reasoning, grid cell E11 is selected for further analysis, as shown in Figure 6.57. It covers an area bordering the eastern side of the city of Groningen.

Figure 6.57: Selection of the grid cell E11 (yellow) for the buildings & infrastructure analysis, as part of the Groningen grid of the entire study area, composed of 156 grid cells (2 ×2 km) based on the grid cells implemented in Bodemdalingskaart 2018.

Since all of the building and infrastructure classes[9], which are identified in grid cell F5 of the South Holland case study, also apply to grid cell E11 in the Groningen case study, the reader is referred to Table 6.7. In addition to these classes, grid cell E11 in the Groningen case study area also contains the class 'inrit' (driveway) as part of the road section attributes, and the class 'transitie' (transition) in both the vegetated and non-vegetated terrain attributes.
The BGT objects, i.e. the buildings, roads, non-vegetated and vegetated terrains, are mapped for grid cell E11 in Figure 6.59, covered by the linear deformation points of descending track 37. Additionally, the extent of the selected grid cell is shown in Figure 6.58 along with the soil type and geomorphology classifications within grid cell F5, shown respectively in Figures 6.60 and 6.61.

[9]With the exception of 'grasland' (grassland) in the vegetated terrain attributes.

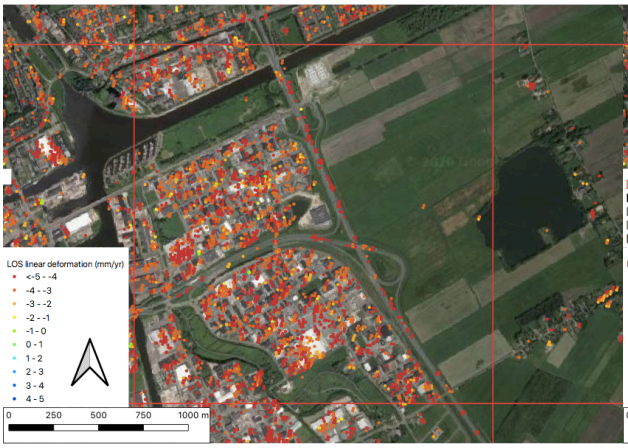

Figure 6.58: Extent of the E11 grid cell.

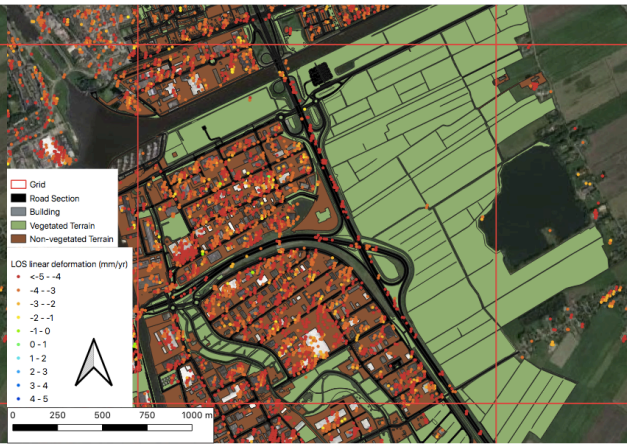

Figure 6.59: Geography classification of the E11 grid cell.

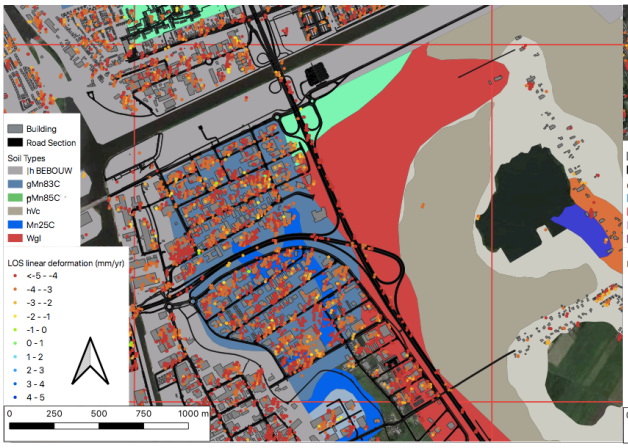

Figure 6.60: Soil type classification of the E11 grid cell.

Figure 6.61: Geomorphology classification of the E11 grid cell.

6.3.4. Method

Similar to the South Holland case study, a two-part deformation analysis is performed in the Groningen case study. THe first part of the deformation analysis uses the soil type and geomorphology classifications identified over the entire Groningen case study extent. The Bodemdalingskaart 2018 definition of total, deep and shallow deformation is used, based on the PSI points of ascending track 15 and descending track 37. The resulting deformation per soil type and geomorphology is presented in Section 6.3.5. in the same output format as for the South Holland case study, i.e. in a sequence of bar graphs. For the second part of the Groningen case study, a more localized deformation analysis is performed, within the extent of the selected grid cell E11, as depicted in Figure 6.58. The buildings and infrastructure classes (BGT) in Figure 6.59, the soil type classes in Figure 6.60 and the geomorphology classes in Figure 6.61 are used for the attribute-enrichment of the PSI points of tracks 15 and 37 within grid cell E11.
The general method for the attribute-enrichment and deformation analyses of the Groningen case study is analogous to the methods used in the South Holland case study in Section 6.2.4. For the theoretical framework behind the implementation of the database, the reader is referred to Chapter 4.

6.3.5. Deformation Analysis 1 – Groningen

This section presents the results of the first part of the Groningen deformation analysis, centered around the soil type and geomorphology classifications from Bodemkaart and GKN, as part of BRO. The full overview of the soil type and geomorphology classes in the full extent of the Groningen case study area can be found in Tables 6.8 and 6.9 (respectively).

Soil Type

The total, deep and shallow (linear) deformation results (2015 - 2019) for the soil types in Groningen are presented in Figure 6.62 for ascending track 15 and Figure 6.63 for descending track 37. Note that the soil 'Wg' has no entry for track 15 in Figure 6.62, but it is included in the deformation results of track 37 in Figure 6.63.

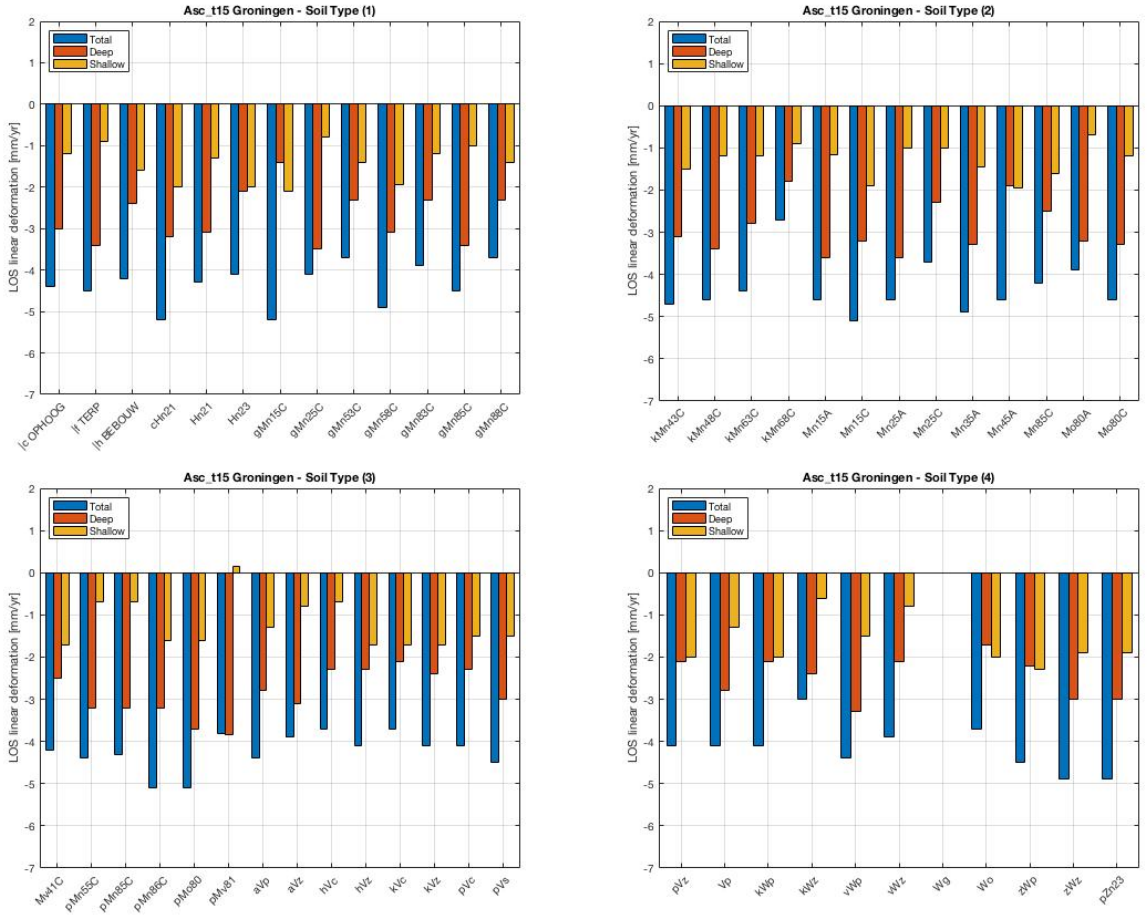

Figure 6.62: Ascending track 15: Total, deep and shallow LOS linear deformation of the main identified Groningen soil types (data: SkyGeo).

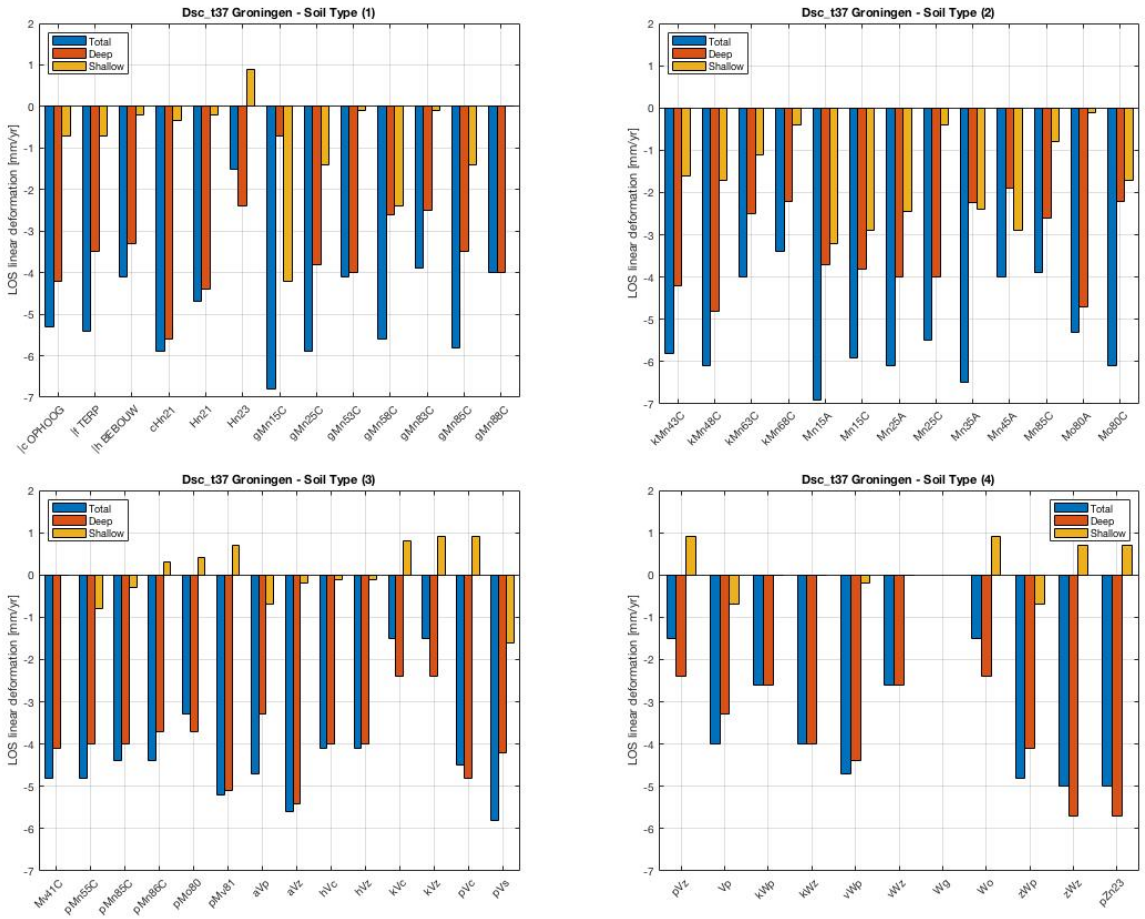

Figure 6.63: Descending track 37: Total, deep and shallow LOS linear deformation of the main identified Groningen soil types (data: SkyGeo).

The same general deformation pattern is observed for all soil type samples within the Groningen area, in which the deep subsidence exceeds the shallow subsidence, resulting in strong total subsidence, typically between -3 and -5 mm/yr in track 15 and between -1.5 and -6 mm/yr in track 37. The only (slightly) positive shallow deformation observed in track 15 is observed for the soil type pMv81 (clay with humus-rich topsoil and underlying swampy material), whereas positive shallow deformation is more common in track 37 as it is observed for 11 of the 51 representative soils, i.e. Hn23, pMn86C, pMo80, pMv81, kVc, kVz, pVc, pVz, Wo, zWz and pZn23. Even though, track 37 tends to deliver more heterogeneous deformation results across most samples, especially in the shallow deformation component of each class.

As in the South Holland case study, most differences are seen within the main soil type groups of the Groningen case study area, i.e. podzolic soils (H), marine clay (M), peat (V), swampy soils (W) and sand (Z). Therefore, any differences in general deformation between the main soil types are more difficult to observe. Most of the strongly negative shallow deformation in track 37 is observed for various marine clay soils, i.e. some of the Mn combinations (marine clay soils with periodically high groundwater levels) with or without the 'g' prefix (low calcium-magnesium ratio). This is also reflected in the relatively large differences between the total and deep deformation components of the (g)Mn soils.

The peat soils (V) show the least amount of deep subsidence, in combination with moderate shallow subsidence (track 15) to slightly positive shallow deformation (track 37), resulting in a generally lesser amount total subsidence. This trend is most notable for the soil combination 'kV' (peat soils with a shallow layer of heavy, lime-poor clay). Furthermore, the swampy soils (W) also show mixed deformation results across the different soil combinations. While the observations for the deep and total deformation are quite similar between W combinations, their shallow deformation results vary substantially, i.e. between -2.2 and -0.5 mm/yr in track 15, and between -0.6 and +0.9 mm/yr in track 37. Finally, the

only representative sand soil (Z) identified in the Groningen area, i.e. pZn23, shows strong deep and total subsidence. This is especially true in track 37, where the deep subsidence component exceeds the total subsidence in combination with shallow uplift.

Geomorphology

The linear deformation results (2015 - 2019) for the geomorphology classes in the Groningen area are presented in Figure 6.64 for ascending track 15 and Figure 6.65 for descending track 37.

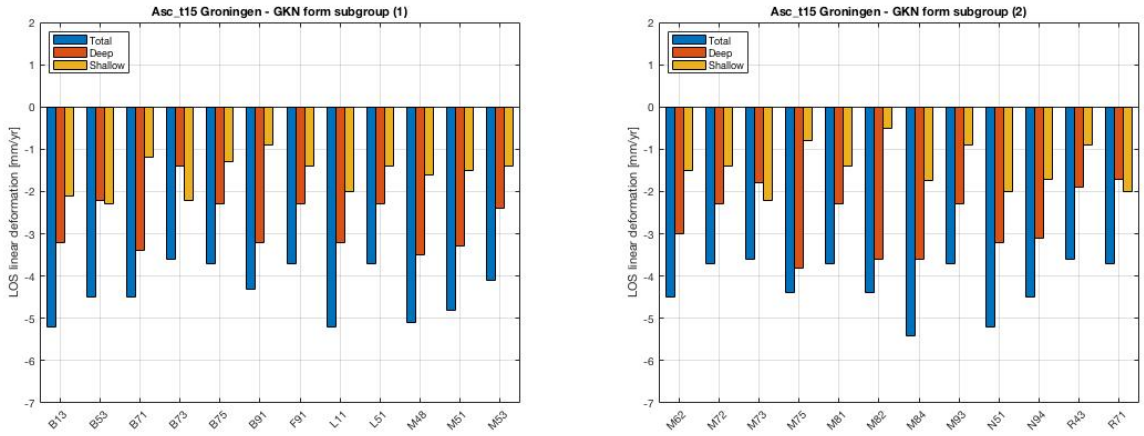

Figure 6.64: Ascending tracks 15: Total, deep and shallow LOS linear deformation of the main identified Groningen GKN landform subgroups (data: SkyGeo).

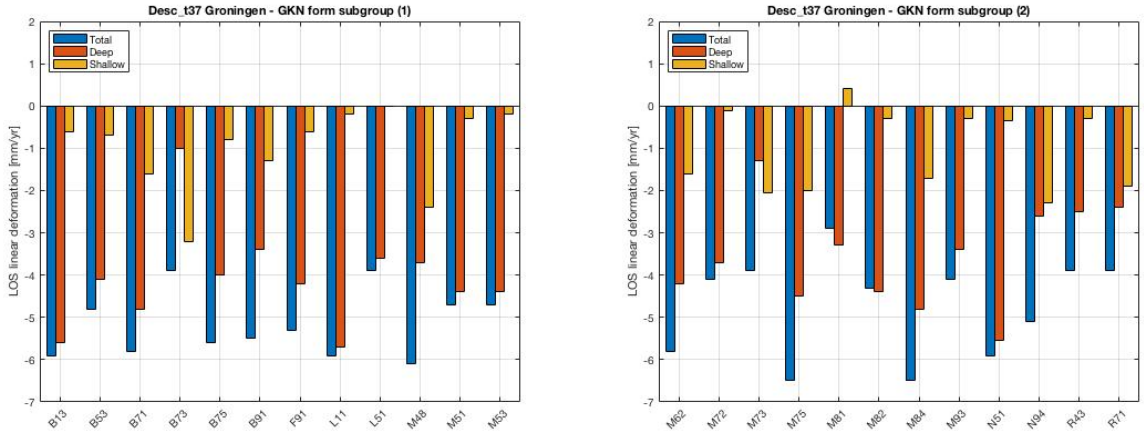

Figure 6.65: Descending tracks 37: Total, deep and shallow LOS linear deformation of the main identified Groningen GKN landform subgroups (data: SkyGeo).

In both tracks 15 and 37, the same general deformation pattern is present in the Groningen study area of strong total subsidence with the largest contribution from the deep deformation and a more moderate contribution from shallow subsidence. Similar to the soil type deformation results, the shallow deformation is found to be close to zero in some instances for descending track 37. Even a slight shallow uplift is observed in the case of form subgroup M81 (reclaimed peat plain) of track 37. In contrast, the strongest shallow subsidence is observed in the linear deformation results of B73 (tide-delta ridge), i.e. -3.2 mm/yr in track 37, exceeding the deep subsidence component and resulting in relatively low-magnitude total subsidence, i.e. -3.9 mm/yr. Other instances in which the negative shallow deformation component exceeds the deep deformation component is found for the form subgroup M73 (plain of tidal-delta deposits) in both tracks, and for the form subgroup R71 (Tide-creek bed, sea-erosion gully) in track 15.
Furthermore, the frequently recurring landform groups B (isolated hills and ridges) and M (plain) show variability in the deformation results of their landform subgroups. Whereas most B subgroups show

relatively strong total and deep subsidence, this subsiding trend is more moderate for B73 (tide-delta ridge) in both tracks, and for B75 (Salt marsh) in ascending track 15. As for the M subgroups, four of them show display strong total subsidence, between -5.8 mm/yr and -6.5 mm/yr in track 37, and between -4.4 mm/yr and -5.4 mm/yr in track 15. These are M48 (riverbowl and tidal bank-like plain), M62 (plain of sea-or-lakebed deposits), M75 (seabay plain), and M84 (swampy plain).
As one of the two identified L (hills and ridges with associated plains and lows) form subgroups, L11 (soilmorene curvatures) is characterized by overall strong total subsidence in both tracks, of which the deep component is the main contributor in track 37. On the other hand, L51 (cover-sand curvatures) has more moderate subsidence results in both tracks. Similar observations are made for N51 (low without sideshore) and N94 (low from excavation) of the N (non-valleyshaped lows) landform group, where the total and deep subsidence components of N51 exceed those of N94. However, in descending track 37, relatively weak shallow subsidence is observed for N51, compared to the moderate shallow component of N94.

6.3.6. Deformation Analysis 2 - Grid Cell E11

As the second part of the Groningen deformation analysis, this section presents the results of the deformation per attribute, i.e. soil type, geomorphology, buildings and infrastructure, within the extent of grid cell F5, as depicted in Figures 6.57 and 6.58. The deformation analysis for Grid cell E11 is similar to the nationwide analysis and the second part of the South Holland deformation analysis (grid cell F5), in its attribute-enrichment of the PSI points and in the output presentation, i.e. in a series of boxplots (Figure 6.66 for ascending track 15 and Figure 6.67 for descending track 37).

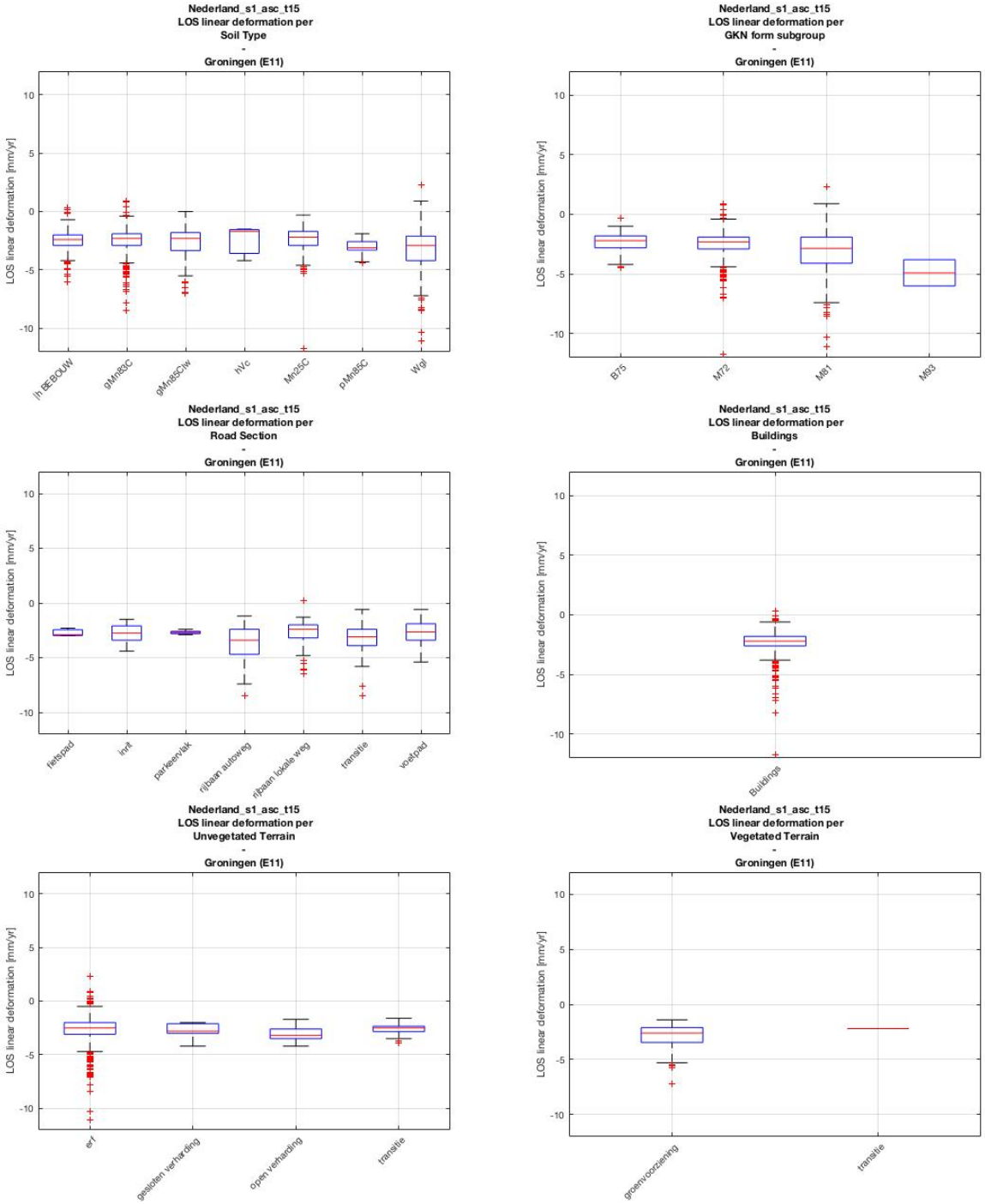

Figure 6.66: Ascending track 15 for the Groningen case study area E11: LOS linear deformation (mm/yr) of the following classes: soil type, GKN form subgroup, road section, buildings, non-vegetated terrain, and vegetated terrain (data: SkyGeo).

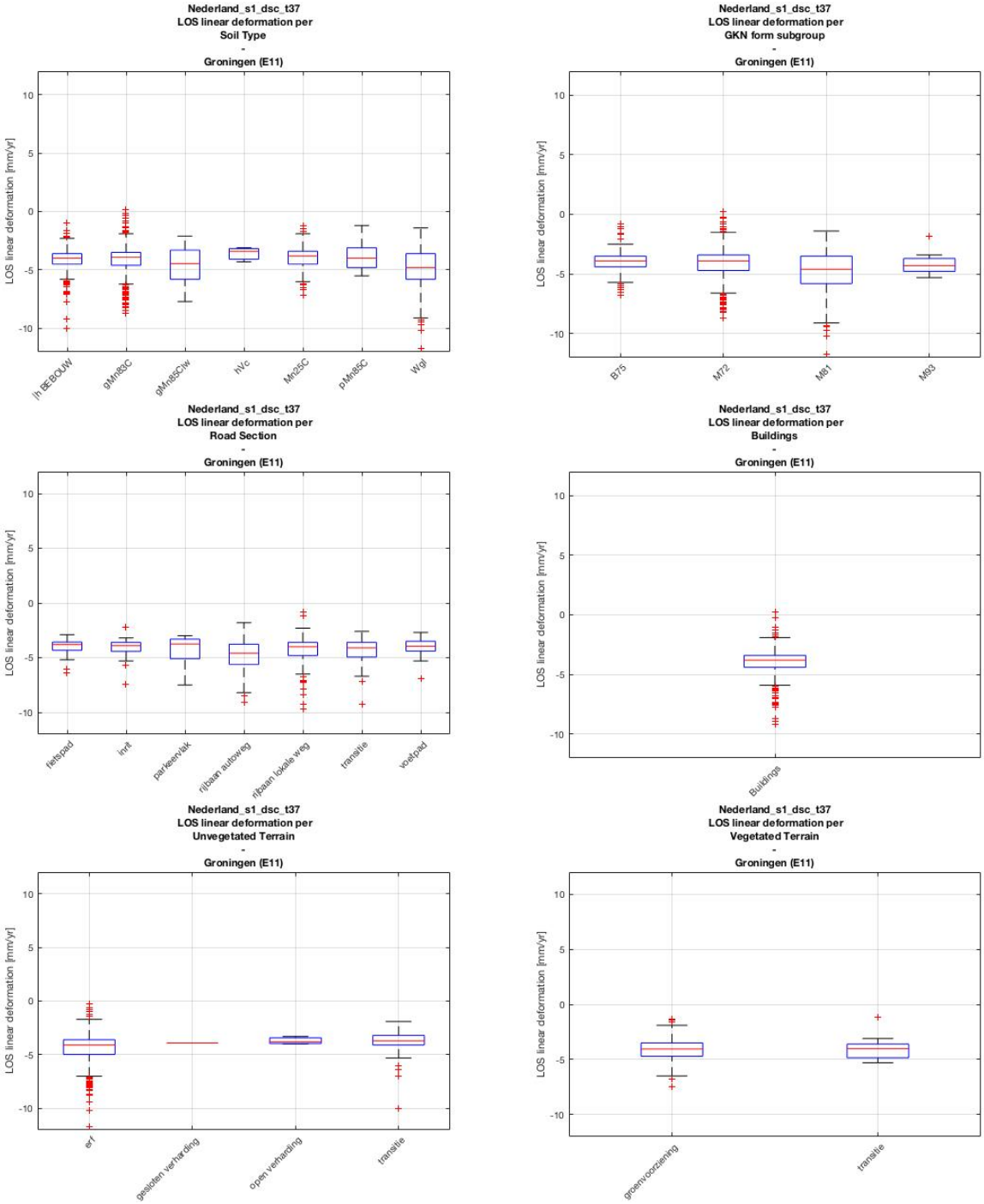

Figure 6.67: Descending track 37 for the Groningen case study area E11: LOS linear deformation (mm/yr) of the following classes: soil type, GKN form subgroup, road section, buildings, non-vegetated terrain, and vegetated terrain (data: SkyGeo).

Considering the median deformation of each class, the general trend of negative linear deformation is observed across all attributes, between 0 mm/yr and -5 mm/yr. Note that the median values of the deformation distributions in track 15 remain relatively centered around -2.5 mm/yr, whereas the median values in track 37 indicate more negative deformation, reaching -4 to -5 mm/yr.
No major differences are observed in the deformation tied to the different soil type classes. The box extent (25th to 75th-percentile) in their distributions are quite similar, except for the soil type hVc (peat with a 'clayey peat' or 'peaty clay' topsoil and an underlying sedgespeat, reed-sedgespeat or mesotrophic peat layer), which has a confined and negatively skewed distribution (best seen in track 15) without outliers. Note that only few PSI points are contained by the hVc polygon in both tracks, which explains its relatively narrow distribution.
Most of the PSI points in the grid cell sample originate from buildings and infrastructure in the western part of grid cell E11 (Oosterpoortwijk), mainly categorized as 'buildings objects', the classes 'local roadway' and 'pavement' as part of the road sections, and as the non-vegetated terrain class 'erf' (property). The 'erf' and 'buildings' classifications give quite similar deformation distributions for both tracks, with relatively narrow boxes, i.e. close to the median, wide whiskers and many outliers. This area, which is home to many small and medium-sized businesses, is characterized by the gMn83C (low calcium-magnesium ratio clay soils with periodically high GWT and low limecontent) soil type and the M72 (plain of tidal deposits) form subgroup. These soil and geomorphology classes, show similar deformation distributions to the 'buildings', 'erf' and 'local roadway' classes, with narrow boxes, extended whiskers and many outliers.
The soil type Wgl (swampy soil with a finesand or clay cover and a swampy inner layer on non-ripened finesand or clay)[10] contains most of the points that mostly originate from the 'roadway' classification found in grid E11 (the 'Beneluxweg', N46), seen in Figures 6.59 and 6.60. The median value of the Wgl class shows the same to slightly more negative deformation compared to the other soil classes. In track 37 the spread between the whiskers of soil type Wgl is largest, ranging from -2 mm/yr to -8.5 mm/yr, with the presence of negative outliers. Following a similar trend, the 'roadway' distribution is slightly more negative compared to the other road section classes and still shows some outliers.
Furthermore, the part of soil type Wgl that contains the roadway (road N46) in grid cell E11 coincides with the geomorphology form subgroup M81 (Reclaimed peat plain), which stretches over the entire eastern part of grid cell E11 (and beyond) in Figure 6.61. Of all geomorphology subgroups, M81 has the widest distribution in terms of its whiskers, reaching negative deformation of -7.5 mm/yr in track 15 and -8.5 mm/yr in track 37. In the northern part of grid cell E11, the land form subgroup M93 (Plain originating from excavation or levelling) shows the strongest negative median, i.e. exactly -5 mm/yr, in track 15, while remaining closer to the other landform subgroups in track 37. The same (M93) area is characterized by the 'buildings' class in the soil type classifications from Bodemkaart, containing outliers around -5 mm/yr. However, the PSI points in this area originate from the same roadway (N46), identified earlier.

6.3.7. Discussion

Similar to the South Holland deformation analysis, the deformation analysis for Groningen is divided in two parts. The first part utilizes the grid cell representation of the entire Groningen study area, and computes the Bodemdalingskaart 2018 definition of total, deep and shallow deformation per grid cell. The soil type and geomorphology classifications are coupled to the grid cells via spatial joins. The results of this analysis are presented in the form of bar graphs, which represent the total, deep and shallow deformation per identified soil type or geomorphology class. In the second part of the deformation analysis, the grid cell E11 (at the eastern part of the city of Groningen) is selected, based on its heterogeneity in attributes, i.e. buildings and infrastructure, soils and landform subgroups. The distributions of linear deformation (mm/yr) of these attributes are represented with the use of boxplots, computed for each class within a particular attribute.

Deformation Analysis 1 – Groningen

For all the soil type and geomorphology classes in the Groningen area, a general trend of strong total subsidence and, to a lesser extent, shallow subsidence is observed. Therefore, the total deformation, following its definition as the sum of deep and shallow deformation, is strongly negative and exceeds

[10] The l suffix refers to the presence of local 'katteklei' (clay that contains iron sulfide minerals) within 80 cm and at least 10 cm thick (de Vries, de Groot, et al. 2003).

(in magnitude) the deep component for most classes. However, for some of the soils and for one of the form subgroups, i.e. M81 (reclaimed peat plain), zero or slightly positive shallow deformation is observed in the results of track 37. This depends on the deviation of the PSI points per track from the spatial reference. As presented in Table 4.17, an offset of +0.12 mm/yr is found for track 15 and an offset of +0.47 mm/yr is found for track 37. Thus, when corrected for the +0.47 mm/yr offset of track 37, the upward shallow deformation disappears for some soil classes, as it reaches zero deformation or it becomes slightly negative (w.r.t. the LOS direction). However, some of the soil types in track 37 keep their net positive shallow deformation after this correction, i.e. almost half of the identified peat soils kVc, kVz, pVc, pVz, and other soil types Hn23, pMv81, Wo, zWz and pZn23.
Furthermore, as in the South Holland case study, the most notable differences are found when comparing the different soils and landform subgroups that belong to the same main soil or landform. These differences are observed for the different topsoil and underlying soil characteristics of a particular main soil group. Additionally, soils of the same 'main group', e.g. marine clay (M), with differing characteristics, i.e. soil texture (based on the grain size and soil profile), GWT characteristics and deposition environment, also show strong differences in their total, deep and shallow deformation. These differences in deformation partly depend on the inherent characteristics of the identified shallow soil classes. However, of greater importance (especially in the Groningen case study) is the location of the different 'shallow' soil types with respect to the 'deep subsidence bowl'. Since the deep deformation component is determined by the processes in the deep gas-bearing layers, the influence thereof is seen at the surface. The influence of deep soil layers is not directly accounted for in the shallow (1.50 m depth) soil classifications from Bodemkaart. The processes of gas extraction in the deep subsurface are the main drivers of the deep subsidence. These processes are more difficult to implement and classify in a contextual environment, for their reliance on 3D models. For example the GeoTOP model provides a detailed three dimensional overview of the Dutch subsurface to a depth of 50m below NAP (DINOloket n.d.).

Deformation Analysis 2 - Grid Cell E11

Grid cell E11, shown in Figures 6.58 to 6.61, is selected in the Groningen subsidence bowl, including the eastern part of the city of Groningen. The linear deformation of multiple attributes, i.e. buildings, infrastructure, soil type and geomorphology is analyzed directly from the PSI points that these classifications are attributed to.
As expected, all identified attributes show strong linear subsidence, which differs per attribute. Groups of attributes are identified, which show similar deformation distributions, based on their properties, their location with respect to one another and based on their location with respect to the 'deep' subsidence bowl. Based on the location of grid cell E11 with respect to the deep subsidence bowl, relatively strong deep deformation is expected to be observed towards the eastern part of the grid cell. The form subgroup M81 (reclaimed peat plain), which is situated in the eastern part of grid cell E11 does show stronger subsidence compared to the other form subgroups. The soil type hVc on the other hand, which is also situated in the easternmost part of grid cell E11 does not necessarily show stronger subsidence compared to its western counterparts. However, the deformation distribution of hVc is only based on 3 PSI points for each track (6 in total) and is therefore not as representative.
As mentioned in the results, the western part of grid cell 11 (Oosterpoortwijk) is where most of the PSI points originate from. This area contains many buildings (mostly business facilities), local roads and non-vegetated terrain, classified as 'erf' (property). These objects, on average, do not necessarily reflect stronger negative deformation. However, since their samples are relatively large, these objects and classes show more variability in their deformation results (both positive and negative) and many outliers. As discussed in the South Holand case, the use of AHN elevation data can be used to improve the geolocation estimates (van Natijne 2018). Buildings and address information from BAG and additional geographic information from BGT can help in improving the location and interpretation of the deformation of buildings. A discussion on both the AHN, BAG and BGT datasets is provided in Appendix B.

7

Conclusion

As a starting point to this research, the main question to be answered is:

Can subsidence due to deep and shallow causes be differentiated using attribute-enriched PS-InSAR data?

Based on the results of this study, partitioned in a nationwide deformation analysis and separate case studies in three locations, it can be said that the use of attribute-enrichment helps in the identification and interpretation of the PS-InSAR observations. A simple 'yes' answer to the research question would imply that the mere process of attribute-enrichment of the PSI points is sufficient to clearly make this distinction. However, surface deformation is caused by a combination of many physical (natural and anthropogenic) processes acting at any depth in the Earth system. Aside from the inherent complexity of subsidence, the research question does bring up the discussion on how the problem of surface deformation can or should be addressed, and whether or not a distinction between 'shallow' or 'deep' causes is entirely relevant.
The answer to the research question may also vary depending on the user's definition and terminology of deep and shallow subsidence. As discussed in the Introduction, there is no single 'fixed' definition for the terms 'deep' and 'shallow' subsidence. More weight can be attributed to the physical processes that cause the estimated subsidence and/or the depths at which these processes take place. Bodemdalingskaart 2018 makes the distinction between shallow and deep subsidence, based on descriptive statistical parameters that characterize the distribution of InSAR observations within a predefined 2 $\times$2 km grid cell.
The set-up of this study on the use of attribute-enriched InSAR data to analyze subsidence in the Netherlands is based on the two sub-questions that form the framework of this research:

1. What are the deformation trends observed in the Netherlands, and how do these relate to the country's soil distribution?

2. How does anthropogenic activity impact the deformation of the Dutch surface, and can these impacts be quantified?

Where the nationwide study focuses on the statistics of deformation attributed to the country's main soil types, the three case studies highlight the importance of anthropogenic activity that affect the (sub)surface deformation. In both studies a database approach is implemented, presented in Chapter 4, that facilitates the storage and operation steps involved in performing the attribute-enrichment. The attribution of contextual classes to the PSI points makes it possible to group them into different categories based on a common characteristic. In this study, the common characteristic is either physically based, e.g. soil type, road section, or risk-based, as is the case for the South Limburg case study (Section 6.1.). Additionally, the classification can potentially be based on common characteristics in the processing of the PS-InSAR points.
The interpretation of the enriched datasets can work in different ways. On the one hand, the auxiliary class-based information tells us something about the origin or causes of the 'measured' deformation.

Alternatively, the deformation points might explain the presence and/or labeling of a particular class or attribute. For example, in the Limburg case study the potential impact zones (EK) are partly based on prior deformation points. In turn these impact zones form useful references for new PSI points, and contain 'auxiliary' information (e.g. fault patterns and locations) that might help to explain more recent deformation patterns.

7.1. Nationwide Deformation Analysis

In relation to the first sub-question, the nationwide analysis is set up to study the deformation of the Netherlands in the context of the country's soil distribution. Soil type and the groundwater table classifications from Bodemkaart, as part of BRO, are used for the attribute-enrichment.

7.1.1. Soil Type

The nationwide deformation analysis of the Netherlands shows trends of both subsidence and uplift affecting different parts of the country with different soil types. Subsidence is predominantly observed in areas where the shallow subsurface (1.5 m depth) is classified as the main soil type 'peat' or 'marine clay'. The marine clay soils also show the strongest linear deformation minima, i.e. strong subsidence. In contrast, an average trend of slight uplift is observed for the soils classified under the main soil type 'river clay' and 'sand'. The 'loam' class shows mixed results in terms of average uplift or subsidence, depending on the track. Additionally, the 'buildings' class is studied which characterizes urban environments and thus contains the majority of PSI points in all samples. For the buildings class, slightly positive deformation is observed. When comparing the deformation time series results (between 2015 and 2019) for the different soil types, differences between classes, i.e. soil types and GWT classes, are shown in their net deformation (increase or decrease) and in the in the phase and amplitude characteristics of their seasonal (oscillating) patterns. Again, the soil types 'marine clay' and 'peat' show net subsidence, whereas the 'river clay' and 'sand' soils show net uplift. Additionally, the peat and marine clay soils appear to be in phase with one another. The same observation holds for the sand and river clay soils, resulting in the two groups being 'out of phase' in most tracks.
In relation to the first sub-question, the observed trends in the Netherlands indicate, on average, strong subsidence for the marine clay soils, i.e. -1.24 mm/yr. This trend of marine clay subsidence is mainly observed in the northern part of the country, i.e. in Groningen as seen in all tracks, except for track 110. Average subsidence is also observed for the peat soils, i.e. -0.48 mm/yr, distributed over the entire country, as seen in tracks 88 and 37. Also for the tracks that exclusively contain the peat soils in the northern part of the country, i.e. tracks 15 and 139, an average trend of subsidence is observed. In contrast, net upward deformation is observed for the sand soils, i.e. +0.54 mm/yr and for the river clay soils, i.e. +0.77 mm/yr which are mostly found in the center-to-eastern part of the Netherlands. Additionally, sand-classified soils are found along the coast and the Wadden Islands, but these show mixed results, based on track 37 showing net uplift, track 88 showing stagnation and tracks 110 showing subsidence. Note that the average deformation values given per 'main' soil type are computed as the mean of the mean deformation values of each track.

7.1.2. GWT

Additionally, the GWT should be accounted for in the answer to the first research question. As such, the nationwide deformation analysis also compares the surface deformation between different GWT attributes, provide an indication of the highest and lowest mean water levels (mm -mv) denoted with the use of Roman numerals, i.e. I representing shallow groundwater levels and VIII representing deep groundwater levels. The shallow GWT classes, i.e. I and II are mostly found in the rural peat areas, which is reflected by their overall negative deformation. Additionally, shallow GWT class I shows strong sub-seasonal fluctuations in its time series profiles. However, this might be explained by the overall lower sample sizes of class I. On average, the deep GWT classes show slightly stronger positive deformation compared to the shallow GWT classes. Finally, the middle-to-deep GWT classes V, VI and VII have the largest sample sizes with the strongly negative outliers.

As discussed in Section 4.3.3., the observations of the different tracks have a certain offset (up to +0.47 mm/yr for track 37) with respect to the spatial reference, which is computed in this study as the mean linear deformation (mm/yr) per track. This does not change the general trends observed in

the nationwide analysis, as the different classes are mostly compared separately for each track. Note that the differences in coverage between the tracks partly influence offset from the spatial reference for each track. Another influence of the track coverage can be found in the statistical distributions of the deformation for each soil type in a particular track. For example, track 88 covers the majority of the Netherlands, whereas track 139 only covers the eastern part of the country, a relatively small part of the eastern side of the Netherlands. Since the only 'marine clay'-classified area that is covered in track 139 coincides with the subsiding natural gas fields in Groningen, these results are not normalized by other marine clay areas outside of the track coverage. This brings into question the issue of correlation vs. causality, and highlights the importance of the larger selections of classifications as a means to improve further interpretations.

7.2. Localized Case Studies

The localized case studies are based around the secon sub-question of how anthropogenic activities impact the deformation of the Dutch surface, and whether or not these impacts be quantified. The extraction of subsurface resources, such as coal, natural gas and groundwater, greatly impacts the deformation of the Netherlands. This, in combination with the natural causes for land deformation is reflected in the three case studies. The South Limburg case study is focused on analyzing the potential deformation from different after-effects of coal mining in the area. It serves as a more 'isolated' case, in which risk-based classifications from Heitfeld, Klunker, et al. 2016 are used to enrich the PSI points. The Delft and Groningen case studies focus on the distinction between shallow and deep deformation in the context of the natural and built environment. In a two-part deformation analysis, the grid cell representation and the statistical definition of total, deep and shallow subsidence from Bodemdalingskaart 2018 are used to analyze the deformation (in the LOS) of different physical attributes, i.e. soil type classifications, (geomorphological) landform subgroups, as well as buildings and infrastructure.

7.2.1. South Limburg – Coal Mining After-Effects

Based on the risk analysis in Heitfeld, Klunker, et al. 2016, the after-effects of coal mining in the area of South Limburg are assessed. Three of the major risks involve differential ground heave induced by rising mine water, the potential failure of mine shafts leading to subsidence or sinkholes, and, lastly, the presence of not-fallen-in voids from near-surface mining (Heitfeld, Klunker, et al. 2016). So-called impact categories (EK) are defined for the after effects, and assigned to the potentially affected areas or 'EK zones'. The deformation of the impact areas of differential ground heave and near-surface are analyzed in this case study.
Since the impact areas of differential ground heave are located along the major faults of the South Limburg area, the northern and southern parts of these areas are separated (with respect to the fault) for the attribute-enrichment procedure. Therefore, the differential deformation can be analyzed separately for each sides of the defined impact areas. Earlier deformation analyses have been performed in the area, combining InSAR and levelling data to map the deformation between 1974 and 2014. The results from this study show slowing trends in mine water rise towards the end of the record. The more recent Sentinel-1 datasets (2015-2019) used in this particular case study indicate an overall slowing in the upward deformation. Additionally, the differences in ground heave between the northern and southern sides of the impact areas along the faults seem to gradually diminish. This has been done by comparing the linear deformation trends between the to records for all three impact areas.
The risk from surface mining relates to the presence of not-fallen-in voids. These occur if the hanging wall of the mined coal seam did not entirely collapse after the seam was mined out (Heitfeld, Klunker, et al. 2016). The distinction between the historical and industrial near-surface mining areas is made in the risk assessment and is applied in the deformation analysis of this case study. The historical mines, confined to a specific part, i.e. project area 1, show near-homogeneous deformation results both in their linear deformation, as well as in their time series. Aside from the homogeneity in results, the historical near-surface minig areas have the most positive (upward) deformation for the EK 1 (red) areas and the least positive deformation for EK 3 (blue). In contrast, the industrial near-surface EK areas are spread out over a larger region, i.e. project areas 2 and 3, and show more heterogeneous deformation results. As opposed to the historical EK classes, EK 1 (red) shows the least positive deformation, whereas EK 3 (blue) shows the most positive deformation.

7.2.2. South Holland – Subsiding Peatlands

The PSI tracks 37 and 110 are used to construct the grid cell representation of deformation, following Bodemdalingskaart 2018. In the first part of the analysis, the grid cells are enriched with soil type and geomorphology attributes. The grid cell representation in the South Holland case study shows strong shallow subsidence for the identified soil types and geomorphology landform subgroups. Considering a correction of the spatial reference offsets per track, the general trend of slightly upward deep deformation is observed, more so in track 37 as opposed to track 110. As a result, total subsidence is observed for all of the soil types and landform subgroups, to a lesser extent than the shallow component.
In the second part of the South Holand deformation analysis, buildings and infrastructure attributes are linked to the PSI points in the selected grid cell F5, as well as the corresponding soil type and geomorphology attributes. This approach allows for the different classifications to be compared in a more direct sense, based on their respective locations, in terms of their deformation patterns. Similarities in the deformation distributions are observed between the overlapping polygons of different attributes. Additionally, the 'road section' classes from BGT are useful in combination with the different soil and geomorphology classes, since most roadways and highways cross a wide range of soil types in non-urban areas, where PSI points are more scarce and thus more difficult to interpret in terms of their deformation trends.

7.2.3. Groningen – Natural Gas Extraction

The Groningen case study uses the same general set-up as the South Holland case study in terms of the two-part deformation analysis. In contrast to the deformation trends observed in South Holland, the Groningen case study shows strong deep subsidence and weaker shallow subsidence, with occasional uplift for some soil and form subgroup samples in track 37 (while considering the spatial reference offset). The resulting total subsidence oftentimes exceeds its deep component. Any differences in deformation between the different soil types and landform subgroups are mostly found within the 'main' soil and landform categories themselves. This highlights the importance in the level of detail in these classifications, including information on e.g. the topsoil and underlying soil characteristics, soil texture and lime content.
The second part of the deformation analysis takes into account the locations of the attributes with respect to each other, and the general deformation pattern, i.e. the 'subsidence bowl in Groningen'. Therefore, grid cell E11 is selected for its variety in classes per attribute and its location at the eastern part of the city of Groningen. For example, in the eastern part of grid cell E11, a reclaimed peat plain (M81) coincides with the soil type 'Wgl' and a roadway (N46), which all show relatively strong negative deformation distributions (mostly in their whiskers) compared to the western attributes.

7.3. Recommendations

Even though this study on the attribute-enrichment of PS-InSAR datasets has delivered promising results in a variety of interesting cases, there are further steps to be undertaken in the research of attribute-enrichment of InSAR data, or other spatial data in general. With the selection of datasets in Chapter 4, the potential for the inclusion of additional datasets, such as AHN, BAG and BRT is hinted at. Brief descriptions of these datasets can be found in Appendix B. Where the AHN datasets, and LiDAR point clouds in general, have shown great potential for the geolocation of InSAR estimates in the work of van Natijne 2018, the BAG and BRT datasets can be implemented in the further attribution of auxiliary data to the InSAR observations, providing greater detail in the building and infrastructure classifications. Furthermore, the inclusion of highly dynamic data may help this research forward, considering the oftentimes underestimated dynamic nature of surface deformation itself and the observation thereof.

7.3.1. Quasi-static vs. Dynamic Data

For the scope of this research, the database approach used in this study serves the purpose of assigning quasi-static attributes to the PSI points. The distinction between quasi-static and dynamic datasets is made depending on the time frame in which the processes and features described in the database take place. For 'quasi-static' datasets it is assumed that the features remain fairly constant over time, and therefore the use of a single attribute is enough to characterize a certain PSI point.
On the other hand, datasets that provide dynamic information may be included in the system as well.

The dynamic nature of a process captured in a dataset would imply observable changes at diurnal to sub-diurnal rates, i.e. weeks, days, or even hours. To accommodate for dynamic data, the storage system would need to be updated accordingly. Examples of highly dynamic natural processes are changing weather conditions, and the associated levels of soil moisture. As such, the contribution of shrinking and swelling behaviour of soils could be better understood.
When considering the desired table structures to accommodate for dynamic data, it should be noted that the process of capturing the physical processes and the dynamic nature of certain datasets can prove to be a challenging task. One approach involves the storage of time-dependent information in separate columns according to the date of observation, i.e. timestamp, date string, or date number. The more sophisticated database systems, intended to store highly dynamic data, should account for frequent updates in the form of new entries within the database. However, this highlights the need for appropriate indexing tools and structures, intended for fast and efficient storage and retrieval of information in the form of queries.

7.3.2. Deep Subsurface Models

The inclusion of deep subsurface models in a three-dimensional space is recommended to better understand the deep deformation processes, which helps the interpretation of the InSAR observations and vice versa. In combination with the Bodemkaart and GKN datasets, which provide detailed classifications of the shallow subsurface (<1.50 m depth), deep subsurface models can either update or be updated by the InSAR observations, following the concept of a feedback loop. Such a system could be applied in the study of subsidence due to natural gas, liquid or solid extraction, with the most noteworthy example in the Netherlands being the Groningen case.

Bibliography

Allison, L. (2019). Binary Trees. URL: http://www.allisons.org/ll/AlgDS/Tree/.

Aref, W. and H. Samet (1991). Extending a DBMS with Spatial Operations. Vol. 525. Zurich, Switzerland: Gunther and H.-J; Schek, editors., Advances in Spatial Databases–2nd Symposium, SSD'91. Springer-Verlag Lecture Notes in Computer Science, pp. 299–318.

Bakhtavar, E. (2010). "Determination of the Optimum Crown Pillar Thickness Between Open-Pit and Block Caving." In: Proceedings of the 29th International Conference on Ground Control in Mining, Morgantown.

Bamler, R. and P. Hartl (1998). "Synthetic Aperture Radar Interferometry". In: Inverse Problems 14, R1–R54.

Bartelme, N. (2000). Geoinformatik – Modelle, Strukturen, Funktionen. 3rd ed. Berlin: Springer.

Bayer, R. (2008). "B-tree and UB-tree". In: Scholarpedia 3(11), p. 7742. DOI: 10.4249/scholarpedia.7742.

Bekendam, R. F. and J. J. Pöttgens (1995). "Ground movements over the coal mines of southern Limburg, The Netherlands, and their relation to rising mine waters". In: Proceedings of the Fifth International Symposium on Land Subsidence, The Hague, October 1995 234, pp. 3–12.

Bland, J. M. and D. G. Altman (1996). "Statistic notes: measurement error". In: BMJ 312(7047), p. 1654. DOI: 10.1136/bmj.312.7047.1654.

Blasby, D. (2001). Building a spatial database in postgresql. URL: http://www.postgis.org/files/OSDB2_PostGIS_Presentation.pdf.

Blaupot Ten Cate, D. H. S. (1910). "De daling van den bodem van Nederland gedurende de laatste twee eeuwen". In: De Ingenieur 40, pp. 1–12.

Bodemdalingskaart (2018). Actuele Bodemdalingskaart Nederland. URL: https://bodemdalingskaart.nl/.

Bouaraba, A., A. Belhadj-Aissa, and D. Closson (2018). "Drastic Improvement of Change Detection Results with Multilook Complex SAR Images Approach". In: Progress In Electromagnetics Research C 82, pp. 55–66. DOI: 10.2528/PIERC17112701.

Brouwer, F., F. de Vries, and D.J.J Walvoort (2018). Basisregistratie Ondergrond (BRO); Actualisatie bodemkaart: herkartering van de bodem in Flevoland. Tech. rep. 143. Wageningen: WOT Natuur & Milieu, p. 52. URL: https://edepot.wur.nl/468672.

Brouwer, F. and M.M. van der Werff (2012). Vergraven gronden: Inventarisatie van 'diepe' grondbewerkingen, ophogingen en afgravingen. Tech. rep. 2336. Wageningen: Alterra, p. 26. URL: https://edepot.wur.nl/217669.

BSG (n.d.). 10 reasons why Geomorphology is important. URL: https://www.geomorphology.org.uk/sites/default/files/10_reasons_geom/index.html.

CBS (2016). Aardgas voor bijna 80 procent op. URL: https://www.cbs.nl/nl-nl/nieuws/2016/37/aardgas-voor-bijna-80-procent-op.

— (2019). Regionale kerncijfers Nederland. URL: https://opendata.cbs.nl/statline/#/CBS/nl/dataset/70072NED/table?dl=2096B.

Ceramicola, S. et al. (2005). "Anomalous Cenozoic subsidence along the 'passive' continental margin from Ireland to mid-Norway". In: Marine and Petroleum Geology 22 (9–10), pp. 1045–1067. DOI: 10.1016/j.marpetgeo.2005.04.005..

Chen, J. et al. (2013). "Research on Geographical Environment Unit Division Based on the Method of Natural Breaks (Jenks)". In: The International Archives of the Photogrammetry, Remote Sensing and Spatial Information Sciences XL-4/W3, pp. 47–50. DOI: 10.5194/isprsarchives-XL-4-W3-47-2013.

Codd, E. F. (1970). "A Relational Model of Data for Large Shared Data Banks". In: Communications of the ACM 13, pp. 377–387. DOI: 362384.362685.

Coevert, M. (2019). "Droogte 2018 laat huizen verzakken". In: Bouwkwaliteit in de Praktijk 3, pp. 18–21.

Comer, D. (1979). “The Ubiquitous B-Tree”. In: Computing Surveys 11 (2), pp. 123–137. DOI: 10.1145/356770.356776.

Commissie Bodemdaling door aardgaswinning (n.d.). Bodemdaling door diepe en ondiepe oorzaken in Groningen. URL: https://www.commissiebodemdaling.nl/files/Microsoft%20Word%20-%20Bodemdaling%20door%20diepe%20en%20ondiepe%20oorzaken%20in%20Groningen2.doc.pdf.

Connolly, T. M. and C. E. Begg (2005). Database Systems – A Practical Approach to Design Implementation and Management. 4th ed. Essex: Pearson Education Limited.

Cuenca, M. C. and R. F. Hanssen (2008). “Subsidence due to peat decomposition in The Netherlands, kinematic observations from radar interferometry”. In: Proceedings of the Fringe 2007 Workshop, pp. 1–6.

Cuenca, M. C., F. J. van Leijen, and R. F. Hanssen (2010). “Shallow subsidence in the Dutch wetlands estimated by satellite radar interferometry”. In: Delft Institute of Earth Observation and Space Systems (DEOS).

de Glopper, R.J. and H.P. Ritzema (2006). “Land subsidence”. In: H. P. Ritzema (Ed.), Drainage Principles and Applications (ILRI Publication) 16, pp. 477–512.

de Man, Y.H.H. (1988). “Surface Subsidence near Douvergenhout and in the Eastern Mining District South-Limburg, the Netherlands.” In: Memoirs of the Centre for Engineering Geology in the Netherlands 58.

de Vries, F., F. Brouwer, and D.J.J. Walvoort (2018). Basisregistratie Ondergrond (BRO); Actualisatie bodemkaart. Herkartering westelijk veengebied Waterschap Drents Overijsselse Delta. Tech. rep. 2887. Wageningen: Wageningen Environmental Research, p. 28. URL: https://edepot.wur.nl/450341.

de Vries, F., D.J. Brus, et al. (2014). Actualisatie bodemkaart veengebieden; Deelgebied 1 en 2 in Noord-Nederland. Tech. rep. 2556. Wageningen: Alterra. URL: https://library.wur.nl/WebQuery/wurpubs/456842.

de Vries, F., W. J. M. de Groot, et al. (2003). De Bodemkaart van Nederland digitaal;. Toelichting bij inhoud, actualiteit en methodiek en korte beschrijving van additionele informatie. Tech. rep. 811. Wageningen: Alterra, Research Instituut voor de Groene Ruimte, p. 48. URL: https://edepot.wur.nl/21850.

de Vries, F., D.J.J. Walvoort, and F. Brouwer (2017). Basisregistratie Ondergrond (BRO); Actualisatie bodemkaart. Herkartering van de eenheden met slappe kleilagen. Tech. rep. 2834. Wageningen: Wageningen Environmental Research, p. 40. URL: https://edepot.wur.nl/423728.

de Waal, J. A., A. G. Muntendam-Bos, and J. P. A. Roest (2015). “Production induced subsidence and seismicity in the Groningen gas field – can it be managed?” In: Proc. IAHS 372, pp. 129–139. DOI: 10.5194/piahs-372-129-2015.

Deltawerken (2004). Geology of the Netherlands. URL: http://www.deltawerken.com/Geology-of-the-Netherlands/112.html.

DINOloket (n.d.). Detaillering van de bovenste lagen met GeoTOP. URL: https://www.dinoloket.nl/detaillering-van-de-bovenste-lagen-met-geotop.

Du, Z. et al. (2018). “Correlating the subsidence pattern and land use in Bandung, Indonesia with both Sentinel-1/2 and ALOS-2 satellite images”. In: Int J Appl Earth Obs Geoinformation 67, pp. 54–68.

Egenhoffer, M. J. (1993). “A Model for Detailed Binary Topological Relationships”. In: Geomatica 47(3&4), pp. 261–273.

Erkens, G., M. J. van der Meulen, and H. Middelkoop (2016). “Double trouble: subsidence and CO2 respiration due to 1,000 years of Dutch coastal peatlands cultivation”. In: Hydrogeol J 24, pp. 551–569. DOI: 10.1007/s10040-016-1380-4.

ESA (n.d.[a]). Level-1 SLC Products. URL: https://sentinel.esa.int/web/sentinel/technical-guides/sentinel-1-sar/products-algorithms/level-1-algorithms/single-look-complex.

— (n.d.[b]). Radar Course 2. 11. Synthetic Aperture Radar (SAR). URL: https://earth.esa.int/web/guest/missions/esa-operational-eo-missions/ers/instruments/sar/applications/radar-courses/content-2/-/asset_publisher/qIBc6NYRXfnG/content/radar-course-2-synthetic-aperture-radar.

— (n.d.[c]). Sentinel-1. URL: https://sentinel.esa.int/web/sentinel/missions/sentinel-1.

— (n.d.[d]). Sentinel-1 – Satellite Description – Orbit. URL: https://sentinel.esa.int/web/sentinel/missions/sentinel-1/satellite-description/orbit.
— (2007). InSAR Principles: Guidelines for SAR Interferometry Processing and Interpretation (ESA TM-19). URL: https://www.esa.int/About_Us/ESA_Publications/InSAR_Principles_Guidelines_for_SAR_Interferometry_Processing_and_Interpretation_br_ESA_TM-19.
— (2014). RADAR and SAR Glossary. URL: https://earth.esa.int/handbooks/asar/CNTR5-2.html#eph.asar.gloss.radsar:RADAR.
ESRI (2005). GIS Topology – An ESRI White Paper.
Fathi, E. (2016). Time Effects on the Mechanisms of Post-Mining Ground Subsidence. URL: http://www.minesurveyors.com.au/files/ISM2016/Presentations/20160913_Tue/B1_2/1340/4_E_Fathi_Salmi.pdf.
Ferretti, A., A. Monti-Guarnieri, et al. (2007). InSAR Principles: Guidelines for SAR Interferometry Processing and Interpretation. Noordwijk, The Netherlands: ESA Publications.
Ferretti, A., C. Prati, and F. Rocca (2000). "Nonlinear Subsidence Rate Estimation Using Permanent Scatterers in Differential SAR Interferometry". In: IEEE Transactions on Geoscience and Remote Sensing 38, pp. 2202–2212. DOI: 10.1109/36.868878.
Finkel, R. A. and J. L. Bentley (1974). "Quad Trees A Data Structure for Retrieval on Composite Keys". In: Acta Informatica 4(1), pp. 1–9. DOI: 10.1007/BF00288933.
Gambolati, G., M. Putti, and P. Teatini (1996). "Land Subsidence". In: Hydrology of Disasters, WSTL 24, pp. 231–268.
Gamma Remote Sensing AG (2007). Interferometric SAR Processing. URL: https://esdynamics.geo.uni-tuebingen.de/wiki/files/remote_sensing/pdf/Docu-InSAR_Processing.pdf.
GITTA (2016). Spatial Queries. URL: http://www.gitta.info/SpatialQueries/en/html/index.html.
Gurevich, A. E. and G. V. Chilingarian (1993). "Subsidence over producing oil and gas fields, and gas leakage to the surface". In: Journal of Petroleum Science and Engineering 9(3), pp. 239–250. DOI: doi.org/10.1016/0920-4105(93)90017-9.
Güting, R. H. (1994). "An Introduction to Spatial Database Systems". In: VLDB 3, pp. 357–399.
Guttman, A. (1984). "R-Trees: A Dynamic Index Structure for Spatial Searching". In: Proceedings of the 1984 ACM SIGMOD international conference on Management of data – SIGMOD '84, pp. 47–57. DOI: 10.1145/602259.602266.
Hanssen, R. F. (2001). Radar Interferometry; Data Interpretation and Error Analysis. Vol. 2. Dordrecht: Kluwer Academic Publishers.
Heitfeld, M., F. Denys, et al. (2015). "Bewertung der Risiken durch Spätfolgen des Steinkohlenbergbaus in Südlimburg/Niederlande." In: Proceedings of the Altbergbau Kolloquium, pp. 130–146.
Heitfeld, M., J. Klunker, et al. (2016). Na-ijlende gevolgen steenkolenwinning Zuid-Limburg – Summary report with integrated Bow-Tie-Analysis. projectgroup GS-ZL.
Hooper, A. et al. (2012). "Recent advances in SAR interferometry time series analysis for measuringcrustal deformation". In: Tectonophysics 514–517, pp. 1–13. DOI: 10.1016/j.tecto.2011.10.013.
HSU (n.d.). Microwave Remote Sensing Overview. URL: http://gsp.humboldt.edu/olm_2016/courses/GSP_216_Online/lesson7-2/overview.html.
Huang, Y. and J.L. van Genderen (2014). Comparison of several multi-look processing procedures in INSAR processing for ERS-12 tandem mode. URL: http://earth.esa.int/workshops/fringe_1996/huang/.
Jena, S.D. and J. Roehrig (2007). A Java Implementation of the OpenGIS^{TM} Feature Geometry Abstract Specification (ISO 19107 Spatial Schema). URL: https://www.researchgate.net/publication/228725565_A_Java_Implementation_of_the_OpenGIS_Feature_Geometry_Abstract_Specification_ISO_19107_Spatial_Schema.
Kadaster (2019). Basisregistratie Topografie: Catalogus en Productspecificaties. URL: https://zakelijk.kadaster.nl/documents/20838/88032/BRT+catalogus+productspecificaties/cb869308-5867-5a9d-626d-2fe290c7e4a6.
Kirscht, M. and C. Rinke (1998). "3D Reconstruction of Buildings and Vegetation from Synthetic Aperture Radar (SAR) Images". In: Hannover University, pp. 1–6.

Knuth, D. E. (2001). The Art of Computer Programming. 2nd ed. Vol. 3: Sorting and Searching. Upper Saddle River, NJ: Addison-Wesley.

Koomen, A.J.M. and G.J. Maas (2004). Geomorfologische Kaart Nederland (GKN); Achtergronddocument bij het landsdekkende digitale bestand. Tech. rep. 1039. Wageningen: Alterra, p. 38. URL: http://content.alterra.wur.nl/Webdocs/PDFFiles/Alterrarapporten/AlterraRapport1039.pdf.

Koster, K. (2017). "3D characterization of Holocene peat in the Netherlands". PhD thesis. Universiteit Utrecht.

Lane, D. M. (n.d.). Online Statistics Education: A Multimedia Course of Study. URL: http://onlinestatbook.com/.

Li, Z. et al. (2019). "Time-series InSAR ground deformation monitoring: Atmospheric delay modeling and estimating". In: Earth-Science Reviews 192, pp. 258–284. DOI: https://doi.org/10.1016/j.earscirev.2019.03.008.

López Dekker, P. et al. (2018a). Lecture notes in Geodesy and Natural Hazards, Module 1: SAR data basics and InSAR processing steps.

— (2018b). Lecture notes in Geodesy and Natural Hazards, Module 6: InSAR Time Series Analysis.

LSU Center for Geoinformatics (n.d.). Tectonic subsidence. URL: http://c4g.lsu.edu/index.php/about-us/fields-of-research/27-tectonic-subsidence.

Martin, J. (1983). Managing the Data Base Environment. 2nd ed. University of California: Pearson Education.

MathWorks (n.d.). Documentation – boxplot. URL: https://nl.mathworks.com/help/stats/boxplot.html.

Maxar Technologies (n.d.). Persistent Scatterer (PS) InSAR. URL: https://mdacorporation.com/geospatial/international/products-services/insar/technology/permanent-scatterer-insar.

McGraw-Hill (2014). Troposphere. URL: https://www.accessscience.com/content/712200.

McKenzie, D. (1978). "Some remarks on the development of sedimentary basins". In: Earth and Planetary Science Letters 40(1), pp. 25–32. DOI: 10.1016/0012-821X(78)90071-7.

McKilliam, R.G. et al. (2010). "Frequency Estimation by Phase Unwrapping". In: IEEE Transactions on Signal Processing 58, pp. 2953–2963.

Minderhoud, P.S.J. et al. (2018). "The relation between land use and subsidence in the Vietnamese Mekong delta". In: Sci Total Environ 634, pp. 715–726. DOI: 10.1016/j.scitotenv.2018.03.372.

Ministerie van Binnenlandse Zaken en Koninkrijksrelaties (2018). Catalogus Basisregistratie Adressen en Gebouwen. URL: https://www.geobasisregistraties.nl/documenten/publicatie/2018/03/12/catalogus-2018.

Ministerie van Infrastructuur en Milieu (2013). Basisregistratie grootschalige topografie Gegevenscatalogus BGT 1.1.1. URL: https://www.geonovum.nl/uploads/standards/downloads/BGTGegevenscatalogus111.pdf.

NAM (n.d.[a]). Aardbevingen (Gr.) URL: https://www.nam.nl/feiten-en-cijfers/aardbevingen.html#iframe=L2VtYmVkL2NvbXBvbmVudC8_aWQ9YWFyZGJldmluZ2Vu.

— (n.d.[b]). Bodemdaling Noord-NL. URL: https://www.nam.nl/feiten-en-cijfers/bodemdaling.html#iframe=L2VtYmVkL2NvbXBvbmVudC8_aWQ9Ym9kZW1kYWxpbmc.

— (2011). Aardgas in Nederland. URL: https://web.archive.org/web/20110809080933/http://www.nam.nl/home/content/nam/general/natural_gas_netherlands/.

Neuendorf, K. K. E., J. P. Mehl Jr., and J. A. Jackson (2005). Glossary of Geology. 5th ed. Alexandria, Virginia: American Geological Institute.

NOS (2019). Gaswinning Groningen stopt al in 2022. URL: https://nos.nl/artikel/2301110-gaswinning-groningen-stopt-al-in-2022.html.

NUS (n.d.). RADARSAT products. URL: https://crisp.nus.edu.sg/rsat/rsat_prod.html.

PDOK (n.d.[a]). AHN3 downloads. URL: https://downloads.pdok.nl/ahn3-downloadpage/.

— (n.d.[b]). Dataset: Basisregistratie Grootschalige Topografie (BGT). URL: https://www.pdok.nl/introductie/-/article/basisregistratie-grootschalige-topografie-bgt-.

— (n.d.[c]). Dataset: Basisregistratie Ondergrond (BRO). URL: https://www.pdok.nl/introductie/-/article/basisregistratie-ondergrond-bro-.

— (n.d.[d]). Dataset: Basisregistratie Topografie (BRT) TOPraster. URL: https://www.pdok.nl/introductie/-/article/dataset-basisregistratie-topografie-brt-topraster.
— (n.d.[e]). PDOK Viewer – Basisregistratie Ondergrond (BRO). URL: https://www.pdok.nl/viewer/.
Peebles P. Z., Jr. (1998). Radar Principles. John Wiley and Sons, Inc.
Penn State College of Earth and Mineral Sciences (2018). The Ionospheric Effect. URL: https://www.e-education.psu.edu/geog862/node/1715.
pgAdmin (n.d.). pgAdmin – PostgreSQL Tools. URL: https://www.pgadmin.org/.
PostGIS (n.d.[a]). Introduction to PostGIS 15. Spatial Indexing. URL: https://postgis.net/workshops/postgis-intro/indexing.html.
— (n.d.[b]). Introduction to PostGIS 2. Introduction. URL: https://postgis.net/workshops/postgis-intro/introduction.html.
— (n.d.[c]). Introduction to PostGIS 8. PostGIS Reference. URL: https://postgis.net/docs/reference.html.
— (n.d.[d]). PostGIS – Spatial and Geographic objects for PostgreSQL. URL: https://postgis.net/.
Radartutorial (n.d.). Synthetic Aperture Radar. URL: https://www.radartutorial.eu/20.airborne/ab07.en.html.
Recare-Hub (2018). Case Study Experiment - decline in organic matter in peat soils. URL: https://www.recare-hub.eu/case-studies/veenweidegebied-the-netherlands.
Rosner, P. (2011). "Der Grubenwasseranstieg im Aachener und Südlimburger Steinkohlenrevier - Eine hydrogeologisch-bergbauliche Analyse der Wirkungszusammenhänge". RWTH Aachen.
Samet, H. (1990). "Applications of Spatial Data Structures". In: Addison-Wesley.
Samieie-Esfahany, S. et al. (2009). "On the effect of horizontal deformation on InSAR subsidence estimates." In: Proceedings of FRINGE.
Schiermeier, Q. (2010). "Few fishy facts found in climate report". In: Nature 466(170), p. 170. DOI: 10.1038/466170a.
SFU (n.d.). Course Central – R-Tree. URL: https://www2.cs.sfu.ca/CourseCentral/454/jpei/slides/R-Tree.pdf.
Simons, M. and P. A. Rosen (2007). "Interferometric Synthetic Aperture Radar Geodesy". In: Treatise on Geophysics 3, pp. 391–446. DOI: https://library.itc.utwente.nl/papers_2016/msc/aes/haque.pdf.
Skolnik, M. I. (1962). Introduction To Radar Systems. 2nd ed. Singapore: McGraw-Hill Book Company.
STIBOKA (1964). Bodemkaart van Nederland 1:50 000 – Toelichting bij kaartblad 43 West Willemstad. URL: https://www.zeeuwsbodemvenster.nl/sites/zl-bodemvenster/files/toelichting_bodemkaart_blad_43west.pdf.
ten Cate, J.A.M. and G.C. Maarleveld (1977). Geomorfologische kaart van Nederland schaal 1 : 50 000. Toelichting op de legenda. Tech. rep. Stichting voor Bodemkartering, Wageningen/Rijks Geologische Dienst, Haarlem.
The PostgreSQL Global Development Group (n.d.). PostgreSQL: The World's Most Advanced Open Source Relational Database. URL: https://www.postgresql.org/.
Thienen-Visser, K. van and P. A. Fokker (2017). "The future of subsidence modelling: compaction and subsidence due to gas depletion of the Groningen gas field in the Netherlands". In: Netherlands Journal of Geosciences —- Geologie en Mijnbouw 96–5, s105–s116. DOI: 10.1017/njg.2017.10.
TU Delft (2014). Coal Mining in the Netherlands. URL: https://www.tudelft.nl/en/ceg/about-faculty/departments/geoscience-engineering/sections/resource-engineering/links/coal-mining-in-the-netherlands/.
— (2018). Nederlandse bodem zakt meer dan verwacht. URL: https://www.tudelft.nl/2018/tu-delft/nederlandse-bodem-zakt-meer-dan-verwacht/.
TU Delft DeepNL (n.d.). Subsidence – Integrating Geodesy and Geophysics to monitor and model the Dutch Subsurface. URL: https://www.tudelft.nl/en/ceg/about-faculty/departments/geoscience-engineering/vacancies/deepnl/tu-delft-vacancies-deepn/subsidence/.
tutorialhorizon (n.d.). Find whether if a Given Binary Tree is Balanced? URL: https://algorithms.tutorialhorizon.com/find-whether-if-a-given-binary-tree-is-balanced/.

UMass (2013). Fundamentals of Consolidation. URL: http://faculty.uml.edu/ehajduk/teaching/14.330/documents/14.3302013consolidation.pdf.

UNAVCO (2014). Principles and Theory of Radar Interferometry. URL: https://www.unavco.org/education/professional-development/short-courses/course-materials/insar/2014-insar-isce-course-materials/InSARPrinciplesTheory_UNAVCO_14.pdf.

USDI (1974). Earth manual: a guide to the use of soils as foundations and as construction materials for hydraulic structures. 2nd ed. U.S. Dept. of the Interior, Bureau of Reclamation.

USGS (2010). Divisions of Geologic Time — Major Chronostratigraphic and Geochronologic Units. URL: https://pubs.usgs.gov/fs/2010/3059/pdf/FS10-3059.pdf.

— (2016). InSAR—Satellite-based technique captures overall deformation "picture". URL: https://volcanoes.usgs.gov/vhp/insar.html.

— (2017). Measuring Land Subsidence. URL: https://ca.water.usgs.gov/land_subsidence/california-subsidence-measuring.html.

USYD (2003). Structures of Sedimentary Basins. URL: http://www.geosci.usyd.edu.au/users/prey/ACSGT/EReports/eR.2003/GroupD/Report2/web%20pages/Types_of_Structures.html.

van den Akker, J. J. H. and R. F. A. Hendriks (2017). "Diminishing peat oxidation of agricultural peat soils by infiltration via submerged drains". In: Proceedings of The Global Symposium on Soil Organic Carbon, pp. 21–23.

van den Born, G. J. et al. (2016). Dalende bodems, stijgende kosten. Den Haag: PBL.

van der Horst, T. (2017). Sinking Yangon; Detection of subsidence caused by groundwater extraction using SAR interferometry and a PSI time-series analysis for Sentinel-1 data. URL: https://repository.tudelft.nl/islandora/object/uuid%3A4b516f68-2e0b-4ffa-99fe-5010523692ab.

van Leijen, F. J. (2014). "Persistent Scatterer Interferometry based on geodetic estimation theory". PhD thesis. Delft University of Technology.

— (2020). Guest Lecture notes in Satellite radar interferometry for deformation measurements.

van Natijne, A. L. (2018). Locating PS-InSAR derived deformation using LiDAR point clouds. URL: https://repository.tudelft.nl/islandora/object/uuid%3Aa3009786-9b1b-4e57-ae1a-23aef33bcfa5?collection=education.

van Waning, H. W. (2014). A feasibility study of building monitoring and forensic engineering with Interferometric Synthetic Aperture Radar. URL: https://repository.tudelft.nl/islandora/object/uuid%3A89d652f8-39c1-4100-86a8-2c975e02ab5d?collection=education.

W3Schools (n.d.). SQL Operators. [Online; accessed 9-December-2019]. URL: https://www.w3schools.com/sql/sql_operators.asp.

Wesselingh, F. (n.d.). Reconstructies tijdvakken – 500 miljoen jaar Nederland. URL: https://www.geologievannederland.nl/tijd.

Wikipedia contributors (2018). Ontstaan van de Nederlandse ondergrond — Wikipedia, The Free Encyclopedia. [Online; accessed 20-March-2019]. URL: https://nl.wikipedia.org/wiki/Ontstaan_van_de_Nederlandse_ondergrond.

— (2019a). Bodemclassificatie — Wikipedia, The Free Encyclopedia. [Online; accessed 28-February-2020]. URL: https://nl.wikipedia.org/wiki/Bodemclassificatie.

— (2019b). Carex — Wikipedia, The Free Encyclopedia. [Online; accessed 1-March-2020]. URL: https://nl.wikipedia.org/wiki/Carex.

— (2019c). Delta Works — Wikipedia, The Free Encyclopedia. [Online; accessed 15-January-2020]. URL: https://en.wikipedia.org/wiki/Delta_Works.

Wong, T. E., D. A. J. Batjes, and J. de Jager (2007). Geology of the Netherlands. 1st ed. Aksant en KNAW.

WUR (n.d.). Bodemkaart 1 : 50 000. URL: https://www.wur.nl/nl/show/Bodemkaart-1-50-000.htm.

— (2017). Geomorfologische kaart van Nederland 1:50 000. URL: https://legendageomorfologie.wur.nl/.

Xie, X. and P. Heller (2006). "Plate tectonics and basin subsidence history". In: Geological Society of America Bulletin 121(1-2), pp. 55–64. DOI: 10.1130/b26398.1..

Xiong, S., J-P. Muller, and G. Li (2017). “The Application of ALOS/PALSAR InSAR to Measure Subsurface Penetration Depths in Deserts”. In: Remote Sensing 9, p. 638. DOI: 10.3390/rs9060638.

Young, A. (1980). Tropical Soils and Soil Survey. 1st ed. New York: Cambridge University Press.

Zhang, X and Z. Du (2017). “Spatial Indexing”. In: The Geographic Information Science Technology Body of Knowledge John P. Wilson. DOI: 10.22224/gistbok/2017.4.12.

A

Spatial function examples from PostGIS

As an extension of table 4.1, table A.1 provides explanations to the mentioned example functions. For a full overview of the extensive list of PostGIS functions, the reader is referred to PostGIS n.d.(c).

Example Function	Meaning
ST_SetSRID	Set the SRID on a geometry to a particular integer value.
ST_Transform	Return a new geometry with its coordinates transformed to a different spatial reference system.
ST_Geohash	Return a GeoHash representation of the geometry.
AddGeometryColumn	Adds a geometry column to an existing table.
DropGeometryColumn	Removes a geometry column from a spatial table.
Find_SRID	Returns the SRID defined for a geometry column.
UpdateGeometrySRID	Updates the SRID of all features in a geometry column, and the table metadata.
GeometryType	Returns the type of a geometry as text.
ST_Boundary	Returns the boundary of a geometry.
ST_Dimension	Returns the topological dimension of a geometry.
ST_Envelope	Returns a geometry representing the bounding box of a geometry.
&&	Returns TRUE if A's 2D bounding box intersects B's 2D bounding box.
@	Returns TRUE if A's bounding box is contained by B's.
~=	Returns TRUE if A's bounding box is the same as B's.
ST_Collect	Creates a GeometryCollection or Multi* geometry from a set of geometries.
ST_MakePoint	Creates a 2D, 3DZ or 4D Point.
ST_MakeLine	Creates a Linestring from Point, MultiPoint, or LineString geometries.
ST_MakePolygon	Creates a Polygon from a shell and optional list of holes.

Table A.1: Example functions and their meanings, as presented in table A.1 from the PostGIS functions catalog in PostGIS n.d.(c).

B

Additional Datasets for PSI Enrichment

Dataset	Organization	Contents	Layers	Record
AHN (1,2,3)	RWS	Elevation [m]	Raster, Vector[1]	1997 – 2019
BAG	Kadaster	Addresses, buildings	Vector	2009
BRT	Kadaster	Topography	Raster, Vector	2012

Table B.1: Overview of auxiliary datasets, recommended for further study, presented alongside their respective organizations, including descriptions of their contents, layer types (vector or raster), and the year of recording. These include three possible sets from Actueel Hoogtebestand Nederland (AHN) by Rijkswaterstaat (RWS), and both from Kadaster; Basisregistratie Adressen en Gebouwen (BAG) and Basisregistratie Topografie (BRT).

B.1. AHN

AHN is a digital elevation model (DEM) for the Netherlands. Height measurements are performed with the use of laser altimetry from an airplane or helicopter. From the laser signal return time and the position of the aircraft, recorded with the use of an inertial measurement unit (IMU), precise elevation results are obtained. This technique is known as 'Light Detection And Ranging' (LiDAR).
Three datasets of AHN are available, with different point densities and levels of precision. These are documented and made available for download as digital terrain models (DTM) or as digital surface models (DSM) by Publieke Dienstverlening Op de Kaart (PDOK). The DTM is designed as a ground level map, in which all the points classified as 'maaiveld', i.e. 'ground level', are resampled to a raster based on the squared inverse distance weighting (IDW) method. Points that belong to other classes, e.g. buildings, bridges, etc. are left out of the resampling procedure. The DSM contains the 'raw' data, in which all points, except for those classified as 'water' are included in the final raster (PDOK n.d.[a]). The AHN datasets are provided at different resolutions: 5m, 25m or 100m for AHN1, and 0.5m or 5m for AHN 2 and AHN 3. Figure B.1 shows the the AHN 2 dataset as 5m resolution DSM rasters. AHN 2 is shown instead of AHN 3, since the latter does not (yet) show the elevation of the entirety of the Netherlands[2], as it does not include parts of Friesland, Groningen, Drenthe and Overijssel.

[2] As of November 2019.

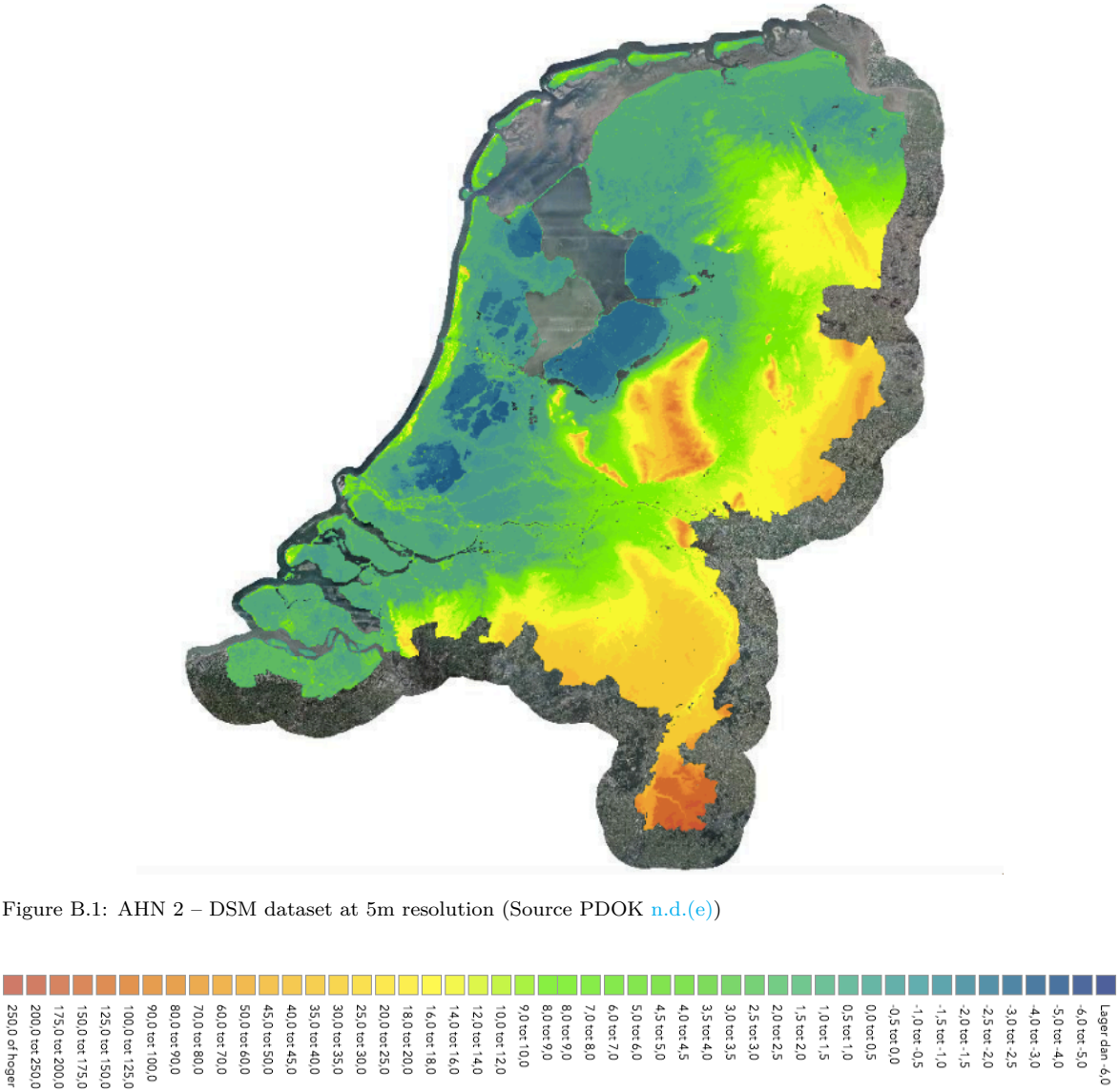

Figure B.1: AHN 2 – DSM dataset at 5m resolution (Source PDOK n.d.(e))

The main reason to include the AHN datasets in this research, and thus to add their information to the database, is the following; As PS points have relatively poor geolocation estimates, this limits the ability to link the deformation behaviour to the targets, i.e. buildings, streets, and other types of infrastructure (van Natijne 2018). Thus, linking precise LiDAR elevation measurements to the S1-InSAR dataset may result in an overall improvement of the geolocation estimates for the observed deformation trends. In the PSI technique the most coherent InSAR points are selected. As these are mainly reflections from stable objects, i.e. buildings, streets, and roads, the DSMs from AHN are more useful references than the DTMs.

B.2. BAG

As part of the Dutch 'basisregistraties', i.e. 'base registers', BAG is the register that contains address, residential and building related information. Moorings and stands for residential, commercial, and recreational usage are also included in the BAG register. Table B.2 provides an overview of the attributes contained in BAG, including their descriptions and identification codes to characterize the different features, or 'objects'.

Object (NL)	Object (EN)	Attributes & Relations
Woonplaats	Residence	name, geometry, status
Openbare Ruimte	Public Space	name, type, status, situated in related residence
Nummeraanduiding	Index	house number, house letter, house number addition, postal code, type of addressable object, status, situated in related residence, situated in related public space
Pand	Building / House	geometry, construction year, status
Verblijfsobject	Accomodation Object	geometry, purpose of use, area, status, part of related building, primary address, secondary address
Standplaats	Stand	geometry, status, primary address, secondary address
Ligplaats	Mooring	geometry, status, primary address, secondary address

Table B.2: Overview of the registered BAG objects and their attributes and relations. The features presented in this table are based on the BAG catalogue by Ministerie van Binnenlandse Zaken en Koninkrijksrelaties 2018.

Made available by Kadaster as an open-source dataset, the information from BAG can be implemented in geographic information systems (GIS). The coupling between InSAR derived deformation and BAG data may in the future be provided to the municipalities, insurance companies, and housing corporations concerned with the objects contained in BAG. With this information at their disposal, the stakeholder parties could more easily carry out the processes of planning and intervening in the construction and maintenance of the private and public space.

B.3. BRT

Basisregistratie Topografie (BRT) contains digital topography records at different scales, which are made available as open data by Kadaster. The open-source information products include TOPNL and TOPraster files. TOPNL datasets are object oriented, whereas TOPraster files contain the same information as the 'analog' map series by Kadaster, but are designed for applications where it is not necessary to alter the map image (PDOK n.d.[d]). Downloads for the raster and vector sets are made available by Kadaster at different scales, as listed in table B.3. The TOP10NL data from BRT is divided into different object classes, summarized in Table B.4. As the TOPNL dataset contains vector shapefiles, the objects are either represented as points, lines, or polygons. As such, table B.4 also specifies the possible geometry types of the different object classes: point, line, or polygon.

Layer	Dataset	Scale
Vector	TOP10NL	1:10.000
	TOP50NL	1:50.000
	TOP100NL	1:100.000
	TOP250NL	1:250.000
	TOP500NL	1:500.000
	TOP1000NL	1:1.000.000
Raster	TOP25raster	1:25.000
	TOP50raster	1:50.000
	TOP100raster	1:100.000
	TOP250raster	1:250.000
	TOP500raster	1:500.000
	TOP1000raster	1:1.000.000

Table B.3: Available vector and raster BRT datasets at different scales, based on PDOK n.d.(d).

Object	Point	Line	Polygon
Road section	+	+	+
Railroad section	+	+	-
Water section	+	+	+
Building	+	-	+
Terrain	-	-	+
Arrangement element	+	+	-
Relief	-	+	-
Elevation	+	+	-
Registrative area	-	-	+
Geographic area	+	-	+
Location	+	-	+
Functional area	+	-	+
Plantopography	+	+	+

Table B.4: Listing of the BRT TOP10NL physical objects and their geometries: point, line, or polygon, based on the BRT catalogue by Kadaster 2019. The + and - signs indicate whether or not the object is available as the respective geometry (point/line/polygon) in BRT.

The characteristics of the individual BRT objects are stored in the dataset as attributes. These

attributes include identification, geometry, temporal, and meta characteristics. The temporal attributes include the start and end dates of the physical objects, as these are replaced when they are no longer up to date. To keep track of these changes, the registration time and end-registration attributes are assigned to the objects.

C

Nationwide Soil Deformation Results – Additional Visualizations

C.1. Deformation – Soil type: satellite track comparisons

An additional analysis is performed on the comparison between the satellite track samples in terms of their differing soil deformation responses. Here, we keep in mind the offset of each track from the spatial reference, as shown in Table 4.5. Thus, instead of comparing the different soil type – deformation responses per satellite track sample, the track sample results are shown and compared as part of their respective Bodemkaart soil classes.

The following sets of figures and tables contain the results for the nationwide deformation analysis, in which the satellite track samples are compared for each of the soil type classes. As an elaboration piece to the deformation – soil type results presented in Chapter 4, the same visual and tabular representations are at hand: Figures C.1 – C.6 contain the normalized histograms of the vertical linear-deformation projection results per soil type class, table C.1 summarizes the linear deformation results, and the median deformation time series are presented in Figures C.7 – C.12.

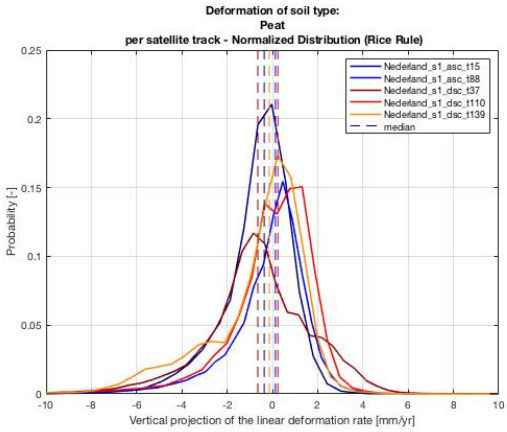

Figure C.1: Soil type – peat: Normalized distribution & median of vertical linear deformation projections (mm/yr) per satellite track sample.

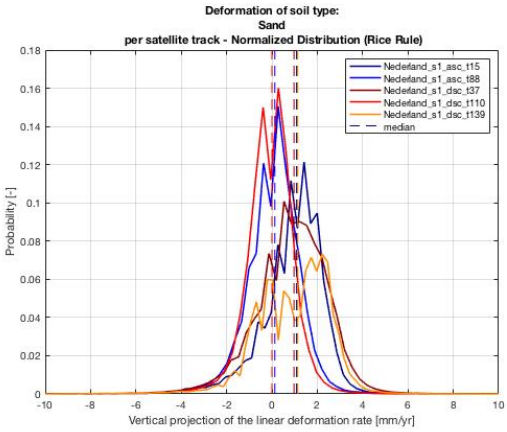

Figure C.2: Soil type – sand: Normalized distribution & median of vertical linear deformation projections (mm/yr) per satellite track sample.

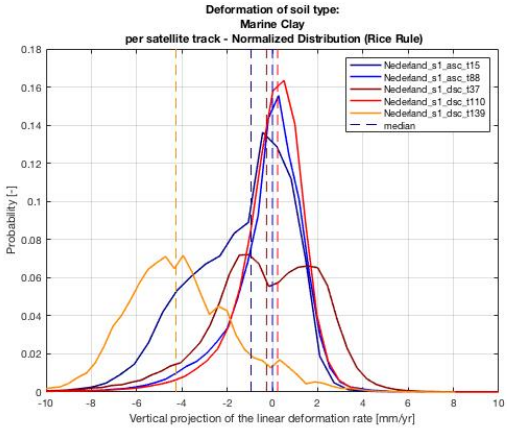

Figure C.3: Soil type – marine clay: Normalized distribution & median of vertical linear deformation projections (mm/yr) per satellite track sample.

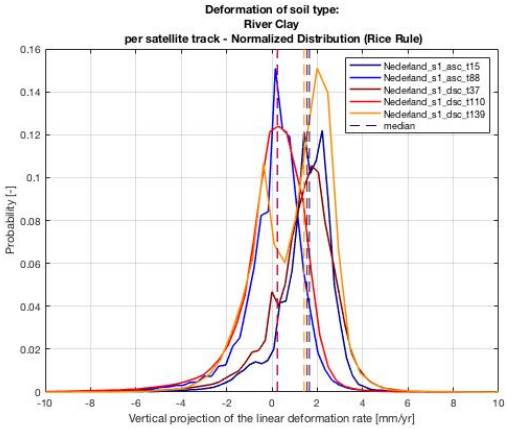

Figure C.4: Soil type – river clay: Normalized distribution & median of vertical linear deformation projections (mm/yr) per satellite track sample.

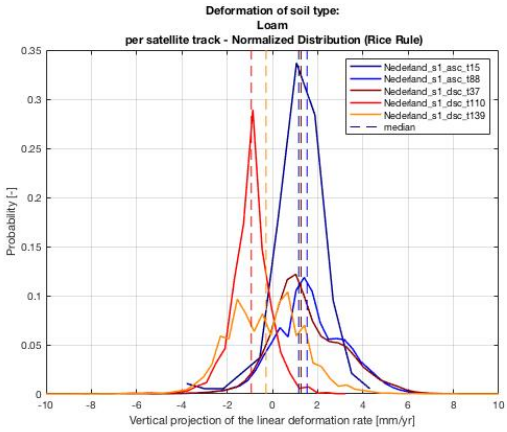

Figure C.5: Soil type – loam: Normalized distribution & median of vertical linear deformation projections (mm/yr) per satellite track sample.

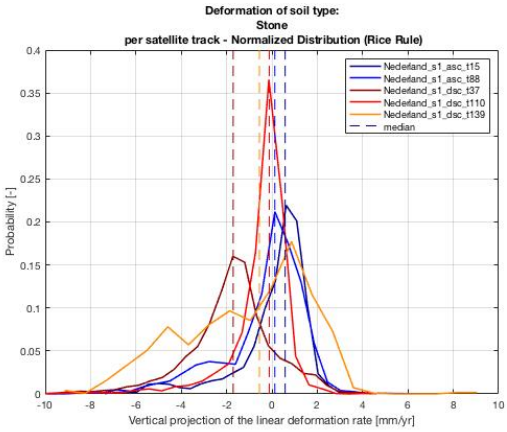

Figure C.6: Soil type – stone: Normalized distribution & median of vertical linear deformation projections (mm/yr) per satellite track sample.

Soil	Track no.	No. pnts [-]	Mean [mm/yr]	Med [mm/yr]	Std [mm/yr]	Skew [-]	Min [mm/yr]	Max [mm/yr]	Pctl10 [mm/yr]	Pctl90 [mm/yr]
Peat	asc_15	76 930	−0.64	−0.36	1.57	−1.70	−43.95	7.60	−2.62	0.95
	asc_88	272 497	−0.25	0.13	2.04	−2.80	−41.56	13.86	−2.38	1.54
	dsc_37	252 935	−0.70	−0.65	2.58	−1.42	−43.94	18.87	−3.54	2.35
	dsc_110	125 952	−0.09	0.24	2.14	−2.91	−45.37	9.82	−2.31	1.84
	dsc_139	66 976	−0.70	−0.14	2.22	−1.45	−37.08	9.88	−3.97	1.41
Sand	asc_15	171 904	0.91	1.09	1.36	−1.04	−12.53	19.47	−0.73	2.35
	asc_88	1 081 513	0.06	0.13	1.19	−0.92	−27.84	38.11	−1.28	1.36
	dsc_37	1 210 432	0.86	0.97	1.61	−0.79	−32.44	38.28	−1.09	2.69
	dsc_110	526 634	−0.08	0	1.05	−0.83	−22.51	31.78	−1.23	1.08
	dsc_139	273 617	0.96	1.14	1.59	−0.76	−19.04	12.24	−0.98	2.71
Marine Clay	asc_15	79 418	−1.41	−0.94	2.25	−0.72	−22.01	31.98	−4.55	1.06
	asc_88	669 297	−0.26	0	1.85	−2.08	−44.66	34.38	−2.47	1.49
	dsc_37	755 141	−0.36	−0.26	2.56	−1.02	−58.18	20.39	−3.42	2.59
	dsc_110	588 999	−0.08	0.23	1.68	−2.34	−45.63	35.66	−1.92	1.51
	dsc_139	57 522	−4.08	−4.26	2.48	0.31	−21.34	8.24	−6.91	−0.85
River Clay	asc_15	70 615	1.46	1.65	1.26	−1.60	−13.32	8.73	0	2.69
	asc_88	578 358	0.04	0.25	1.50	−2.43	−35.79	16.23	−1.48	1.45
	dsc_37	619 884	1.33	1.55	1.66	−2.03	−35.41	14.45	−0.52	2.95
	dsc_110	271 141	0.01	0.23	1.62	−2.49	−34.41	12.91	−1.64	1.58
	dsc_139	76 494	1.01	1.41	1.62	−0.62	−19.79	20.15	−1.13	2.72
Loam	asc_15	190	1.15	1.17	1.16	−0.97	−3.73	4.66	−0.06	2.49
	asc_88	69 858	1.67	1.53	1.62	−0.19	−18.00	11.12	−0.25	3.80
	dsc_37	86 460	1.50	1.26	1.67	−0.04	−19.95	12.82	−0.26	3.75
	dsc_110	5045	−0.98	−0.94	0.91	−1.03	−10.28	2.27	−1.99	0
	dsc_139	45 712	−0.27	−0.28	1.63	0.13	−12.87	13.83	−2.28	1.71
Stone	asc_15	2302	0.10	0.58	1.61	−1.83	−7.31	4.55	−1.87	1.44
	asc_88	5768	−0.33	0.13	1.88	−1.24	−13.46	7.23	−3.11	1.52
	dsc_37	7783	−1.80	−1.71	2.00	−0.89	−15.16	5.28	−4.08	0.56
	dsc_110	4127	−0.45	−0.12	1.37	−3.06	−13.89	4.77	−1.76	0.59
	dsc_139	1242	−1.10	−0.56	2.78	−0.37	−9.26	9.43	−5.08	2.11
Buildings	asc_15	518 645	0.15	0.37	1.76	−0.90	−20.53	34.67	−2.32	2.11
	asc_88	3 527 478	0.15	0.25	1.53	−1.43	−42.08	37.45	−1.45	1.66
	dsc_37	3 716 239	0.50	0.76	2.16	−1.02	−44.48	40.21	−2.13	2.85
	dsc_110	2 195 013	0.03	0.12	1.42	−2.49	−45.27	16.88	−1.40	1.46
	dsc_139	731 678	0.15	0.57	2.51	−1.20	−28.96	11.05	−3.54	2.69

Table C.1: Statistics of the vertical linear deformation projections (mm/yr) comparing the different S1 satellite track responses per soil type sample. These statistics include: Number of points, mean, median, standard deviation, skewness, minimum, maximum, 10th percentile, -and 90th percentile values of the points in a certain satellite track. The colour coding is as follows: Green indicates the highest or 'most positive' statistic found for a certain satellite track. Red indicates the lowest or 'most negative' statistic found for a certain satellite track. Highlighted green indicates the highest or 'most positive' statistic found for a certain satellite track, that re-occurs for the majority of the soil types. Highlighted red indicates the lowest or 'most negative' statistic found for a certain satellite track, that re-occurs for the majority of the soil types.

C.1.1. Linear deformation

As part of Appendix B, the linear deformation results in terms of the comparison between different satellite tracks are presented in Figures C.1 – C.6 and in Table C.1.

Number of points – For the linear deformation results, it should be noted that the different tracks contain different amounts of measurement points, with the most measurements belonging to track 37. This holds for all soil types, except for peat which has more points in track 88. Track 15 contains the least amount of points for most soil type classes, i.e. sand, river clay, loam, and 'buildings'. For the remain soil type classes (peat, marine clay and 'stone'), the least amount of points belong to descending track 139.

Mean & Median deformation – For the majority of the soil types, i.e. sand, river clay, loam and 'buildings', the lowest mean and median linear deformation is observed for descending track 110. However, for the soil type classes 'peat' and 'marine clay', track 110 shows the highest mean and median linear deformation. In the case of marine clay, a strongly negative mean and median deformation trend in the order of -4mm/yr is observed for track 139, as seen in the prior results. Aside from this supposed anomaly, the lowest mean and median results for marine clay are observed in track 15. In terms of upward mean and median linear deformation, there is no clear trend to be observed when comparing the different satellite tracks.

Standard deviation & Skewness – Overall, the highest standard deviation in the deformation results belongs to track 37, which is also the track with the highest number of points for almost all of the soil classes. However, for the buildings class, which has the largest share of measurements in all track samples, the highest standard deviation is found for track 139 which differs by roughly 0.4mm/yr compared to the closest sample, i.e. track 37. For most of the soil type classes, track 110 delivers the lowest standard deviation in its deformation distributions.
In terms of the skewness of the different satellite tracks, presented in Table C.1, track 110 shows the most negative skewness in the linear deformation distributions for all of the soil type classes. In the majority of the cases, i.e. for sand, river clay and 'stone', track 139 shows the lowest level of negative skewness, and positive skewness for marine clay and loam.

Minimum, Maximum, 10th, and 90th-percentile deformation – Whereas descending track 37 shows a trend for the lowest (most negative) linear deformation minima, the lowest 10th-percentile deformation values are mostly observed in track 139. The more moderate (least negative) minima belong to track 15, whereas this 'moderate' trend is found in terms of the 10th-percentile deformation values for track 110.
In terms of the most positive linear deformation maxima for the different soil classes, the results do not show strong differences between the tracks. Track 37 and 139 provide the most positive maximum linear deformation entries across the different soil types. In addition, track 37 shows the most positive 90th-percentile values compared to the other tracks.

Time series deformation

The time series deformation results in terms of the comparison between different satellite tracks are presented in Figures ?? – C.12. In terms of the increase, decrease or stagnation of the satellite track deformation profiles for the different soil type classes, there are a few points of discussion. The most apparent increasing trends in the profiles are observed for the soil types: sand, river clay, and loam. Note that in most cases, tracks 110 and 139 tend to show opposite deformation behavior in comparison to the other tracks. The following examples illustrate this opposite behaviour:

- An increase in the track 110 profile for the peat class, where the other profiles gradually subside (Figure: C.7).
- An decrease in the track 110 profile for the sand class, where the other profiles gradually show a decrease (Figure: C.8).
- A strong decrease in the track 139 profile for the marine clay, where the other profiles show a more gradual decrease to stagnation (Figure: C.9).

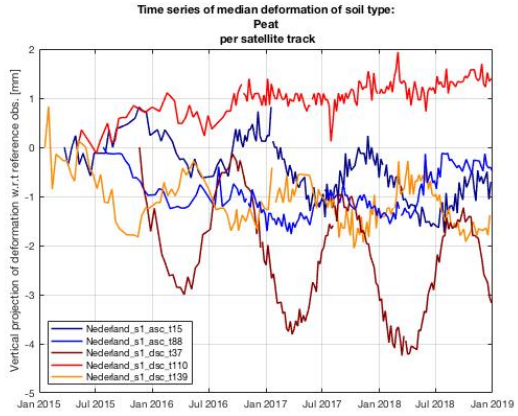

Figure C.7: Soil type – peat: time series of median vertical deformation-rate projections (mm) w.r.t. the respective epoch per satellite track sample.

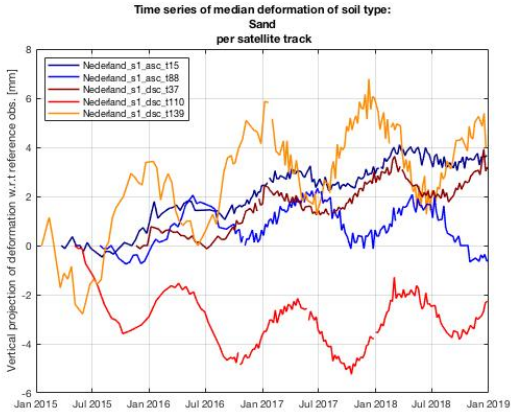

Figure C.8: Soil type – sand: time series of median vertical deformation-rate projections (mm) w.r.t. the respective epoch per satellite track sample.

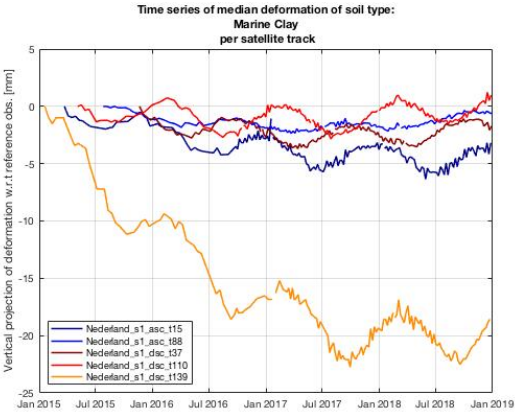

Figure C.9: Soil type – marine clay: time series of median vertical deformation-rate projections (mm) w.r.t. the respective epoch per satellite track sample.

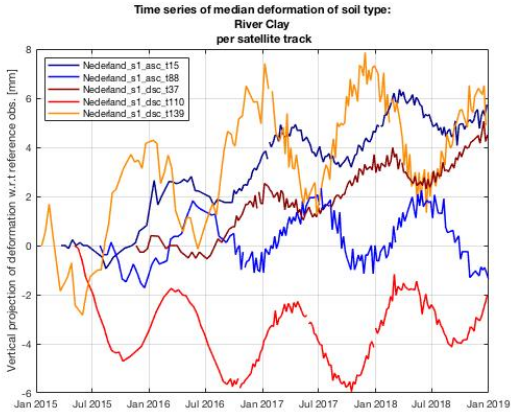

Figure C.10: Soil type – river clay: time series of median vertical deformation-rate projections (mm) w.r.t. the respective epoch per satellite track sample.

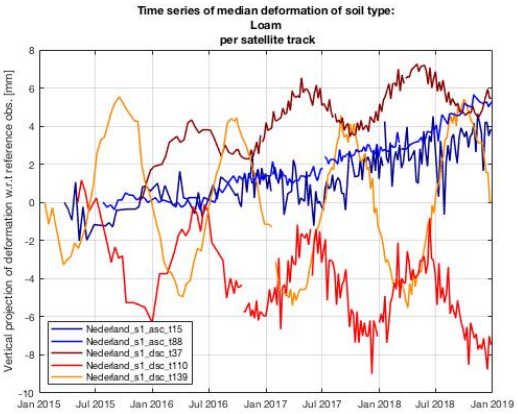

Figure C.11: Soil type – loam: time series of median vertical deformation-rate projections (mm) w.r.t. the respective epoch per satellite track sample.

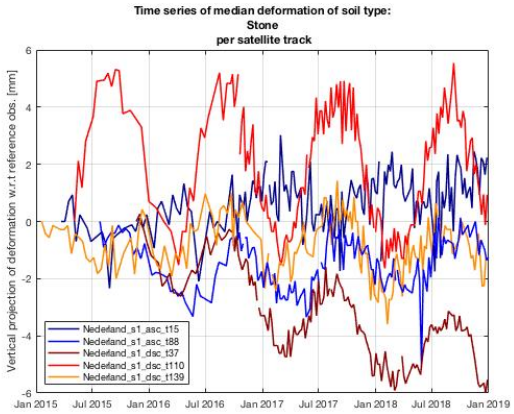

Figure C.12: Soil type – stone: time series of median vertical deformation-rate projections (mm) w.r.t. the respective epoch per satellite track sample.

- A stagnation and slight decrease under the zero-deformation mark in the track 110 profile for the river clay and loam classes (respectively), where most of the other profiles show a gradual increase (Figures: C.10 and C.11).

Furthermore, as observed in most of the soil type – deformation time series figures, the amplitude of the descending track profiles, i.e. tracks 37, 110 and 139, seem to be larger than in the ascending track profiles, i.e. tracks 15 and 88. Especially tracks 110 and 139 show high amplitude profiles, except in the deformation profile of 'peat', in which the amplitude of track 37 is highest.
The differences in the phases of the oscillating time series profiles are once again apparent in the nationwide deformation analysis. No clear distinction can be made in the oscillating behaviour in terms of the ascending or descending nature of the different track profiles. In other words, the phase differences can also be observed internally between the ascending and descending entries within a group, e.g. in the peat time deformation series profile (C.7) when comparing the oscillations of tracks 110 and 139 (both descending).

C.2. Deformation – Soil type: overlap area

An additional soil type – deformation analysis is performed to compare the different satellite track samples based on their common coverage area. The overlap area is presented in Figure C.13, including the convex hulls of Sentinel-1 ascending tracks 15 and 88, and descending tracks 37 and 110 that have been used to perform the intersections needed to define the overlap area. The soil deformation samples of track 139 were left out of this particular analysis, as track 139 does not overlap with track 110. Thus the samples of track 110 are selected instead of the track 139 samples, as up until this part of the study, track 110 has shown more consistent deformation results with respect to the other samples. Note that the soil type 'loam' is left out of this particular analysis, since it is not present in the overlap area.

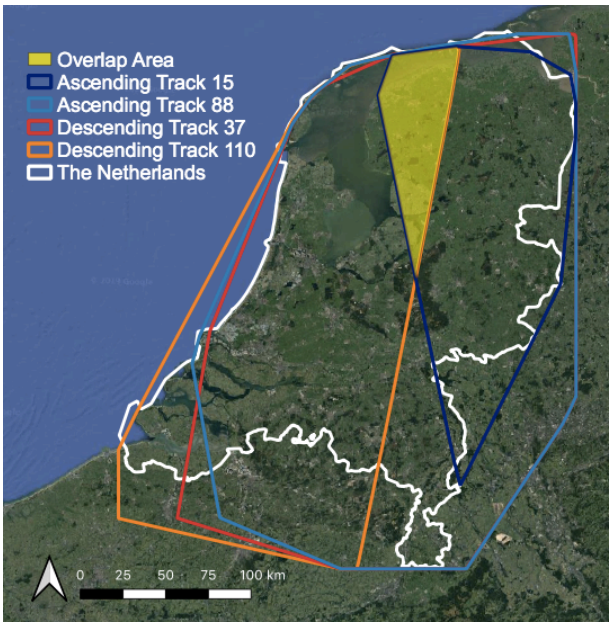

Figure C.13: Overlap coverage area of the following Sentinel-1 satellite tracks; ascending tracks 15 & 88, and descending tracks 37 & 110. These representations are the convex hulls of the point sets, per individual track. A Google satellite map is featured in the background.

The deformation – soil type results from the overlapping satellite coverage area, presented in Figure C.13, are visualized in the following sets of figures and tables. Figures C.14 – C.19 contain the normalized histograms of the vertical linear-deformation projection results per soil type class, table C.2 summarizes the linear deformation results, and the median deformation time series are presented in Figures C.20 – C.25.

C.2.1. Linear deformation

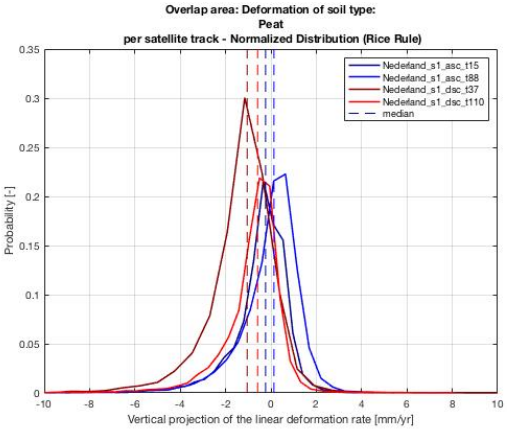

Figure C.14: Soil type – peat: Normalized distribution & median of vertical linear deformation projections (mm/yr) per satellite track sample for the overlapping cover area of all satellite tracks.

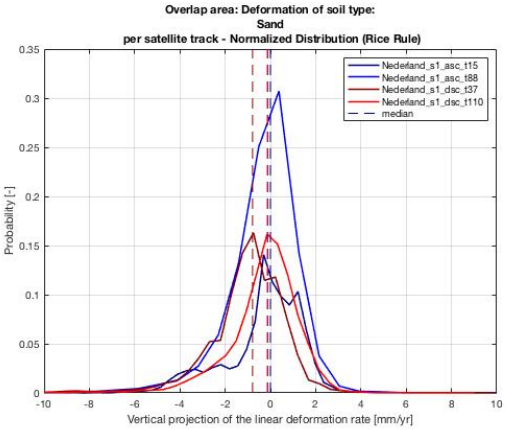

Figure C.15: Soil type – sand: Normalized distribution & median of vertical linear deformation projections (mm/yr) per satellite track sample for the overlapping cover area of all satellite tracks.

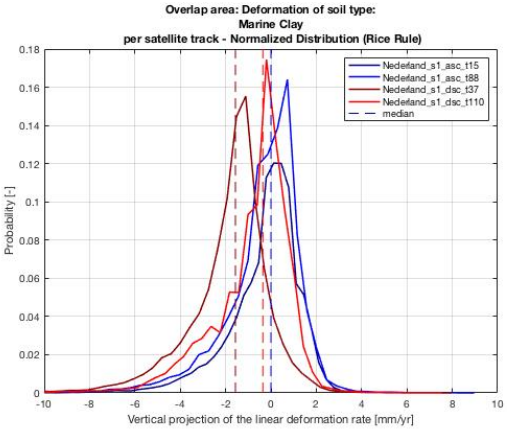

Figure C.16: Soil type – marine clay: Normalized distribution & median of vertical linear deformation projections (mm/yr) per satellite track sample for the overlapping cover area of all satellite tracks.

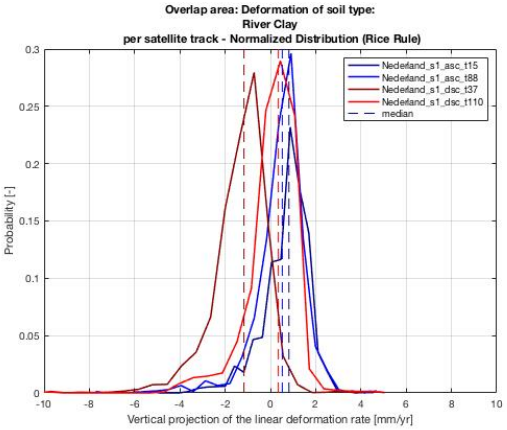

Figure C.17: Soil type – river clay: Normalized distribution & median of vertical linear deformation projections (mm/yr) per satellite track sample for the overlapping cover area of all satellite tracks.

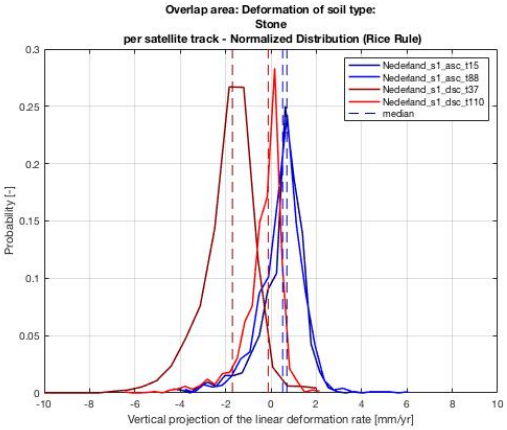

Figure C.18: Soil type – stone: Normalized distribution & median of vertical linear deformation projections (mm/yr) per satellite track sample for the overlapping cover area of all satellite tracks.

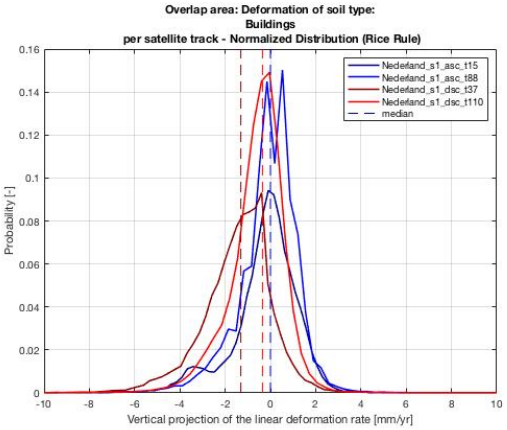

Figure C.19: Buildings: Normalized distribution & median of vertical linear deformation projections (mm/yr) per satellite track sample for the overlapping cover area of all satellite tracks.

Soil	Track no.	No. pnts [-]	Mean [mm/yr]	Med [mm/yr]	Std [mm/yr]	Skew [-]	Min [mm/yr]	Max [mm/yr]	Pctl10 [mm/yr]	Pctl90 [mm/yr]
Peat	asc_15	24 199	−0.45	−0.23	1.28	−2.25	−19.46	5.47	−1.89	0.71
	asc_88	29 718	−0.09	0.13	1.43	−2.40	−21.33	10.76	−1.69	1.19
	dsc_37	33 665	−1.29	−1.05	1.61	−2.23	−30.69	18.87	−3.00	0.13
	dsc_110	26 325	−0.84	−0.59	1.42	−2.59	−18.35	8.30	−2.34	0.35
Sand	asc_15	14 131	−0.32	0	1.74	−0.99	−11.10	7.09	−3.09	1.51
	asc_88	15 555	−0.30	−0.13	1.61	−1.13	−14.74	29.04	−2.08	1.30
	dsc_37	23 930	−1.06	−0.79	1.80	−1.57	−17.72	10.15	−2.99	0.78
	dsc_110	14 986	−0.30	−0.12	1.59	−1.36	−12.85	9.20	−2.21	1.40
Marine Clay	asc_15	44 306	−0.29	0	1.62	−1.58	−15.54	7.87	−2.33	1.29
	asc_88	67 993	−0.39	0	1.79	−1.94	−26.07	9.19	−2.53	1.30
	dsc_37	77 663	−1.86	−1.57	1.89	−1.81	−26.64	8.12	−4.14	0
	dsc_110	57 639	−0.84	−0.36	1.79	−1.82	−23.49	7.68	−3.23	0.83
River Clay	asc_15	2558	0.69	0.82	1.05	−1.37	−6.08	4.68	−0.67	1.76
	asc_88	1705	0.45	0.52	1.12	−1.65	−7.84	4.83	−0.65	1.57
	dsc_37	3201	−1.33	−1.17	1.24	−1.73	−12.71	5.32	−2.72	−0.26
	dsc_110	2244	0.11	0.35	1.15	−2.32	−11.29	5.24	−1.16	1.16
Stone	asc_15	1715	0.50	0.70	1.03	−1.37	−4.42	4.55	−0.70	1.51
	asc_88	1953	0.46	0.52	1.03	−0.36	−3.91	6.12	−0.78	1.56
	dsc_37	2617	−1.87	−1.70	1.28	−2.18	−15.15	2.22	−3.40	−0.65
	dsc_110	2439	−0.37	−0.12	0.90	−1.92	−6.37	2.23	−1.41	0.35
Buildings	asc_15	64 252	−0.23	0	1.46	−1.03	−12.36	6.68	−2.22	1.31
	asc_88	86 468	−0.11	0	1.33	−1.08	−20.00	9.87	−1.73	1.20
	dsc_37	101 688	−1.46	−1.31	1.57	−0.88	−18.38	7.14	−3.40	0.26
	dsc_110	77 505	−0.56	−0.35	1.27	−1.22	−15.00	14.87	−2.12	0.71

Table C.2: Satellite overlap coverage area: Statistics of the vertical linear deformation projections (mm/yr) comparing the different S1 satellite track responses per soil type sample. These statistics include: Number of points, mean, median, standard deviation, skewness, minimum, maximum, 10th percentile, -and 90th percentile values of the points in a certain satellite track. The colour coding is as follows: Green indicates the highest or 'most positive' statistic found for a certain satellite track. Red indicates the lowest or 'most negative' statistic found for a certain satellite track. Highlighted green indicates the highest or 'most positive' statistic found for a certain satellite track, that re-occurs for the majority of the soil types. Highlighted red indicates the lowest or 'most negative' statistic found for a certain satellite track, that re-occurs for the majority of the soil types.

Number of points – For all soil types, the majority of the measurement points in the coverage overlap area belong to track 37, whereas the lowest amount of points within the area are attributed to track 15. This indicates an overall higher point density for track 37 in the cover area, since it is fixed for all the tracks involved.

Mean & Median deformation – Contrary to the nationwide results, the lowest mean and median linear deformation values within the overlap area are observed for descending track 37 instead of descending track 110. For the majority of the soil types, the highest mean and median deformation is attributed to ascending track 15, and in the remaining instances to ascending track 88.

Standard deviation & Skewness – Track 37, which contains the highest amount of points within the coverage area (and in general), shows the largest standard deviation in its distribution for all soil types. The trend for lowest standard deviation varies per soil type between tracks 15 and 110. The most negative levels of skewness belong mostly to track 110, i.e. for soil types peat, river clay, and for the buildings class.

Minimum, Maximum, 10th, and 90th-percentile deformation – The most cases of 'extreme' subsidence, i.e. the minimum and 10th-percentile linear deformation, are identified for track 37, which also shows the strongest negative mean and median deformation results for all soil types. In addition, the lowest (least positive) 90th-percentile linear deformation values are observed in track 37. The most positive deformation in terms of the maximum and 90th-percentile linear trend, is observed mostly in track 88, followed by track 15.

C.2.2. Time series deformation

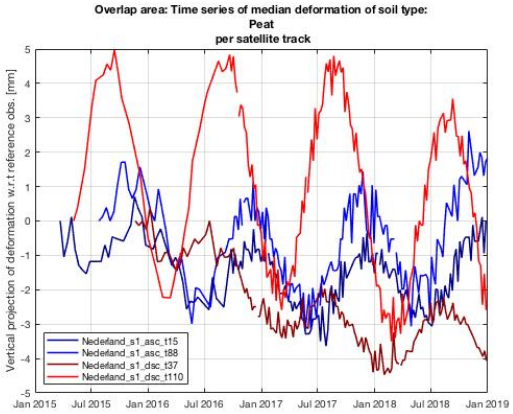

Figure C.20: Soil type – peat: time series of median vertical deformation-rate projections (mm) w.r.t. the respective epoch per satellite track sample for the overlapping cover area of all satellite tracks.

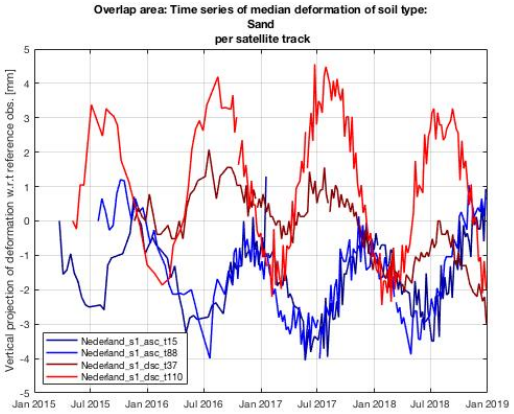

Figure C.21: Soil type – sand: time series of median vertical deformation-rate projections (mm) w.r.t. the respective epoch per satellite track sample for the overlapping cover area of all satellite tracks.

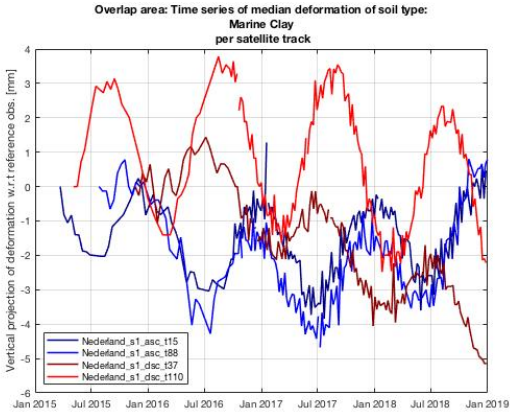

Figure C.22: Soil type – marine clay: time series of median vertical deformation-rate projections (mm) w.r.t. the respective epoch per satellite track sample for the overlapping cover area of all satellite tracks.

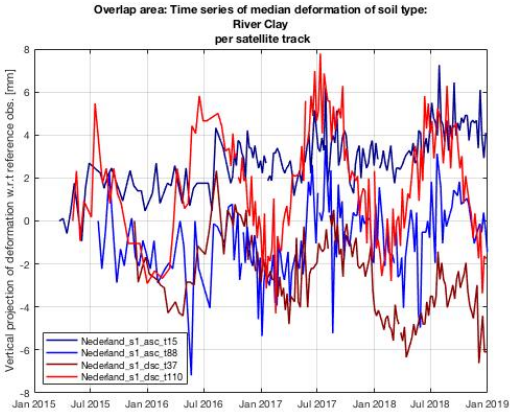

Figure C.23: Soil type – river clay: time series of median vertical deformation-rate projections (mm) w.r.t. the respective epoch per satellite track sample for the overlapping cover area of all satellite tracks.

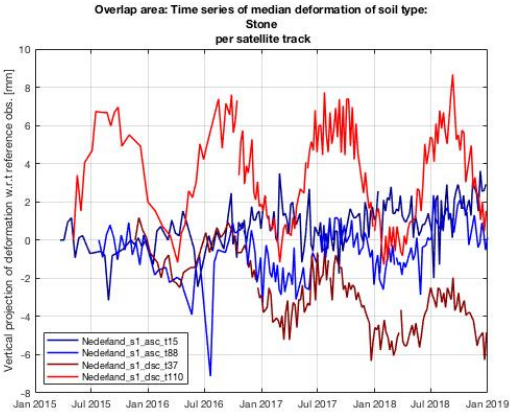

Figure C.24: Soil type – stone: time series of median vertical deformation-rate projections (mm) w.r.t. the respective epoch per satellite track sample for the overlapping cover area of all satellite tracks.

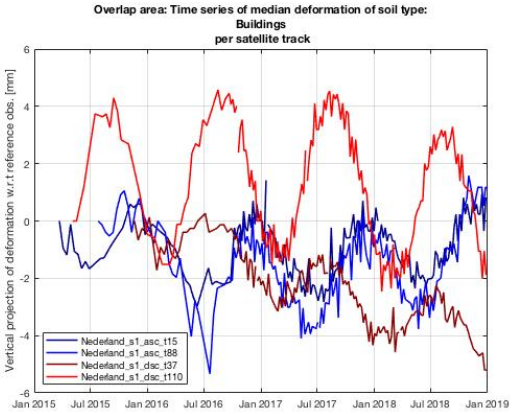

Figure C.25: Buildings: time series of median vertical deformation-rate projections (mm) w.r.t. the respective epoch per satellite track sample for the overlapping cover area of all satellite tracks.

When comparing the different median deformation time series for the different satellite tracks per soil class, no significant difference in the increase or decrease of the profiles is observed. The main differences between the different tracks are seen in the amplitude and phase signatures. Most apparent is the relatively high amplitude in the median profiles of descending track 110, whereas the amplitudes of the remaining track profiles (15, 88 and 37) are quite similar.
Perhaps most interesting is the difference between the ascending and descending satellite track profiles in terms of their phase. Across all soil type samples, the two ascending tracks, i.e. tracks 15 and 88, seem to be in phase with one another, as is the case for the descending tracks, i.e. tracks 37 and 110. For some of the soil types, the ascending profiles seem to be completely 'out of phase' with the descending track profiles. The clearest example of this is found for the sand class in Figure C.21, where the two profile groups almost seem 'mirrored' along a common horizontal axis.

D

South Limburg – Additional Tables and Figures

D.1. Fault System & Mining Concessions

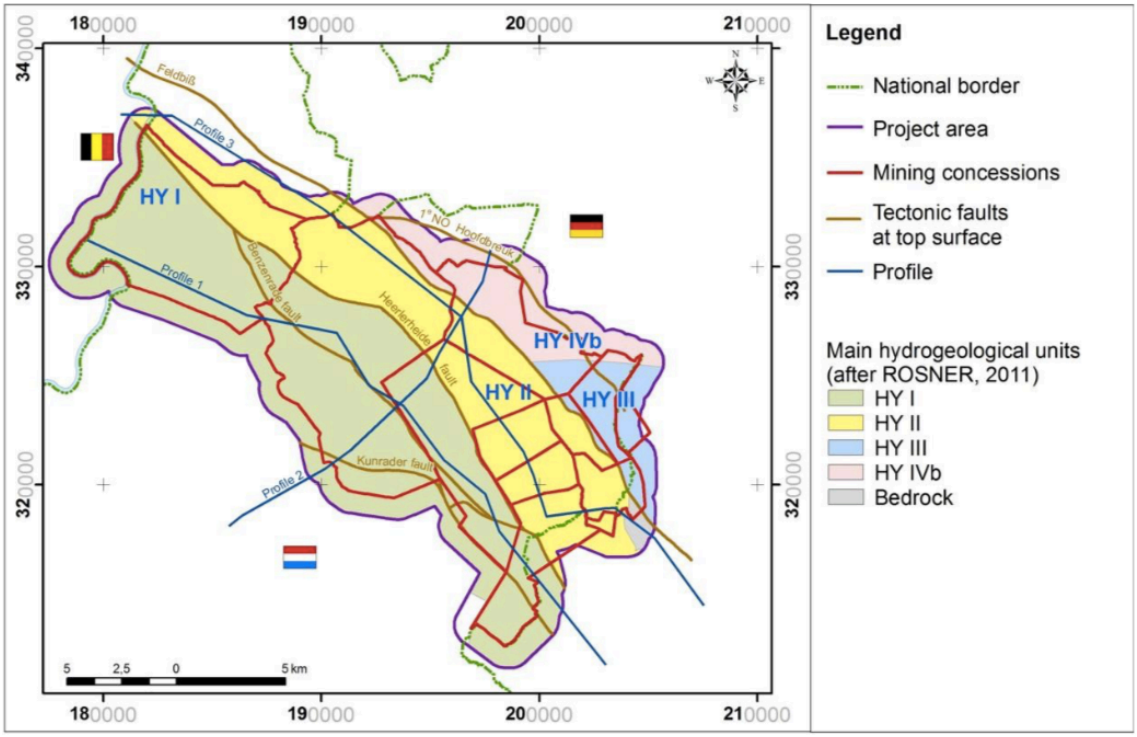

Figure D.1: Main faults and hydrogeological units in the overburden level (HY I – HY IVb) in the South Limburg mining concessions area. Profiles 1, 2, and 3 are given in figures D.2, D.3 and D.4 (Source: Heitfeld, Klunker, et al. 2016; Rosner 2011).

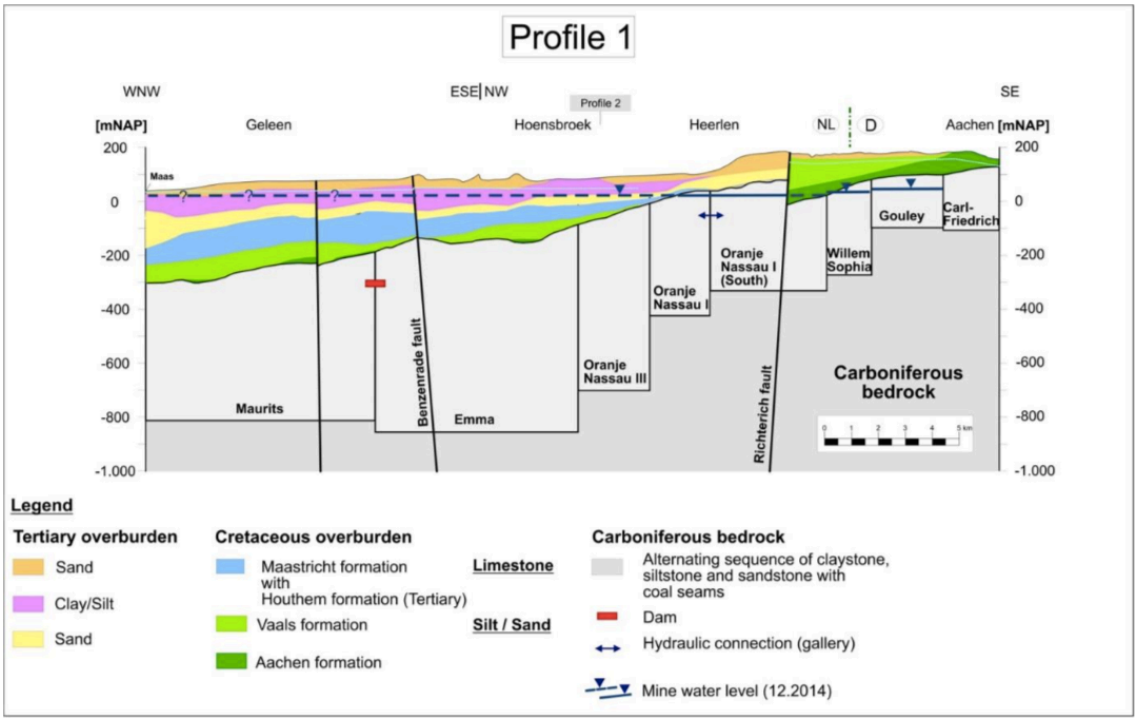

Figure D.2: Cross-section profile 1 (NW-SE) with associated mining concessions. Depth is given in m w.r.t. NAP (Source: Heitfeld, Klunker, et al. 2016; Rosner 2011).

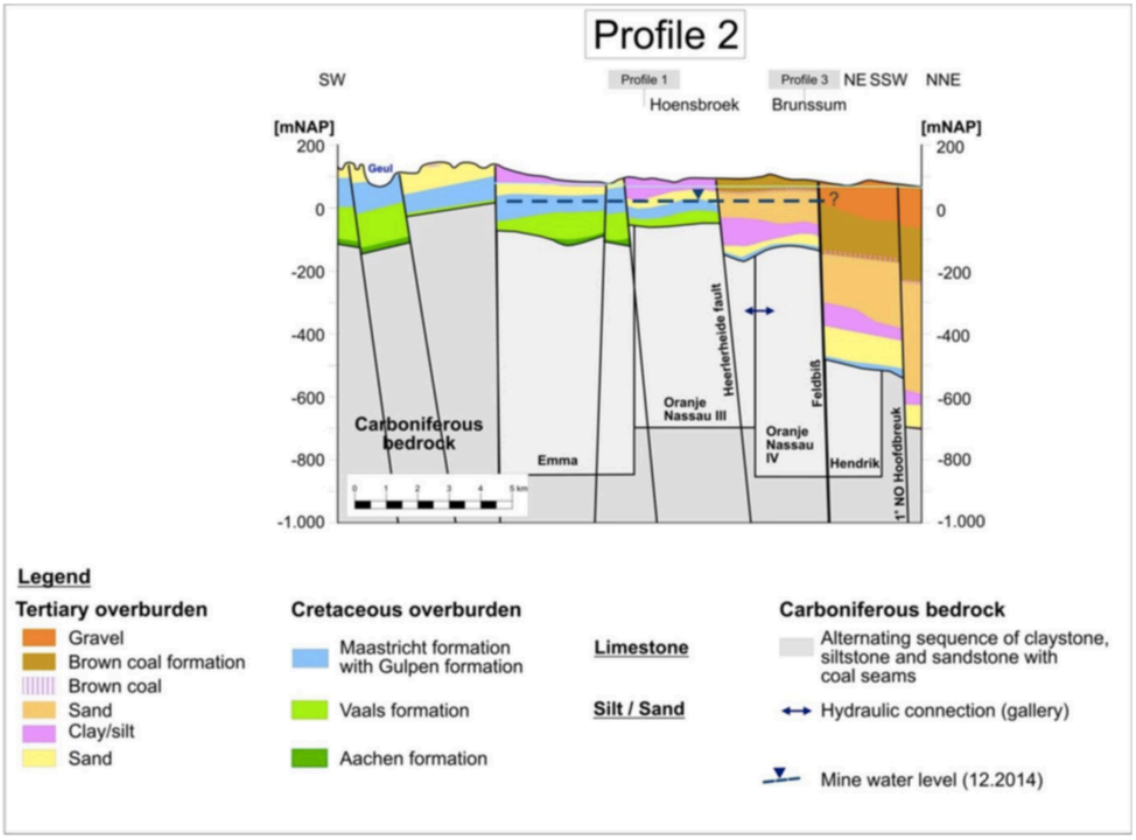

Figure D.3: Cross-section profile 2 (SW-NNE) with associated mining concessions. Depth is given in m w.r.t. NAP (Source: Heitfeld, Klunker, et al. 2016; Rosner 2011).

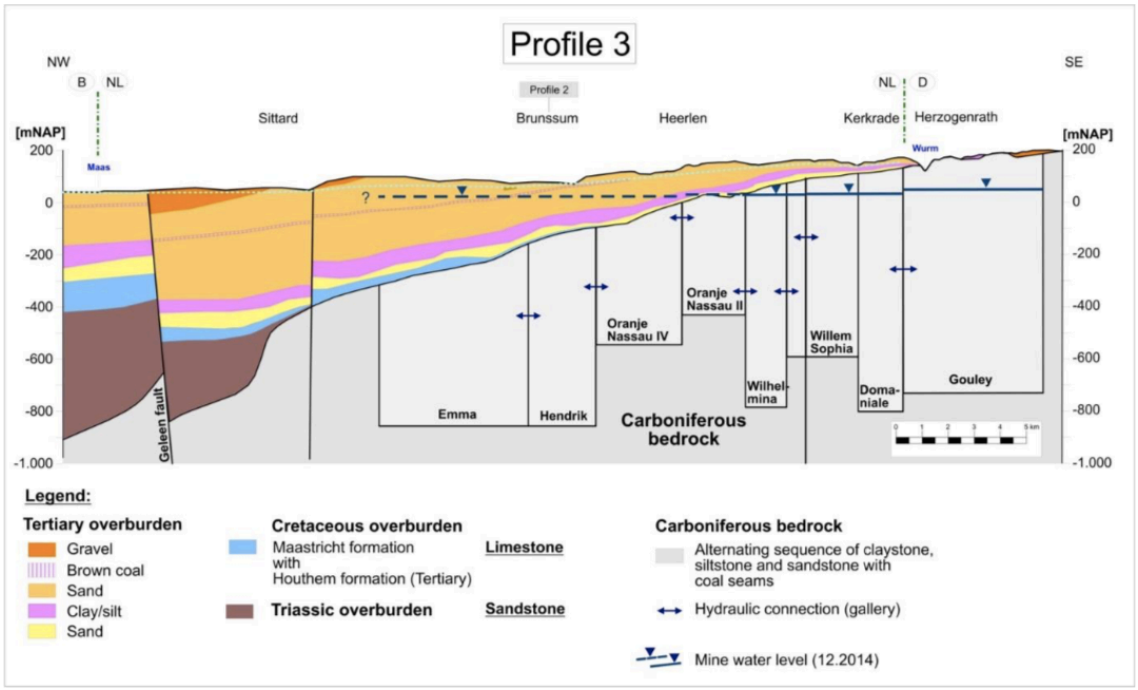

Figure D.4: Cross-section profile 3 (NW-SE) with associated mining concessions. Depth is given in m w.r.t. NAP (Source: Heitfeld, Klunker, et al. 2016; Rosner 2011).

D.2. Historical Near-Surface Mining – Impact Area (EK) Classifications

Impact Category	Color Code	Classification Criteria	Relative probability for future sinkholes/subsidence
EK 1	red	If dip ≥ 36°: – Documentation of past sinkholes. – Evidence of near-surface mining. – Mining activities above uppermost gallery.	high
EK 2	yellow	If dip ≥ 36°: – Documentation of mining in mineable coal seams on level of uppermost gallery. – Outcrop of main coal seam at top of Carboniferous bedrock. If dip < 36°: – main or mineable coal seams show evidence of near-surface mining. – main or mineable coal seams show indication of mining activities above the uppermost gallery.	medium
EK 3	blue	If dip ≥ 36°: – Outcrop of mineable coal seams without documentation of near-surface mining but with likeliness of mining because of the general tectonic situation. If dip < 36°: – Outcrop of main coal seams at the top of the Carboniferous bedrock, even by uncertain documentation.	low
EK 4	green	Remediation measures have been done.	-

Table D.1: Impact categories EK for the outcrops of coal seams in project area 1 (historical near-surface mining), with their selection criteria and relative probability for future sinkholes and/or subsidence, based on Heitfeld, Klunker, et al. 2016.

D.3. Differential Ground Heave – Time Series Deformation (Median, Minimum and Maximum)

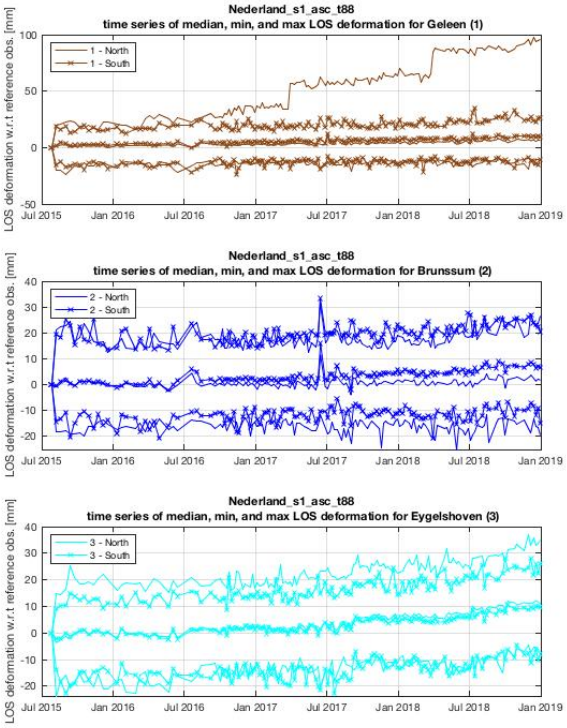

Figure D.5: S1 Ascending Track 88: Time series of the median, minimum and maximum LOS deformation (mm) w.r.t. the epoch (2015-07-26) of the three potential ground heave impact areas in South Limburg.

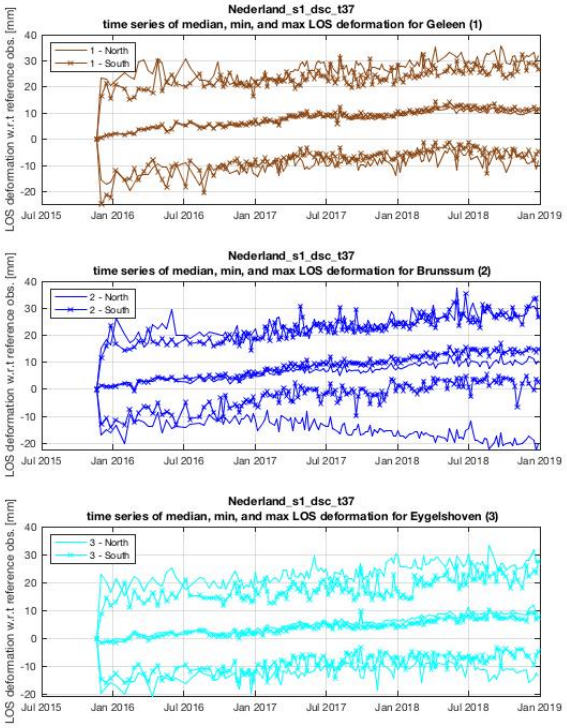

Figure D.6: S1 Descending Track 37: Time series of the median, minimum and maximum LOS deformation (mm) w.r.t. the epoch (2015-11-20) of the three potential ground heave impact areas in South Limburg.

E

South Holland: Total, Deep and Shallow Linear Deformation – Additional Visualizations

E.1. Soil Type Classification Results & Overview

This section provides the total, deep and shallow LOS linear deformation (mm/yr) for all the soil types (shown per soil code) identified within the study area, grouped and listed alphabetically. From all soil classes, a description is provided of the 31 main soil types in table 6.5, selected for analysis in Chapter 6.

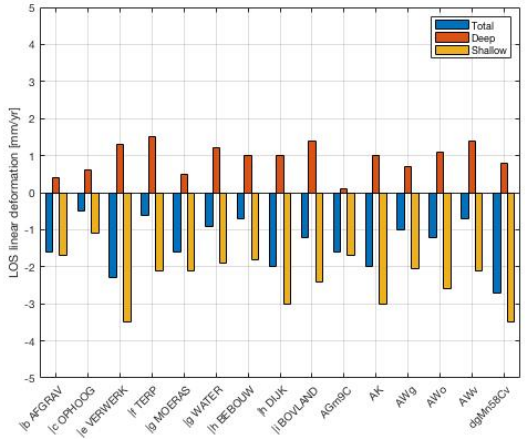
Total
Deep
Shallow
LOS linear deformation [mm/yr]
5
4
3
2
1
0
-1
-2
-3
-4
-5
|b AFGRAV
|c OPHOOG
|e VERWERK
|f TERP
|g MOER4S
|g WATER
|h BEBOUW
|h DIJK
|j BOVLAND
AGmsC
AK
AWg
AWo
AWw
dgMm58Cv

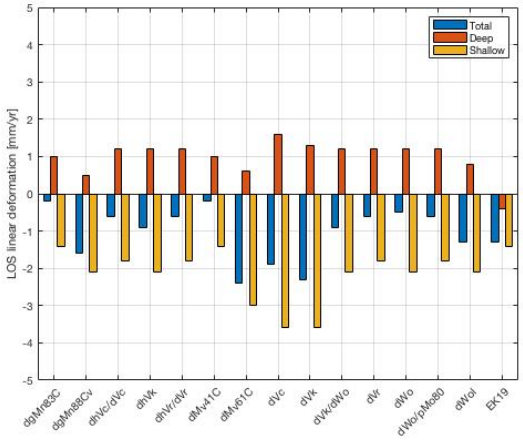
Total
Deep
Shallow
LOS linear deformation [mm/yr]
5
4
3
2
1
0
-1
-2
-3
-4
-5
dgMm83C
dgMm88Cv
dhVc/dVc
dhVk
dhVr/dVr
dMv41C
dMv61C
dVc
dVk
dVk/dWo
dVr
dWo
dWo/pMo80
dWol
EK19

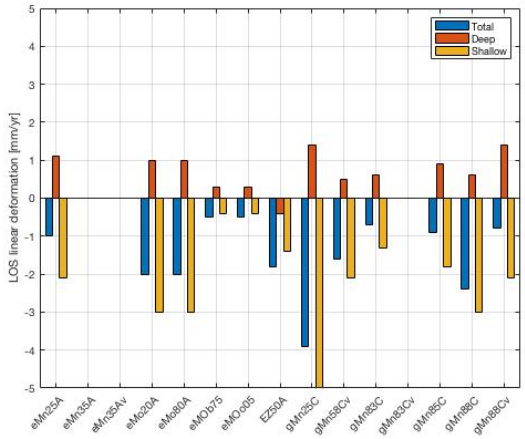
Total
Deep
Shallow
LOS linear deformation [mm/yr]
5
4
3
2
1
0
-1
-2
-3
-4
-5
eMm25A
eMm35A
eMm35Av
eMo20A
eMo80A
eMOb75
eMOo05
EZ50A
gMm25C
gMm58Cv
gMm83C
gMm83Cv
gMm85C
gMm88C
gMm88Cv

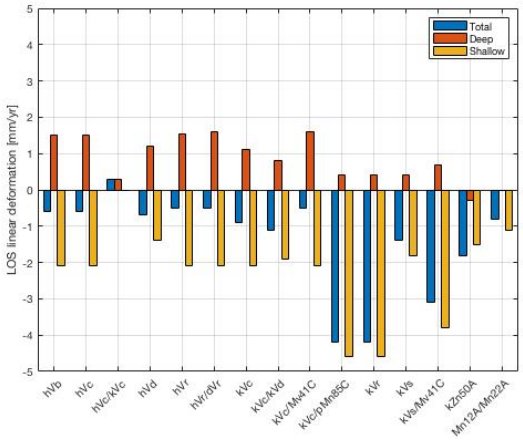
Total
Deep
Shallow
LOS linear deformation [mm/yr]
5
4
3
2
1
0
-1
-2
-3
-4
-5
hVb
hVc
hVc/kVc
hVd
hVr
hWr/dVr
kVc
kVc/kVd
kVc/Mv41C
kVc/pMm85C
kVr
kVs
kVs/Mv41C
kZm50A
Mm12A/Mm22A

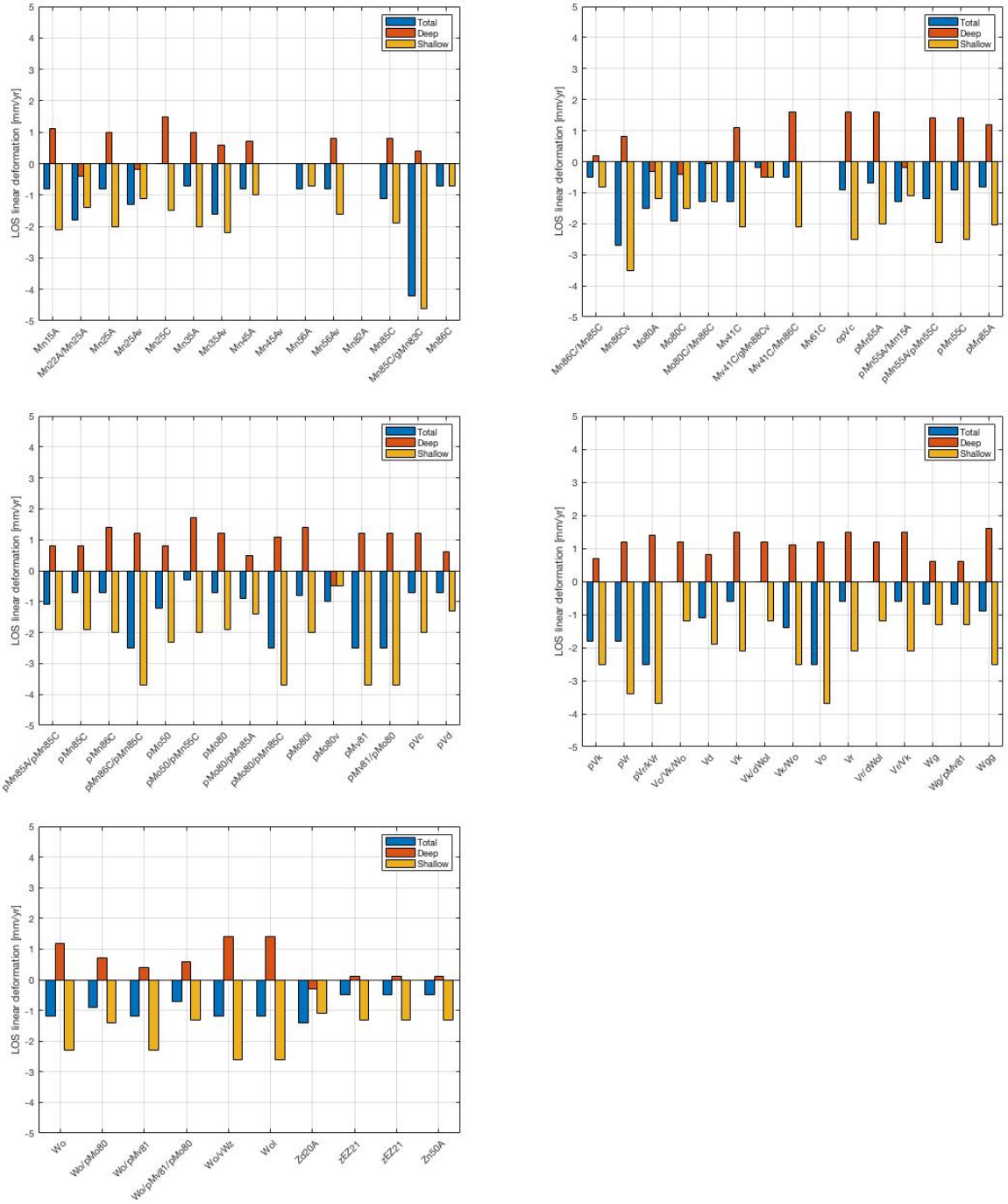

Figure E.1: Descending track 37: Total, deep and shallow LOS linear deformation (mm/yr) of all identified South Holland soil types, in alphabetical order (data: SkyGeo).

E.2. Combined Classification Results & Overview

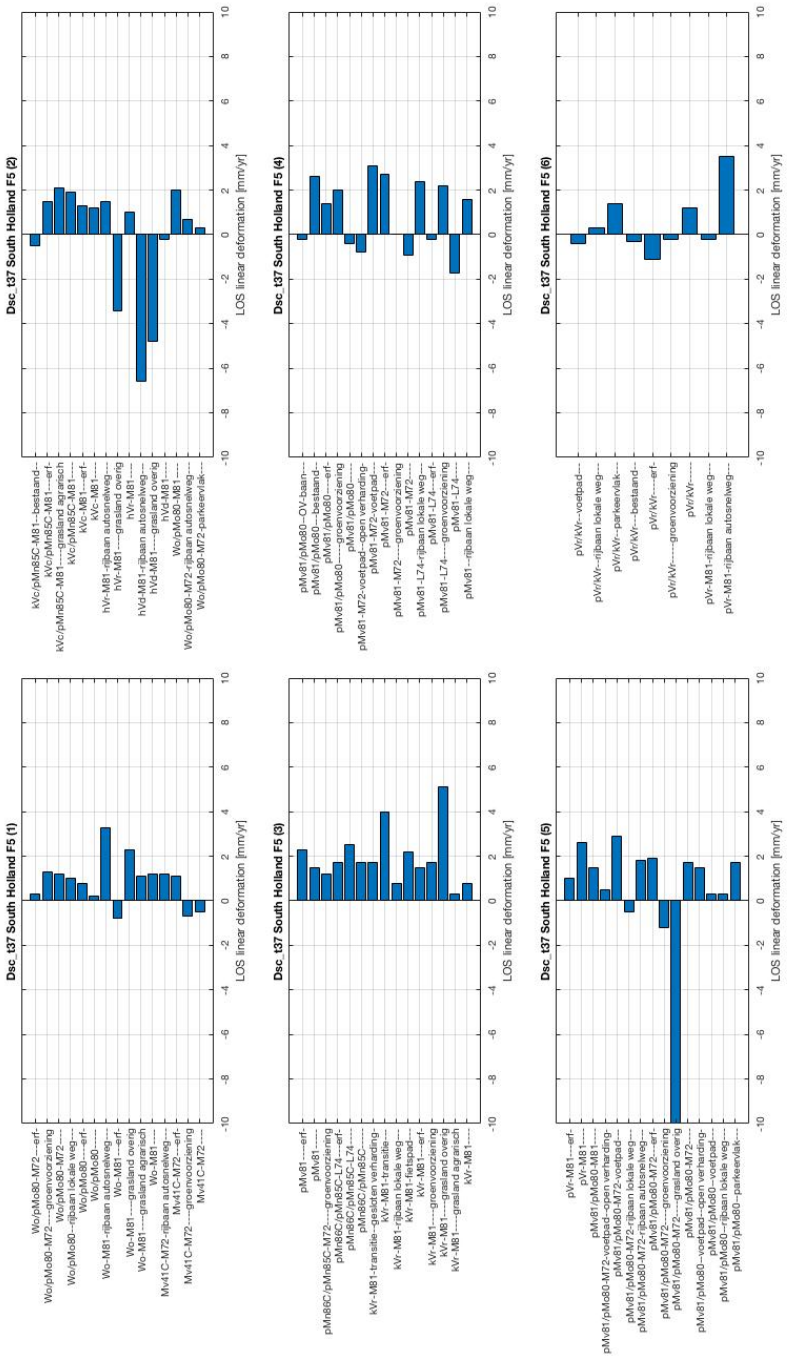

Figure E.2: Descending track 37: LOS linear deformation (mm/yr) of all unique class combinations of grid F5 in South Holland (data: SkyGeo).